The Analysis of Offshore Foundations Subjected to Combined Loading

by

Cong Luan NGO-TRAN

Brasenose College

A thesis submitted for the degree of

Doctor of Philosophy

at

the University of Oxford

Michaelmas Term, 1996

Abstract

The Analysis of Offshore Foundations Subjected to Combined Loading

A thesis submitted for the degree of Doctor of Philosophy

Cong Luan NGO-TRAN

Brasenose College, Oxford

Michaelmas Term, 1996

This thesis is concerned with four different types of offshore foundations, namely gravity foundations, jack-up foundations, the mudmats for piled jacket structures and caisson foundations for jacket structures. In most applications, these can be idealised as circular rigid foundations. Unlike onshore foundations, offshore foundations are subjected to large horizontal and moment loads. This research used the finite element method to examine the elastic behaviour and stability of circular footings under combined loading. Due to the circular shape of the footings and the combination of vertical, horizontal and moment loads, three dimensional finite element analysis was used.

In-depth analyses of the elastic behaviour of circular footings under combined loading (V, H,M) were performed. The vertical stiffness coefficient was investigated using two dimensional axi-symmetric analyses whereas three dimensional analyses were used to examine the other coefficients. Different features of offshore foundations such as footing embedment and cone angle were taken into consideration. Based on the numerical results, a set of empirical expressions for elastic stiffess coefficients was derived.

For footing stability calculations, large horizontal or moment loads can cause the footing to lose contact with the soil, or cause the footing to slide relative to the soil. In finite element analyses, this loss of contact and sliding are modelled by interface elements. A new zero-thickness iso-parametric interface element was formulated for both two and three dimensional analyses. An exact close formed solution for integration of the stress–strain relationship (for the two dimensional interface element) was found. The element is then used to explore footing stability. It was shown that by using a yield criteria which allows the interface to behave as either frictional or cohesive interface, depending upon the normal stress, numerical stability is achieved.

The footing stability was examined by establishing the bearing capacity envelope. The envelopes for footings on undrained clays were established for surface flat strip footings and for surface flat circular footings. The effects of soil strength varying with depth, cone angle and embedment on the bearing capacity envelope were also investigated.

Acknowledgement

I would like to thank my supervisor, Professor Guy Houlsby, who conceived the overall programme of research and gave me invaluable guidance throughout. Professor Houlsby also generously allowed me to use his programs OXMESH, 2CAN.

My thanks also go to Dr Harvey Burd, who supervised me and others during the development of the new version of OXFEM. Various parts of the new version of OXFEM were written by Charles Augarde, Liu Gang and Dr Jiang-Qing Zhou, whose co-operation and excellent programming skill are gratefully appreciated. I am also very grateful to Dr Brendan Ruck for proof reading my thesis with care and a great sense of humour.

I gratefully acknowledge the support I have received as an ICI Scholar from Imperical Chemical Industries, the British Foreign and Commonwealth Office and Oxford University. In particular, I would like to extend my sincere thanks to Mr P. K. Williams, HM Ambassador to Vietnam, for the honour. I am also very grateful to Ms Chew Gaik Hean and Mr Michael Simmons of ICI for their constant encouragement. The grant from the Overseas Research Scheme (ORS) is also gratefully acknowledged.

May I take this chance to thank Clive Wood, Shinji Kayama, Mary and Martin Gainsborough, Derbie and Richard Bradley, Steve Gough, Rachel Duncan, Lindsey Shepherd and many other friends of mine who have made my three years in this country, from the beginning, such an enjoyable time and an unforgetable memory.

I am indebted to Professor Le Ba Luong, who inspired me to further study in soil mechanics. I must also record my gratitude to my friends and classmates from my childhood in the province of Long An and from my student days in Sai Gon.

I owe this thesis to my father and mother, whose lifetimes have been devoted to the luxury of education for all four of us. I also owe all to Thi, who stoically withstood time and distance in the last three long years. So to my family I wish to dedicate this thesis.

To my mother, my wife and my daughter.

Contents

List of Figures

List of Tables

List of Symbols

A	plan area of footing
A'	effective plan area of footing under eccentric load
A, B, C	least-squares fitting parameters for rotated ellipses
B	width of strip footing
B	$(= R\sqrt{\pi})$ side length of square footing having the same area as circular footing
$\mathbf{B}$	matrix relating strains for continuum finite elements, or relative displacements for interface elements, to nodal displacements
B'	width of the effective plan area of strip footings under eccentric load; width of the equivalent rectangular effective area of circular footing under eccentric load
c	cohesion of the interface
$\mathbf{C}$	matrix of direction cosines of the transformation
$\mathbf{D}$	material stiffness matrix
e	$(= M/V)$ eccentricity of footing load
e	eccentricity parameter of least square ellipses
$\mathbf{e}_1, \mathbf{e}_2, \mathbf{e}_3$	three base unit vectors of the local co-ordinate system of the interface
E	Young modulus
f	yield function
F_1	vertical flexibility coefficient
F_2	horizontal flexibility coefficient
F_3	rotation flexibility coefficient
F_4	horizontal and rotational cross coupling flexibility coefficient
g	plastic potential
G	elastic shear modulus
H	horizontal load
H_0	maximum horizontal load capacity when $M = 0$

J	Jacobian of the transformation from global to local coordinates
K	elastic bulk modulus
K_n	normal stiffness of interface elements
K_s	shear stiffness of interface elements
K_1	vertical stiffness coefficient
K_2	horizontal stiffness coefficient
K_3	rotation stiffness coefficient
K_4	horizontal and rotational cross coupling stiffness coefficient
M	moment load
M_0	maximum moment load capacity when $H = 0$
$\mathbf{N}$	shape function matrix
p'	effective mean normal stress
p'_0	effective mean normal stress during isotropic normal consolidation; reference size of (p', q) yield locus
q	deviator stress
$\mathbf{r}$	global co-odinates of a point in the interface
R	footing radius
$\mathbf{R}$	global nodal co-odinates matrix
s_e	standard error of the estimate
$s_{e,i}$	standard error of individual regression parameter i
s_u	undrained shear strength
s_{um}	s_u at mud line level
t	time
$u, \dot{u}$	horizontal displacement and horizontal displacement rate
v	specific volume
V	vertical load
V_0	maximum vertical load capacity
w	vertical displacement
z_D	footing embedment depth
z_m	metacentre depth
α	inclination angle of footing load (from vertical); local co-ordinate axis of the interface

α_s	α at transition from sliding to bearing failure
β	footing cone angle; local co-ordinate axis of the interface
β_1, β_2	exponent in the equation for (V,H) and (V,M) loci
γ'	effective unit weight of the soil
$\varepsilon_1, \varepsilon_2, \varepsilon_3$	tangent relative displacements and normal relative displacement, respectively (interface elements)
$\boldsymbol{\epsilon}$	$(= [\varepsilon_1\ \ \varepsilon_2\ \ \varepsilon_3]^T$ for two dimensional elements, or $[\varepsilon_s\ \ \varepsilon_n]^T$ for one dimensional elements) matrix of relative displacements (interface elements)
ϕ	angle of friction
ψ	angle of dilation
μ_{cone}	reduction factors due to cone angle for elastic stiffness coefficients
μ_{trench}	reduction factors due to footing embedment for elastic stiffness coefficients
ν	Poisson's ratio
ω	direction of displacement increment in $(u/R, \theta)$ space
Ω	direction of load increament in $(H, M/R)$ space
θ	footing rotational displacement
$\dot{\theta}$	footing rotational displacement rate
ρ	rate of undrained strength increase with depth
ρ	rotation of cross sectional ellipse of the bearing capacity envelope
σ	normal stress of interface element
$\boldsymbol{\sigma}$	$(= [\tau_1\ \ \tau_2\ \ \sigma]^T$ for two dimensional elements, or $[\tau\ \ \sigma]$ for one dimensional elements) matrix of stresses (interface elements)
τ	shear stress of one dimensional interface element
τ_1, τ_2	shear stresses of two dimensional interface element
χ^2	least squares merit function

Subscripts

cone	conical footing
int	intersection between cross sectional ellipse of the bearing capacity envelope and the (H,M) coordinate axes
surf	surface footing

flat	flat footing
trench	embedded footing
u	upper layer of the interface
l	lower layer of the interface

Supercripts

e	elastic component
ep	combined elastic and plastic component
m	(stiffness cofficient at) the metacentre
p	plastic compoment
s	stiffness cofficient at the soil surface level
u	upper layer of the interface
l	lower layer of the interface

Chapter 1

Introduction

1.1 Offshore foundations

There are five main types of offshore foundations: gravity, jack-up, piled, compliant platforms and jackets on caisson foundations. Gravity platforms depend on their own weight to provide foundation stability against the vertical and horizontal loads imposed by the environmental conditions. They are generally supported by relatively large foundation elements bearing on the unprepared ocean floor. Fig. 1.1 illustrates a typical concrete gravity platform, the Statfjord in the North Sea. The base of the structure consists of 24 cells in a honeycomb configuration, each cell being about 20 m across with walls of 1 m thick; these cells serve as storage units for crude oil and diesel fuel.

The second type of offshore platforms – jack-up rigs – is used extensively offshore around the world to drill oil and gas wells in water depths up to about 100 m. A mobile jack-up rig is a floatable drilling platform (self-propelled or towed by tugs) with legs that can be moved up and down as shown in Fig. 1.2. The rig is floated to the well site with its legs elevated (Fig. 1.2a). When it reaches the site, the legs are lowered and jacked into the sea bottom to produce a foundation. A process of preloading is then started with water being pumped into ballast tanks in the hull, forcing the footings to penetrate deeper into the seabed (Fig. 1.2b). Once the ballast tanks are emptied, the hull is jacked to the operation elevation as shown in Fig. 1.2c.

The vast majority of present day jack-up rigs are of the independent leg type as shown in Fig. 1.3. Some typical foundations of independent leg jack-up rigs (commonly known as

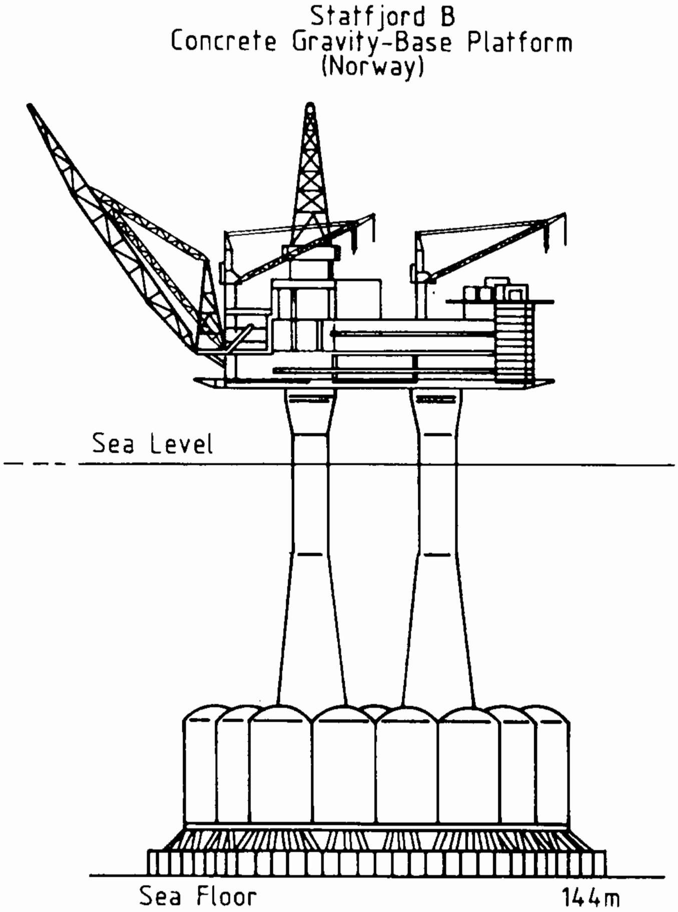

Figure 1.1: A typical gravity platform (after Ellers, 1982).

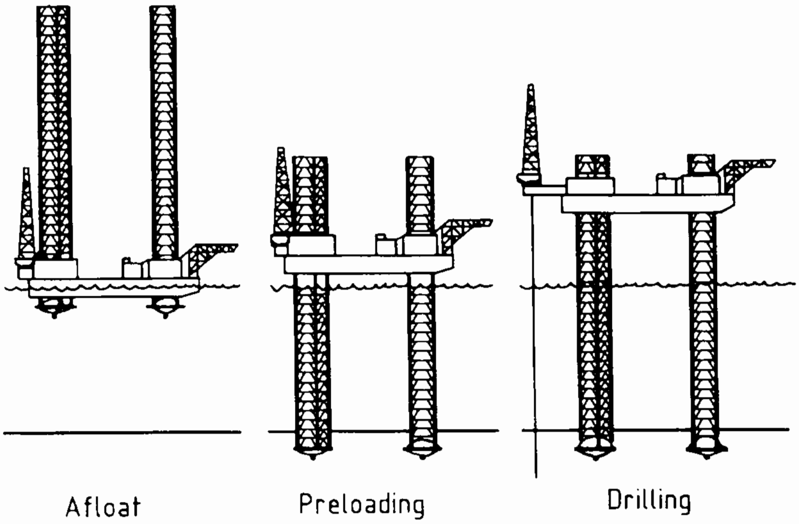

Figure 1.2: Operational modes of jack-up rigs (after McClelland et al., 1982).

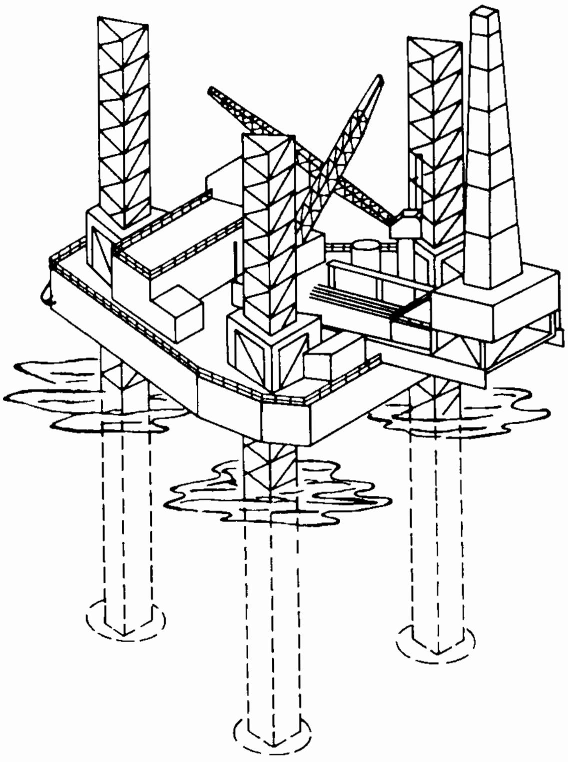

Figure 1.3: Jack-up rig with independent leg unit (after Hambly, 1985).

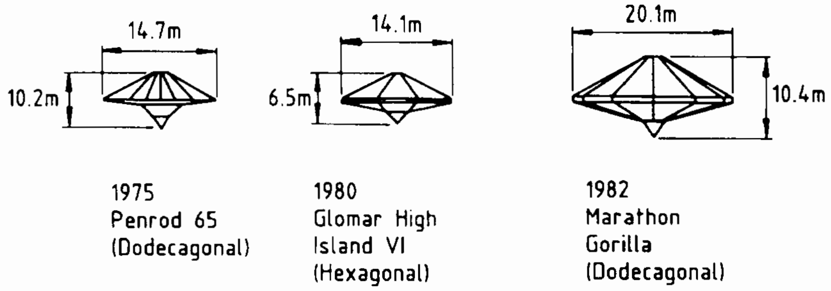

Figure 1.4: Typical footing (spudcan) configuration (after McClelland et al., 1982).

'spudcan' footings) are shown in Fig. 1.4. Most spudcans are approximately circular in plan, typically with a shallow conical underside profile and a sharp protruding spigot to facilitate initial location and to provide extra horizontal stability.

Whilst the two types of offshore platforms mentioned above achieve stability through the action of the foundation bearing on the sea bed, platforms of the third type achieve their stability through a piled foundation that anchors the structure to the sea bed. Prior to foundation pile installation, the pile jacket structures require temporary support. One method to provide this temporary support is using mudmat foundations; a typical mudmat foundation is shown in Fig. 1.5.

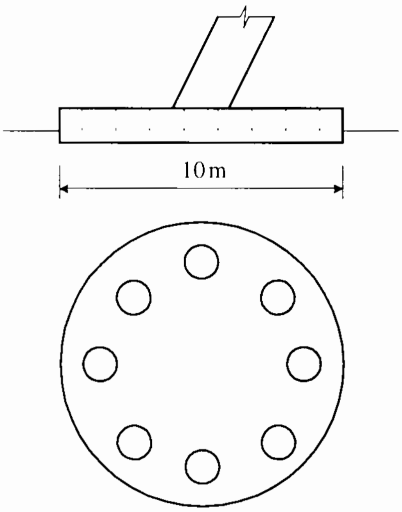

Figure 1.5: An example of mudmat foundations.

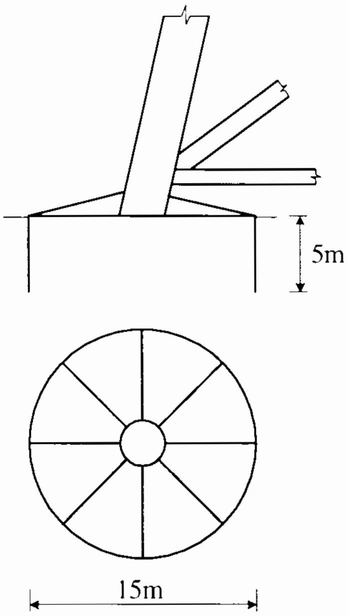

Figure 1.6: An example of caisson foundations.

Whilst gravity and piled platforms are fixed, compliant platforms such as tension leg platforms and guyed towers move with wind, waves and current. The problem of compliant platforms is, however, out of scope of this thesis, but further details on tension leg platforms can be found in Poulos (1988).

Caisson foundations (also called 'bucket foundations') consists of a circular plated base attached to the jacket leg. The circular plated base is connected to a perimeter skirt which, when installed, penetrates into the seabed. Fig. 1.6 shows an example of the bucket foundations.

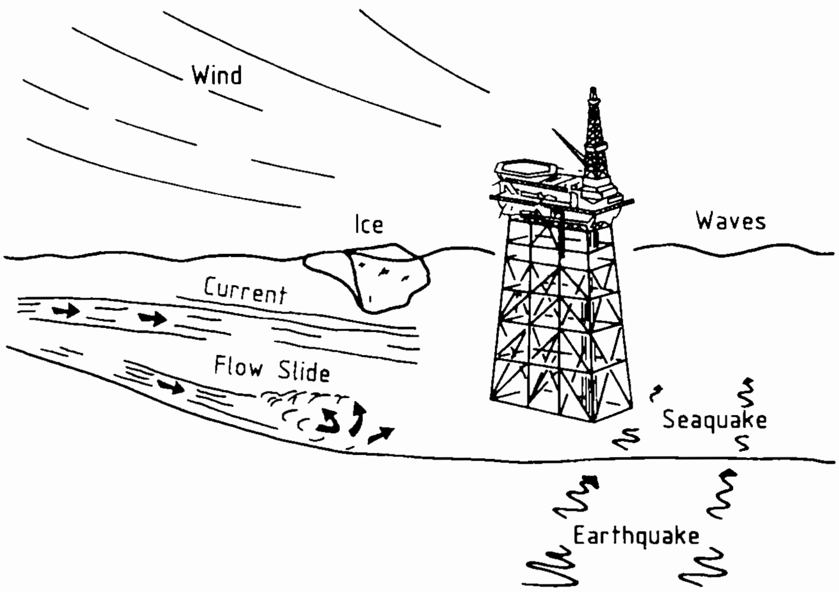

Figure 1.7: Environmental forces on offshore structures (after Selnes, 1982).

Though the four types of foundations (gravity, jack-up, mudmat and caisson foundations) vary largely in size and are designed for different purposes, they share some common features. Firstly, offshore structures of all types are subjected to a combination of environmental forces such as waves, currents, wind and possibly earthquakes (see Fig. 1.7). These forces are usually more hostile than those on conventional onshore structures. The lateral load is a substantial fraction of the vertical load, and the overturning moment is also very large compared to those on onshore structures. Furthermore, there is a major cyclic component of vertical load and horizontal load.

Secondly, compared to onshore foundations, offshore foundations are usually very large. One of the implications of this large scale is that the variation of soil properties with depth becomes significant and needs to be accounted for (see, for example, Davis & Booker, 1973).

Thirdly, footing embedment is an important feature for some offshore foundations. As embedment into the seabed can significantly improve the performance of shallow offshore foundations, jack-up rigs are usually preloaded so that they penetrate into the seabed before operation. Also, with the perimeter skirt penetrating into the seabed, caisson foundations are essentially embedded footings.

In addition, the sea bed deposits are often normally consolidated and extrememely soft and compressible near the sea floor (Poulos, 1988); some also exhibit unusual behavioural characteristics (e.g. calcareous sands, diatomaceous sands, etc.)

1.2 Design of offshore foundations

The design of offshore foundations consists of two main stages: stability analyses and deformation analyses. In the preliminary analysis of foundation stability, semi-empirical bearing capacity formulae (such as Meyerhof, 1956; Hansen, 1970; Vesic, 1975) are usually used. One feature these bearing capacity formulae have in common is that they are based on limit-equilibrium solutions, which are then combined using empirical and semi-empirical factors to take into account the footing (planar) shape, footing embedment depth, and the load inclination and eccentricity. In final stages of design, more accurate analyses using, for example, the finite element method, are performed for modern platforms.

The problem with analyses using both semi-empirical formulae and rigorous finite element analyses is that, as argued by Butterfield (1981), this process results in "a single number which the designer is obliged to accept without either any measure of its real validity or how it will vary in relation to changes of load inclination or eccentricity". Butterfield (1981; 1993) further demonstrated that using the conventional bearing capacity formulae it is difficult to determine the safety factor of the footing and that any factor may be misleading. He therefore suggested an alternative approach called 'interaction diagrams' (or bearing capacity envelopes) in the $(V, H, M/B)$ space. Note that a similar approach was suggested by Roscoe & Schofield (1956). In the same way as the yield surface is used in the plasticity theory, the bearing capacity envelope defines a boundary surface for combined loads in the load space (V,H,M). This approach is discussed in more detail in Chapter 6.

Another concern about the bearing capacity formulae is that they are primarily intended for use for conventional shallow foundations. In contrast to these, offshore foundations are subjected to large horizontal and moment loads, and sliding failure is frequently critical. Also, typical jack-up foundations have a conical underside profile to provide extra horizontal stability, which is not taken into account by the conventional bearing capacity formulae.

The predictions of vertical, horizontal and rotational movements are usually made using either (a) a simple hand method which employs the theory of elasticity (reviewed in Chapter 2); or (b) the finite element method (Poulos, 1988). For most cases of offshore foundations under combined loading, these elasticity formulae are inexact and only approximate methods. Also, there is a lack of solutions for embedded or conical footings which are usually used in offshore foundations.

In addition, the usual approach does not allow accurate analyses in which the interaction between soil and structure is taken into consideration. A numerical model for the behaviour of spudcan shaped foundations on an undrained clay under combined loads based on the work hardening plasticity theory is proposed by Martin (1994). This model allows prediction of both bearing capacity and displacements of the footing under combined loadings.

1.3 Aims of this study

The purpose of this research is to develop benchmark solutions to a broad category of problems. Parametric studies will be carried out to cover ranges of values of appropriate parameters such as footing cone angle, footing embedment, as well as soil strength varying with depth. As the gravity, jack-up, mudmat and caisson foundations can be in most cases be idealised as large rigid circular footings, this research will be focused on the behaviour of circular footings.

The finite element method is used so that a wide range of problems with different boundary conditions, footing geometry and soil profile can be addressed. Due to horizontal and moment loads, three dimensional finite elements are used. Note that with problems of axi-symmetric geometry subject to non-symmetrical loading, the standard two dimensional axi-symmetric method can be extended to deal with non-symmetric loading approximately using harmonic loading method (Wilson, 1965; Zienkiewicz, 1983). This method has been used for the problem similar to that of this research by Noble Denton & Associates (1987). This research, however, uses the truly three dimensional finite element method. This is possible thanks to the advance of computer processing power. Comparison with the harmonic loading method can thus be made in the future.

Elastic behaviour of circular footings under all vertical, horizontal and moment loads is investigated in detail. As a result, a new set of empirical formulae are proposed to be used to calculate the elastic deformations of a wide range of circular footings. Most common features of offshore foundations, such as footing cone angle and embedment, are addressed.

Accurate solutions for large horizontal loads and moments require a special finite element called an 'interface element' (or slip element) to model the relative movement between the footing and the soil (i.e. sliding or losing the contact). This thesis is, therefore, also concerned with the development a new interface element. Though only two dimensional interface elements are needed for three dimensional analyses, a one dimensional interface element is first formulated for two dimensional plane strain analsyses; it is used to investigate the stability behaviour of a strip footing in order to validate the interface.

The stability behaviour of circular footings subjected to combined undrained loading is investigated and the bearing capacity envelopes are established. In addition to that of a flat, surface footing on uniform soil, the bearing capacity envelopes (or interaction diagrams) for different conical footings is also established. The effects of soil strength varying with depth and footing embedment are also considered.

Note that even though the assumption of circular shape is not necessary in three dimensional finite element analyses, it is used for this parametric studies in order to simplify parameters to be considered. Data for circular footings can also be used to approximate the performance of footings of other geometric shapes.

This thesis is concerned with the undrained behaviour of footing under monotonic loading. The problems of cyclic loading and consolidation are, of course, very important for offshore foundations, but are beyond the scope of this research. In addition, all the calculations in this thesis are small-strain analyses.

1.4 Outline of thesis

Each chapter from Chapter 2 to Chapter 7 addresses one of the above-mentioned topics. Note that the previous literature relevant to the topic of each chapter is reviewed at the beginning of the chapter.

Chapter 2 is concerned with the elastic behaviour of circular footings. Because two dimensional axi-symmetrical analyses are well-established and fast to run, the vertical stiffness coefficients are calculated using axi-symmetrical finite element analyses. The study is then extended to investigate other stiffness coefficients using three dimensional finite element analyses. Based on the results obtained from these numerical analyses, empirical formulae are established for the calculation of all stiffness coefficients.

In Chapter 3 and Chapter 4, the formulation of one and two dimensional interface elements are presented. Though both elements are iso-parametric and use the same plasticity theory frameworks, their formulation differ significantly in terms of the kinematic equations and stress updating routines. An exact close form solution for the integration of the stress–strain relationship for the two dimensional interface element is presented in Chapter 4.

The one dimensional interface element is then used in a number of plane strain analyses in Chapter 5 to explore the (V, H, M) bearing capacity envelope of strip footings.

Chapter 6 presents the results of detailed three dimensional finite element analyses, and the bearing capacity envelope of a flat surface circular footing on a uniform soil profile. An in-depth analysis of the results is also made and an empirical mathematical expression for the envelope is derived.

In Chapter 7, the effects of soil strength varying with depth, footing cone angle, and footing embedment on the bearing capacity envelope are examined.

Chapter 8 summarises the main findings of this research, and suggests some areas requiring further work.

Chapter 2

Elastic Behaviour of Circular Footings

2.1 Introduction

Besides the ultimate bearing capacity, which is essential to the design of offshore foundations, the elastic behaviour of offshore foundations is also important. It is used to estimate initially the deformations caused by the applied loads (Poulos, 1988). In addition, the elastic behaviour is used to represent the compressibility of the foundation soil for structural analyses of offshore structures. The aim of this study of elastic behaviour of the footing is to determine the dimensionless stiffness coefficients K_1, K_2, K_3, K_4 which are defined by the following equation:

$$\begin{aligned} \left\{ \begin{array}{c} V/(GR^2) \\ H/(GR^2) \\ M/(GR^3) \end{array} \right\} &= \begin{bmatrix} K_1 & 0 & 0 \\ 0 & K_2 & K_4 \\ 0 & K_4 & K_3 \end{bmatrix} \left\{ \begin{array}{c} w/R \\ u/R \\ \theta \end{array} \right\} \\ &= \mathbf{Ku} \end{aligned} \tag{2.1}$$

where w, u, θ are vertical displacement, horizontal displacement and rotation angle, respectively, and V, H, M are the corresponding forces and moment; G is the elastic shear modulus; R is the radius of the footing; K_1, K_2, K_3, K_4 are vertical, horizontal, moment and coupling stiffness coefficients, respectively. The other terms in the matrix $\mathbf{K}$ must be zero from symmetry considerations.

Various features of offshore footings such as embedment, and cone angle are taken into account in this study. The problem is depicted schematically in Fig. 2.1. Also shown in the figure is the sign convention of loads and displacements.

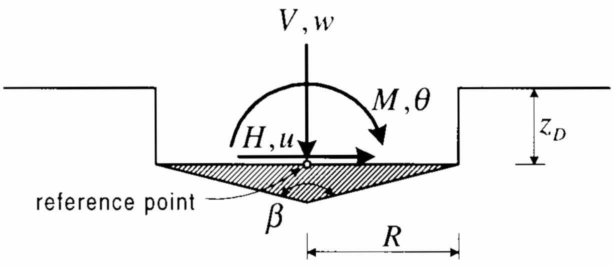

Figure 2.1: Definition of parameters to be examined.

The study has two main parts. First of all, because two-dimensional axi-symmetrical analyses are well-established and fast to run, the stiffness coefficients are calculated using axi-symmetrical finite element analyses. With axi-symmetrical analyses, embedment, and cone angle of the footing can be taken account but only the vertical stiffness coefficient K_1 can be calculated. Therefore, in the second part of this study, three dimensional analyses are used to calculate K_2, K_3, K_4.

The purpose of this study is to extend the work of Bell (1991) in this area.

2.2 Literature review

2.2.1 Surface and flat footing

For vertical loading solutions are available for both cases of rough and smooth footings and they are exact solutions. For rough footings, the work by Spence (1968) gives:

$$w = \left[\frac{1-2\nu}{4GR\ln(3-4\nu)}\right]V \tag{2.2}$$

For a smooth footing, the solution given by Poulos & Davies (1974) is as follows:

$$w = \frac{1-\nu}{4GR}V \tag{2.3}$$

Equ. 2.1 can be rewritten to express deformations in terms of loads by inverting the stiffness relationship:

$$\begin{Bmatrix} w/R \\ u/R \\ \theta \end{Bmatrix} = \begin{bmatrix} F_1 & 0 & 0 \\ 0 & F_2 & F_4 \\ 0 & F_4 & F_3 \end{bmatrix} \begin{Bmatrix} V/(GR^2) \\ H/(GR^2) \\ M/(GR^3) \end{Bmatrix} \tag{2.4}$$

Table 2.1: Numerical results for horizontal and moment loading of a rough flat surface footing (after Bell, 1991).

ν	*Horizontal displacement* K_2	K_4	w_{edge}/u (%)	*Rotation* K_4	K_3	u/w_{edge} (%)
0·0	4·271	-0·7364	22·8	-0·7364	3·227	17·2
0·1	4·443	-0·6634	19·3	-0·6634	3·441	14·9
0·2	4·639	-0·5682	15·3	-0·5682	3·716	12·2
0·3	4·868	-0·4401	10·8	-0·4401	4·088	9·04
0·4	5·145	-0·2590	5·60	-0·2590	4·628	5·03
0·49	5·474	-0·0144	0·27	-0·0144	5·410	0·26

where the coefficients of the matrices **F** and **K** are related as follows:

$$\begin{aligned} F_1 &= \frac{1}{K_1} \\ F_2 &= \frac{K_3}{K_2K_3 - K_4^2} \\ F_3 &= \frac{K_2}{K_2K_3 - K_4^2} \\ F_4 &= \frac{-K_4}{K_2K_3 - K_4^2} \end{aligned} \tag{2.5}$$

One feature of both Equ. 2.1 and Equ. 2.4 is the coupling of horizontal and moment loading through the coefficient K_4. Bell (1991), using finite element analyses, shows that such a coupling effect exists for rough footings on a compressible material. In order to measure the significance of the coupling effect, for the case of pure horizontal loading, he uses the ratio w_{edge}/u which can be determined as follows:

$$\frac{w_{\mathrm{edge}}}{u} = \frac{F_4}{F_2} \tag{2.6}$$

where $w_{\mathrm{edge}} = R\theta$ is the maximum vertical displacement of the edge of the footing corresponding to the rotation θ. Similarly, for the case of pure moment loading, the following relationship results:

$$\frac{u}{w_{\mathrm{edge}}} = \frac{F_4}{F_3} \tag{2.7}$$

The two ratios are included in Table 2.1 with the stiffness factors and they show a significant coupling between rotational and horizontal displacement. For $\nu = 0{\cdot}2$, which is a representative value for drained sand, the ratios are in the range of 12% to 15%. It also shows that the two components become independent at $\nu = 0{\cdot}49$, with K_4 approaching zero.

This existence of the coupling effect is, however, not accounted for in any analytical solutions dealing with this problem. Two solutions exist for the horizontal loading of a rigid, rough circular footing. The first solution, which is given by Bycroft (1956):

$$u = \frac{7-8\nu}{32GR(1-\nu)}H \tag{2.8}$$

is apparently based on the assumption that the footing should not deflect vertically at any point. However, it turns out that the resulting solution does involve some vertical deformation (Bell, 1991) and is therefore not exact.

The second solution, by Gerrard & Harrison (1970), allows a vertical displacement, but freely, rather than conforming to the rotation of a rigid footing as it should be. The solution takes the form:

$$u = \frac{2-\nu}{8GR}H \tag{2.9}$$

This solution is therefore not exact either. However, the fact that it allows vertical displacement, though not exactly rigid rotation, may be the reason for it being in better agreement with Bell's (1991) numerical result, in which the footing is rigid, than Bycroft's (1956). This is shown in Fig. 2.2. In the range of Poisson's ratio from 0 to 0·49, the Gerrard & Harrison (1970) solution is consistently higher that the finite element solution, whereas the Bycroft (1956) solution overestimates K_2 at low Poisson's ratio but underestimates at high Poisson's ratio.

For smooth footings, no horizontal load can be applied and the solution for moment loading can be found in Poulos & Davies (1974) (which refers to Borowicka, 1943) as follows:

$$\theta = \frac{3(1-\nu)}{8GR^3}M \tag{2.10}$$

which is an exact solution for a smooth footing.

2.2.2 Solutions for embedded footings

When a footing is placed at a depth below the soil surface, the settlement, in general, will be smaller than that of the same footing located on the surface. This is because, for an embedded footing, the overlying soil mass restricts the footing movement, whilst a surface footing under the same loading condition can deform without that restriction.

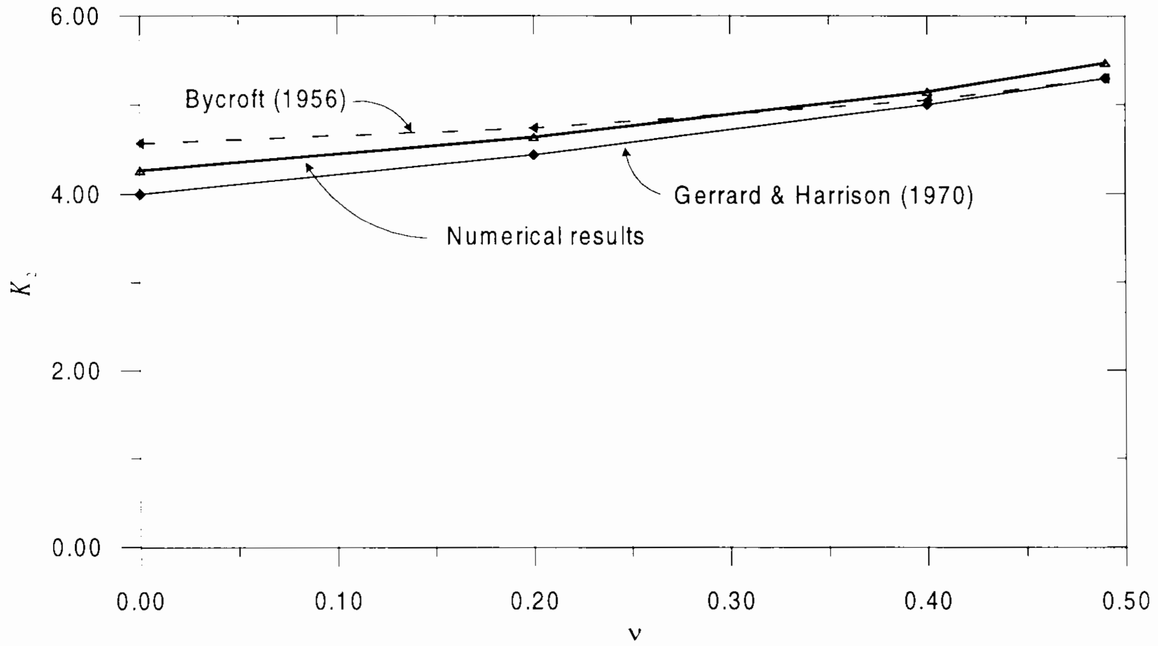

Figure 2.2: Results of elastic horizontal loading analyses of a flat surface footing (after Bell, 1991).

(a) Case 1 (b) Case 2 (c) Case 3

Figure 2.3: Cases of embedment: (a) bottom of a trench; (b) covered footing; (c) full sidewall contact.

Three cases of embedment are illustrated in Fig. 2.3. The footing of case 1 is at the bottom of the trench and there is no contact between the sidewall and the footing. This is particularly relevant to spudcan footings, which penetrate the soil during preloading. Because it is common that the sidewall collapses into the trench, covered footings (case 2) have also been examined in the literature by several authors (Butterfield & Banjerjee, 1971). Case 3, which resembles mudmats or gravity foundations, takes into account the contact between the sidewall and the footing.

Whereas the footing of case 1 is considered reasonable for the case of spudcan foundations, there are doubts about how well the other two cases can model real problems. In case 2, the assumption of the soil being homogeneous (i.e. the soil that collapses to cover the footing has the same characteristics as the soil below) could overestimate the stiffness of the footing. A more realistic solution would be rather complicated in the sense that more parameters need to be introduced. A footing of case 3 predictably would have a higher stiffness, particularly K_2, K_3, and K_4, than footings of the first two cases. This is due to transfer of the load to the soil through the sidewall. However, there is uncertainty about whether, in reality, the soil and the footing at the sidewall remain in contact during horizontal and moment loading. As the horizontal and moment loading are, in reality, associated with significant vertical loading, the contact of the bottom of the footing against the soil base is retained, but the contact at the sidewall may still be lost. Because of these difficulties with cases 2 and 3, only case 1 is investigated in this research.

Unfortunately, there are no exact closed-form solutions for any case of embedment. The only known analytical elastic solution for an embedded rigid circular footing under combined loading is provided by Gerrard (1980). However, the solution is not in closed form and would need a computer-based technique to solve.

As far as empirical solutions are concerned, Gazetas et al. (1985) give an analytical expression for estimating the elastic vertical settlement of an arbitrarily shaped embedded rigid foundation as follows:

$$w = \mu_{\text{wall}}\,\mu_{\text{trench}}\,w_{\text{surf}} \tag{2.11}$$

where w_{surf} is the vertical settlement of an equivalent surface footing, μ_{trench} is the reduction in settlement for a footing embedded in a trench (with no side wall contact, i.e. embedment case 1), and μ_{wall} is the further reduction in settlement due to sidewall contact. Gazetas et al. (1985) develop expressions for μ_{trench} and μ_{wall} for Poisson's ratio in the range of 0·25 to 0·49, and for embedment depth ranging from 0 to $2{\cdot}5R$. Given the circular shape, the original solution for an arbitrarily shaped embedded rigid foundation reduces to:

$$\begin{aligned} w_{\text{surf}} &= 0{\cdot}99\left[\frac{1-\nu}{4GR}\right]V \\ \mu_{\text{trench}} &= 1-0{\cdot}08\frac{z_D}{R} \\ \mu_{\text{wall}} &= 1-0{\cdot}23\left(\frac{z_D}{R}\right)^{0{\cdot}54} \end{aligned} \tag{2.12}$$

and because only the embedment case 1, which allows no sidewall contact, is being considered here, μ_{wall} can also be omitted. Note that in the above equation μ_{trench} is independent of Poisson's ratio. Note also that w_{surf} in Equ. 2.12 has the same form as that of smooth footings (Equ. 2.3), differing in magnitude by only 1%.

Another empirical solution is also established for embedded footings under horizontal loads by Gazetas & Tassoulas (1987). Using stiffness, rather than flexibility, coefficients, they found that for surface footings the horizontal stiffness coefficient can be determined by the following expression:

$$K_{2,\text{surf}} = \frac{2LG}{2-\nu}\left(2+2{\cdot}5\left(\frac{A_b}{4L^2}\right)\right) \tag{2.13}$$

For circular footings,

$$\begin{aligned} \frac{A_b}{4L^2} &= \frac{\pi}{4} \\ L &= R \end{aligned} \tag{2.14}$$

and hence the horizontal stiffness coefficient is determined by:

$$K_{2,\text{surf}} = 4{\cdot}04\,\frac{2RG}{2-\nu} \tag{2.15}$$

which also differs in magnitude with the closed form solution for horizontal loading (Equ. 2.9) by 1%.

Having performed boundary element analyses for footings embedded at $z_D/R = 0{\cdot}5$, 1, 1·5 and 2 on an elastic soil with $\nu = 0{\cdot}33, 0{\cdot}4$ and $0{\cdot}49$, Gazetas & Tassoulas (1987) conclude that Poisson's ratio has practically no effect on the trench factor μ_{trench} of the horizontal stiffness coefficient. An expression for μ_{trench} is given:

$$\mu_{\text{trench}} = \frac{1}{1+0{\cdot}15\sqrt{\frac{z_D}{R}}} \tag{2.16}$$

and it is shown that the data points obtained from the boundary element analysis scatters within ±2·5% around the curve of Equ. 2.16.

There is no solution, exact or approximate, known to be available for moment loading except finite element analyses. Bell (1991) performed three dimensional finite element analyses for embedded footings in addition to surface footings. For the vertical stiffness coefficient K_1, Bell (1991) showed that (Fig. 2.4a) the embedment has a significant effect on the coefficient; for undrained loading $\nu = 0{\cdot}49$, at the embedment depth of one radius, the vertical stiffness coefficient increases by 15%. At the embedment depth of $z_D/R = 4$, which is the deepest embedment depth investigated by Bell (1991), the trench factor μ_{trench} is still decreasing.

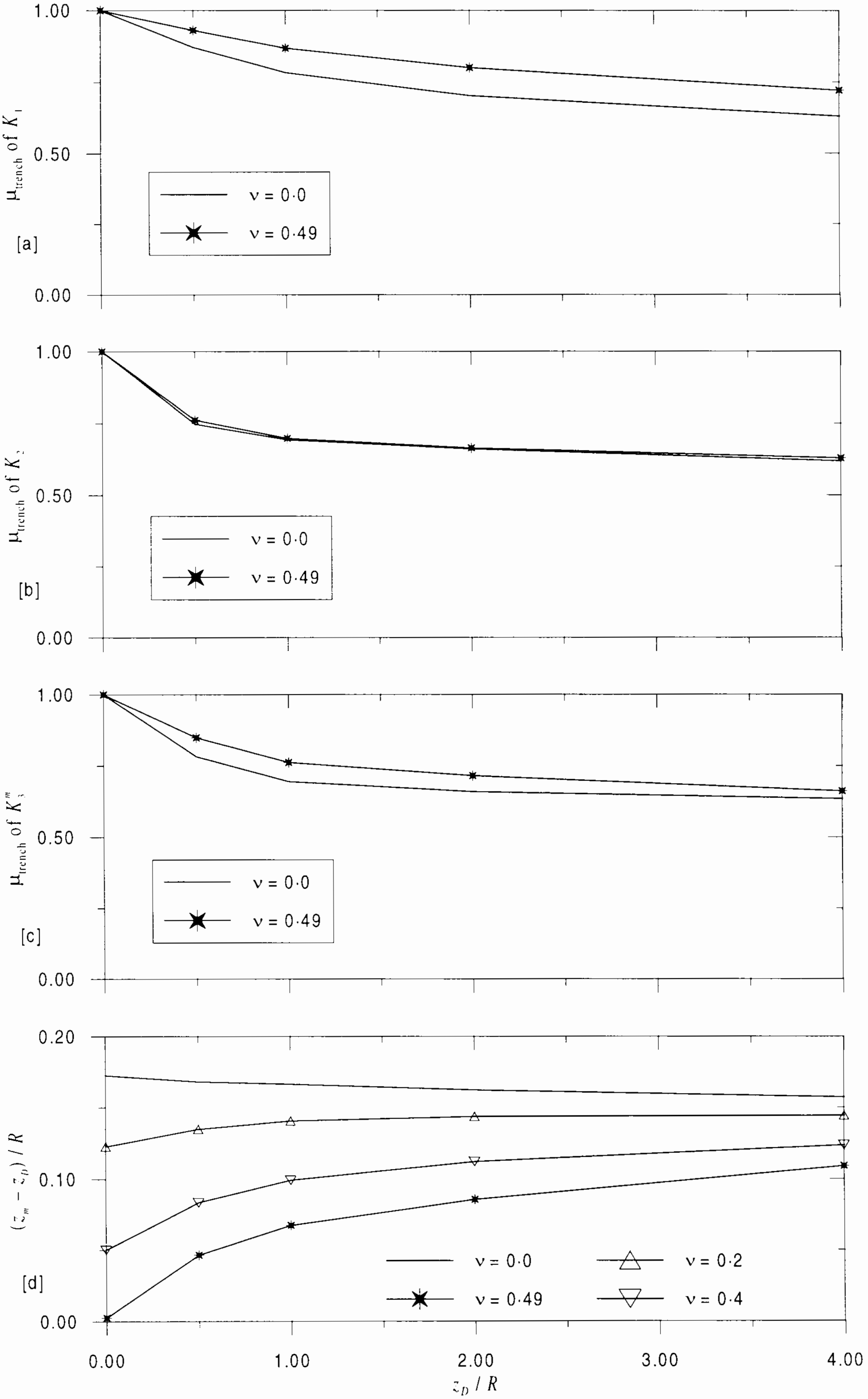

Figure 2.4: Effect of embedment on stiffness coefficients (data from Bell, 1991).

On the other hand, the horizontal stiffness coefficient K_2 change very little after the embedment depth reaches about $z_D/R = 2$ as shown in Fig. 2.4b. At this embedment depth, K_2 is 40% higher than that of a surface footing.

It is also shown in Figs. 2.4a and b that whilst the effect of embedment on K_1 varies significantly with Poisson's ratio, that is not the case for K_2. At $z_D/R = 2$, the trench factor μ_{trench} of the vertical stiffness coefficient (Fig. 2.4a) is 0·63 for $\nu = 0{\cdot}49$, and 0·72 for $\nu = 0$, which is a difference of 18%. Also, at this embedment ($z_D/R = 2$), the trench factor μ_{trench} of the horizontal stiffness coefficient (Fig. 2.4b) is 0·63 and 0·62 for $\nu = 0$ and $\nu = 0{\cdot}49$, respectively – a difference of only 1·6%.

Bell (1991) proposes the use of 'metacentre' for analysis of the moment stiffness coefficients and the coupling effect. The metacentre is the reference point at which the coupling stiffness coefficient K_4 is zero. Thus instead of using the set of parameters corresponding to the default reference point (K_3 and K_4), two parameters corresponding to the metacentre (location of the metacentre z_m and the moment stiffness at the metacentre K_3^m) can be used to analyse the behaviour of the footing. In fact, as shown by Bell (1991), the two parameters corresponding to the metacentre provide a simpler way to describe the footing behaviour. As can be seen in Fig. 2.4c, the moment stiffness coefficient at the metacentre K_3^m varies with embedment in a similar way to K_1 and K_2. Fig. 2.4d shows the distance from the footing default reference point to the metacentre. Positive values for the distance mean that the metacentre always lies below the default reference point. As the curves of $\nu = 0$ and $\nu = 0{\cdot}49$ are different, all four values of Poisson's ratios are shown. The variation of the distance with embedment depth is therefore dependent on Poisson's ratio. For lower Poisson's ratio, the distance does not vary so much as for higher Poisson's ratio. Except for $\nu = 0{\cdot}49$, the distance almost reaches its steady value at about $z_D/R = 2$. More detailed discussion of the metacentre is given in Section 2.5.3.2.

Bell (1991) does not consider conical footings. Neither is there a known exact or closed-form solution for conical footings.

2.3 Evaluation of elastic stiffness coefficients using finite element analyses

As it is easier in a finite element analysis to apply displacements than loads, three sets of boundary conditions are applied in order to calculate K_1, K_2, K_3, K_4.

Rigid vertical displacement

The boundary conditions are:

$$w \neq 0; \quad u = 0; \quad \theta = 0 \tag{2.17}$$

and therefore from Equ. 2.1:

$$K_1 = \frac{V}{GRw} \tag{2.18}$$

Rigid horizontal displacement

The boundary conditions are:

$$w = 0; \quad u \neq 0; \quad \theta = 0 \tag{2.19}$$

and therefore from Equ. 2.1:

$$\begin{aligned} K_2 &= \frac{H}{GRu} \\ K_4 &= \frac{M}{GR^2u} \end{aligned} \tag{2.20}$$

The default point of reference to calculate the moment load is the intersection of the footing centre line and the plane containing the rim of the footing as shown in Fig. 2.1.

Rigid rotation

The boundary conditions are:

$$w = 0; \quad u = 0; \quad \theta \neq 0 \tag{2.21}$$

and therefore also from Equ. 2.1:

$$\begin{aligned} K_4 &= \frac{H}{GR^2\theta} \\ K_3 &= \frac{M}{GR^3\theta} \end{aligned} \tag{2.22}$$

The coupling stiffness coefficient K_4 can be calculated from both cases of horizontal and moment loadings.

Table 2.2: The effect of mesh dimensions on the accuracy of elastic analysis (after Bell, 1991).

Mesh dimensions $(D \times D)$	R/D (%)	Number of Nodes	Number of Elements	Error in Stiffness (%)
$10R \times 10R$	10·0	452	205	+10·3
$50R \times 50R$	2·0	528	239	+2·4
$200R \times 200R$	0·5	586	265	+1·1

Notes:

i. Results corresponding to a vertically loaded smooth rigid circular footing (radius *R*) placed at the surface of an elastic half-space with $\nu = 0.25$;

ii. The mesh consists of 6-noded triangular elements and is analysed using OXFEM.

2.4 Axi-symmetric analyses

2.4.1 Mesh dimensions and topology

For elastic analyses the required mesh size is much larger than that for plastic analyses. The effect of mesh dimensions on the accuracy of elastic analysis is tabulated in Table 2.2 (after Bell, 1991) showing the difference of numerical results done with three different mesh sizes against the exact solution. Bell therefore adopted a $200R \times 200R$ mesh size for his elastic analyses. The mesh adopted in the following studies is also $200R \times 200R$ in size as depicted in Fig. 2.5a. Figs. 2.5b and c, which are scaled 8 times with respect to Fig. 2.5a, show details of mesh grading in the region close to the footing, and particularly at the footing corner, (b) corresponding to the cone angle $\beta = 30°$; (c) to $\beta = 180°$.

A total of 42 different meshes are generated to cover various footing cone angles and embedment ratios. Those cone angles are 30°, 60°, 90°, 120°, 150°, 180°. Because Bell's (1991) results show that at $z_D/R = 4$ the effect of embedment depth on the vertical stiffness is still changing significantly, the depth to be investigated in this research is extended to $z_D/R = 5$. The embedment depths investigated z_D/R are 0, 0·5, 1, 2, 3, 4, 5. A utility called DFGEN is used to generate 42 input files for OXMESH. OXMESH then generates 42 meshes for OXFEM. Each of the meshes is then combined with one value of Poisson's ratio of 0·0, 0·1, 0·2, 0·3, 0·4, 0·49 creating 252 input files for OXFEM.

Fifteen-noded triangular elements with 13 Gauss points in each element are used in all

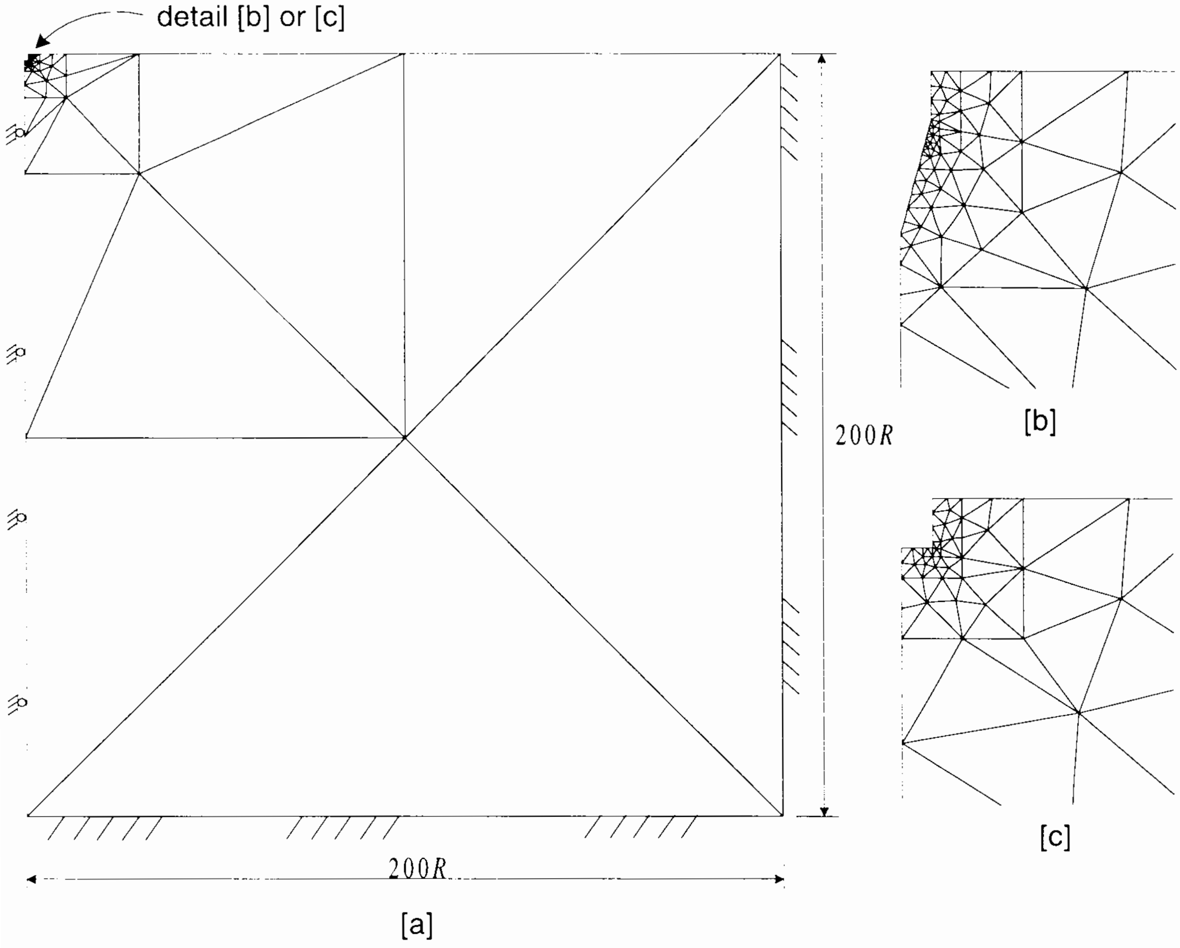

Figure 2.5: General mesh dimensions and grading: 278 15-noded triangular elements and 2353 nodes for $\beta = 30°$ and $z_D/R = 5$; 126 15-noded triangular elements and 2353 nodes for $\beta = 180°$ and $z_D/R = 0$ (flat surface footing).

Table 2.3: Vertical stiffness coefficients K_1: comparison between the exact solution, Bell's results and this study.

Solution	Poisson's ratio ν					
	0·00	0·10	0·20	0·30	0·40	0·49
Exact	4·3944	4·7776	5·2564	5·8779	6·7294	7·8441
Bell	4·5070 (2·56%)		5·3880 (2·50%)		6·9250 (2·91%)	8·1510 (3·91%)
This study	4·4621 (1·54%)	4·8497 (1·51%)	5·3340 (1·48%)	5·9624 (1·44%)	6·8257 (1·43%)	7·9864 (1·81%)

analyses.

2.4.2 Results and comparison with analytical solutions

In Table 2.3 the results for flat and surface footing ($\beta = 180°, z_D/R = 0$) for which the exact solution is available are compared with the exact analytical solution mentioned earlier. The percentage shown is the deviation from the analytical exact solution Equ. 2.2. The numerical solution compares well with the exact one. Bell's results are also reproduced for completeness. The axi-symmetric analyses are considered very accurate as the error is in the range from +1·43% to +1·81%, which is small. Therefore, other results found numerically in this study for embedded and/or conical footings (for which exact solutions are not avali-able) can be considered accurate and can be used as benchmark values for three dimensional calculations as presented in Section 2.5. The full set of results is given in Table 2.4.

In order to examine the effect of embedment on elastic behaviour, the trench factor μ_{trench} for flat footings is calculated by:

$$\mu_{\text{trench}} = \frac{K_{1,\text{surf},\text{flat}}}{K_1} \tag{2.23}$$

where $K_{1,\text{surf,flat}}$ is the vertical stiffness coefficient of a surface flat footing as determined by the finite element analyses for each Poisson's ratio.

The trench factor μ_{trench} is plotted against embedment in Fig. 2.6. It can be seen that in general the factor μ_{trench} does not vary linearly with depth as given by Gazetas et al. (1985) (see Equ. 2.12). Fig. 2.6 shows the maximum difference between numerical and Gazetas et al.'s (1985) result. In the range of embedment from 0 to 2·5, in which Equ. 2.12 is meant to be effective, the numerical results are consistently lower than Gazetas et al.'s (1985) values,

Table 2.4: Vertical stiffness coefficients K_1.

Embedment ratio	Cone angle β (degree)	Poisson's ratio ν					
		0·00	0·10	0·20	0·30	0·40	0·49
$z_D / R = 0\cdot00$	30°	8·4454	8·8474	9·3156	9·8732	10·5580	11·3400
	60°	5·7415	6·0911	6·5124	7·0344	7·7059	8·5136
	90°	5·2439	5·6099	6·0530	6·6050	7·3210	8·1964
	120°	4·8644	5·2403	5·7014	6·2853	7·0575	8·0198
	150°	4·6239	5·0067	5·4810	6·0895	6·9104	7·9713
	180°	4·4621	4·8497	5·3340	5·9624	6·8257	7·9864
$z_D / R = 0\cdot5$	30°	8·9948	9·3706	9·8062	10·3251	10·9676	11·7173
	60°	6·5784	6·9124	7·3114	7·8049	8·4478	9·2599
	90°	5·8109	6·1469	6·5571	7·0771	7·7729	8·6636
	120°	5·4407	5·7838	6·2088	6·7571	7·5064	8·4883
	150°	5·2189	5·5684	6·0060	6·5783	7·3741	8·4406
	180°	5·0445	5·3962	5·8415	6·4341	7·2834	8·4933
$z_D / R = 1\cdot0$	30°	9·6055	9·9740	10·4002	10·9078	11·5381	12·2788
	60°	7·1654	7·4899	7·8778	8·3595	8·9932	9·8127
	90°	6·3767	6·7028	7·1010	7·6073	8·2893	9·1734
	120°	5·9887	6·3222	6·7354	7·2700	8·0050	8·9784
	150°	5·7570	6·0976	6·5244	7·0839	7·8662	8·9250
	180°	5·5673	5·9117	6·3489	6·9340	7·7815	9·0155
$z_D / R = 2\cdot0$	30°	10·5803	10·9394	11·3568	11·8579	12·4878	13·2404
	60°	7·9847	8·3008	8·6817	9·1603	9·8009	10·6557
	90°	7·1187	7·4388	7·8326	8·3379	9·0263	9·9329
	120°	6·6829	7·0131	7·4250	7·9621	8·7080	9·7089
	150°	6·4230	6·7629	7·1913	7·7569	8·5551	9·6479
	180°	6·2034	6·5496	6·9926	7·5915	8·4714	9·7843
$z_D / R = 3\cdot0$	30°	11·2424	11·5924	12·0030	12·5016	13·1377	13·9111
	60°	8·4847	8·7954	9·1737	9·6548	10·3087	11·2003
	90°	7·5518	7·8699	8·2644	8·7757	9·4802	10·4199
	120°	7·0793	7·4098	7·8252	8·3717	9·1381	10·1775
	150°	6·7976	7·1397	7·5739	8·1518	8·9744	10·1119
	180°	6·5571	6·9071	7·3585	7·9739	8·8880	10·2733
$z_D / R = 4\cdot0$	30°	11·7105	12·0521	12·4564	12·9527	13·5943	14·3866
	60°	8·8162	9·1227	9·4991	9·9827	10·6480	11·5693
	90°	7·8323	8·1488	8·5444	9·0612	9·7798	10·7482
	120°	7·3327	7·6636	8·0822	8·6369	9·4209	10·4936
	150°	7·0353	7·3791	7·8181	8·4062	9·2495	10·4251
	180°	6·7801	7·1330	7·5908	8·2193	9·1603	10·6021
$z_D / R = 5\cdot0$	30°	12·0577	12·3917	12·7903	13·2844	13·9300	14·7364
	60°	9·0516	9·3546	9·7294	10·2150	10·8892	11·8337
	90°	8·0282	8·3434	8·7398	9·2609	9·9908	10·9820
	120°	7·5083	7·8394	8·2605	8·8215	9·6193	10·7183
	150°	7·1991	7·5442	7·9868	8·5828	9·4421	10·6476
	180°	6·9334	7·2883	7·7509	8·3891	9·3505	10·8353

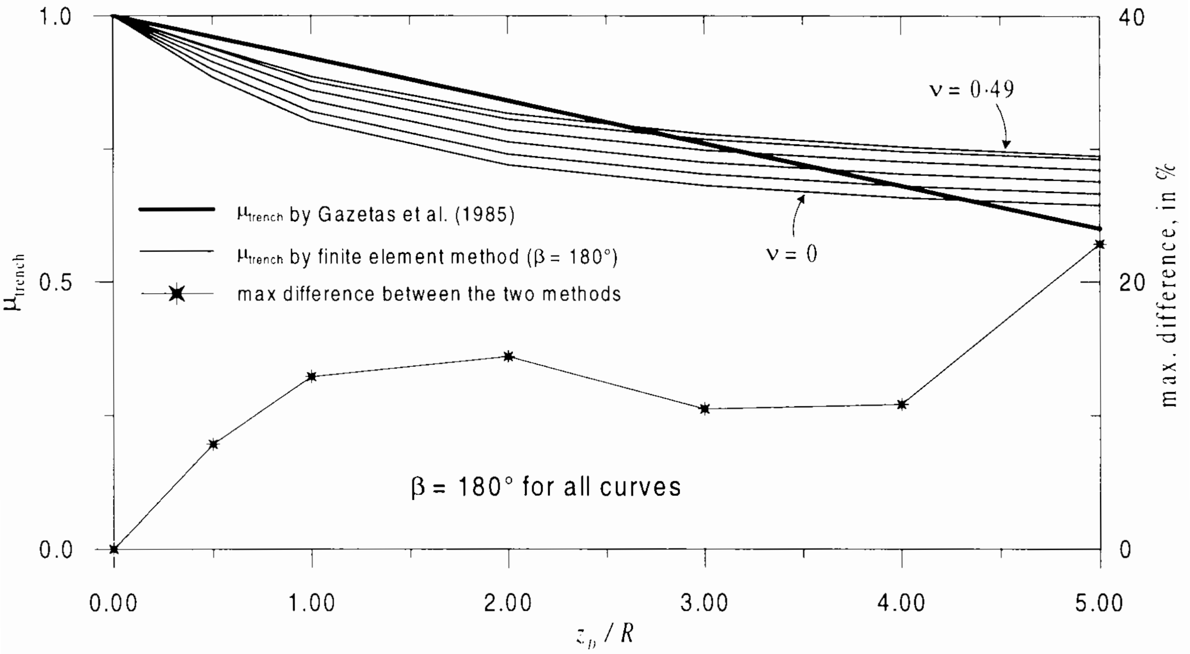

Figure 2.6: Reduction of elastic settlement due to embedment depth μ_{trench}: $\beta = 180°$.

and the difference reaches 14% at $z_D/R = 2$.

In addition, the trench factor μ_{trench} is shown to be dependent on the Poisson's ratio and this is not taken into account in Gazetas et al.'s (1985) work (see Equ. 2.12).

Based on these observations, an empirical expression for μ_{trench} has been derived as follows. From Fig. 2.6, a simple expression is devised to predict μ_{trench} for different embedment depth and Poisson's ratio as follows:

$$\mu_{\text{trench}} = \frac{a\,\dfrac{z_D}{R} + 1}{b\,\dfrac{z_D}{R} + 1} \tag{2.24}$$

where a and b depend upon Poisson's ratio.

Using a least-squares fit, the factors a and b can be determined for each value of Poisson's ratio $\nu = 0, 0{\cdot}1, 0{\cdot}2, 0{\cdot}3, 0{\cdot}4, 0{\cdot}49$. The factors are plotted against Poisson's ratio in Fig. 2.7a. It can be seen that a and b vary linearly with Poisson's ratio and can be written as follows:

$$\begin{aligned} a &= -0{\cdot}377\nu + 0{\cdot}458 \\ b &= -0{\cdot}783\nu + 0{\cdot}814 \end{aligned} \tag{2.25}$$

The trench factor μ_{trench} is back-calculated using Equ. 2.24 and Equ. 2.25. The results are plotted in Fig. 2.7b, which shows that the expressions give good prediction on μ_{trench}.

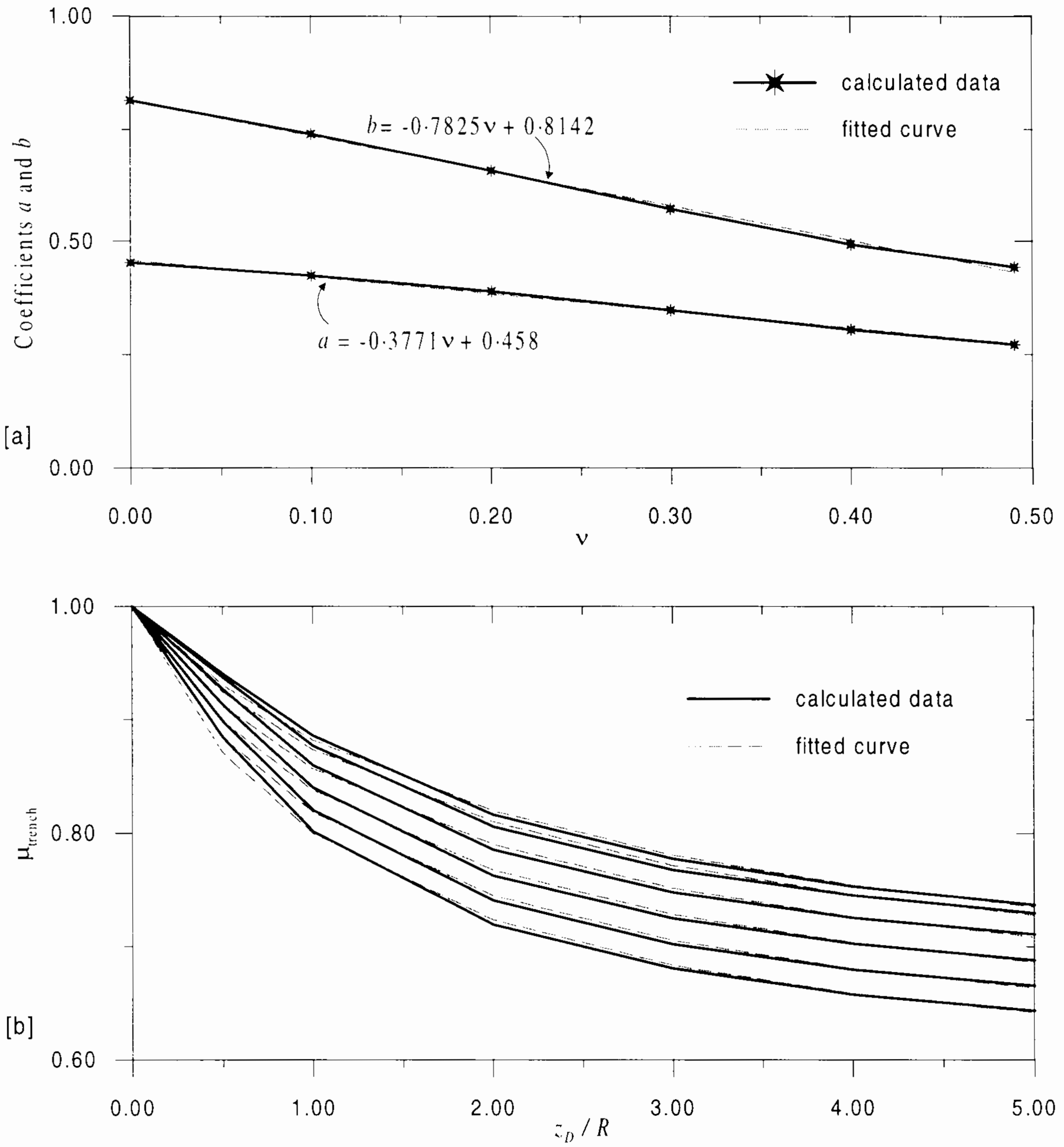

Figure 2.7: Determining μ_{trench} (a) Variation of coefficients a and b with Poisson's ratio (b) Comparison between calculated and predicted μ_{trench}.

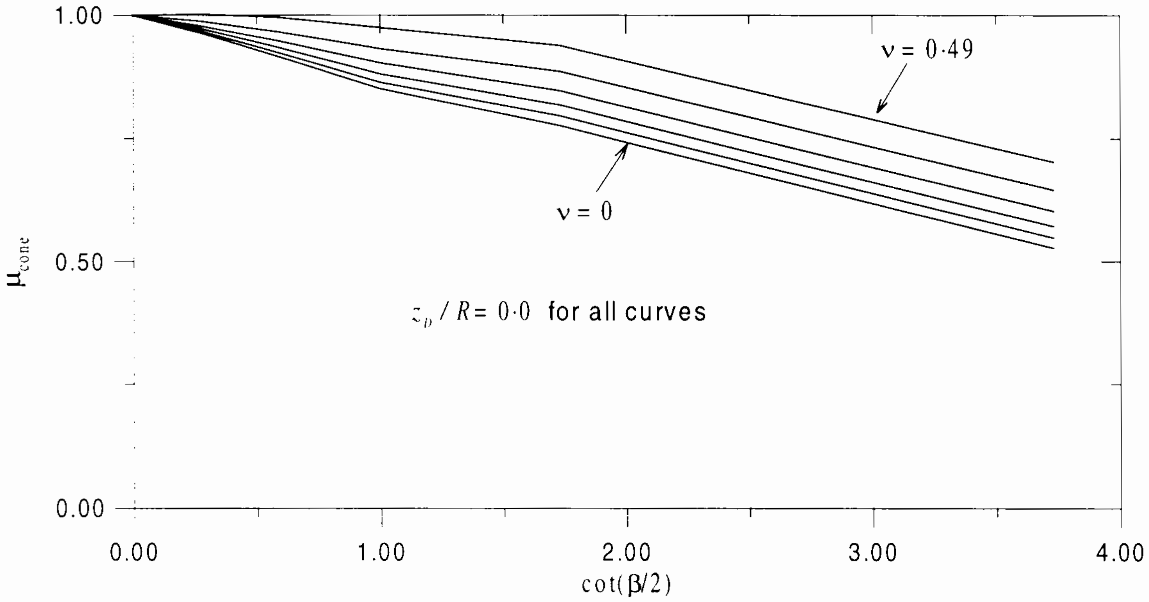

Figure 2.8: Reduction of elastic settlement due to conical angle μ_{cone}.

The effect of cone angle on elastic behaviour can be examined in a similar way as the trench factor. Equ. 2.11 can be extended to include the cone angle term as follows:

$$\begin{aligned} w &= \mu_{\text{trench}}\ \mu_{\text{cone}}\ w_{\text{surf,flat}}, \text{or} \\ K_1 &= \frac{K_{1,\text{surf,flat}}}{\mu_{\text{trench}}\ \mu_{\text{cone}}} \end{aligned} \tag{2.26}$$

where $w_{\text{surf,flat}}$ and $K_{1,\text{surf,flat}}$ are settlement and vertical stiffness coefficient of a flat, surface footing, respectively.

Fig. 2.8 shows the variation of μ_{cone} with $\cot\frac{\beta}{2}$ for surface footings with different cone angles. It is interesting to see that the variation of μ_{cone} with cone angle is similar to the variation of μ_{trench} with embedment depth in many ways. Firstly, the relation between μ_{cone} and cone angle is not linear, but it has a simple trend and could be fitted well using a simple mathematical model. In addition, there is an influence of Poisson's ratio on the behaviour of μ_{cone}. Also, an examination of μ_{cone} for different embedment depths revealed that the relation between μ_{cone} and $\cot(\beta/2)$ is almost identical at different embedment depths. This confirms that the form of Equ. 2.26 is appropriate.

With the trench factor μ_{trench} determined, the cone factor μ_{cone} for footings with different embedment depths and cone angles can be calculated from Equ. 2.26. An expression similar

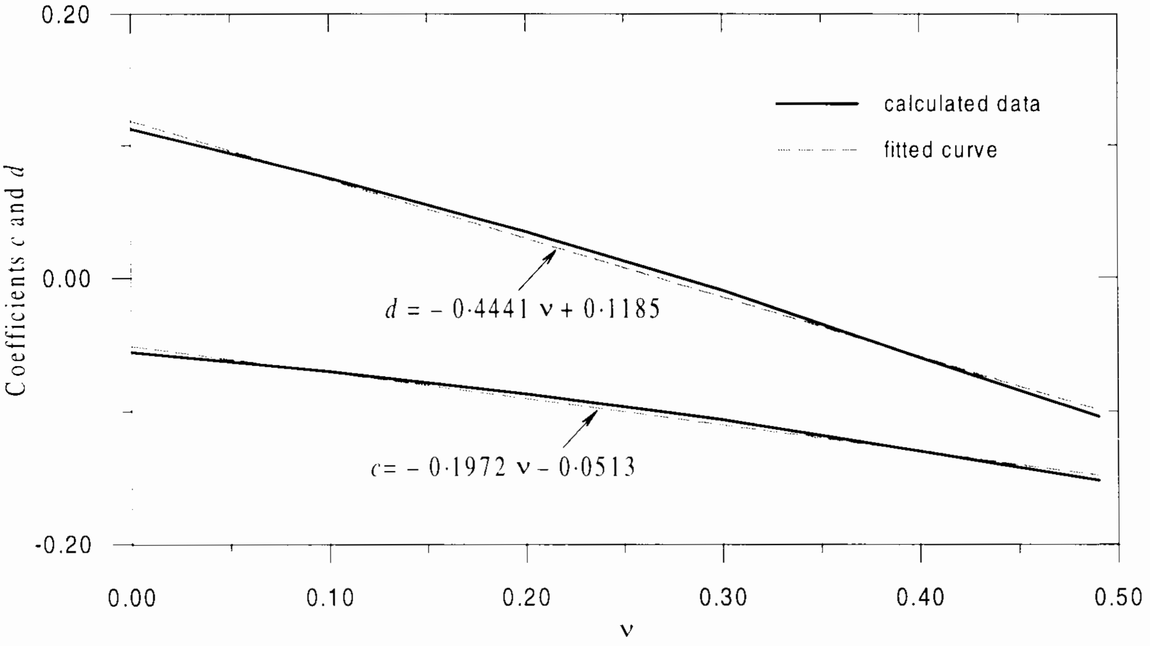

Figure 2.9: Variation of *c* and *d* with Poisson's ratio.

to that of μ_{trench} is chosen to fit μ_{cone} (cf. Equ. 2.24):

$$\mu_{\text{cone}} = \frac{c\cot\frac{\beta}{2}+1}{d\cot\frac{\beta}{2}+1} \tag{2.27}$$

where *c* and *d* are factors depending upon Poisson's ratio. Using a least-squares regression with the data of μ_{cone} calculated by Equ. 2.26, *c* and *d* can be determined . Their values for different Poisson's ratio are plotted in Fig. 2.9. Using a linear relation between *c*, *d* and Poisson's ratio the factors *c* and *d* can be written as:

$$\begin{aligned} c &= -0{\cdot}197\nu - 0{\cdot}0513 \\ d &= -0{\cdot}444\nu + 0{\cdot}119 \end{aligned} \tag{2.28}$$

Substituting Equations 2.24, 2.25, 2.27 and 2.28 into Equ. 2.26, w or K_1 for embedment depth z_D/R between 0 and 5, and cone angle β between 30° and 180° can be calculated. Back-calculation on 252 combinations of cone angles and embedment depths shows that the difference between the predicted values and observed values to be in the range from -6% to $+4\%$. The highest error ocurs with surface footings with $\beta = 30°$ for which the errors are in the range from -6% to -3%. For the remaining majority, the difference ranges from -2% to $+4\%$.

With the effect of embedment depth μ_{trench} and cone angle μ_{cone} having been established, the vertical stiffness coefficient K_1 for a general case of conical, embedded footings can be calculated using Equ. 2.26 with the vertical stifness coefficient $K_{1,\mathrm{surf,flat}}$ for surface flat footings determined using Spence's (1968) exact solution:

$$K_{1,\mathrm{surf,flat}} = \frac{4\ln(3-4\nu)}{1-2\nu} \qquad (2.29)$$

2.5 Three dimensional analyses

With the vertical stiffness coefficient K_1 having been investigated thoroughly in the previous section using axi-symmetric analyses, the main purpose of three dimensional analyses in this section is to investigate the other three stiffness coefficients K_2, K_3, K_4.

2.5.1 Mesh dimension and grading

Different meshes are generated for different footing embedment depths and cone angles. Because three dimensional analyses take significantly longer than two dimensional axi-symmetric analyses, the range of embedment depths and cone angles to be examined by three dimensional analyses is narrower than that of the two dimensional axi-symmetric analyses. Three values of cone angle which are the most relevant to spudcan foundations are investigated: $\beta = 120°, 150°, 180°$.

As Bell's (1991) results show (see Fig. 2.4), the effect of embedment depth on the horizontal stiffness coeffiecient and the moment stiffness coefficient (at the metacentre) does not change significantly for embedment depth greater than $z_D/R = 2$. Therefore four footing embedment depths are investigated: $z_D/R = 0,\ 0{\cdot}5,\ 1,\ 2$.

The three dimensional meshes have the same dimension as their two dimensional counterparts. The meshes are generated using I-DEAS. Special care is taken to generate very fine elements around the edge of the footing. In order to do this, the solid is partitioned into several parts as shown in Fig. 2.10. The mesh grading can then be controlled by specifying the number of elements to be allocated along edges of different features of the mesh (e.g. the rim of the footing) the boundary edge of the parts, etc. as shown in Fig. 2.10. A representative mesh, which is for the case $z_D = 0{\cdot}5R$, is given in Fig. 2.11. The number of nodes and elements generated are: (a) $z_D/R = 0$: 5219 nodes and 3148 elements; (b) $z_D/R = 0{\cdot}5$: 6054 nodes and 3825 elements; (c) $z_D/R = 1{\cdot}0$: 6881 nodes and 4392 elements; and (d) $z_D/R = 2{\cdot}0$: 7369 nodes and 4627 elements.

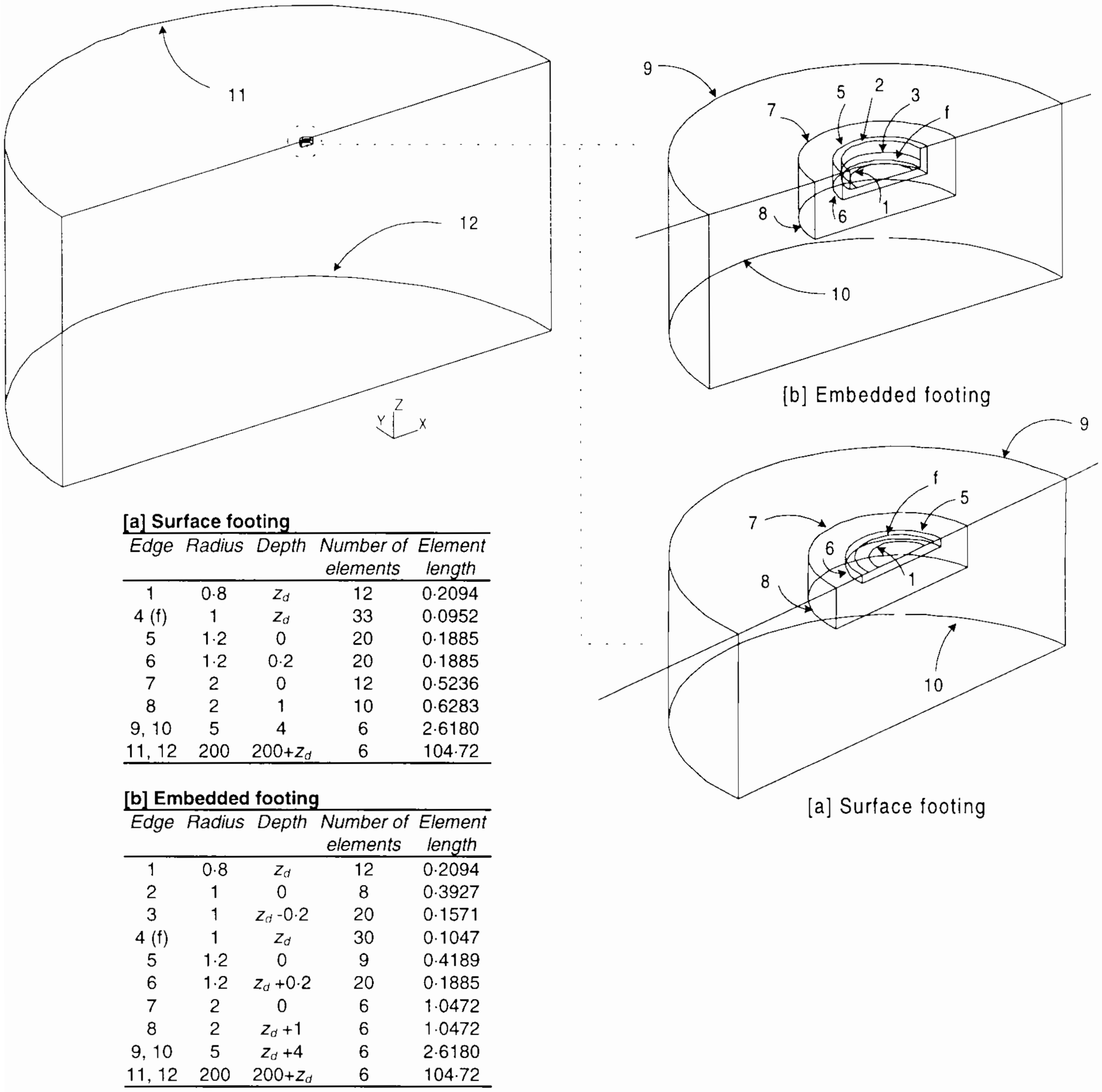

[a] Surface footing

Edge	Radius	Depth	Number of elements	Element length
1	0·8	z_d	12	0·2094
4 (f)	1	z_d	33	0·0952
5	1·2	0	20	0·1885
6	1·2	0·2	20	0·1885
7	2	0	12	0·5236
8	2	1	10	0·6283
9, 10	5	4	6	2·6180
11, 12	200	200+z_d	6	104·72

[b] Embedded footing

Edge	Radius	Depth	Number of elements	Element length
1	0·8	z_d	12	0·2094
2	1	0	8	0·3927
3	1	z_d-0·2	20	0·1571
4 (f)	1	z_d	30	0·1047
5	1·2	0	9	0·4189
6	1·2	z_d +0·2	20	0·1885
7	2	0	6	1·0472
8	2	z_d +1	6	1·0472
9, 10	5	z_d +4	6	2·6180
11, 12	200	200+z_d	6	104·72

Figure 2.10: Mesh grading control (a) Surface footing; (b) Embedded footing.

For all the meshes, all the nodes in the $y = 0$ plane are constrained in the y direction. Those nodes which are on the radial and bottom boundaries are constrained in all three x, y and z directions.

Two values of Poison's ratio are used: (a) $\nu = 0{\cdot}49 \approx 0{\cdot}50$, which represents undrained loading; and (b) $\nu = 0{\cdot}20$, which is a typical value for sand under drained loading.

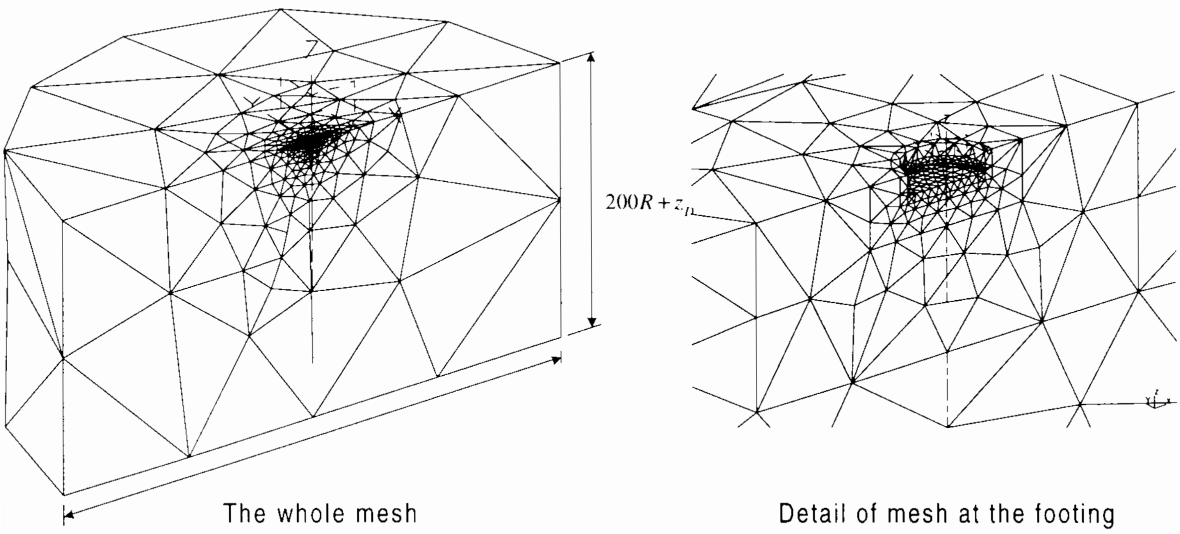

The whole mesh

Detail of mesh at the footing

Figure 2.11: Generated 10-noded tetrahedral mesh: $z_D = 0{\cdot}5R$.

2.5.2 Results and comparison with other solutions

The results are given in Table 2.5. The results of the vertical stiffness coefficient K_1 are first compared with the exact solution Equ. 2.2 (for flat, surface footings) and with the axi-symmetrical solutions (for embedded and/or conical footings). The difference is shown in Table 2.6. It shows that the three dimensional analyses give consistent results with the axi-symmetrical ones. However, the three dimensional analyses are less accurate with $\nu = 0{\cdot}49$ than with $\nu = 0{\cdot}20$. This seems to indicate that when the condition of material incompressibility is imposed (in this case $\nu = 0{\cdot}49$), the ten-noded tetrahedral element begins to lose some accuracy. The axi-symmetrical results are calculated with 15-noded triangular elements, which are higher order elements, and are therefore more accurate than the three dimensional results. The three dimensional results are, however, considered acceptable because the error is less than 5%.

The three dimensional results are also compared with those of Bell (1991). Bell (1991) calculates the stiffness coefficients for various embedment depths and Poisson's ratios but only for flat footings. The comparison is shown in Table 2.7. The two sets of results compare well, except for the coupling coefficient K_4 for the case $\nu = 0{\cdot}49$ and $z_D/R = 0{\cdot}5$.

Table 2.5: Stiffness coefficients.

Embed-ment	*Cone angle*	K_1		K_2		K_3		K_4	
	β	ν = 0·2	ν = 0·49	ν = 0·2	ν = 0·49	ν = 0·2	ν = 0·49	ν = 0·2	ν = 0·49
z_D/R= 0·0	180°	5·4058	8·1971	4·6517	5·5541	3·8161	5·5627	-0·5734	-0·0148
	150°	5·5643	8·2998	4·9739	5·9450	4·0661	5·7684	-0·7589	-0·0737
	120°	5·7790	8·3429	5·4976	6·6326	4·6563	6·0640	-1·1966	-0·4862
z_D/R= 0·5	180°	5·9509	8·8098	6·1173	7·2258	4·5860	6·5826	-0·8425	-0·4020
	150°	6·0893	8·8102	6·4086	7·5634	4·8308	6·5728	-1·0197	-0·4504
	120°	6·2850	8·8438	6·8879	8·1766	5·4227	6·8440	-1·4398	-0·8166
z_D/R= 1	180°	6·4950	9·2537	6·4992	7·5899	5·0156	7·1627	-0·9360	-0·5691
	150°	6·6361	9·2510	6·8183	7·9544	5·2733	7·1301	-1·1228	-0·6086
	120°	6·8383	9·2830	7·3376	8·6101	5·8902	7·3744	-1·5638	-0·9762
z_D/R= 2	180°	7·0817	9·9857	6·7742	7·7012	5·1903	7·6739	-0·9786	-0·7327
	150°	7·2633	10·0702	7·1262	8·1210	5·5033	7·8269	-1·1645	-0·7070
	120°	7·4950	9·9811	7·6962	9·1741	6·1621	7·8945	-1·6233	-1·0750

Table 2.6: Elastic stiffness coefficient K_1: comparison with axi-symmetric finite element solution and exact solution.

Embed-ment	*Cone angle*	ν = 0·2				ν = 0·49			
	β	*This study*	*Axi-symmetric*	*Exact*[†]	*Difference*	*This study*	*Axi-symmetric*	*Exact*[†]	*Difference*
z_D/R= 0·0	180°	5·4058	5·3340	5·2564	1·3% 2·8%[‡]	8·1971	7·9864	7·8441	2·6% 4·5%[‡]
	150°	5·5643	5·4810	NA	1·5%	8·2998	7·9713	NA	4·0%
	120°	5·7790	5·7014	NA	1·4%	8·3429	8·0198	NA	4·0%
z_D/R= 0·5	180°	5·9509	5·8415	NA	1·9%	8·8098	8·4933	NA	3·7%
	150°	6·0893	6·0060	NA	1·4%	8·8102	8·4406	NA	4·4%
	120°	6·2850	6·2088	NA	1·2%	8·8438	8·4883	NA	4·2%
z_D/R= 1	180°	6·4950	6·3489	NA	2·3%	9·2537	9·0155	NA	2·6%
	150°	6·6361	6·5244	NA	1·7%	9·2510	8·9250	NA	3·7%
	120°	6·8383	6·7354	NA	1·5%	9·2830	8·9784	NA	3·4%
z_D/R= 2	180°	7·0817	6·9926	NA	1·3%	9·9857	9·7843	NA	2·1%
	150°	7·2633	7·1913	NA	1·0%	10·0702	9·6479	NA	4·4%
	120°	7·4950	7·4250	NA	0·9%	9·9811	9·7089	NA	2·8%

Notes:

[†] NA means not available.

[‡] Comparison with the exact solution. The other percentage numbers are comparisons with the axi-symmetric analyses.

Table 2.7: Stiffness coefficients K_2, K_3, K_4 of flat footings: comparison with Bell's solution.

Embed-ment	Solution	K_2		K_3		K_4	
		$\nu = 0{\cdot}2$	$\nu = 0{\cdot}49$	$\nu = 0{\cdot}2$	$\nu = 0{\cdot}49$	$\nu = 0{\cdot}2$	$\nu = 0{\cdot}49$
z_D/R= 0·0	Bell	4·6390	5·4740	3·7160	5·4100	-0·5682	-0·0144
	This study	4·6517	5·5541	3·8161	5·5627	-0·5734	-0·0148
	Difference	*0·3%*	*1·5%*	*2·7%*	*2·8%*	*0·9%*	*2·8%*
z_D/R= 0·5	Bell	6·1270	7·1860	4·5740	6·3900	-0·8258	-0·3346
	This study	6·1173	7·2258	4·5860	6·5826	-0·8425	-0·4020
	Difference	*-0·16%*	*0·55%*	*0·26%*	*3%*	*2%*	*20%*
z_D/R= 1	Bell	6·5880	7·8350	5·1110	7·1360	-0·9256	-0·5305
	This study	6·4992	7·5899	5·0156	7·1627	-0·9360	-0·5691
	Difference	*-1·4%*	*-3·1%*	*-1·9%*	*0·4%*	*1·1%*	*7·3%*
z_D/R= 2	Bell	6·8830	8·2370	5·3950	7·6050	-0·9885	-0·7042
	This study	6·7742	7·7012	5·1903	7·6739	-0·9786	-0·7327
	Difference	*1·6%*	*6·5%*	*-3·8%*	*0·9%*	*1%*	*4%*

2.5.3 Discussion and analysis of the results

This section examines the effect of embedment depth and cone angle on the stiffness coefficients K_2, K_3, K_4. The purpose is to establish an expression like Equ. 2.26, for instance, for the horizontal stiffness coefficient K_2 such that:

$$K_2 = \frac{K_{2,\mathrm{surf,flat}}}{\mu_{\mathrm{trench}}\ \mu_{\mathrm{cone}}} \tag{2.30}$$

where μ_{cone} and μ_{trench} are the cone and trench factor for the horizontal stiffness coefficient K_2.

2.5.3.1 Horizontal stiffness coefficient K_2

The effect of embedment on flat footings can be quantified by:

$$\mu_{\mathrm{trench}} = \frac{K_{2,\,\mathrm{surf,\,flat}}}{K_2} \tag{2.31}$$

where K_2 is the stiffness coefficient for flat footings as shown in Table 2.5, and $K_{2,\mathrm{surf,flat}}$ is the stiffness of a flat surface footing. The variation of μ_{trench} with Poisson's ratio and embedment depths is shown in Fig. 2.12. In contrast to the vertical stiffness coefficient K_1 (Fig. 2.7), the effect of embedment on the horizontal stiffness coefficient K_2 is fairly independent on Poisson's ratio. At $z_D/R = 2$ at which the difference between μ_{trench} of

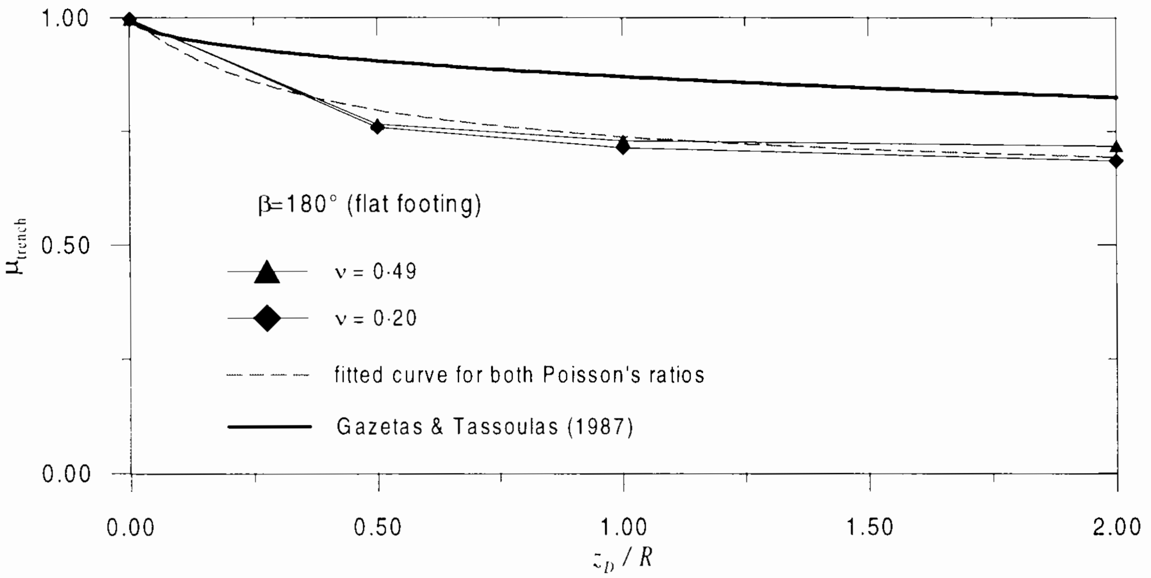

Figure 2.12: Effect of embedment depth and Poisson's ratio on K_2.

$\nu = 0{\cdot}2$ and $\nu = 0{\cdot}49$ is the largest, the difference is only 3%. This confirms the observation made by Gazetas & Tassoulas (1987) and Bell (1991).

It will be recalled that the two curves in Fig. 2.12 have a similar shape to the curves of μ_{trench} for the vertical stiffness coefficient K_1 as shown in Fig. 2.6. Therefore, they are fitted using an expression similar to Equ. 2.24:

$$\mu_{\text{trench}} = \frac{a\,\dfrac{z_D}{R} + 1}{b\,\dfrac{z_D}{R} + 1} \tag{2.32}$$

with one set of constants a and b:

$$a = 1{\cdot}55 \quad \text{and} \quad b = 2{\cdot}46 \tag{2.33}$$

for both $\nu = 0{\cdot}2$ and $\nu = 0{\cdot}49$.

Fig. 2.12 also shows Gazetas & Tassoulas's (1987) prediction of μ_{trench} (Equ. 2.16). In the range of embedment depth $z_D/R = 0$ to $z_D/R = 2$, the Gazetas & Tassoulas (1987) prediction gives a much softer response of footings to horizontal loads. The maximum difference between the finite element results and the Gazetas & Tassoulas (1987) prediction is up to 22% at $z_D/R = 1$.

The factor μ_{cone} which takes into account the effect of conical angle of the footing is calculated in the same way as for vertical stiffness factor K_1 (Equ. 2.26). Fig. 2.13 shows

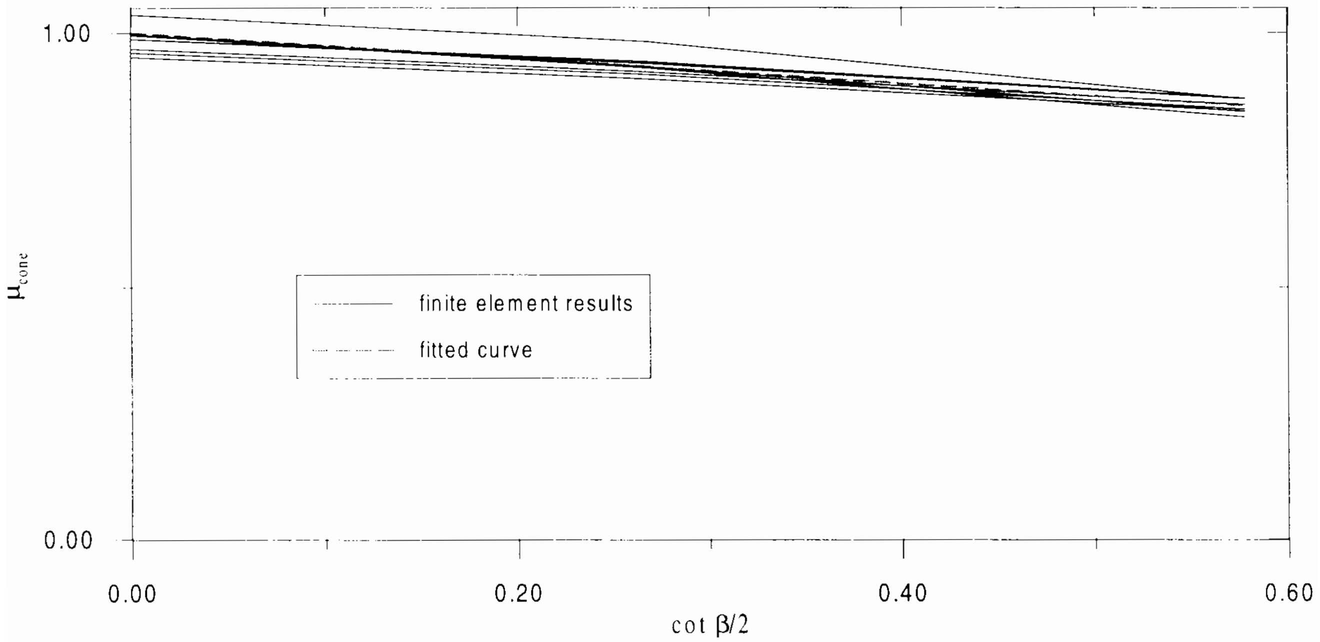

Figure 2.13: Effect of cone angle on K_2.

the variation of μ_{cone} with cone angles β for different embedment depths and Poisson's ratios (resulting in 8 curves). A close examination of the plot shows that there is no clear relation between curves of the same embedment depths or between curves of the same Poisson's ratio. Nonetheless, all the data (of the 8 curves) can be fitted with one single expression (cf. Equ. 2.27):

$$\mu_{cone} = c\cot(\beta/2) + 1 \tag{2.34}$$

where c is a constant:

$$c = -0{\cdot}251 \tag{2.35}$$

Using Equs. 2.32 to 2.35, the horizontal stiffness coefficient K_2 can be calculated. A back-calculation of K_2 showed that the difference between the finite element results and the mathematical model (Equs. 2.32 to 2.35) is from $-4{\cdot}8\%$ to $+5{\cdot}3\%$.

As mentioned in Section 2.2.1, Gerrard & Harrison's (1970) solution for flat surface footings under horizontal loading (Equ. 2.9) is exact at $\nu = 0{\cdot}5$. The corresponding horizontal stiffness coefficient is calculated by:

$$K_2^* = \frac{8}{2-\nu} \tag{2.36}$$

Though the above expression is not exact for $\nu < 0{\cdot}5$, it can be used as an adequate approximation of the true value. For $\nu = 0{\cdot}49$ the finite element result of this study is $+4{\cdot}8\%$ higher than K_2^*, suggesting that the finite element solution overestimates the true behaviour. Equ. 2.36 becomes inexact for $\nu < 0{\cdot}5$. On the other hand, as discussed earlier (Section 2.5.2), when the material is incompressible or near incompressible, the finite element solution is less accurate. Thus the finite element solution at $\nu = 0{\cdot}2$ is closer to the true behaviour than that at $\nu = 0{\cdot}49$.

However, the finite element results are consistently higher than Equ. 2.36 at the same percentage: at $\nu = 0{\cdot}2$, the difference is $+4{\cdot}7\%$ (cf. $+4{\cdot}8\%$ at $\nu = 0{\cdot}49$). Bell's (1991) results for $\nu = 0, 0{\cdot}2, 0{\cdot}4, 0{\cdot}49$ also show a similar trend. At $\nu = 0{\cdot}49$, Bell's (1991) result is $+3{\cdot}3\%$ higher than K_2^*. For other Poisson's ratios (0, 0·2 and 0·4) the difference varies within 5% from $+2{\cdot}9\%$ to $+6{\cdot}8\%$. This means that Equ. 2.36 underestimates the true stiffness for $\nu < 0{\cdot}5$.

However, with the difference between finite element solution and Equ. 2.36 of about $+5\%$ this underestimation should be less than -5% (assuming that the finite element solution still overestimates the true stiffness at low Poisson's ratio, which is likely.)

Therefore in the lack of an exact solution, it is assumed that Equ. 2.36 can adequately estimate the horizontal stiffness coefficient for the whole range of Poisson's ratio from 0 to 0·5.

2.5.3.2 Moment and coupling stiffness coefficients K_3 and K_4

The values of K_3 and K_4 in Table 2.5 use the intersection of the footing centre line with the plane containing the rim of the footing (or the footing base for flat footings) as the point of reference (Fig. 2.1). These two coefficients, however, are dependent on the reference point adopted (while the other two coefficients K_1 and K_2 are not). For a footing base located at a depth z_D, the stiffness coefficients K_3^z and K_4^z corresponding to a depth z can be shown to be:

$$\begin{aligned} K_3^z &= K_2\left(\frac{z_D}{R}-\frac{z}{R}\right)^2 - 2K_4\left(\frac{z_D}{R}-\frac{z}{R}\right) + K_3 \\ K_4^z &= K_4 - K_2\left(\frac{z_D}{R}-\frac{z}{R}\right) \end{aligned} \qquad (2.37)$$

Varying the position of this point of reference vertically along the footing centre line affects the horizontal displacement and footing moment. In analysing the results of K_3 and

K_4 in Table 2.5, there are three particular positions of points of reference which can be used. The first position is the intersection of the footing base and the centre line as the point of reference (Fig. 2.1), which is the position used in calculating the stiffness coefficients in Table 2.5. The second position, which is commonly used in structural analyses is the surface (or seabed) level ($z = 0$). For this reference point, Equ. 2.37 reduces to:

$$\begin{aligned} K_3^s &= K_2\left(\frac{z_D}{R}\right)^2 - 2K_4\left(\frac{z_D}{R}\right) + K_3 \\ K_4^s &= K_4 - K_2\left(\frac{z_D}{R}\right) \end{aligned} \tag{2.38}$$

The third position is called 'the metacentre' and is characterised by the uncoupling of the horizontal and moment components, i.e. $K_4 = 0$ and the stiffness matrix $\mathbf{K}$ becomes diagonal. Therefore, a moment applied at the metacentre will not produce any horizontal translation at that point. From Equ. 2.37 the depth of the metacentre z_m can be found to be:

$$\left(\frac{z_m}{R}\right) = \left(\frac{z_D}{R}\right) - \frac{K_4}{K_2} \tag{2.39}$$

and the moment stiffness coefficient at the metacentre is:

$$K_3^m = K_3 - \frac{K_4^2}{K_2} \tag{2.40}$$

Bell's (1991) analyses of the effect of embedment z_D/R on the moment and coupling stiffness coefficients for the three reference points revealed that by using the metacentre a simpler interaction between the embedment depth z_D/R and the coefficients (which then becomes K_3^m and z_m/R for metacentre) can be achieved. As shown in the following sections, this advantage of simplicity of the metacentre is also retained for conical footings. Therefore, the analyses presented in the following sections are based on the metacentre.

Moment stiffness coefficient at metacentre K_3^m

As discussed in Section 2.2.1, there is no exact solution for the general case of rough, surface, flat footings under moment loading. However, for Poisson's ratio $\nu = 0{\cdot}5$, the solution for a smooth footing under moment loading Equ. 2.10 becomes exact for a rough footing. As in such a case the metacentre is also located at the surface, the moment stiffness coefficient with respect to metacentre can be calculated from Equ. 2.10 as:

$$K_3^* = \frac{8}{3(1-\nu)} \tag{2.41}$$

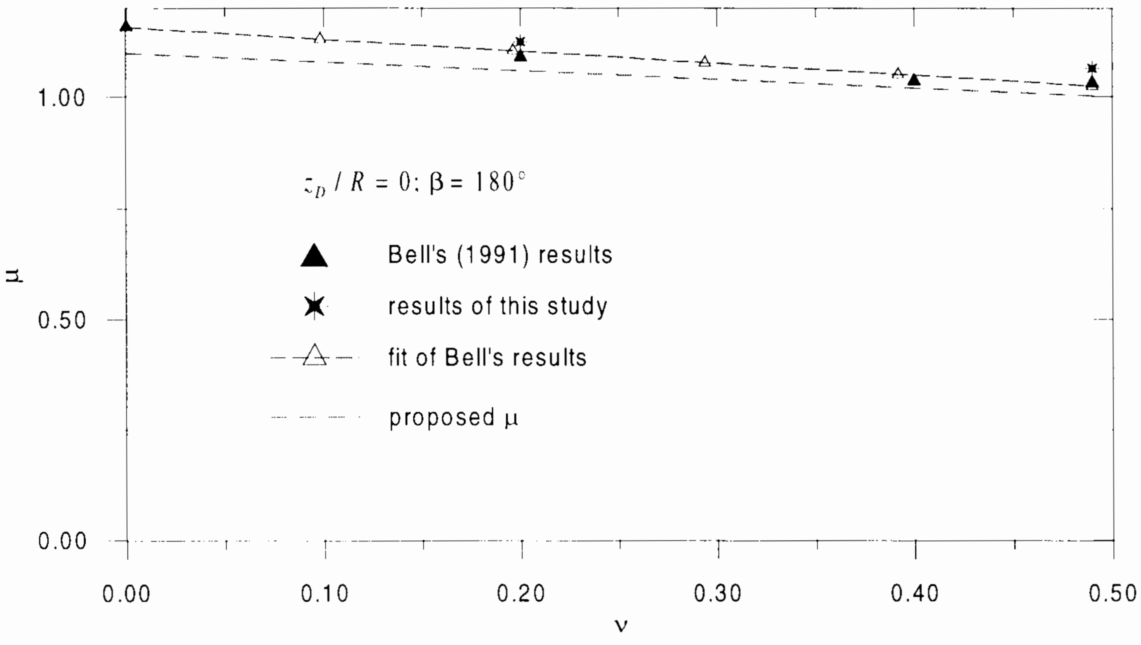

Figure 2.14: Variation of K_3^m / K_3^* with Poisson's ratio for surface, flat footings.

Though this expression is not exact for $\nu < 0{\cdot}5$, it can be shown that the exact value of $K^m_{3,\mathrm{surf,flat}}$ relates to K_3^* by a correction factor μ:

$$\mu = \frac{K^m_{3,\mathrm{surf,flat}}}{K_3^*} \tag{2.42}$$

Fig. 2.14 shows the variation of μ with Poisson's ratio with $K^m_{3,\mathrm{surf,flat}}$ obtained from the finite element analyses. This means that with lower Poisson's ratio, Equ. 2.41 increasingly underestimates the moment stiffness coefficient. In this research only two Poisson's ratios $\nu = 0{\cdot}2$ and $0{\cdot}49$ are investigated. This is not sufficient to recognise the trend of this underestimation with Poisson's ratio. However, as also shown in Fig. 2.14, Bell's (1991) results at $\nu = 0$, $0{\cdot}2$, $0{\cdot}4$ and $0{\cdot}49$ show that this trend can be adequately approximated using a linear relation. Turning back to this study with the results at $\nu = 0{\cdot}2$ and $\nu = 0{\cdot}49$ (which are adjusted to eliminate the error of the finite element analysis at $\nu \approx 0{\cdot}5$), the relation between μ and ν is found to be:

$$\mu = 0{\cdot}0975(1 - 2\nu) + 1 \tag{2.43}$$

The effect of embedment on a flat footing can be examined by deriving μ_{trench} as follows:

$$\mu_{\mathrm{trench}} = \frac{K^m_{3,\mathrm{surf,flat}}}{K_3} \tag{2.44}$$

Fig. 2.15 shows the variation of μ_{trench} with embedment depth. It shows that with the increase of embedment depth, μ_{trench} decreases (or the moment stiffness coefficient increases). The

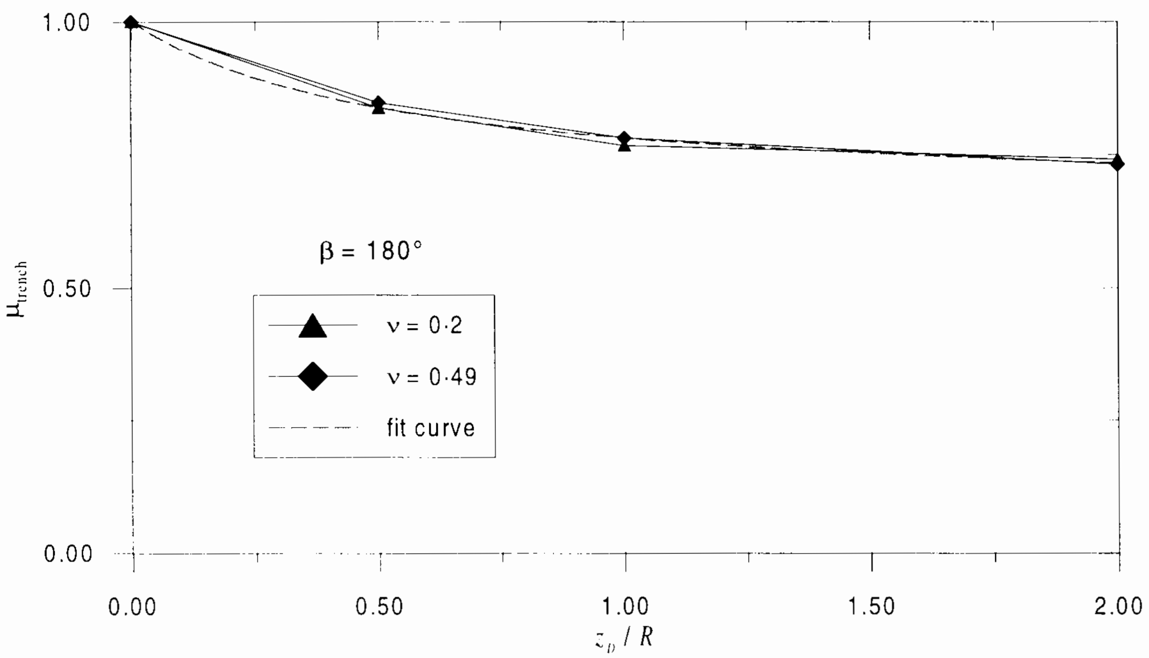

Figure 2.15: Effect of embedment on K_3^m of flat footings.

curves for two different Poisson's ratios, $\nu = 0{\cdot}2$ and $0{\cdot}49$, are very close. Furthermore, the curves in Fig. 2.15 are also similar to those in Fig. 2.6 and Fig. 2.12, which are for the vertical and horizontal stiffness coefficients, respectively. The fitted curve shown in Fig. 2.15 has the same formula as Equ. 2.24:

$$\mu_{\text{trench}} = \frac{a\frac{z_D}{R} + 1}{b\frac{z_D}{R} + 1} \tag{2.45}$$

with:

$$a = 1{\cdot}2 \text{ and } b = 1{\cdot}82 \tag{2.46}$$

As shown in the figure, it provides a good fit to the data.

The effect of cone angle on the moment stiffness can then be quantified using the same expression of vertical stiffness Equ. 2.26 with K_1 replaced by K_3^m. The variation of μ_{cone} with cone angle for footings of different embedment depths and Poisson's ratios is shown in Fig. 2.16. In general the cone factor μ_{cone} decreases as the cone becomes sharper. It can also be seen from the figure that the factor μ_{cone} decreases more quickly with $\cot(\beta/2)$ for $\nu = 0{\cdot}2$ than for $\nu = 0{\cdot}49$. In the same manner as for K_1 and K_2, the following expression is found suitable to describe μ_{cone}:

$$\mu_{\text{cone}} = c\cot\frac{\beta}{2} + 1 \tag{2.47}$$

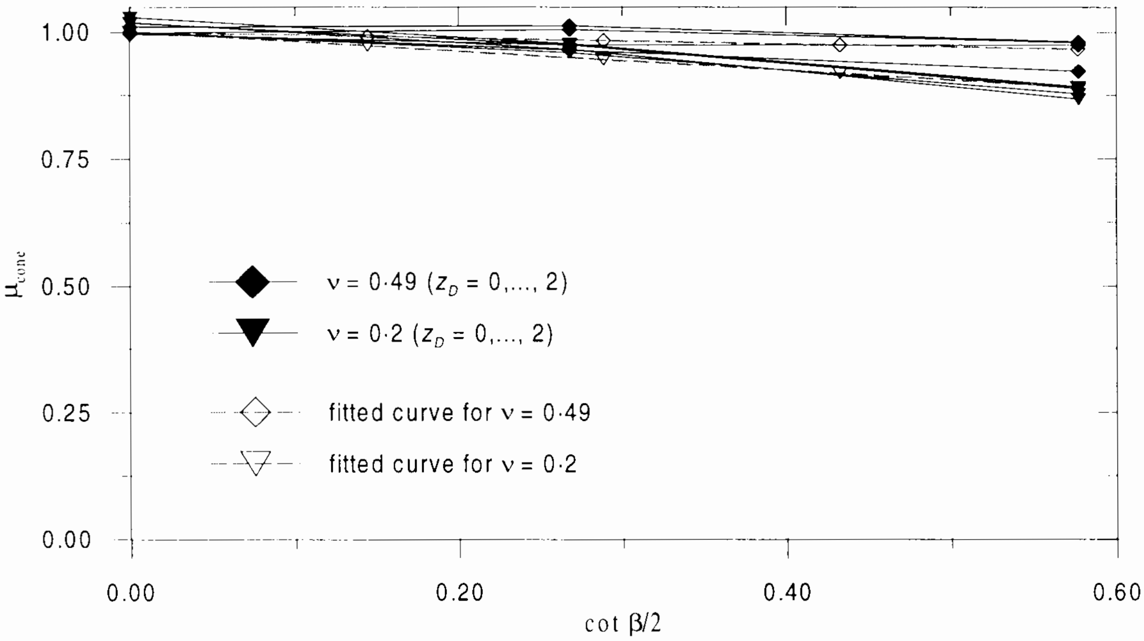

Figure 2.16: Effect of cone angle on moment stiffness coefficient.

where c is independent of Poisson's ratio:

$$c = -0{\cdot}1235 \tag{2.48}$$

Using Equs. 2.41 to 2.48, the moment stiffness coefficient at metacentre K_3^m can be calculated. A back-calculation of K_3^m showed that the difference between the finite element results and the mathematical model (Equs. 2.41 to 2.48) is from $-6{\cdot}5\%$ to $+5{\cdot}6\%$.

Location of the metacentre

Fig. 2.17 shows the variation of the location of metacentre for flat surface footings with Poisson's ratio. In order to examine the trend of this variation, Bell's (1991) results are also shown because Bell (1991) performed analysis for various Poisson's ratios ranging from 0 to 0·49. As can be seen from Fig. 2.17, Bell's (1991) results are in close agreement with the results from this study at $\nu = 0{\cdot}2$ and $\nu = 0{\cdot}49$; the maximum difference is only 0·0007. Bell's (1991) results also show that at lower Poisson's ratio, the metacentre lies deeper under the footing centre. The variation is not linear, but can be fitted well by an expression of the form:

$$\frac{z_{m,\mathrm{surf,flat}}}{R} = \frac{a(1-2\nu)}{b\nu+1} \tag{2.49}$$

where a and b are constants:

$$a = 0{\cdot}171 \text{ and } b = -0{\cdot}779 \tag{2.50}$$

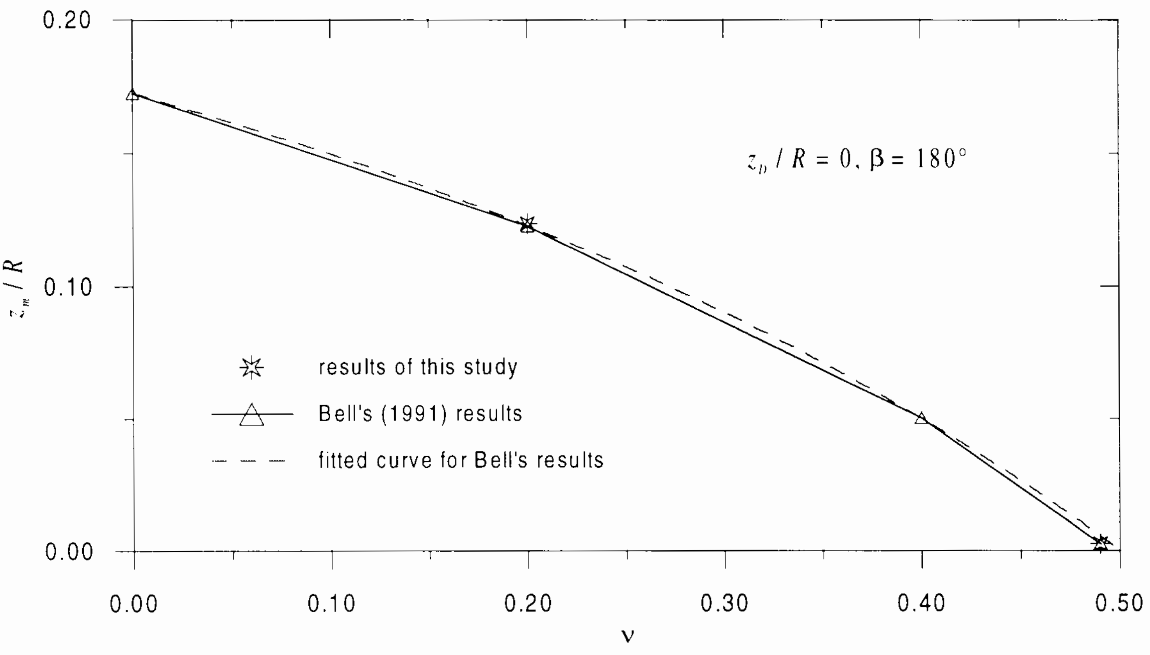

Figure 2.17: Location of the metacentre for flat surface footings.

Fig. 2.18 shows the variation of the distance between the location of the metacentre and the default reference point $(z_m - z_D)/R$ for flat footings with embedment depth. For $\nu = 0{\cdot}49$, the distance increases fastest with embedment depth, whereas for $\nu = 0$, as Bell's (1991) results show, the distance actually decreases. The curves in Fig. 2.18 can be fitted using the following expression:

$$\frac{z_m - z_D}{R} = \frac{c\frac{z_D}{R}}{d\frac{z_D}{R} + 1} + \frac{z_{m,\text{surf,flat}}}{R} \tag{2.51}$$

where c and d are dependent on Poisson's ratio. Fig. 2.19 shows the variation of parameters c and d with Poisson's ratio. As this study involves only two Poisson's ratios, Bell's (1991) results are drawn in to examine the trend of c and d over the whole range of Poisson's ratio. As Fig. 2.19 shows, whilst the parameter c increases linearly with ν, the parameter d increases to a peak value at $\nu = 0{\cdot}2$ then falls when $\nu > 0{\cdot}2$. Due to this rather complicated varation of d, d is chosen to take the average value. Therefore,

$$\begin{aligned} c &= 0{\cdot}365\nu \\ d &= 2{\cdot}07 \end{aligned} \tag{2.52}$$

In order to take into account the effect of cone angle on the location of the metacentre, it

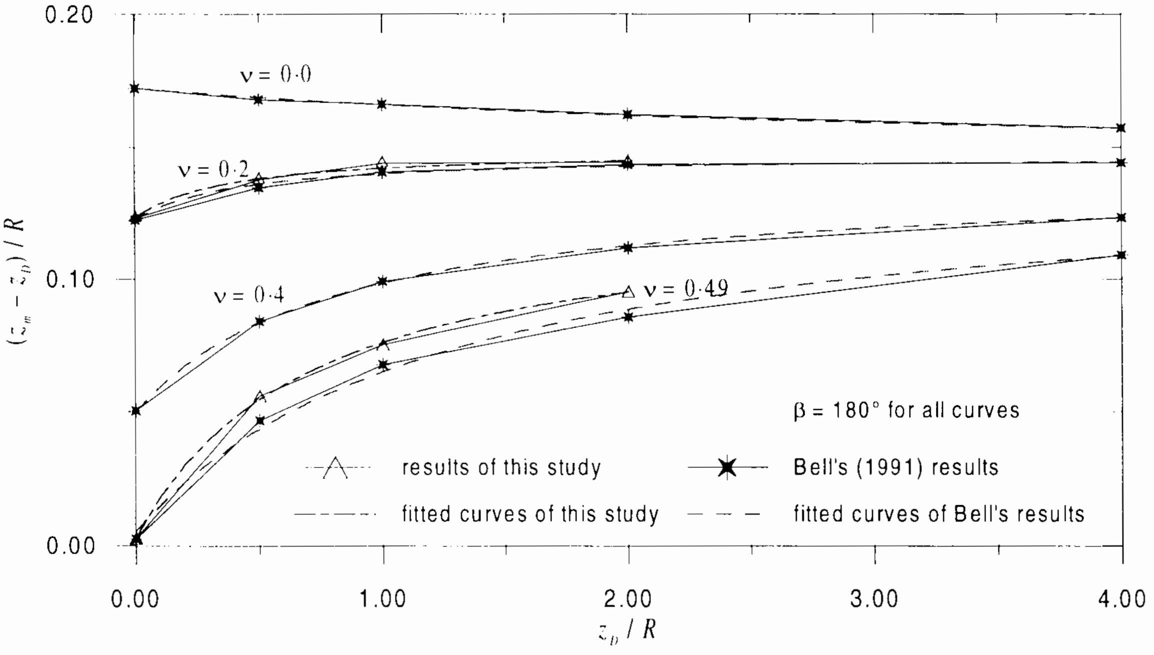

Figure 2.18: Variation of the distance between the metacentre and the default reference point $(z_m - z_D)/R$ with footing embedment depth for flat footings.

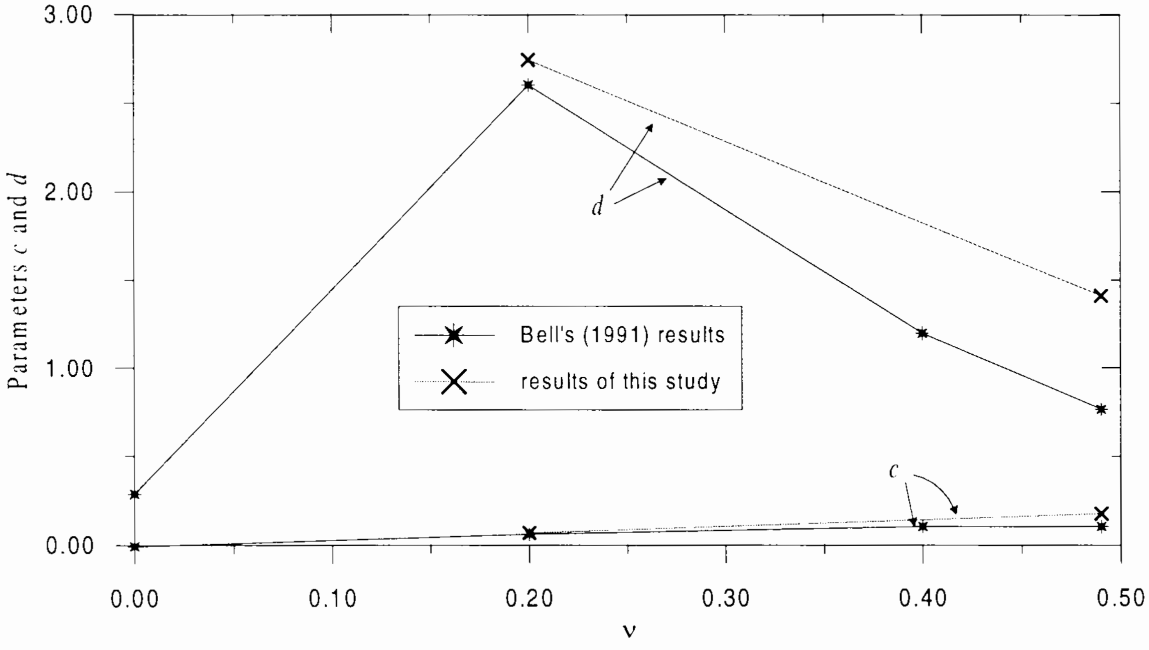

Figure 2.19: Variation of parameters *c* and *d* with Poisson's ratio.

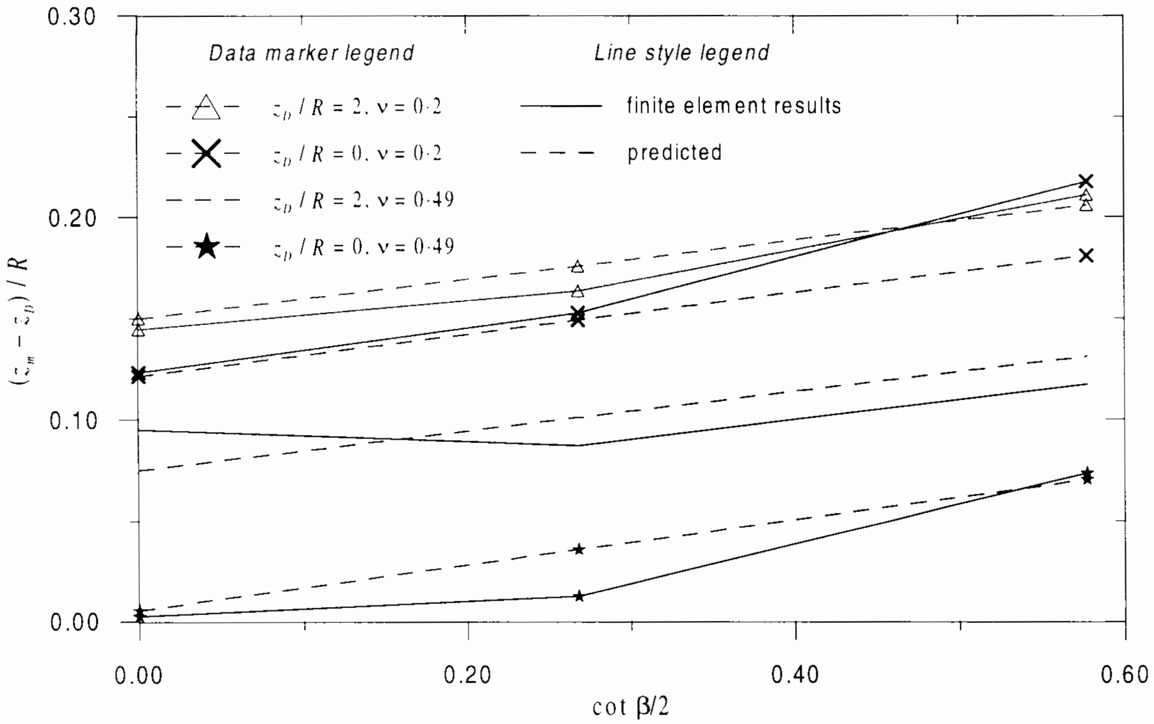

Figure 2.20: Comparison between the finite element results and the predicted distance between the metacentre and the default reference point for embedded and conical footings.

is found that the modified version of Equ. 2.51:

$$\frac{z_m}{R} - \left(\frac{z_D}{R} + e\cot\frac{\beta}{2}\right) = \frac{z_{m,\mathrm{surf,flat}}}{R} + \frac{c\left(\frac{z_D}{R} + e\cot\frac{\beta}{2}\right)}{d\left(\frac{z_D}{R} + e\cot\frac{\beta}{2}\right) + 1} \tag{2.53}$$

where e is a constant, can model the effect of both the cone angle and embedment depth on the location of the metacentre well. The parameter e is found to be:

$$e = 0{\cdot}0964 \tag{2.54}$$

Using Equs. 2.49 to 2.54, the distance from the location of the metacentre to the footing default reference point can be calculated. A back-calculation of $(z_m - z_D)/R$ showed that the difference between the finite element results and the mathematical model (Equs. 2.49 to 2.54) is from $-0{\cdot}037$ to $+0{\cdot}023$. Fig. 2.20 shows the predicted distance between the metacentre and the default reference point, in comparison with the finite element results, for embedded and conical footings with two Poisson's ratios. It shows that Equ. 2.53 models the behaviour of the footing well.

Table 2.8 gives a summary of all the formulae derived in this section for calculating the stiffness coefficients K_1, K_2, K_3 and the location of the metacentre.

Table 2.8: Stiffness coefficients K_1, K_2, K_3^m and metacentre location z_m/R.

K_1, K_2 and K_3^m are calculated using the following formula:

$$K_i = \frac{K_{i,\mathrm{surf.flat}}}{\mu_{\mathrm{trench}}\mu_{\mathrm{cone}}}$$

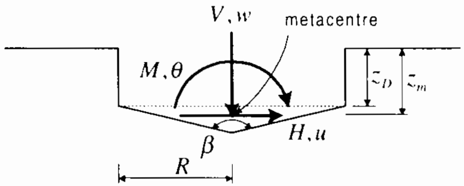

Stiffness coefficients K_i	Formulae for flat, surface footings $K_{i,\mathrm{surf.flat}}$	$\mu_{\mathrm{trench}} = \frac{a(z_D/R)+1}{b(z_D/R)+1}$	$\mu_{\mathrm{cone}} = \frac{c\cot(\beta/2)+1}{d\cot(\beta/2)+1}$
K_1	$\frac{4\ln(3-4\nu)}{1-2\nu}$	$a = -0\cdot 377\nu + 0\cdot 46$ $b = -0\cdot 783\nu + 0\cdot 814$	$c = -0\cdot 197\nu - 0\cdot 051$ $d = -0\cdot 444\nu + 0\cdot 119$
K_2	$\frac{8}{2-\nu}$	$a = 1\cdot 55$ $b = 2\cdot 46$	$c = -0\cdot 251$ $d = 0$
K_3^m	$(0\cdot 0975(1-2\nu)+1) \times \frac{8}{3(1-\nu)}$	$a = 1\cdot 2$ $b = 1\cdot 82$	$\nu = 0\cdot 2$: $c = -0\cdot 189$ $d = 0$ $\nu = 0\cdot 49$: $c = -0\cdot 0581$ $d = 0$

Location of the metacentre:

$$\frac{z_m}{R} = \xi + \frac{z_{m,\mathrm{surf.flat}}}{R} + \frac{c\xi}{d\xi + 1}$$

where:

$$\xi = \frac{z_D}{R} + 0\cdot 0964\cot\frac{\beta}{2}$$

$$\frac{z_{m,\mathrm{surf.flat}}}{R} = \frac{0\cdot 171(1-2\nu)}{-0\cdot 779\nu + 1}$$

$$c = 0\cdot 365\nu$$

$$d = 2\cdot 073$$

Note:

The formulae are meant to be used for embedment depth up to $z_D/R = 2$ (except for K_1, which can be used up to $z_D/R = 5$), for cone angle β from 120° (except for K_1, which can be used for β from 30°).

Putting the results of K_1, K_2, K_3''' together, the effect of embedment to each of the coefficients can be compared. Take the case of undrained loading ($\nu = 0{\cdot}5$), at an embedment of one radius, the cone factors μ_{cone} for K_1, K_2, K_3''', calculated from the formulae in Table 2.8, are: 0·894, 0·737 and 0·780, repectively. These results can also be verified visually in Figs. 2.6, 2.12 and 2.15. It shows that embedment does not only have significant effect on the vertical stiffness coefficient, but it also does for the horizontal and moment stiffness. In fact the effect on the horizontal and moment stiffness is more significant.

Analogously, for the same Poisson's ratio, a footing cone angle of $\beta = 120°$, for example, has cone factors μ_{cone} for K_1, K_2, K_3''' of 0·971, 0·855 and 0·966, respectively. This means the cone angle has more effect on the horizontal stiffness than the vertical and moment stiffness.

Chapter 3

Formulation of One Dimensional Interface Elements (Embedded in Plane Strain Two Dimensional Continuum)

3.1 Introduction

Interface elements are powerful tools in the modelling of discontinuities in different kinds of structures where conventional finite elements are not applicable. The physical phenomena to be modelled involve debonding and/or sliding along the discontinuity. The term *debonding* describes the separation of the two blocks of continuum adjacent to the joint surface, which were initially in contact. Subsequent recontact can also develop by the movement of the two blocks backs towards each other. The term *sliding* defines the relative motion along the joint surface when the shearing force exceeds the shear strength of the joint. In the area of geotechnics, interface elements have been used to model rock joints, soil- reinforcement interaction, etc.

The implementation of interface elements is essential to this research. Due to large horizontal and moment loading, the footing can slide or debond relative to the soil elements with which it was initially in contact.

Section 3.2 reviews some formulations of interface elements in the literature. As most formulations can be extended to two dimensional elements embedded in a three-dimensional continuum, this chapter serves as a review for both one-dimensional and two-dimensional

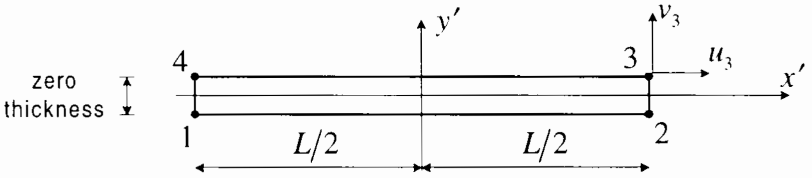

Figure 3.1: Joint element (after Goodman et al., 1968).

interface elements. Note that a new formulation of two-dimensional interface elements is described in detail in Chapter 4. Section 3.3 establishes the equations which calculate relative displacements at any point in the interface element from the nodal displacements. Section 3.4 details the constitutive laws used for the interface element. It also discusses the effect of the constitutive law on the stability of analyses involving the interface. The formulation of the element stiffness matrix based on this constitutive law is detailed in Section 3.5. In Section 3.6, a general algorithm for updating stresses for a given strain increment is described. The interface is then tested as described in Section 3.7.

3.2 Literature review

3.2.1 Goodman et al.'s (1968) one dimensional interface element

The first interface element was developed by Goodman et al. (1968) to model rock joints. As shown in Fig. 3.1, the interface element is a straight line interface element with zero thickness. The main feature of this element is that the constitutive stress–strain relationship in the conventional continuum elements is replaced with the relationship between stresses and relative displacements between the top and bottom layer of the interface:

$$\boldsymbol{\sigma} = \mathbf{C}\mathbf{u} \tag{3.1}$$

where $\boldsymbol{\sigma} = [\sigma_s \;\; \sigma_n]^{\mathrm{T}}$ are the shear and normal stress on the interface; **u** is the relative displacement in the local co-ordinate sustem (x', y') between the top and the bottom layer of the interface:

$$\mathbf{u} = \left\{ \begin{array}{c} u \\ v \end{array} \right\} = \left\{ \begin{array}{c} u_T - u_B \\ v_T - v_B \end{array} \right\} \tag{3.2}$$

where u_T, v_T are the shear and normal displacements of the top layer of the interface; u_B, v_B are the respective displacements of the bottom layer. The four displacements can be determined using the conventional shape function for this geometry.

The constitutive matrix **C** is defined as follows:

$$\mathbf{C} = \begin{bmatrix} K_s & 0 \\ 0 & K_n \end{bmatrix} \qquad (3.3)$$

where K_s and K_n are the shear and normal stiffness of the interface. K_s, K_n are generally not constant and depend on the relative displacements. They are usually set to very large values as the joint closes and very close to zero as the joint debonds. Assigning a very small value to K_s also allows the interface to model sliding. Using a standard procedure (Zienkiewicz, 1983), the element stiffness matrix **K** can be obtained.

3.2.2 Other interface element formulations

Since the Goodman et al. interface element, there have been further developments on interface elements; a full literature review of various interfaces can be found in Hohberg (1992). These developments have been made mainly on two fronts.

Firstly, in terms of the kinematic equation (Equ. 3.2), the simple straight line element in Goodman et al.'s (1968) is extended to cover a wide range of iso-parametric elements. Burd & Brocklehurst (1991) and Brocklehurst (1993) developed a one dimensional interface element. The interface element is mapped from one-dimensional local co-ordinate system (α) onto a global one (x, y). The formulation is described in details in Section 3.3. Gens et al. (1988) and Gens et al. (1995) developed a quadratic quadrilateral 16-noded quadrilateral interface element as shown in Fig. 3.2. Another formulation of quadrilateral interface elements are also shown in Schellekens & de Borst (1993).

Secondly, in later developments, the simple constitutive matrix **C** (Equ. 3.3) is replaced. A more sophisticated approach of the theory of plasticity are used to model different behaviours of the interface such as elastic phase (in which no significant additional deformations occurs) and plastic phase (in which the interface slides). Using this approach Burd & Brocklehurst (1991) and Brocklehurst (1993) develop a one dimensional interface element which can model dilatant interfaces. Special attention is also paid to the choice the yield criterion used for the interface model. The Mohr-Coulomb yield criteria is used in Burd & Brocklehurst (1991), Brocklehurst (1993), and Ghaboussi et al. (1973). Gens et al. (1990)

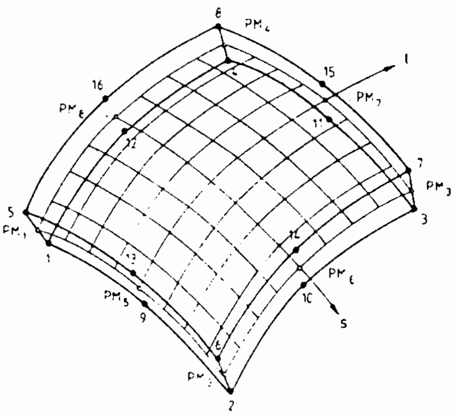

Figure 3.2: Quadrilateral interface element for three dimensional analyses (after Gens et al., 1988).

proposes the following hyperbolic yield criteria for the problem of rock joints:

$$f = \tau_1^2 + \tau_2^2 - \tan^2\phi\left(\sigma^2 + 2a\sigma\right) \tag{3.4}$$

where a and $\tan\phi$ are hardening parameters.

It should be noted that there is another class of interface elements which is usually referred to as 'thin layer elements'. They are continuum finite elements with small but finite thickness (Ghaboussi et al., 1973; Zienkiewicz et al., 1970; Pande & Sharma, 1979; Desai et al., 1984; Griffiths, 1985). If the thickness is large, the thin layer element will behave essentially as a solid element. As demonstrated in Hohberg (1992), thin layer elements and zero-thickness elements are not fundamentally different from the numerical point of view and a similar performance can be obtained from both zero thickness and thin layer elements.

3.2.3 Numerical instability when using interface elements

There are two major problems that might occur when interface elements are used. The first problem is the oscillation of shear stress distribution along the interface elements may occur as reported in Gens et al. (1988), Gens et al. (1995) and Schellekens & de Borst (1993). This problem is encountered when the interface undergoes a large sliding, which is, unfortunately, by far the most common failure mode in rock joints, the soil-reinforcement interfaces.

The second problem is the instability of the overall solution which may cause fluctuation seen in the load–displacement plot. This is usually associated with large nodal unbalanced forces. Finite element analyses involving interface elements may even fail due to the overall instability (Ghaboussi et al., 1973; Wilson, 1977; Pande & Sharma, 1979; Bell, 1991).

The reasons for each of the two problems, as well as their remedies, have been treated in the literature. For the first problem, several researchers note the effect of the integration scheme used to evaluate the stiffness matrix on the stability of the solution (Schellekens & de Borst, 1993; Gens et al., 1989). Gens et al. (1989) observe that for one-dimensional elements, spurious oscillations of the shear stress resulted when a Gaussian integration scheme is used and can be removed if a Newton-Cotes scheme is adopted. Burd & Brocklehurst (1991) found in their studies, also for one-dimensional elements, that the stress distribution is stable if sliding failure is not the dominant mode of deformation. For two-dimensional interface elements, Gens et al. (1989) suggest that the performance of interface elements is relatively unaffected by the integration scheme used.

Large off-diagonal terms or small diagonal terms in the global stiffness matrix is considered the major source of the second problem. It causes problems for the equation solver in which computer round-off errors take place. Wilson (1977) gives simple examples of the use of one dimensional interface elements to illustrate how computer round-off errors can cause numerical ill-conditioning.

Pande & Sharma (1979) elucidate this issue by performing several test on different machines of different accuracy, and show that in low accuracy machines, calculations involving interface elements may fail.

It is worth noting that the problem of overall instability led Ghaboussi et al. (1973) to develop a different interface element formulation. In their formulation, the displacement degree of freedom of one side of the interface surface are transformed into the relative displacements between the two sides of the interface as follows:

$$\begin{aligned} u^T_{ni} &= u_{ni} + \Delta_{ni} \\ u^T_{si} &= u_{si} + \Delta_{si} \qquad (3.5) \\ &\text{etc.} \end{aligned}$$

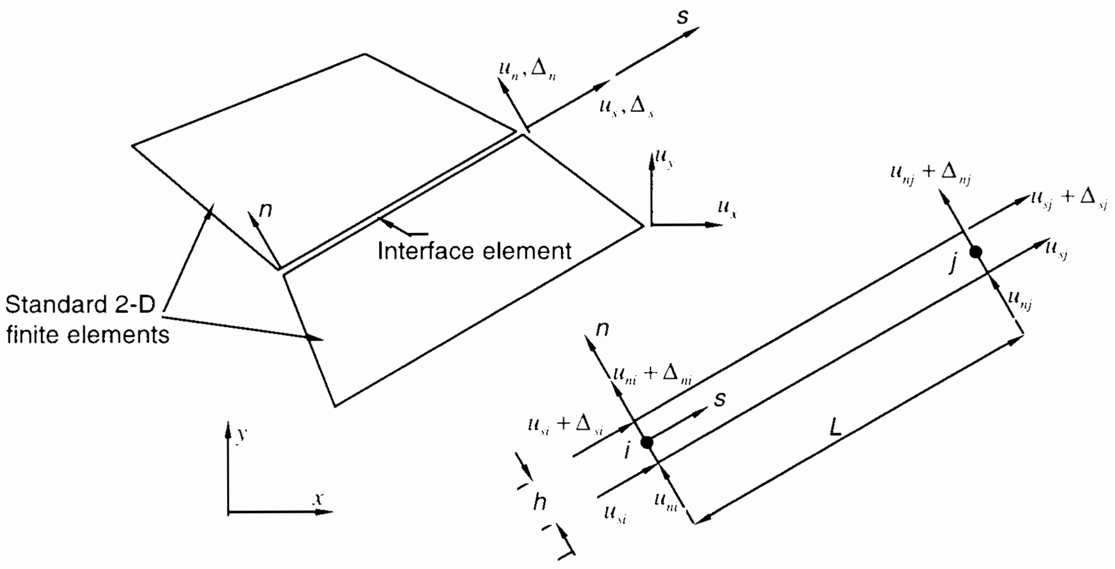

Figure 3.3: Two-dimensional interface element (after Ghaboussi et al., 1973).

or

$$
\begin{aligned}
\mathbf{u}^T &= \begin{Bmatrix} u^T_{ni} \\ u^T_{si} \\ u^T_{nj} \\ u^T_{sj} \end{Bmatrix} = \begin{bmatrix} 1 & 0 & 0 & 0 & 1 & 0 & 0 & 0 \\ 0 & 1 & 0 & 0 & 0 & 1 & 0 & 0 \\ 0 & 0 & 1 & 0 & 0 & 0 & 1 & 0 \\ 0 & 0 & 0 & 1 & 0 & 0 & 0 & 1 \end{bmatrix} \\
& \quad \begin{bmatrix} u_{ni} & u_{si} & u_{nj} & u_{sj} & \Delta_{ni} & \Delta_{si} & \Delta_{nj} & \Delta_{sj} \end{bmatrix}^T \\
&= \mathbf{a}\mathbf{u}^* \qquad (3.6)
\end{aligned}
$$

The notations are depicted in Fig. 3.3. Therefore the stiffness matrix of the standard element on the upper side of the interface will be increased in size in order to replace the conventional absolute displacements at its interface nodes with the sum of relative displacements of the interface and the absolute displacements. This formulation is believed to solve the problem of significant change in stiffness of the different elements (i.e. continuum and interface elements). Wilson (1977) also gives a simple example that ill-conditioning due to conventional formulation of interface element can be avoided if relative displacements are used as independent degrees of freedom. However, Pande & Sharma (1979) show that though Ghaboussi et al.'s (1973) formulation is more stable on low precision machine (24-bit mantissa), the conventional formulation is also stable on high precision computers (36- or 48-bit mantissa).

From the literature it appears that the two above-mentioned problems of oscillatory stress distribution and overall solution instability are uncoupled, i.e. they are not considered con-

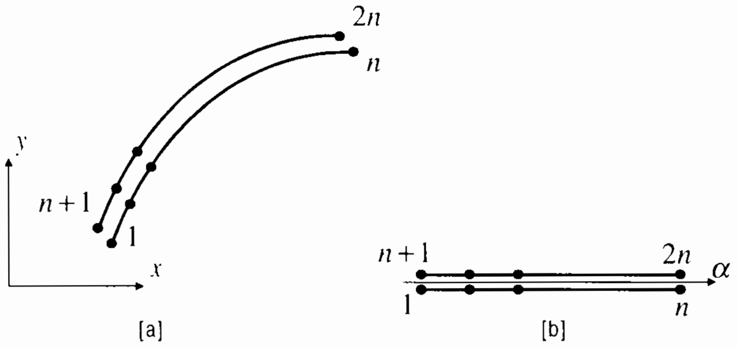

Figure 3.4: One-dimensional interface element (after Burd & Brocklehurst, 1991) (a) parent element; (b) mapped element.

currently in literature, and treatments for one problem are not necessarily effective for the other.

This study found that the instability can also be caused by the yield criteria used for the interface. This instability was overcome by the use of a two-part yield criterion which will be described later in Section 3.4.

3.3 Kinematic equations (after Burd & Brocklehurst, 1991)

This interface element is a zero-thickness interface. The interface element is mapped from one-dimensional local co-ordinate system (α) onto a global one (x, y) as shown in Fig. 3.4.

The vector of the global co-ordinates $\mathbf{r}$ of two arbitrary points a and b at a certain infinitesimal portion of the interface element, as shown in Fig. 3.5, is related to the global nodal co-ordinates $\mathbf{R}$ by:

$$\mathbf{r} = \mathbf{NR} \tag{3.7}$$

where $\mathbf{N}$, the shape function matrix, is a function of α.

Analogously the velocity vector of the two points $\mathbf{u}$ is related to nodal velocity vector $\mathbf{U}_a$ by

$$\mathbf{u} = \begin{Bmatrix} u_a^x \\ u_a^y \\ u_b^x \\ u_b^y \end{Bmatrix} = \mathbf{NU}_a \tag{3.8}$$

The velocities may be resolved into directions parallel to, and perpendicular to, the local

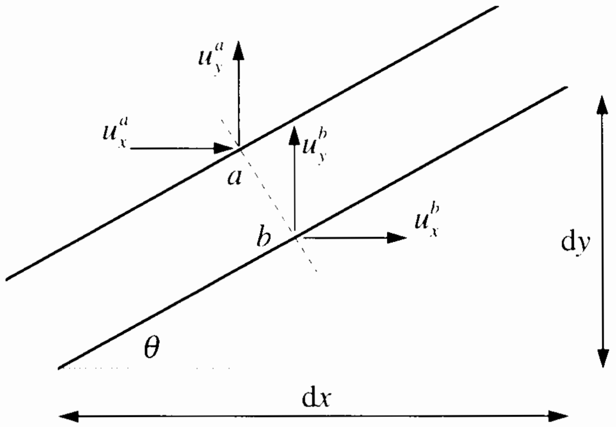

Figure 3.5: Interface element velocities.

slope of the element, and the relative velocities can then be found, as shown in Fig. 3.5, as follows:

$$\begin{aligned}\varepsilon_s &= (u_b^x - u_a^x)\cos\theta + (u_b^y - u_a^y)\sin\theta \\ \varepsilon_n &= (u_b^y - u_a^y)\cos\theta - (u_b^x - u_a^x)\sin\theta\end{aligned} \tag{3.9}$$

or

$$\begin{aligned}\epsilon &= \begin{bmatrix}\cos\theta & \sin\theta \\ -\sin\theta & \cos\theta\end{bmatrix}\begin{bmatrix}-1 & 0 & 1 & 0 \\ 0 & -1 & 0 & 1\end{bmatrix}\mathbf{u} \\ \epsilon &= \mathbf{SLu} = \mathbf{SLNU}_a = \mathbf{BU}_a\end{aligned} \tag{3.10}$$

where $\mathbf{B} = \mathbf{SLN}$ and $\epsilon = [\varepsilon_s \ \varepsilon_n]^{\mathrm{T}}$.

The terms of **S** can be written as:

$$\begin{aligned}\cos\theta &= \frac{dx/d\alpha}{J_1} \\ \sin\theta &= \frac{dy/d\alpha}{J_1}\end{aligned}$$

where $J = \sqrt{(dx/d\alpha)^2 + (dy/d\alpha)^2}$ is the Jacobian of the transformation.

3.4 Constitutive equations

The behaviour of the interface is based on the Mohr-Coulomb yield function, $f(\sigma)$. The yield function and the plastic potential are defined, respectively, by:

$$f(\sigma) = |\tau| - c + \sigma\tan\phi = 0 \tag{3.11}$$

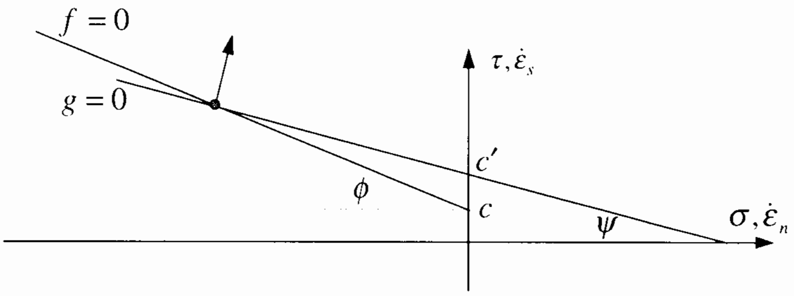

Figure 3.6: Yield surface and plastic potential.

$$g(\sigma) \quad = \quad |\tau| - c' + \sigma \tan\psi = 0 \tag{3.12}$$

where τ is the shear stress and σ is the normal stress; c, ϕ and ψ are the cohesion, angle of friction and angle of dilation, respectively. The yield function and the plastic potential are depicted in Fig. 3.6.

The relation between stress increment and strain increment is:

$$\dot{\sigma} = \mathbf{D}^{ep}\dot{\epsilon} = \mathbf{D}^{ep}\mathbf{B}\dot{\mathbf{U}} \tag{3.13}$$

where $\mathbf{D}^{ep}$ is determined as follows:

$$\mathbf{D}^{ep} = \mathbf{D}^{e} + \mathbf{D}^{p} \tag{3.14}$$

and $\mathbf{D}^{e}$ and $\mathbf{D}^{p}$ are determined by the following formulae (Brocklehurst, 1993):

$$\mathbf{D}^{e} = \begin{bmatrix} K_s & 0 \\ 0 & K_n \end{bmatrix} \tag{3.15}$$

$$\mathbf{D}^{p} = \frac{-\mathbf{D}^{e}\left\{\dfrac{\partial g}{\partial \sigma}\right\}\left\{\dfrac{\partial f}{\partial \sigma}\right\}^{T}\mathbf{D}^{e}}{\left\{\dfrac{\partial f}{\partial \sigma}\right\}^{T}\mathbf{D}^{e}\left\{\dfrac{\partial g}{\partial \sigma}\right\}} \tag{3.16}$$

$$\mathbf{D}^{ep} = \frac{K_s K_n}{K_s + K_n \tan\phi \tan\psi}\begin{bmatrix} \tan\phi\tan\psi & -\text{sign}(\tau)\tan\phi \\ -\text{sign}(\tau)\tan\psi & 1 \end{bmatrix} \tag{3.17}$$

where sign(x) is a function returning $+1$ if x is greater than 0, -1 if x is smaller than 0, and zero otherwise.

In the modified Euler solution scheme, after each calculation step unbalanced forces are calculated and added into the load increment applied in the next step. Fluctuation in overall

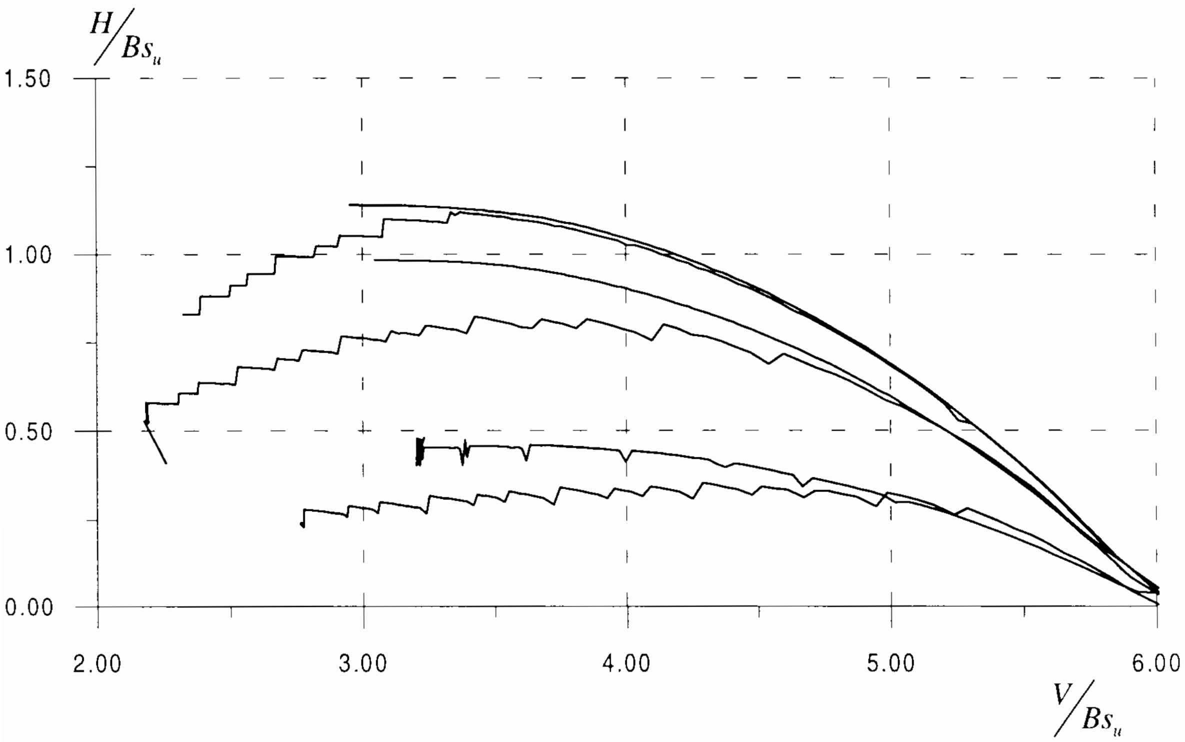

Figure 3.7: (V, H) interaction: instability of purely cohesive interface elements.

performance is observed in this study if debonding happens at a certain step. This happens becasue the stiffness matrix of the interface element is formed assuming the element is in contact while the stress updating subroutine later finds the element has been relaxed and therefore assigns stress to zero. This may result in large unbalanced forces in the next step, causing the interface nodes to oscillate.

This oscillation can be seen in Fig. 3.7 and Fig. 3.8 which are the result of some of the analyses carried out in Chapter 5 to establish the bearing capacity envelope of a strip footing. In these runs, a vertical displacement is applied until the footing reaches the vertical bearing capacity ($V/Bs_u \approx 6$). Combinations of horizontal and rotational displacements are then applied in order to construct the bearing capacity envelope for strip footings. The interface elements used are purely cohesive governed by Equ. 3.12 with:

$$c = 2/\sqrt{3};\ \phi = 0^\circ;\ \psi = 0^\circ \tag{3.18}$$

Fig. 3.7 shows that in the region of low normal stress oscillations happen. Some analyses have such large unbalanced forces that they could not be completed due to floating point errors.

This oscillation can be explained by the cohesive term. When the interface element is at

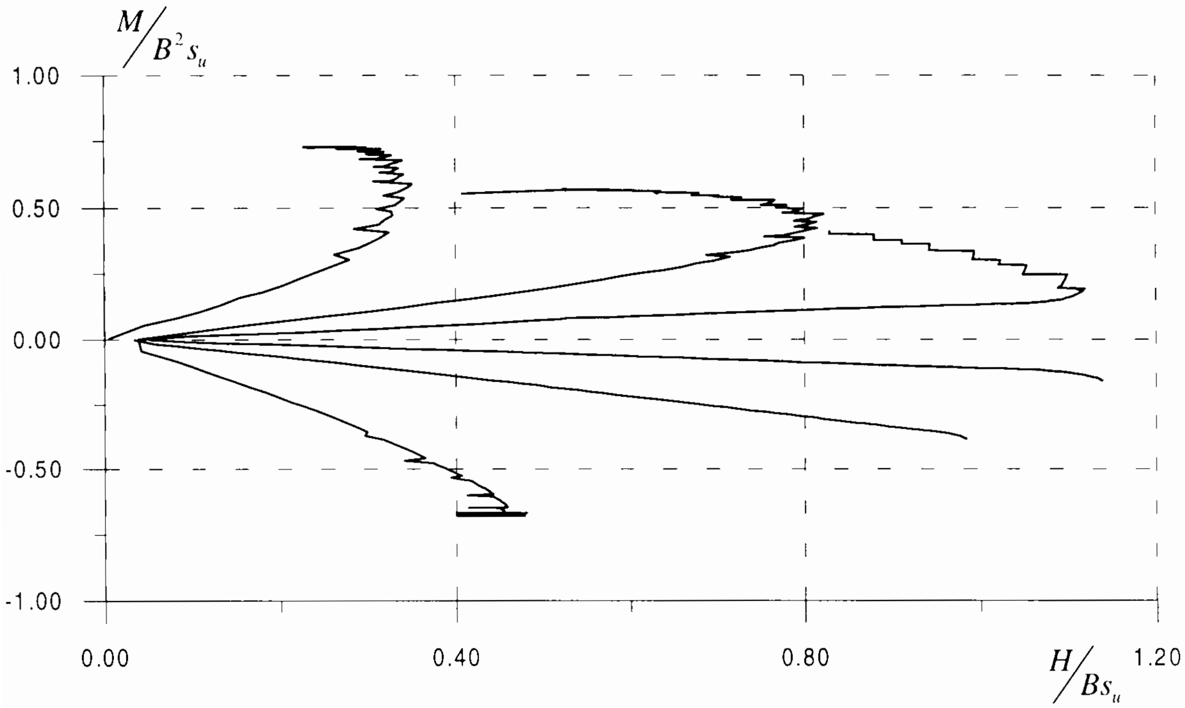

Figure 3.8: (H, M) interaction: instability of purely cohesive interface elements.

the threshold of debonding (σ is then negative but close to zero), the interface shear stress τ can still have a horizontal stress of up to c. This causes a jump, which could be up to c in magnitude, in the shear stress of the interface when the interface changes from bonding to debonding status, or vice versa. At the same time this may induce large unbalanced forces causing the analsysis to fail.

As the relationship between normal stress and normal relative displacement is continuous, the normal stress does not suffer from such a jump. This is the reason for fluctuation to be principally in the H component only. The load path in (V, M) space for the same analyses is still smooth as shown in Fig. 3.9.

A modification of the yield criterion for the interface is therefore needed. The yield criterion is now comprised of two parts. At low levels of compressive stress, the interface is governed by cohesionless frictional behaviour. At high levels of compressive stress, the interface is governed by frictionless cohesive behaviour. The yield criterion of the interface is illustrated in Fig. 3.10. The frictional part of the yield surface, in effect, assumes the drained behaviour in the soil under low vertical load. This is reasonable as under low vertical load (and significant horizontal load), the deforming zone in the soil under the footing is shallow, i.e. the drainage path is short. In addition, there is experimental evidence for this

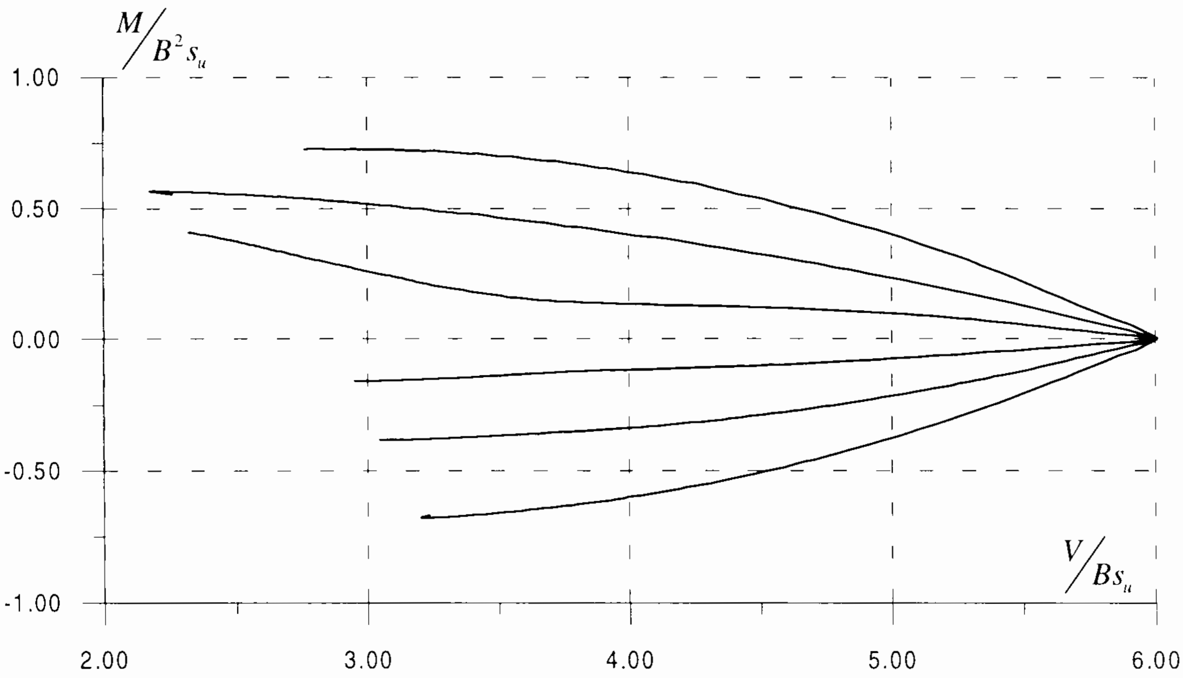

Figure 3.9: (V, M) interaction: instability of purely cohesive interface elements.

drained behaviour in model tests conducted by Martin (1994). It was found in Martin's (1994) *undrained* combined loading tests that when the vertical load reduces to zero, the horizontal load capacity of the footing also decreases to zero. Martin's (1994) experiments will be reviewed in Chapter 5.

The value of friction angle $\phi = 30°$ is, however, only a representative one. In using this interface in the computer programme OXFEM, this value can be changed. The size and shape of the bearing capacity envelope under low vertical load is dependent on the friction angle ϕ. More details on the dependence of the bearing capacity envelope on ϕ are given in Section 5.4.3.2 and Section 6.4.2.

The two-part yield surface is used throughout this research and results in smooth performance as seen in Chapter 5 and Chapter 6.

3.5 Element stiffness matrix

Let $\dot{\mathbf{P}}$ define the equivalent nodal forces. Applying an arbitrary set of virtual nodal displacement increments $\dot{\mathbf{U}}^*$, we have the equation from the theory of virtual work:

$$\dot{\mathbf{U}}^{*T}\dot{\mathbf{P}} = \int_E \dot{\epsilon}^{*T}\dot{\sigma}dE \tag{3.19}$$

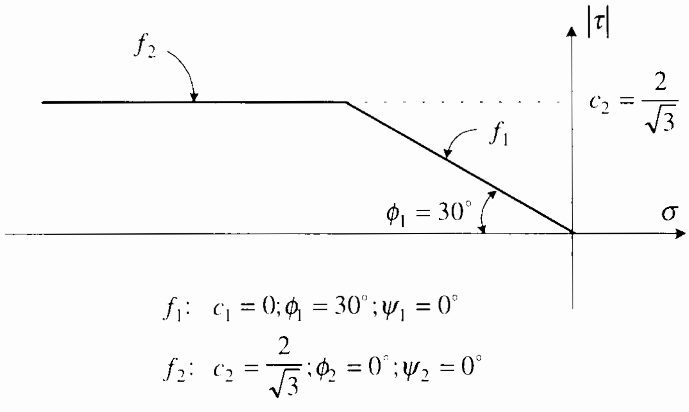

Figure 3.10: Two-part yield criterion for interface element.

where $\dot{\epsilon}^*$ are the relative displacements that are compatible with the virtual nodal displacements $\dot{\mathbf{U}}^{*T}$. Substituting Equ. 3.10 and Equ. 3.13 into the above equation, we have:

$$\dot{\mathbf{U}}^{*T}\dot{\mathbf{P}} = \int_E \dot{\mathbf{U}}^{*T}\mathbf{B}^T\dot{\sigma}\,dE = \int_E \dot{\mathbf{U}}^{*T}\mathbf{B}^T\mathbf{D}^{ep}\mathbf{B}\dot{\mathbf{U}}\,dE = \dot{\mathbf{U}}^{*T}\int_E \mathbf{B}^T\mathbf{D}^{ep}\mathbf{B}\dot{\mathbf{U}}\,dE \tag{3.20}$$

Since the virtual displacement are arbitrary, we can write:

$$\dot{\mathbf{P}} = \int_E \mathbf{B}^T\mathbf{D}^{ep}\mathbf{B}\dot{\mathbf{U}}\,dE = \mathbf{K}^e\dot{\mathbf{U}} \tag{3.21}$$

where $\mathbf{K}^e = \int_E \mathbf{B}^T\mathbf{D}^{ep}\mathbf{B}\,dE = \int \mathbf{B}^T\mathbf{D}^{ep}\mathbf{B}J\,d\alpha$ is the element stiffness matrix and J is the Jacobian of the transformation as defined in Fig. 3.11.

3.6 Stress updating

The stress updating routine calculates the stress increment at Gauss points for a given strain increment. Various cases, as outlined below, must be examined. The stress updating routine described in this study uses the cumulative relative displacement, instead of normal stress, as the criteria to determine whether the interface element is in contact or relaxed.

3.6.1 Relaxed – relaxed or bonding – relaxed

First it is checked that if at the end of the current calculation step, the interface is relaxed (i.e. loss of contact). If it is, regardless of the interface being relaxed or bonding (i.e. the two sides of the interface are in contact) at the end of the last calculation step, the cumulative stress is set to zero.

Loss of contact of the interface occurs if:

$$\varepsilon_{n,t=1} > 0 \tag{3.22}$$

In that case, the cumulative stress at time t_1 is assigned to zero. The interface element is flagged as 'relaxed' and the stiffness will be assigned very small values in the next step of calculation.

If at the end of the current step, the interface is bonding, there are possibilities that the interface was either relaxed or bonding at the end of the last step. The two cases are considered below.

3.6.2 Relaxed – bonding

The relative displacement velocities are assumed to change linearly during the time step. The time at which the interface regains contact can therefore be calculated as follows:

$$t_c = \frac{\varepsilon_{n,t=0}}{\varepsilon_{n,t=0} - \varepsilon_{n,t=1}} \tag{3.23}$$

At the time $t = t_c$, the stress is zero. The stress path from t_c to $t = 1$ is updated as for the case bonding–bonding which is described in the following section.

3.6.3 Bonding – bonding

When the interface undergoes a relative displacement increment during which the interface remains in contact (i.e. bonding – bonding), the stress update routine for interface elements is similar to that of continuum elements. The stress is first updated assuming the interface behaves elastically. The stress at the end of the step is therefore calculated as follows:

$$\sigma_1^e = \sigma_0 + \mathbf{D}^e \dot{\epsilon} \Delta t \tag{3.24}$$

The stress is then checked for the yield status. The resulting yield status, together with the status at the beginning of the update is then checked against the following cases, and the stress will be updated accordingly.

3.6.3.1 Elastic – elastic or plastic – elastic

The interface is thus being unloaded. The assumption of the interface behaving elastically is therefore correct. The update is then completed.

3.6.3.2 Elastic – plastic or plastic – plastic

Regardless whether the starting yield status is elastic or plastic, if the ending yield status is plastic, the normal stress σ can be updated elastically as follows:

$$\sigma_1 = \sigma_0 + K_n \dot{\varepsilon}_n (t_1 - t_0) \tag{3.25}$$

as the interface element of interest of this research is non-dilatant.

The shear stress can then be calculated based on the new normal stress:

- If $\tau_1^e > c - \sigma_1 \tan\phi$,

  $$\tau_1 = c - \sigma_1 \tan\phi \tag{3.26}$$

  and the interface is flagged as 'positive yielding'.

- If $\tau_1^e < -c + \sigma_1 \tan\phi$,

  $$\tau_1 = -c + \sigma_1 \tan\phi \tag{3.27}$$

  and the interface is flagged as 'negative yielding'.

If the stress changes its yield status from positive yield to negative yield, or vice versa, in one calculation step, the stress path has in fact gone through an elastic stress update (unloading) and then plastic update. However, the element stiffness matrix is calculated for the current step and the next step as elasto-plasticity matrix. This can result in the fact that the interface fails to take into account the change of direction/magnitude of applied loads, which were experienced in one test to validate this formulation. In order to fix this situation, if the stress changes its yield status from positive yield to negative yield, or vice versa, in one step, the yield status of the interface is flagged as 'elastic'.

3.7 Numerical validation of the interface

Several different tests are carried out to validate the interface. In all of these tests, the interfaces are governed by the constitutive equation composed of two parts as discussed in Section 3.4. The numerical values the interface properties are:

$$K_s = K_n = 1000$$

$$c_1 = 0; \phi_1 = 30°; \psi_1 = 0°$$

$$c_2 = \frac{2}{\sqrt{3}}; \phi_2 = 0°; \psi_2 = 0°$$

The verification of the interface element formulation consists of several tests, out of which two significant ones are described later. The tests contain continuum elements along with interface elements and involve combined loading. The relevant analytical solutions are therefore not straightforward. These tests hence need be interpreted qualitatively. Smooth, non-oscillating performance which is physically reasonable is the primary aim. Numerical results cannot be compared with exact solutions because the latter are not available.

3.7.1 Test One

In this test, a large compression is applied followed by a small slide such that no plastic sliding occurs. The compression is then reduced to zero. At a certain stage of the decompression the interface starts to slide and the upper and lower continuum elements recover their initial square shape, leaving the interface skew.

The system is illustrated in Fig. 3.11. In this test, the plastic state is reached by the reduction in compression. The continuum elements at the same time recover their initial shape.

The total forces acting at the top nodes of the sample are plotted in Fig. 3.12. At the end of the second load regime (steps 10-30) the horizontal force is still increasing (i.e. the interface is still behaving elastically). The horizontal force stays roughly unchanged during decompression until the vertical force is small enough to let the interface element slide plastically. Together with the reduction of vertical force towards zero, the horizontal force is also reduced to zero.

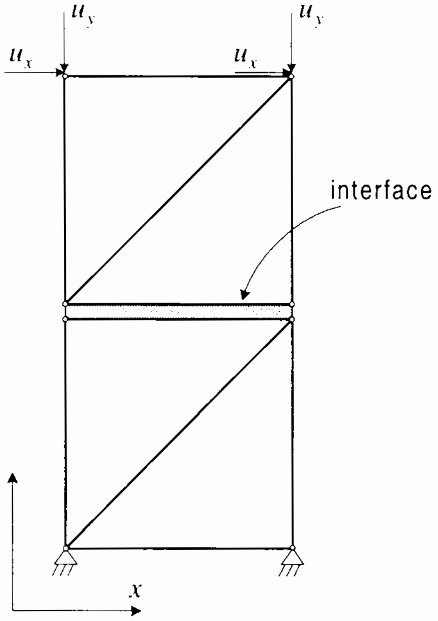

Figure 3.11: Mesh for Test One.

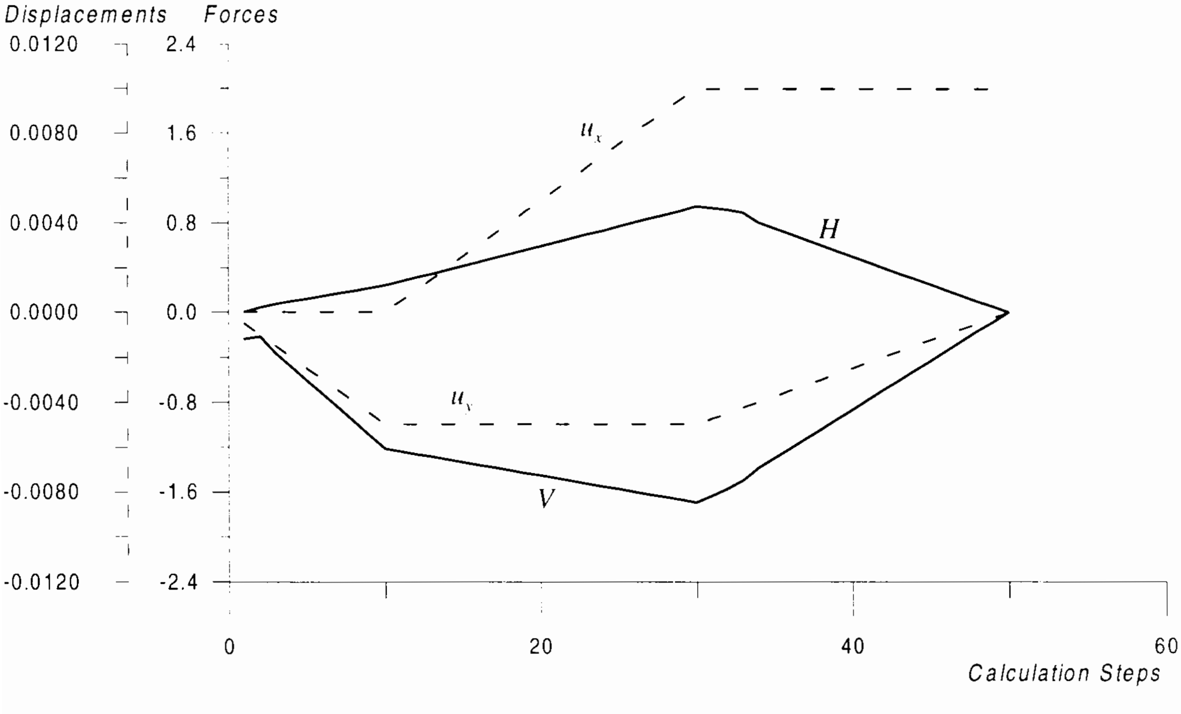

Figure 3.12: Result of Test One.

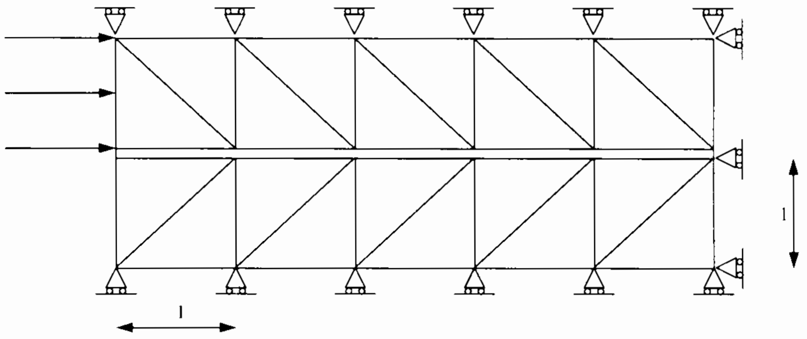

Figure 3.13: Validating the interface: Test Two.

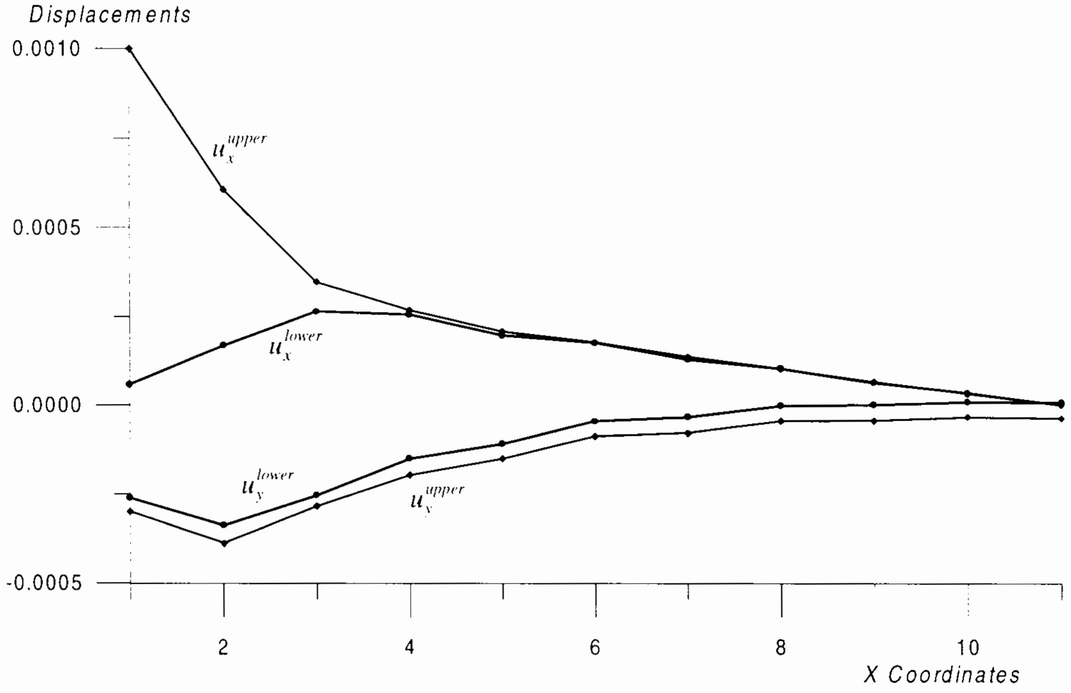

Figure 3.14: Result of Test Two.

3.7.2 Test Two

The system as well as the applied displacements is illustrated in Fig. 3.13. Displacements are imposed at one end of the upper half of the specimen while the other end is kept fixed; the stress and strain along the interface varies more drastically in this test than in the previous tests.

The result of this test is plotted in Fig. 3.14. The plotted value is the relative displacement at integration points of the inteface. The curves are smooth, the difference in horizontal displacement being large at left end, reducing to zero at the right end where all horizontal movement is fixed as expected.

Chapter 4

Formulation of Two Dimensional Interface Elements (Embedded in Three Dimensional Continuum)

4.1 Introduction

This chapter deals with the application of the interface elements to three dimensional finite element analyses. As the research includes a study of an axi-symmetrical footing under combined loadings, such an interface element is needed.

The chapter is organised as follows. Section 4.2 establishes the equation which calculates relative displacements at any point in the interface element from the nodal relative displacement. Section 4.3 details the constitutive laws used for the interface element, which leads to the formation of the element stiffness matrix detailed in Section 4.4. In Section 4.5 a general algorithm for updating stresses from strain increments is presented. A closed-form solution to integrate the elasto-plastic stress–strain relationship is given in Section 4.6. In Section 4.7 the solution is then compared, for a special case of strain increment, with Krieg & Krieg's (1977) solution in order to validate the new solution. The chapter ends with Section 4.8 describing several validating tests conducted on this formulation. As the section shows, the interface behaves as expected.

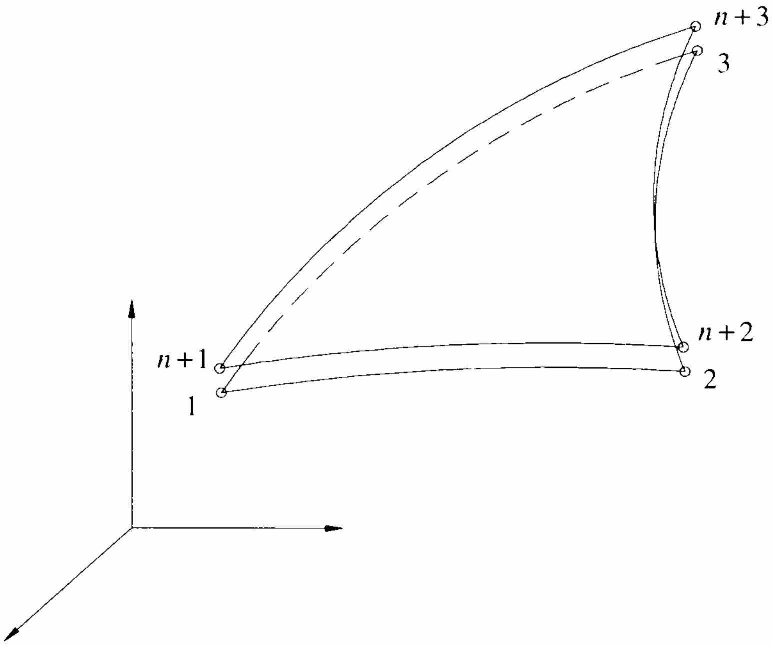

Figure 4.1: Two dimensional interface elements.

4.2 Kinematic equations:

Consider a two dimensional interface element that has $2n$ nodes as shown in Fig. 4.1. Note that the coordinates of the upper nodes are identical to those of the respective lower nodes.

The relative displacements at any point in the surface can be determined by:

$$\dot{\mathbf{u}}_r = \begin{Bmatrix} \dot{u}_x^r \\ \dot{u}_y^r \\ \dot{u}_z^r \end{Bmatrix} = \begin{Bmatrix} \dot{u}_x^u - \dot{u}_x^l \\ \dot{u}_y^u - \dot{u}_y^l \\ \dot{u}_z^u - \dot{u}_z^l \end{Bmatrix} = \begin{bmatrix} -\mathbf{I} & \mathbf{I} \end{bmatrix} \begin{Bmatrix} \dot{\mathbf{u}}_l \\ \dot{\mathbf{u}}_u \end{Bmatrix} = \mathbf{L} \begin{Bmatrix} \dot{\mathbf{u}}_l \\ \dot{\mathbf{u}}_u \end{Bmatrix} \tag{4.1}$$

where $\dot{\mathbf{u}}_u$, $\dot{\mathbf{u}}_l$ are velocities of the upper and lower parts of the interface element, and are defined by:

$$\begin{Bmatrix} \dot{\mathbf{u}}_l \\ \dot{\mathbf{u}}_u \end{Bmatrix} = \begin{bmatrix} \mathbf{N}_c \dot{\mathbf{U}}_l \\ \mathbf{N}_c \dot{\mathbf{U}}_u \end{bmatrix} = \begin{bmatrix} \mathbf{N}_c & \mathbf{0} \\ \mathbf{0} & \mathbf{N}_c \end{bmatrix} \begin{Bmatrix} \dot{\mathbf{U}}_l \\ \dot{\mathbf{U}}_u \end{Bmatrix} \tag{4.2}$$

where $\mathbf{N}_c$ is the shape function matrix, defined as:

$$\mathbf{N}_c = \begin{bmatrix} \mathbf{N}_1 & \dots & \mathbf{N}_n \end{bmatrix} \tag{4.3}$$

$$\mathbf{N}_i = \begin{bmatrix} N_i & 0 & 0 \\ 0 & N_i & 0 \\ 0 & 0 & N_i \end{bmatrix} = N_i\mathbf{I} \tag{4.4}$$

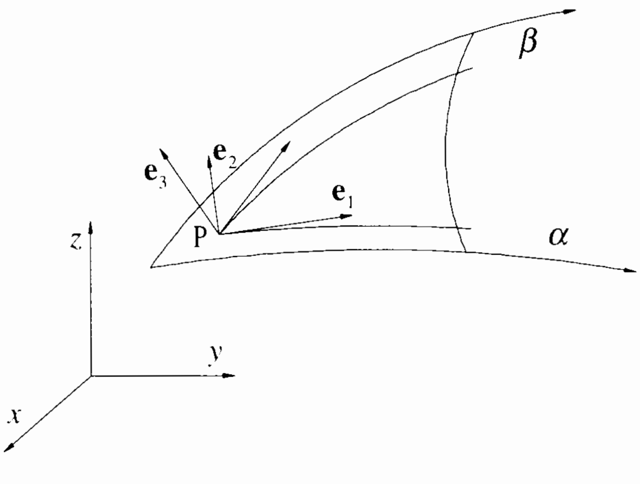

Figure 4.2: Coordinate transformation.

and $\dot{\mathbf{U}}_u$, $\dot{\mathbf{U}}_l$ are velocities of the upper and lower nodes respectively:

$$\dot{\mathbf{U}}_l = \begin{bmatrix} \dot{u}_x^1 & \dot{u}_y^1 & \dot{u}_z^1 & \dots & \dot{u}_x^n & \dot{u}_y^n & \dot{u}_z^n \end{bmatrix}^T \tag{4.5}$$

$$\dot{\mathbf{U}}_u = \begin{bmatrix} \dot{u}_x^{n+1} & \dot{u}_y^{n+1} & \dot{u}_z^{n+1} & \dots & \dot{u}_x^{2n} & \dot{u}_y^{2n} & \dot{u}_z^{2n} \end{bmatrix}^T \tag{4.6}$$

Finally we obtain:

$$\dot{\mathbf{u}}_r = \mathbf{L}\mathbf{N}\dot{\mathbf{U}} \tag{4.7}$$

in which $\mathbf{L} = \begin{bmatrix} -\mathbf{I} & \mathbf{I} \end{bmatrix}$, $\mathbf{N} = \begin{bmatrix} \mathbf{N}_c & \mathbf{0} \\ \mathbf{0} & \mathbf{N}_c \end{bmatrix}$ and $\dot{\mathbf{U}}$ is the nodal velocities of the interface element, $\dot{\mathbf{U}} = \begin{Bmatrix} \dot{\mathbf{U}}_l \\ \dot{\mathbf{U}}_u \end{Bmatrix}$.

In order to apply the constitutive law for the interface, a local coordinate system is established. The origin of the system is at the point of interest P (c_1, c_2) on the surface. The first axis is tangential to the curve $\beta = c_2$. The second one is perpendicular to the first and lies on the plane tangential with the surface at the point P. The remaining axis is normal to the surface. The unit base vectors $\mathbf{e}_1, \mathbf{e}_2, \mathbf{e}_3$ of the system are shown in Fig. 4.2.

The following section determines the components of the three base unit vectors $\mathbf{e}_1, \mathbf{e}_2, \mathbf{e}_3$ of the rectangular coordinate system (e_1, e_2, e_3). We have:

$$\mathbf{e}_1 = \begin{Bmatrix} \cos\alpha_{11} \\ \cos\alpha_{12} \\ \cos\alpha_{13} \end{Bmatrix}, \mathbf{e}_2 = \begin{Bmatrix} \cos\alpha_{21} \\ \cos\alpha_{22} \\ \cos\alpha_{23} \end{Bmatrix}, \mathbf{e}_3 = \begin{Bmatrix} \cos\alpha_{31} \\ \cos\alpha_{32} \\ \cos\alpha_{33} \end{Bmatrix} \tag{4.8}$$

where $\cos\alpha_{pq}$, $p, q = 1,2,3$, are the direction cosines of the transformation.

If **r** is a position vector of the surface, using the matrix notation $\begin{bmatrix} x & y & z \end{bmatrix}^{\mathrm{T}}$ to denote a vector $x\mathbf{i}+y\mathbf{j}+z\mathbf{k}$, we have

$$\mathbf{r}=\begin{bmatrix} x & y & z \end{bmatrix}^{\mathrm{T}}=\mathbf{N}_c\mathbf{X} \tag{4.9}$$

where **X** is the vector of nodal coordinates in the global three dimensional coordinate system.

As $\frac{\partial \mathbf{r}}{\partial \alpha}$ is a vector tangent to the curve $\beta = c_2$, $\mathbf{e}_1$ can be determined as follows:

$$\mathbf{e}_1=\frac{\frac{\partial \mathbf{r}}{\partial \alpha}}{\left|\frac{\partial \mathbf{r}}{\partial \alpha}\right|}=\frac{1}{J_1}\frac{\partial \mathbf{r}}{\partial \alpha}=\frac{1}{J_1}\begin{Bmatrix} \frac{\partial x}{\partial \alpha} \\ \frac{\partial y}{\partial \alpha} \\ \frac{\partial z}{\partial \alpha} \end{Bmatrix} \tag{4.10}$$

where $J_1=\left|\frac{\partial \mathbf{r}}{\partial \alpha}\right|=\sqrt{\left(\frac{\partial x}{\partial \alpha}\right)^2+\left(\frac{\partial y}{\partial \alpha}\right)^2+\left(\frac{\partial z}{\partial \alpha}\right)^2}$ is the Jacobian of mapping a curve from (x,y,z) space to one dimensional space (α) and the notation $|\mathbf{a}|$ is used to denote the magnitude of a vector **a**.

Because $\frac{\partial \mathbf{r}}{\partial \alpha}$ and $\frac{\partial \mathbf{r}}{\partial \beta}$ are tangential to the surface, the normal vector $\mathbf{e}_3$ can be found as:

$$\mathbf{e}_3=\frac{\frac{\partial \mathbf{r}}{\partial \alpha}\times\frac{\partial \mathbf{r}}{\partial \beta}}{\left|\frac{\partial \mathbf{r}}{\partial \alpha}\times\frac{\partial \mathbf{r}}{\partial \beta}\right|}=\frac{1}{J}\begin{vmatrix} \mathbf{i} & \mathbf{j} & \mathbf{k} \\ \frac{\partial x}{\partial \alpha} & \frac{\partial y}{\partial \alpha} & \frac{\partial z}{\partial \alpha} \\ \frac{\partial x}{\partial \beta} & \frac{\partial y}{\partial \beta} & \frac{\partial z}{\partial \beta} \end{vmatrix}=\frac{1}{J}\begin{Bmatrix} \frac{\partial y}{\partial \alpha}\frac{\partial z}{\partial \beta}-\frac{\partial z}{\partial \alpha}\frac{\partial y}{\partial \beta} \\ -\frac{\partial x}{\partial \alpha}\frac{\partial z}{\partial \beta}+\frac{\partial z}{\partial \alpha}\frac{\partial x}{\partial \beta} \\ \frac{\partial x}{\partial \alpha}\frac{\partial y}{\partial \beta}-\frac{\partial y}{\partial \alpha}\frac{\partial x}{\partial \beta} \end{Bmatrix} \tag{4.11}$$

where $J=\left|\frac{\partial \mathbf{r}}{\partial \alpha}\times\frac{\partial \mathbf{r}}{\partial \beta}\right|$ is the Jacobian of mapping a surface from the (x,y,z) space to the two dimensional space (α,β).

The vector $\mathbf{e}_2$ can be formulated directly from the direction cosines of the vectors $\mathbf{e}_1,\mathbf{e}_3$:

$$\mathbf{e}_2=\begin{Bmatrix} \cos\alpha_{21} \\ \cos\alpha_{22} \\ \cos\alpha_{23} \end{Bmatrix}=\mathbf{e}_3\times\mathbf{e}_1 = \begin{vmatrix} \mathbf{i} & \mathbf{j} & \mathbf{k} \\ \cos\alpha_{31} & \cos\alpha_{32} & \cos\alpha_{33} \\ \cos\alpha_{11} & \cos\alpha_{12} & \cos\alpha_{13} \end{vmatrix}$$

$$= \begin{Bmatrix} \cos\alpha_{32}\cos\alpha_{13}-\cos\alpha_{12}\cos\alpha_{33} \\ -\cos\alpha_{31}\cos\alpha_{13}+\cos\alpha_{11}\cos\alpha_{33} \\ \cos\alpha_{31}\cos\alpha_{12}-\cos\alpha_{11}\cos\alpha_{32} \end{Bmatrix} \tag{4.12}$$

According to this formulation, the direction of $\mathbf{e}_3$ is the direction of separation of the second layer of interface nodes from the first one. Therefore, the node numbering scheme is important.

In Equs. 4.10, 4.11 and 4.12, $\frac{\partial x}{\partial \alpha}$, etc. can be determined by using the first partial derivatives of shape functions of one layer of interface element nodes.

The relative displacement increment in the directions of $(\mathbf{e}_1, \mathbf{e}_2, \mathbf{e}_3)$ can be then determined as follows:

$$\begin{aligned}\dot{\epsilon} &= \begin{Bmatrix} \dot{\varepsilon}_1 \\ \dot{\varepsilon}_2 \\ \dot{\varepsilon}_3 \end{Bmatrix} = \begin{bmatrix} \cos\alpha_{11} & \cos\alpha_{12} & \cos\alpha_{13} \\ \cos\alpha_{21} & \cos\alpha_{22} & \cos\alpha_{23} \\ \cos\alpha_{31} & \cos\alpha_{32} & \cos\alpha_{33} \end{bmatrix} \begin{Bmatrix} \dot{u}_x^r \\ \dot{u}_y^r \\ \dot{u}_z^r \end{Bmatrix} \\ &= \mathbf{C}\dot{\mathbf{u}}_r = \mathbf{CLN}\dot{\mathbf{U}} = \mathbf{B}\dot{\mathbf{U}} \end{aligned} \tag{4.13}$$

where $\mathbf{C}$ is the matrix of direction cosines of the transformation, and $\mathbf{B} = \mathbf{CLN}$.

4.3 Constitutive equations

The interface element uses the Mohr-Coulomb yield function:

$$f = \tau_1^2 + \tau_2^2 - (\sigma \tan\phi - c)^2 = 0 \tag{4.14}$$

and the plastic potential g is as follows:

$$g = \tau_1^2 + \tau_2^2 - (\sigma \tan\psi - c')^2 = 0 \tag{4.15}$$

where $c' = \sigma(\tan\psi - \tan\phi) + c$. The yield function and the plastic potential are depicted in Fig. 4.3. As mentioned in Chapter 3, using a two-part yield function, the numerical instability which is often encountered when interface elements are used can be avoided. Therefore, a two-part yield function is also used for this two dimensional interface element. This two-part yield function requires no change in the mathematical formulation of the interface presented in this chapter. Nonetheless, in the implementation of the element into a computer program, checks are made to ensure that the proper yield surface and plastic potential are used.

The relationship between stress increment and strain increment is:

$$\dot{\boldsymbol{\sigma}} = \mathbf{D}^{ep}\dot{\epsilon} = \mathbf{D}^{ep}\mathbf{B}\dot{\mathbf{U}} \tag{4.16}$$

where $\boldsymbol{\sigma} = [\tau_1 \ \ \tau_2 \ \ \sigma]^{\mathrm{T}}$ and the matrix $\mathbf{D}^{ep}$ is determined as follows:

$$\mathbf{D}^{ep} = \mathbf{D}^e + \mathbf{D}^p \tag{4.17}$$

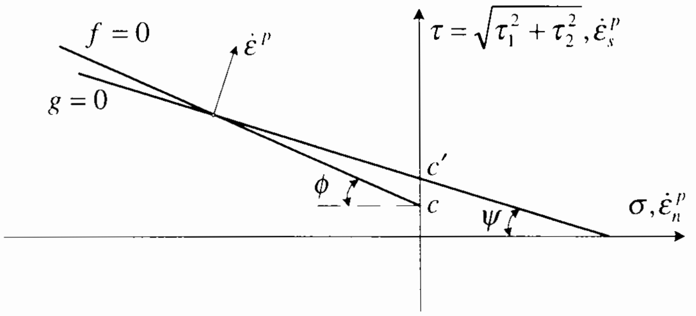

Figure 4.3: Yield surface and plastic potential.

where $\mathbf{D}^e$ and $\mathbf{D}^p$ are determined by the following formulae:

$$\mathbf{D}^e = \begin{bmatrix} K_s & 0 & 0 \\ 0 & K_s & 0 \\ 0 & 0 & K_n \end{bmatrix}; \tag{4.18}$$

and

$$\mathbf{D}^p = \frac{-\mathbf{D}^e \left\{\dfrac{\partial g}{\partial \sigma}\right\} \left\{\dfrac{\partial f}{\partial \sigma}\right\}^T \mathbf{D}^e}{\left\{\dfrac{\partial f}{\partial \sigma}\right\}^T \mathbf{D}^e \left\{\dfrac{\partial g}{\partial \sigma}\right\}} \tag{4.19}$$

thus:

$$\mathbf{D}^{ep} = \frac{1}{s} \begin{bmatrix} (\tau_2^2 K_s + a)K_s & -\tau_1\tau_2 K_s^2 & \tau_1 \sigma \tan^2\phi K_s K_n \\ -\tau_1\tau_2 K_s^2 & (\tau_1^2 K_s + a)K_s & \tau_2 \sigma \tan^2\phi K_s K_n \\ \tau_1 \sigma \tan\phi \tan\psi K_s K_n & \tau_2 \sigma \tan\phi \tan\psi K_s K_n & (\tau_1^2+\tau_2^2) K_s K_n \end{bmatrix} \tag{4.20}$$

where $s = \tau_1^2 K_s + \tau_2^2 K_s + \sigma^2 \tan^3\phi \tan\psi K_n$ and $a = \sigma^2 \tan^3\phi \tan\psi K_n$.

4.4 Element stiffness matrix

Let $\dot{\mathbf{P}}$ define the equivalent nodal forces. Applying an arbitrary set of virtual nodal displacement increments $\dot{\mathbf{U}}^*$, we have from the theory of virtual work:

$$\dot{\mathbf{U}}^{*T}\dot{\mathbf{P}} = \int_E \dot{\epsilon}^{*T} \dot{\sigma} dE \tag{4.21}$$

where $\dot{\epsilon}^*$ is the relative displacements that are compatible with the virtual nodal displacements $\dot{\mathbf{U}}^{*T}$. Substituting Equ. 4.13 and Equ. 4.16 into the above equation, we have:

$$\dot{\mathbf{U}}^{*T}\dot{\mathbf{P}} = \int_E \dot{\mathbf{U}}^{*T}\mathbf{B}^T\dot{\sigma}\,dE = \int_E \dot{\mathbf{U}}^{*T}\mathbf{B}^T\mathbf{D}^{ep}\mathbf{B}\dot{\mathbf{U}}\,dE = \dot{\mathbf{U}}^{*T}\int_E \mathbf{B}^T\mathbf{D}^{ep}\mathbf{B}\dot{\mathbf{U}}\,dE \tag{4.22}$$

Since the virtual displacement are arbitrary, we can write:

$$\dot{\mathbf{P}} = \int_E \mathbf{B}^T\mathbf{D}^{ep}\mathbf{B}\dot{\mathbf{U}}\,dE = \mathbf{K}^e\dot{\mathbf{U}} \tag{4.23}$$

where $\mathbf{K}^e = \int_E \mathbf{B}^T\mathbf{D}^{ep}\mathbf{B}\,dE = \int\int_E \mathbf{B}^T\mathbf{D}^{ep}\mathbf{B}\,J\,d\alpha\,d\beta$ is the element stiffness matrix and J is the Jacobian of the transformation as defined for Equ. 4.11.

4.5 Stress updating

The stress updating routine calculates the stress increment at Gauss points. In the stress updating procedure, the interface is first checked for its bonding or relaxed status. Then if it is in contact, the stress is updated according the yield function and elastic or plastic behaviour. The stress updating routine described in this study uses the cumulative relative displacement, instead of normal stress, as the criterion to determine whether the interface element is in contact or relaxed. The detailed descriptions of the different cases are as follows:

4.5.1 Relaxed – relaxed or bonding – relaxed

In this context, the cumulative relative displacements of the interface element at the time $t = 1$ are greater than zero:

$$\varepsilon_{3,t=1} \geq 0 \tag{4.24}$$

The cumulative relative displacements at the time $t = 0$ can be either greater or smaller than zero:

$$\varepsilon_{3,t=0} \geq 0 \text{ or } \varepsilon_{3,t=0} \leq 0 \tag{4.25}$$

The cumulative stresses are then assigned to zero and the terms of the matrix $\mathbf{D}^e$ are assigned to very small values in the next step.

4.5.2 Relaxed – bonding

The interface element falls into this case if:

$$\varepsilon_{3,t=0} \geq 0 \text{ and } \varepsilon_{3,t=1} < 0 \tag{4.26}$$

Assuming the relative displacements are changed linearly with time, we can calculate the time t_c when the two sides of the interface rebond as follows:

$$t_c = \frac{\varepsilon_{3,t=0}}{\varepsilon_{3,t=0} - \varepsilon_{3,t=1}} \tag{4.27}$$

At the time $t = t_c$, all the cumulative stresses are zero. The stress increments from the time $t = t_c$ to the time $t = 1$ is calculated using the same routine as of the case of bonding–bonding which is described next.

4.5.3 Bonding – bonding

In this case, the interface is in contact status and its behaviour can be determined using yielding criteria. In order to generalise the routine, the stress increments are calculated from the time $t = t_0$, where $t_0 = 0 \, \text{or} \, t_c$, to the time $t = 1$ which is at the end of the increment.

Following the conventional routine, the stresses are assumed to change with strain elastically during the time change. The stresses at the end of the time change are therefore calculated as follows:

$$\sigma = \sigma_0 + \mathbf{D}^e \dot{\epsilon} \Delta t \tag{4.28}$$

in which $\Delta t = t_1 - t_0$.

The two sets of stresses are checked against the yield function for the yielding status of the material at the beginning and the end of the time change. The following operations will then happen according to the following cases of initial and ending yielding status:

4.5.3.1 Elastic – elastic or plastic – elastic

The previous assumption of elastic behaviour is therefore true. The stress updating is completed.

4.5.3.2 Elastic – plastic

The stress path is divided into two stages: one of elastic behaviour, at the end of which the material reaches the yielding point, and the other of plastic behaviour. The time t_y when the material reaches the yielding point can be determined by substituting $\boldsymbol{\sigma}$ from the Equ. 4.28 to the yield function (Equ. 4.14). A quadratic equation can then be obtained, letting $s_{e1} = K_s\dot{\varepsilon}_1$, $s_{e2} = K_s\dot{\varepsilon}_2$, $s_{e3} = K_n\dot{\varepsilon}_3$:

$$\begin{aligned}&\left(s_{e1}^2 + s_{e2}^2 - s_{e3}^2\tan^2\phi\right)(t_y - t_0)^2\\ &\quad + 2\left(\tau_{10}s_{e1} + \tau_{20}s_{e2} - \left(\sigma_0 s_{e3}\tan^2\phi - s_{e3}c\tan\phi\right)\right)(t_y - t_0)\\ &\quad + \left(\tau_{10}^2 + \tau_{20}^2 - (\sigma_0\tan\phi - c)^2\right) = 0 \end{aligned} \tag{4.29}$$

from which t_y, $t_0 \leq t_y \leq t_1$, is determined as follows:

$$t_y = t_0 + \frac{-a_2 + \sqrt{d}}{2a_1} \tag{4.30}$$

where

$$\begin{aligned} a_1 &= \left(s_{e1}^2 + s_{e2}^2 - s_{e3}^2\tan^2\phi\right)\\ a_2 &= 2\left(\tau_{10}s_{e1} + \tau_{20}s_{e2} - \left(\sigma_0 s_{e3}\tan^2\phi - s_{e3}c\tan\phi\right)\right)\\ a_3 &= \left(\tau_{10}^2 + \tau_{20}^2 - (\sigma_0\tan\phi - c)^2\right)\\ d &= a_2^2 - 4a_1a_3 \end{aligned} \tag{4.31}$$

The stresses at $t = t_y$ are calculated by the following formula:

$$\boldsymbol{\sigma}_y = \boldsymbol{\sigma}_0 + \mathbf{D}^e\dot{\boldsymbol{\epsilon}}(t_y - t_0) \tag{4.32}$$

and at $t = t_1$ by:

$$\boldsymbol{\sigma} = \boldsymbol{\sigma}_y + \int_{t_y}^{t_1}\mathbf{D}^{ep}\dot{\boldsymbol{\epsilon}}\,dt \tag{4.33}$$

The integration of Equ. 4.33 is dealt with in detail in Section 4.6.

4.5.3.3 Plastic – plastic

In the case where the material both starts and ends in plastic status, there are two possibilities (a) and (b) as shown in Fig. 4.4:

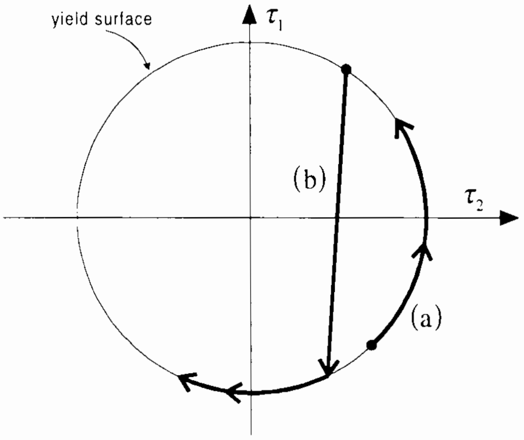

Figure 4.4: Two possible paths of plastic – plastic case of stress path.

a During the time change, the stress point moves along on the yield surface. The cumulative stresses can then be calculated by integrating the stress – strain relationship as described in Section 4.6.

b The stress point crosses the elastic region to end up at another position on the yield surface. The behaviour is divided into two stages as for the case of elastic – plastic behaviour: one of elastic behaviour and the other of plastic behaviour. The time t_y ($t_y - t_0$ must not be zero), stresses $\boldsymbol{\sigma}_y$ and $\boldsymbol{\sigma}$ are also found by equations Equ. 4.29 to Equ. 4.33.

The above-mentioned procedure may still yield bad results. The reason is that even though the stress is updated partly with elastic characteristic matrix $\mathbf{D}^e$, in both the current increment and the next increment, the stiffness matrices are calculated as for plastic behaviour. To overcome this problem, it was found that better results were obtained if the stiffness matrix was set as elastic at the end of the increment.

The two cases can be distinguished by computing the derivative of f with respect to time.

$$\left.\frac{df}{dt}\right|_{t=t_1} = 2\left(\tau_{10}s_{e1} + \tau_{20}s_{e2} - s_{e3}\left(\sigma_0 \tan^2\phi - c\tan\phi\right)\right) \tag{4.34}$$

If $\left.\frac{df}{dt}\right|_{t=t_1} > 0$, then the stresses are updated with stress path sliding on the yield surface as case (a). If $\left.\frac{df}{dt}\right|_{t=t_1} \leq 0$, the stresses are to be updated as case (b).

4.6 Integration of the stress–strain relationship

In this section, the exact solution for the integration of stress–strain relationship (Equ. 4.33) is found in a closed form. The result can be found numerically but a closed form solution is in many ways a more efficient way because numerical solutions usually require an iterative process which is much slower to achieve a certain level of accuracy. In case of a non-dilatant interface, a closed-form solution can be found as follows.

Letting $u = \sigma \tan\phi - c$, and therefore $\dot{u} = \dot{\sigma}\tan\phi$, we have:

$$f = \tau_1^2 + \tau_2^2 - u^2 = 0 \tag{4.35}$$

$$\frac{df}{dt} = \tau_1\dot{\tau}_1 + \tau_2\dot{\tau}_2 - u\dot{u} = 0 \tag{4.36}$$

The yield function can be written in the form:

$$\tau_1 = u\cos\alpha, \quad \tau_2 = u\sin\alpha \tag{4.37}$$

and hence,

$$\dot{\tau}_1 = \dot{u}\cos\alpha - \dot{\alpha}u\sin\alpha \tag{4.38}$$

$$\dot{\tau}_2 = \dot{u}\sin\alpha + \dot{\alpha}u\cos\alpha \tag{4.39}$$

The plastic potential (Equ. 4.15) leads to:

$$\left\{\frac{\partial g}{\partial \sigma}\right\} = \left\{\begin{array}{c} 2\tau_1 \\ 2\tau_2 \\ -2\left(\sigma\tan\phi - c\right)\tan\psi \end{array}\right\} = \left\{\begin{array}{c} 2\tau_1 \\ 2\tau_2 \\ -2u\tan\psi \end{array}\right\} \tag{4.40}$$

As the displacement vector is perpendicular to the plastic potential, we obtain:

$$\begin{aligned} \dot{\varepsilon}_1 &= \frac{\dot{\tau}_1}{K_s} + \lambda\tau_1 \\ \dot{\varepsilon}_2 &= \frac{\dot{\tau}_2}{K_s} + \lambda\tau_2 \\ \dot{\varepsilon}_3 &= \frac{\dot{\sigma}}{K_n} - \lambda u\tan\psi \end{aligned} \tag{4.41}$$

For the case of non-dilatant model, we have:

$$\begin{aligned} \dot{\varepsilon}_1 &= \frac{\dot{\tau}_1}{K_s} + \lambda\tau_1 \\ \dot{\varepsilon}_2 &= \frac{\dot{\tau}_2}{K_s} + \lambda\tau_2 \\ \dot{\varepsilon}_3 &= \frac{\dot{\sigma}}{K_n} \end{aligned} \tag{4.42}$$

The third equation in Equ. 4.43 can be directly integrated to give:

$$\sigma = \sigma_0 + \dot{\varepsilon}_3 K_n t \tag{4.43}$$

Combining the first two equations of Equ. 4.42 and using the yield function, we have:

$$\begin{aligned}\lambda &= \frac{s_{e1}\tau_1 + s_{e2}\tau_2 - s_{e3}u\tan\phi}{u^2 K_s} \\ &= \frac{s_{e1}\cos\alpha + s_{e2}\sin\alpha - s_{e3}\tan\phi}{uK_s}\end{aligned} \tag{4.44}$$

Substituting this back into Equ. 4.42, we obtain:

$$\begin{aligned}s_{e1} &= \dot{u}\cos\alpha - \dot{\alpha}u\sin\alpha + K_s u\cos\alpha\frac{s_{e1}\cos\alpha + s_{e2}\sin\alpha - s_{e3}\tan\phi}{uK_s} \\ &= \dot{u}\cos\alpha - \dot{\alpha}u\sin\alpha + s_{e1}\cos^2\alpha + s_{e2}\cos\alpha\sin\alpha - s_{e3}\tan\phi\cos\alpha \\ &= -\dot{\alpha}u\sin\alpha + s_{e1}\cos^2\alpha + s_{e2}\cos\alpha\sin\alpha\end{aligned} \tag{4.45}$$

or:

$$0 = \dot{\alpha}u + s_{e1}\sin\alpha - s_{e2}\cos\alpha \tag{4.46}$$

If $u_0 = \sigma_0\tan\phi - c = 0$, α can be determined by:

$$\alpha = \arctan\frac{\dot{\varepsilon}_2}{\dot{\varepsilon}_1} \tag{4.47}$$

If $s_{e1} = s_{e2} = 0$,

$$\dot{\alpha} = 0 \text{ or } \alpha = \alpha_0 \tag{4.48}$$

Otherwise, Equ. 4.46 is a separable differential equation which can be written as follows:

$$\begin{aligned}\int\frac{d\alpha}{-s_{e1}\sin\alpha + s_{e2}\cos\alpha} &= \int\frac{dt}{u} + d \\ &= \int\frac{dt}{\sigma\tan\phi - c} + d\end{aligned} \tag{4.49}$$

Letting:

$$\delta_1 = \arcsin\left(\frac{s_{e2}}{b}\right) = \arccos\left(\frac{-s_{e1}}{b}\right) \tag{4.50}$$

$$b = \sqrt{s_{e1}^2 + s_{e2}^2} \tag{4.51}$$

the above equation can be written as:

$$\frac{1}{b}\ln\left|\tan\frac{1}{2}(\alpha + \delta_1)\right| = \int\frac{dt}{\sigma\tan\phi - c} + d \tag{4.52}$$

The integral on the right hand side can be evaluated according to two distinguishing cases of $\dot{\varepsilon}_3$ as follows:

In case of $\dot{\varepsilon}_3 \neq 0$ and $\phi \neq 0$

The equation Equ. 4.52 becomes:

$$\frac{1}{b}\ln\left|\tan\frac{1}{2}(\alpha+\delta_1)\right| = \frac{\ln|\sigma\tan\phi - c|}{s_{e3}\tan\phi} + d \tag{4.53}$$

At the time $t = 0, \alpha = \alpha_0 = \arctan\dfrac{\tau_{20}/u}{\tau_{10}/u}$, where τ_{10} and τ_{20} are the shear stresses at $t = 0$. Therefore, the constant d can be determined by the following equation:

$$d = \frac{1}{b}\ln\left|\tan\frac{1}{2}(\alpha_0+\delta_1)\right| - \frac{1}{s_{e3}\tan\phi}\ln|\sigma_0\tan\phi - c| \tag{4.54}$$

In order to calculate τ_1, τ_2 at the time t, we calculate α at the time t by rewriting the equation Equ. 4.53 as:

$$\alpha = 2\arctan\left[\exp\left(\frac{b}{s_{e3}\tan\phi}\ln|\sigma\tan\phi - c| + db\right)\right] - \delta_1 \tag{4.55}$$

and finally τ_1, τ_2 can be determined using Equ. 4.37.

In case of $\dot{\varepsilon}_3 = 0$ or $\phi = 0$

The equation Equ. 4.52 becomes:

$$\frac{1}{b}\ln\left|\tan\frac{1}{2}(\alpha+\delta_1)\right| = \frac{t}{\sigma_0\tan\phi - c} + d \tag{4.56}$$

where d is determined by:

$$d = \frac{1}{b}\ln\tan\frac{1}{2}(\alpha_0+\delta_1) \tag{4.57}$$

Therefore,

$$\alpha = 2\arctan\left(\exp\left(\frac{tb}{\sigma_0\tan\phi - c}\right)\tan\frac{1}{2}(\alpha_0+\delta_1)\right) - \delta_1 \tag{4.58}$$

Substituting α into Equ. 4.37, we obtain $\boldsymbol{\sigma}$.

4.7 Comparing with Krieg & Krieg's (1977) solution for the integration of stress–strain relationship

If the normal relative displacement increment is zero and $\sigma_0 \tan\phi = 0$, the yield function Equ. 4.14 becomes:

$$f = \tau_1^2 + \tau_2^2 - c^2 = 0 \tag{4.59}$$

which is virtually the function of von Mises yield criteria in two dimensional stress space for which the solution of Krieg & Krieg (1977) or Booker (1984) is used. The purpose of this section is to prove that with such a special case of normal relative displacement increment, the solution found here (for the case of non-dilatant model) gives an identical answer to those by Krieg and Krieg's solution.

Adopting Booker's notation, we have:

$$\alpha_b = \sigma_0 \tan\phi, \tag{4.60}$$

$$\beta_b = b, \tag{4.61}$$

$$G = \frac{K_s}{2} \tag{4.62}$$

The solution by Krieg & Krieg (1977) gives:

$$\begin{aligned} \tau_1\eta &= \tau_{10} + 2G\dot{\varepsilon}_1\xi \\ \tau_2\eta &= \tau_{20} + 2G\dot{\varepsilon}_2\xi \end{aligned} \tag{4.63}$$

where:

$$\begin{gathered} \eta = \cosh\left(\frac{\beta_b}{\alpha_b}t\right) + \chi\sinh\left(\frac{\beta_b}{\alpha_b}t\right) \\ \xi = \frac{\alpha_b}{\beta_b}\sinh\left(\frac{\beta_b}{\alpha_b}t\right) + \frac{\alpha_b}{\beta_b}\chi\cosh\left(\frac{\beta_b}{\alpha_b}t\right) - \frac{\alpha_b}{\beta_b}\chi \\ 2\alpha_b\beta_b\chi = 2G(\tau_{10}2\varepsilon_1 + \tau_{20}2\varepsilon_2) \end{gathered} \tag{4.64}$$

Because it is very difficult to prove the identity of the two solutions symbolically, they will be compared numerically.

The initial stresses are chosen at all quadrant points on the yield locus. Purely horizontal displacements, purely vertical displacements and combined displacements are then applied. The magnitude of purely horizontal displacements and purely vertical displacements is $\varepsilon =$

Table 4.1: Comparison of updated stresses (vertical relative displacement only).

Quadrant points	*Displace-ment*	*Booker's solution*		*This solution*	
		τ_1	τ_2	τ_1	τ_2
0	Negative	0·995020748953227	-0·099667994624956	0·995020748953226	-0·099667994624956
0	Positive	0·995020748953227	0·099667994624956	0·995020748953226	0·099667994624956
$\pi/4$	Positive	0·657264595340141	0·753659904540742	0·657264595340141	0·753659904540742
$\pi/2$	Positive	0·000000000000000	1·000000000000000	0·000000000000000	1·000000000000000
$3\pi/4$	Positive	-0·657264595340141	0·753659904540742	-0·657264595340141	0·753659904540742
π	Positive	-0·995020748953227	0·099667994624956	-0·995020748953226	0·099667994624956
π	Negative	-0·995020748953227	-0·099667994624956	-0·995020748953226	-0·099667994624956
$5\pi/4$	Negative	-0·657264595340141	-0·753659904540742	-0·657264595340141	-0·753659904540742
$3\pi/2$	Negative	0·000000000000000	-1·000000000000000	0·000000000000000	-1·000000000000000
$7\pi/4$	Negative	0·657264595340141	-0·753659904540742	0·657264595340141	-0·753659904540742

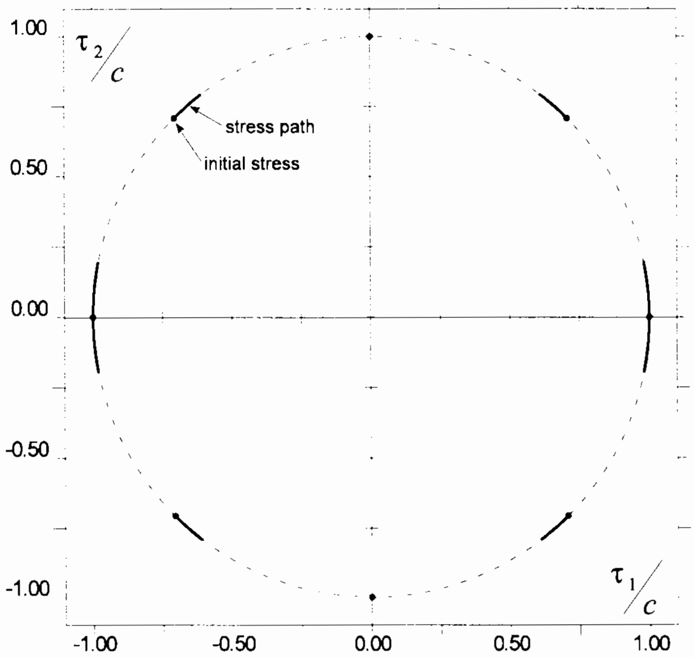

Figure 4.5: Initial stresses and stress paths (vertical relative displacement only).

$\frac{c/K_s}{5}$ (a fifth of the radius of the yield surface). The numerical results are listed in Tables 4.1, 4.2, 4.3. The corresponding stress paths are also shown in Fig. 4.5, Fig. 4.6, Fig. 4.7. As it can be seen from the tables, the results for all cases obtained from the two methods are identical up to the order of 1×10^{-14}. It is concluded that the two methods give the same output for the cases examined.

Table 4.2: Comparison of updated stresses (horizontal relative displacement only).

Quadrant points	*Displacement*	*Booker's solution*		*This solution*	
		τ_1	τ_2	τ_1	τ_2
0	Positive	1·000000000000000	0·000000000000000	1·000000000000000	0·000000000000000
$\pi/4$	Positive	0·753659904540742	0·657264595340141	0·753659904540742	0·657264595340141
$\pi/2$	Positive	0·099667994624956	0·995020748953227	0·099667994624956	0·995020748953227
$\pi/2$	Negative	-0·099667994624956	0·995020748953227	-0·099667994624956	0·995020748953226
$3\pi/4$	Negative	-0·753659904540742	0·657264595340141	-0·753659904540742	0·657264595340141
π	Negative	-1·000000000000000	0·000000000000000	-1·000000000000000	0·000000000000000
$5\pi/4$	Negative	-0·753659904540742	-0·657264595340141	-0·753659904540742	-0·657264595340141
$3\pi/2$	Negative	-0·099667994624956	-0·995020748953227	-0·099667994624956	-0·995020748953226
$3\pi/2$	Positive	0·099667994624956	-0·995020748953227	0·099667994624955	-0·995020748953227
$7\pi/4$	Positive	0·753659904540742	-0·657264595340141	0·753659904540742	-0·657264595340141

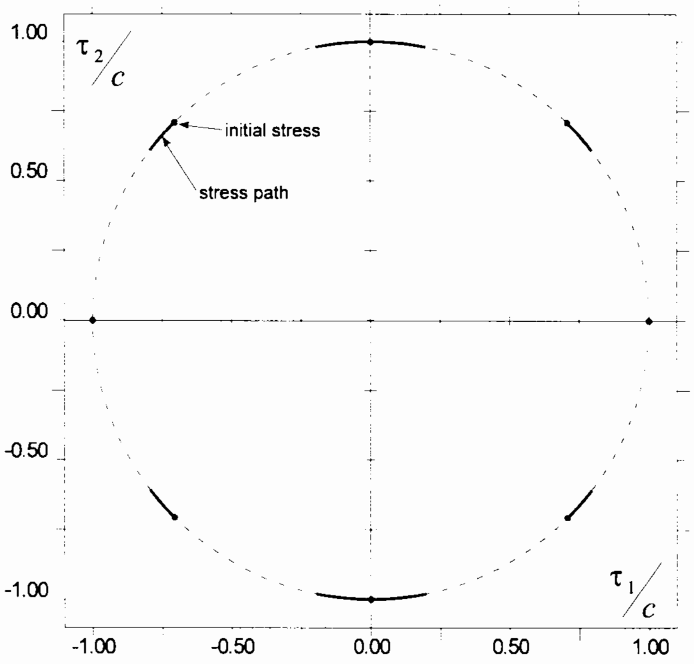

Figure 4.6: Initial stresses and stress paths (horizontal relative displacement only).

Table 4.3: Comparison of updated stresses (combined relative displacements).

Quadrant points	*Displacement direction*	*Booker's solution*		*This solution*	
		τ_1	τ_2	τ_1	τ_2
0	$7\pi/4$	0·995489406640707	-0·094872763563271	0·995489406640707	-0·094872763563271
0	$\pi/4$	0·995489406640707	0·094872763563271	0·995489406640707	0·094872763563271
$\pi/4$	$\pi/4$	0·707106781186548	0·707106781186547	0·707106781186547	0·707106781186548
$\pi/2$	$\pi/4$	0·094872763563271	0·995489406640707	0·094872763563271	0·995489406640707
$\pi/2$	$3\pi/4$	-0·094872763563271	0·995489406640707	-0·094872763563271	0·995489406640707
$3\pi/4$	$3\pi/4$	-0·707106781186547	0·707106781186548	-0·707106781186547	0·707106781186548
π	$3\pi/4$	-0·995489406640707	0·094872763563271	-0·995489406640707	0·094872763563271
π	$5\pi/4$	-0·995489406640707	-0·094872763563271	-0·995489406640707	-0·094872763563271
$5\pi/4$	$5\pi/4$	-0·707106781186548	-0·707106781186547	-0·707106781186548	-0·707106781186547
$3\pi/2$	$5\pi/4$	-0·094872763563271	-0·995489406640707	-0·094872763563271	-0·995489406640707
$3\pi/2$	$7\pi/4$	0·094872763563271	-0·995489406640707	0·094872763563271	-0·995489406640707
$7\pi/4$	$7\pi/4$	0·707106781186547	-0·707106781186548	0·707106781186547	-0·707106781186548

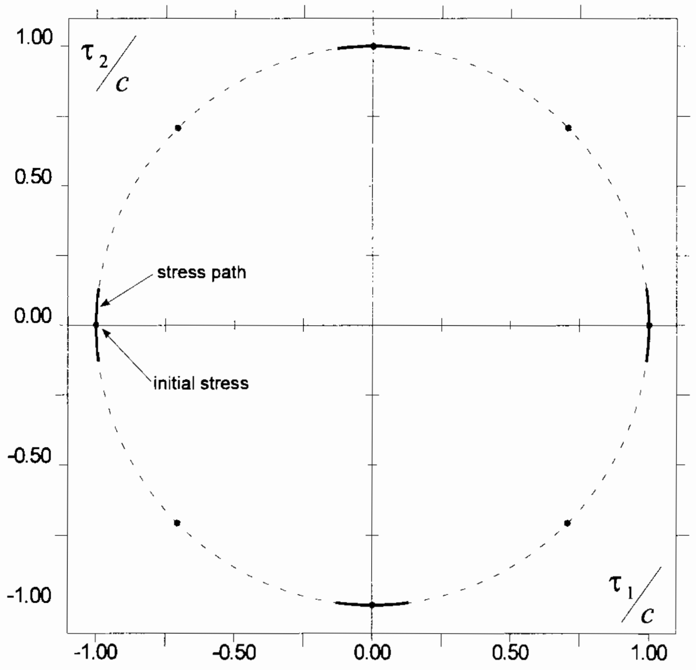

Figure 4.7: Initial stresses and stress paths (combined relative displacements).

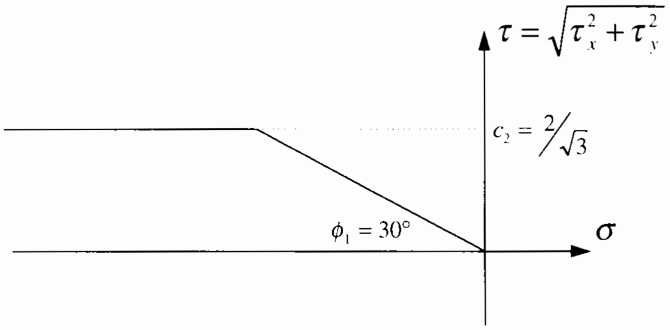

Figure 4.8: Characteristics of the interface.

4.8 Numerical validation of the interface

Two different tests are carried out to validate the interface. In all of these tests, the interface is governed by the constitutive equation composed of two parts: at a low level of compressive stress, the interface is governed by cohesionless frictional behaviour; at a high level of compressive stress, the interface is governed by frictionless cohesive behaviour, as shown in Fig. 4.8. The numerical values the interface properties are:

$$K_s = K_n = 1000$$

$$c_1 = 0; \phi_1 = 30°; \psi_1 = 0°$$

$$c_2 = \frac{2}{\sqrt{3}}; \phi_2 = 0°; \psi_2 = 0°$$

All of the tests are controlled by nodal displacements, and the load paths are to be obtained to verify the behaviour of the interface.

4.8.1 Test One

The first test is comprised of two interface elements forming a square as depicted in Fig. 4.9. There are three analyses carried out on this sample. The total area of the sample is unity. There are two analyses designed to test the behaviour of the interface in two cohesive sliding and frictional sliding modes of behaviour; both involve sliding in only one direction x. The third analysis includes also sliding in the y direction.

In the first analysis, a vertical displacement is applied (steps 0-5), followed by a horizontal displacements in the positive direction (steps 5-15) and then the negative direction (steps 15-35) of the x axis. The sample is then uncompressed to zero stress. Fig. 4.10 shows

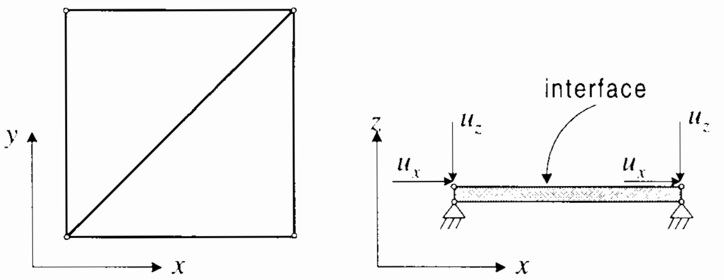

Figure 4.9: Validating the interface: Test One.

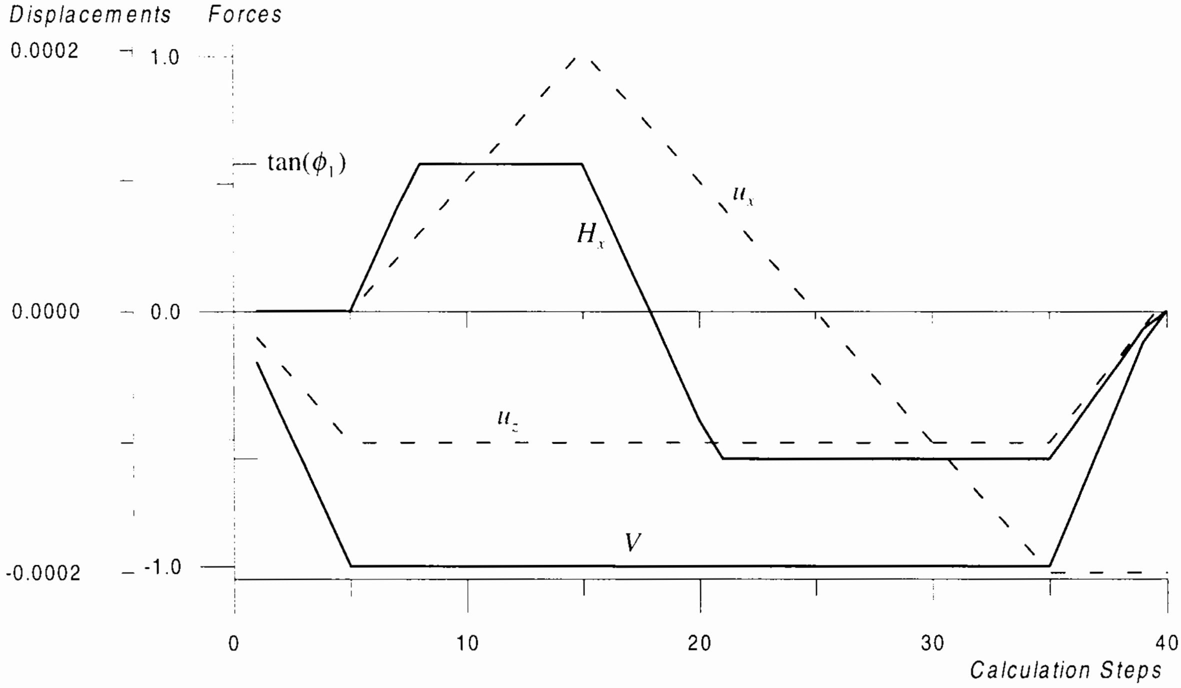

Figure 4.10: Result of Test One – Analysis One.

the variation of vertical and horizontal displacement u_z and u_x during the analysis. As seen from Fig. 4.10 in the first regime of load (steps 0-5) the vertical load increases. The shear stress then increases with the horizontal displacement in the second load regime, and levels off when the interface starts to slide plastically. When the displacement changes its direction in the third regime, the shear stress is unloaded and changes to the opposite (negative) sign. It also reaches the yielding state when the interface starts to slide the other way. When the interface is uncompressed, both stresses of the interface change to zero.

The vertical displacement in this analysis is chosen to be small enough so that in the second load regime (with horizontal displacement) the interface can yield (slide) due to the frictional yield surface. As seen from Fig. 4.10, the maximum shear stress is 0·57735, which is $\tan(\phi_1) = \tan(30^\circ)$ as expected.

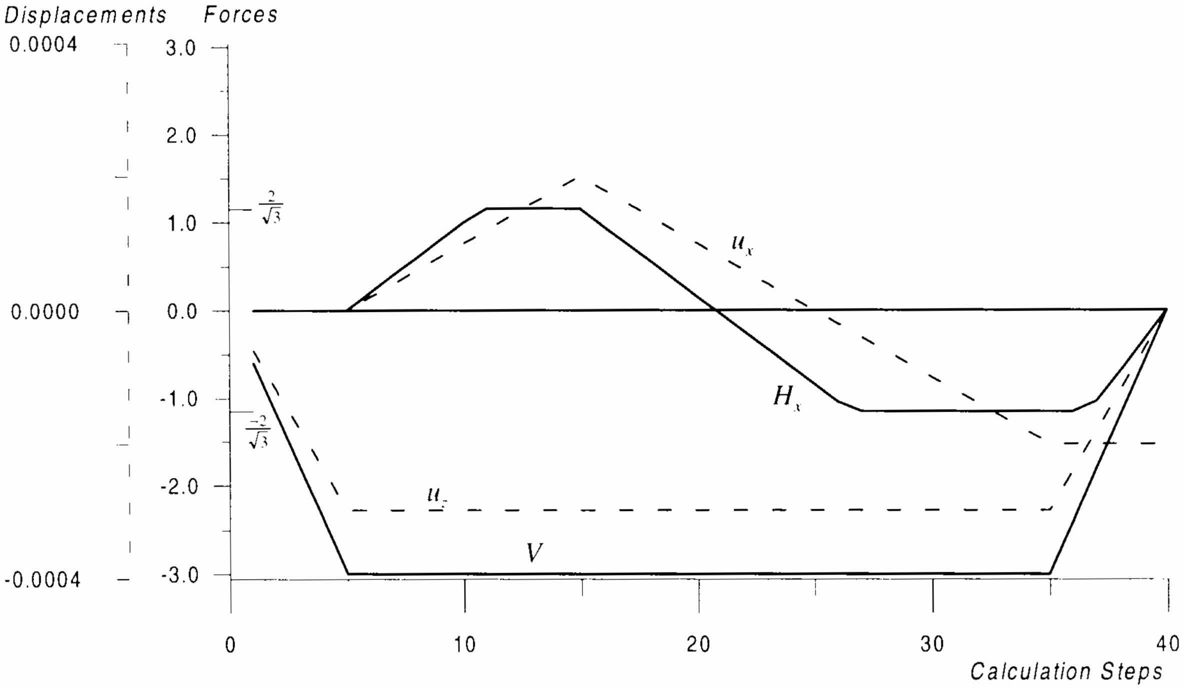

Figure 4.11: Result of Test One – Analysis Two.

In contrast to the first analysis, the vertical displacement in the second analysis is large enough so that the cohesive yield surface is hit when the horizontal displacement is applied. The resultant load path are similar to that of the first analysis, with the only difference being the maximum shear stress is now 1·1547, which is the cohesion of the interface.

The problem is then tried with a third combination of displacements which includes also horizontal displacement in the y direction. This analysis is aimed at testing the closed form solution of the stress-strain integration as found in this research.

The interface is first loaded vertically. It is then slid in the positive direction in the x axis. The shear stress τ_x can be seen, from Fig. 4.12, to increase and then level off at 0·57735. After that positive displacement in the y direction is applied. The stress τ_x is decreased to 0·0 and τ_y is increased to 0·57735 as u_y gets higher. Both components of the horizontal displacement are then reversed to negative directions which results in an equivalent horizontal displacement directed at $-135°$ from the x axis. The figure shows both stresses τ_x and τ_y change elastically. After that, the stress path hits the yield surface, and the stresses become steady at $\tau_x = \tau_y = -0{\cdot}57735/\sqrt{2}$. The displacement path is plotted with the resultant forces in Fig. 4.12.

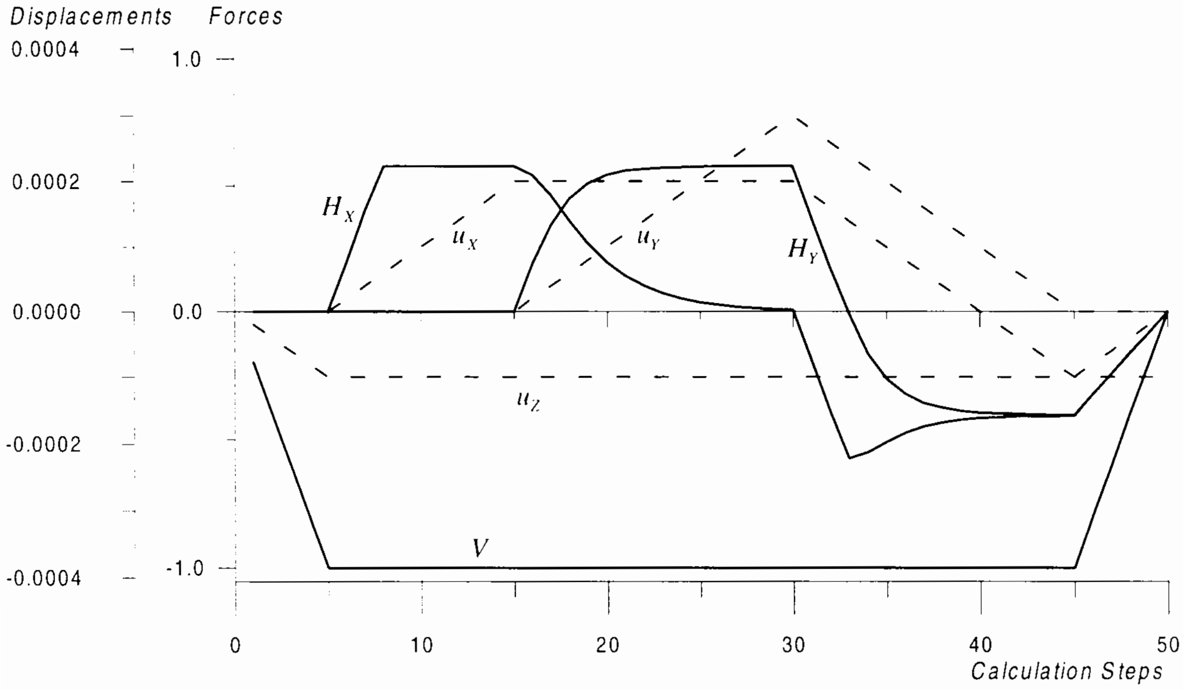

Figure 4.12: Result of Test One – Analysis Three.

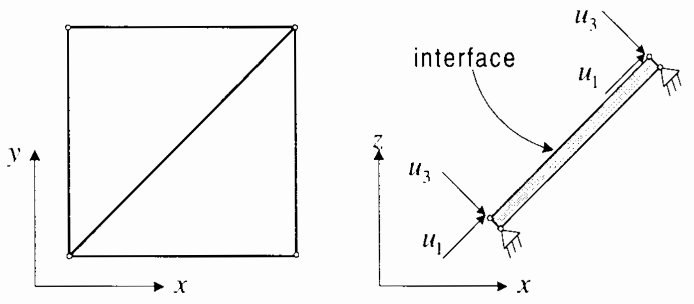

Figure 4.13: Validating the interface: Test Two.

4.8.2 Test Two

The second test is identical to Test One except it is rotated at an angle of 45° about the y axis in order to test the kinematic equations established in Section 4.2.

The application of displacements is similar to the first analysis of the first test, which includes a compression (vertical to the surface of the interface) in steps 1-5, then a pure slide (steps 5-15), and a reverse slide (steps 15-35), then uncompression (steps 35-40).

The problem is depicted in Fig. 4.13, and the result is plotted in Fig. 4.14. Fig. 4.15 shows forces and displacements of this test transformed into the local coordinate system of the interface, which is identical to the result of the first analysis of Test One as it should be.

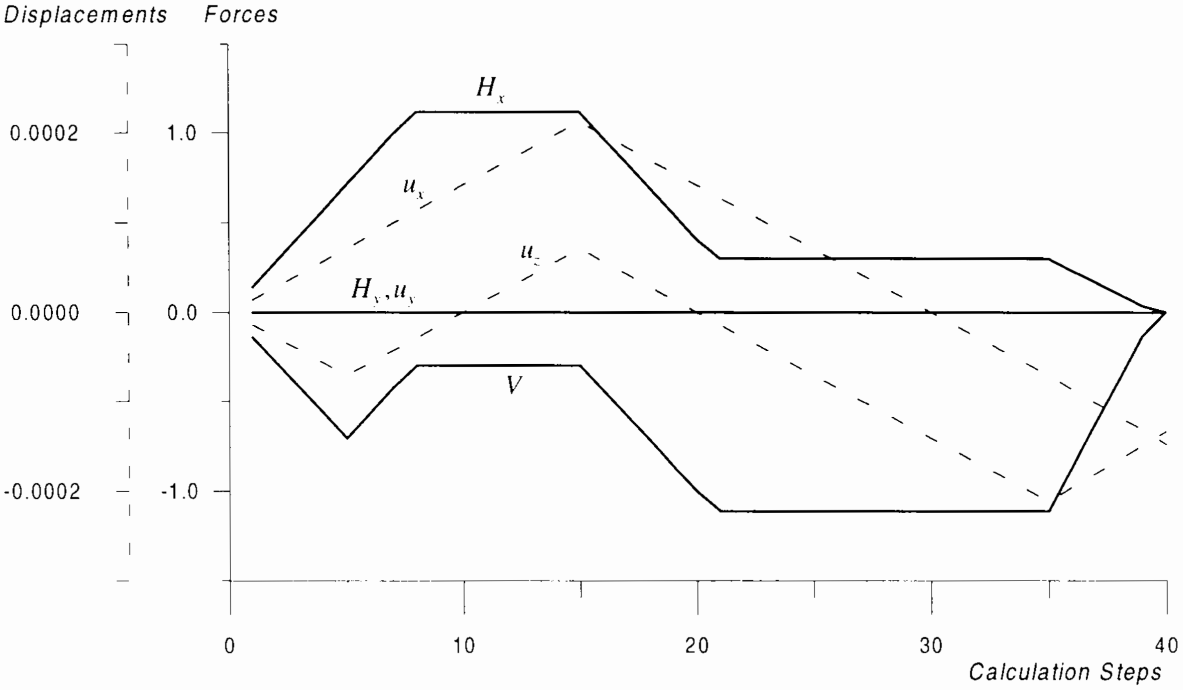

Figure 4.14: Result of Test Two.

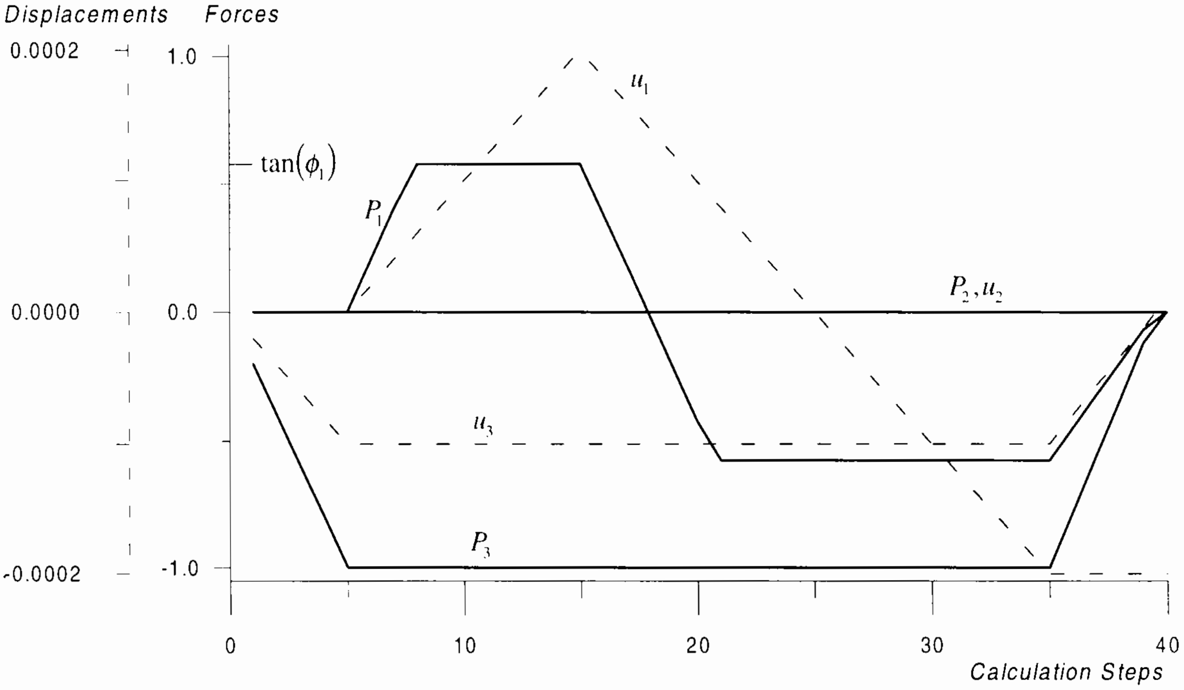

Figure 4.15: Result of Test Two (with forces and displacements transformed into the local coordinate system of the interface).

Chapter 5

Bearing Capacity Envelope of Strip Footings

5.1 Introduction

The aim of this chapter is to contribute to the understanding of the bearing capacity envelope for the case of strip footings on an undrained clay, and to assist in the interpretation of the more complex problem of a circular footing studied in Chapter 6. Also of interest is the capability of the interface element developed in Chapter 3 to model the loss of contact between the footing and the soil. Offshore foundations are in some cases designed with the simplifying assumption of plane strain conditions; thus the current study may also have direct application.

This chapter starts with a review of commonly-used solutions applicable to the problem of bearing capacity of footings under combined loading. This includes several well-known semi-empirical bearing capacity formulae (such as Meyerhof, 1953; Hansen, 1970; Vesic, 1975) and some recent experimental research. Several techniques which can be used to determine the bearing capacity envelope are also reviewed. These procedures are then used in a number of finite element analyses to compare the efficiency and accuracy of each technique in determining the envelope. After that a series of analyses is conducted to construct the envelope, and the results are then compared with the methods previewed. In addition, the results of this chapter form a part of a joint research programme in which the bearing capacity envelope for strip footings is constructed using different methods: the finite element method as used by this research, and the finite element method which is implemented in a computer package called FLAC. The close similarity of the bearing capacity envelopes derived from the two numerical methods, the finite element method of this study and the finite difference method using FLAC, is an important outcome of this work.

5.2 Literature review

5.2.1 Bearing capacity

5.2.1.1 Vertical bearing capacity

From the theory of plasticity, the exact solution for a strip footing on the surface of a weightless Tresca material clay can be derived (see, for example, Atkinson, 1993):

$$V_0 = (\pi + 2) s_u B \tag{5.1}$$

where B is the width of the footing; s_u is the soil undrained shear strength. For a von Mises material, the value is increased by a factor of $\frac{2}{\sqrt{3}}$ since the undrained strength in plain strain is $2s_u/\sqrt{3}$ if s_u is used for the triaxial undrained shear strength.

5.2.1.2 Bearing capacity interaction between vertical load and moment

Under combined loads V and M, bearing capacity is usually studied as the statically equivalent problem of an eccentric vertical load (Fig. 5.1). Meyerhof (1953) develops the concept of effective area as illustrated in Fig. 5.2. The eccentric vertical load is assumed to act on a reduced area on which the load acts centrally. For a strip footing (Fig. 5.2a) the effective width is $B' = B - 2e$. This leads to a (V, M) bearing capacity interaction diagram defined as follows:

$$\frac{M}{M_0} = 4\frac{V}{V_0}\left(1 - \frac{V}{V_0}\right) \tag{5.2}$$

where V_0 is the bearing capacity under central vertical loading. This means that moment capacity reaches its peak value at $V = V_0/2$, which corresponds to the eccentricity of $e = B/4$ and the peak value of moment of $M_0 = BV_0/8$. In Fig. 5.3, $(V/V_0, M/BV_0)$ interaction of Meyerhof method for strip footings is plotted given that V_0 is determined by Equ. 5.1. The

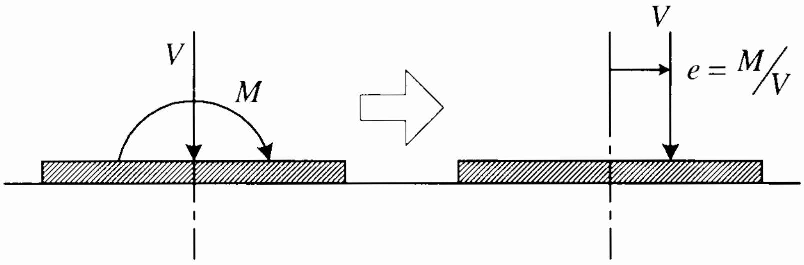

Figure 5.1: Equivalent eccentric load.

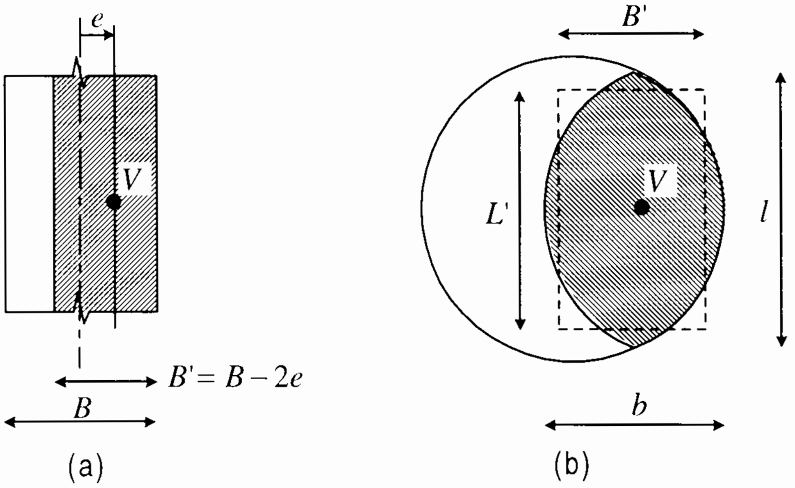

Figure 5.2: Effective area concept: (a) strip footing (Meyerhof, 1953); (b) circular footing (Hansen, 1970).

effective area assumption is also used by other authors for circular footings. This is reviewed in more detail in the next chapter which deals with the bearing capacity envelope of circular footings.

5.2.1.3 Bearing capacity interaction between vertical and horizontal load

An exact solution for the case of a rough strip footing subjected to combined vertical and horizontal loading on homogeneous clay is found by Bolton (1979). The maximum horizontal load is determined by:

$$H_0 = As_u = \left(\frac{1}{\pi+2}\right) V_0 \tag{5.3}$$

and sliding failure occurs at this load (constantly) if $V/V_0 \leq 0{\cdot}5$. For larger vertical loads the (V, H) failure envelope is:

$$\frac{V}{V_0} = \frac{\pi + 1 + \sqrt{1-(H/H_0)^2} - \sin^{-1}(H/H_0)}{\pi+2} \tag{5.4}$$

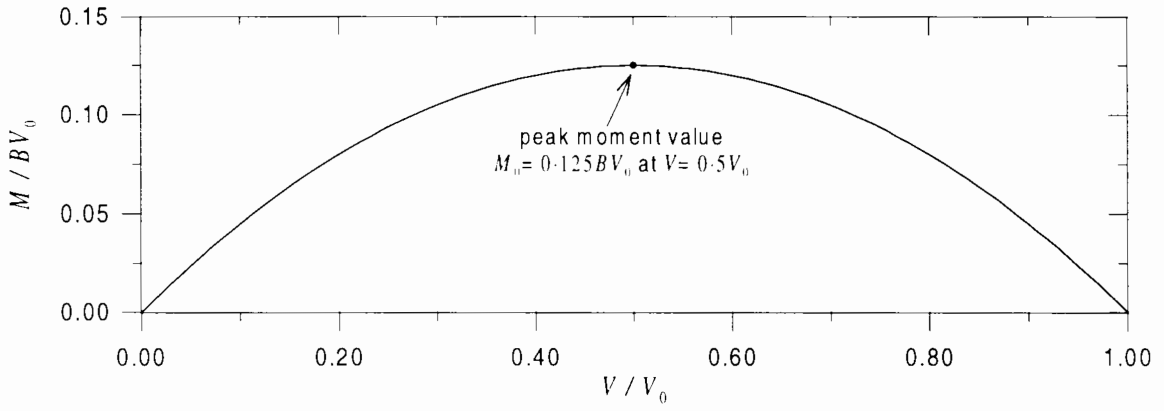

Figure 5.3: (V, M) interaction chart of a strip footing.

In early geotechnical papers combined vertical and horizontal loading is usually referred to as inclined loading. Having found that the vertical bearing capacity was significantly reduced as the angle of inclination $\alpha = \tan^{-1}(H/V)$ increased, Meyerhof (1956) introduced 'inclination factors'. For either a strip or circular footing on clay, the (V, H) failure envelope is defined as:

$$\frac{V}{V_0} = \left(1 - \frac{\alpha^\circ}{90^\circ}\right)^2 \tag{5.5}$$

The maximum horizontal load is again $H_0 = As_u$ for rough footings on clay. Thus Equ. 5.5 only holds for angles of load inclination

$$\alpha \leq \alpha_s = \tan^{-1}(H_0/V) \tag{5.6}$$

For greater inclinations it is assumed that the footing fails by sliding. It can be shown that for rough strip footings, $\alpha_s = 15{\cdot}986^\circ$, at which the vertical load is $V = 0{\cdot}6763V_0$.

The Meyerhof (1956) concept of an empirical inclination factors was retained by both Hansen (1970) and Vesic (1975). For a central inclined load on strip footings, Hansen's (1970) formula reduces to:

$$\frac{V}{V_0} = 1 - 0{\cdot}5(1 - \sqrt{1 - H/H_0}), \quad H \leq H_0 = As_u \tag{5.7}$$

Note that the transition point from bearing failure to sliding failure of the (V, H) failure envelope is at $V = V_0/2$. Vesic's (1975) formula for strip footings takes the form:

$$\frac{V}{V_0} = 1 - \frac{2H}{(\pi + 2)H_0}; \quad H \leq H_0 = As_u \tag{5.8}$$

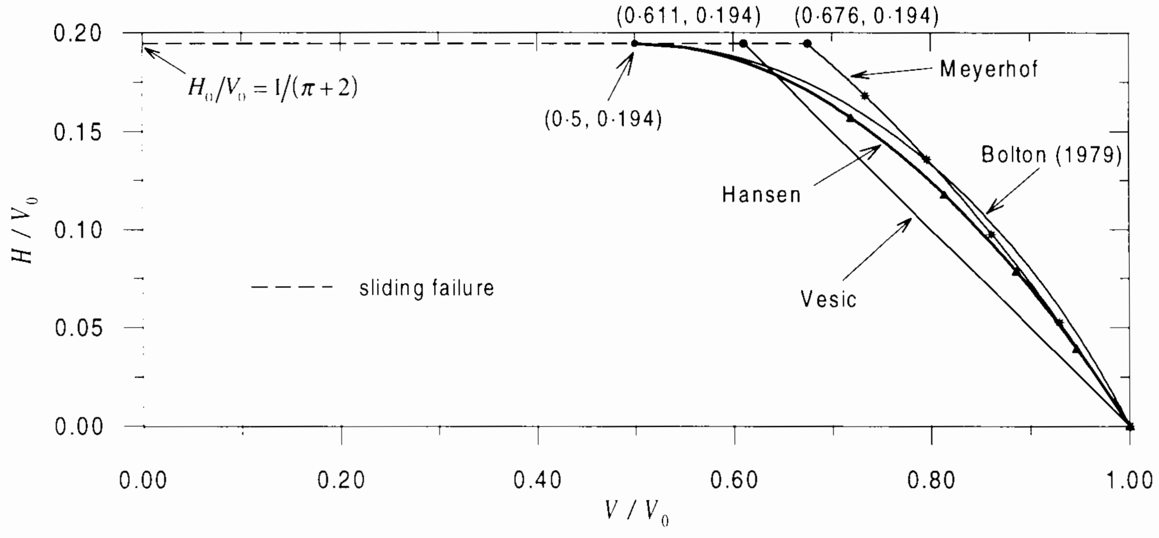

Figure 5.4: Combined vertical and horizontal loading (inclined loads) of strip footings.

The four formulae for the (V, H) failure envelope are plotted in Fig. 5.4. It shows that whereas the three methods by Meyerhof (1956), Hansen (1970) and Bolton (1979) give very similar prediction of the normalised V/V_0, H/V_0 failure envelope, Vesic's (1975) method gives a different and rather more conservative envelope than the other three. The four methods also differ in their predictions of the vertical load level at which the transition from bearing failure to sliding failure occures. Meyerhof's (1956) method predicts a transition at the highest vertical load. Both Hansen (1970) and Bolton (1979) predict the transition at lowest vertical load, $V = V_0/2$. In addition, they give a smooth transition, whereas the other two methods (Vesic, 1975; Meyerhof, 1956) give pointed $(V/V_0$, $H/V_0)$ interaction curves.

5.2.1.4 Bearing capacity interaction between vertical, horizontal loads and moment

This case has usually been approached in the manner first suggested by Meyerhof (1956): an inclined load of magnitude $\sqrt{V^2+H^2}$ is assumed to act centrally on a reduced foundation area determined by the eccentricity $e = M/V$ as depicted in Fig. 5.2. For a surface strip footing on clay, the methods by Meyerhof (1956), Hansen (1970), Vesic (1975), Bolton (1979) can be used to define the following (V, H, M) failure envelopes:

Meyerhof (1956):

$$\frac{V}{V_0} = \left(1 - \frac{\alpha^\circ}{90^\circ}\right)\frac{A'}{A}, \; H \leq A's_u \tag{5.9}$$

Hansen (1970):

$$\frac{V}{V_0} = \left(1 - 0{\cdot}5\left(1 - \sqrt{1 - H/A's_u}\right)\right)\frac{A'}{A}, \; H \le A's_u \tag{5.10}$$

Vesic (1975):

$$\frac{V}{V_0} = \left(1 - \frac{2H}{(\pi+2)A's_u}\right)\frac{A'}{A}, \; H \le A's_u \tag{5.11}$$

Bolton (1979):

$$\frac{V}{V_0} = \frac{\pi + 1 + \sqrt{1 - (H/A's_u)^2} - \sin^{-1}(H/A's_u)}{\pi+2}\frac{A'}{A}, \; H \le A's_u \tag{5.12}$$

Because of the approach used, the above equations are in effect comprised of two components: the inclination factor (due to horizontal load) and the reduction of footing area (due to moment). The above equations are used to plot contours of the envelope in $(H/V_0, M/BV_0)$ space in Figs. 5.5 and 5.6. Bearing failure is plotted in solid lines, and sliding failure in dashed lines. In a similar way to the $(V/V_0, H/V_0)$ plot, in the $(H/V_0, M/BV_0)$ space the contours using Meyerhof's (1956) and Vesic's (1975) equations give pointed transitions from sliding to bearing failure, whereas the Hansen's (1970) and Bolton's (1979) equations give a smooth transition. At higher vertical load levels, for the Meyerhof and Vesic methods the relationship between H/V_0 and M/BV_0 is almost linear. At lower vertical load levels, where the sliding failure mode begins to appear, the contour has two segments, which are also almost straight, connected at the transition points. With the same peak moment (when $H = 0$) and very close peak horizontal load (when $M = 0$, see Fig. 5.4) at each V/V_0 level, the contours of the other two methods (Hansen, 1970; Bolton, 1979) are almost identical. In addition to a smooth transition from sliding to bearing failure, both show a non-linear relation between horizontal and moment loads.

Note that when there is no vertical load $V/V_0 = 0$, it is usually accepted from experiments that the horizontal load and moment should also be zero and the contour reduces to a point at the origin shown on the contour plot. However, the theoretical solutions given in Section 5.2.1.3 however give a horizontal failure load of $H = H_0$; all the above solutions do not give any special treatment for the vertical load at low values.

5.2.1.5 Interaction charts

Equs. 5.9, 5.10, 5.11 and 5.12 are complicated by the fact that they are based on limit-equilibrium solutions, which are then combined using empirical and semi-empirical factors.

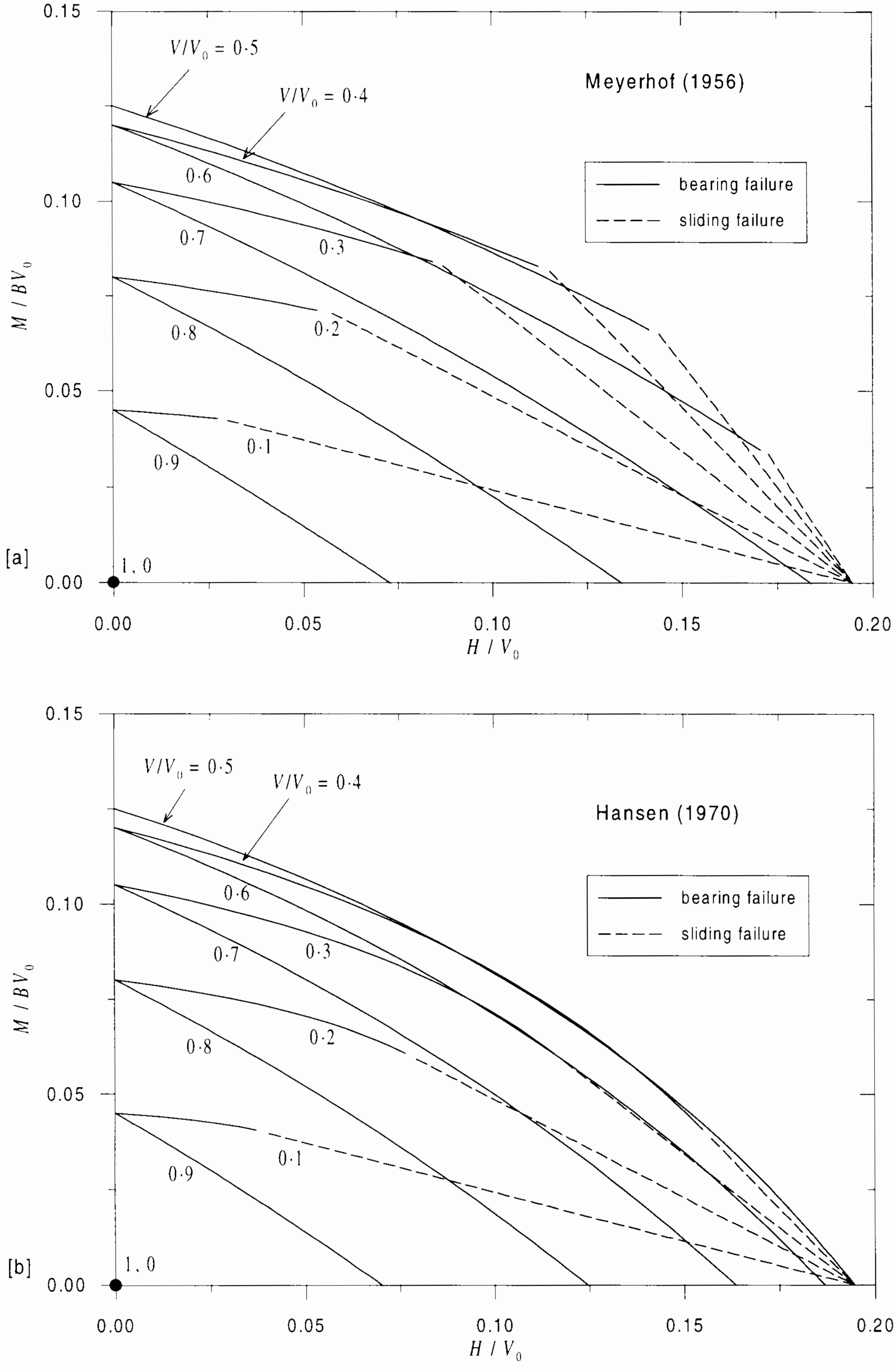

Figure 5.5: Failure envelope contours in $(H/V_0, M/BV_0)$ space: (a) Meyerhof's method; (b) Hansen's method.

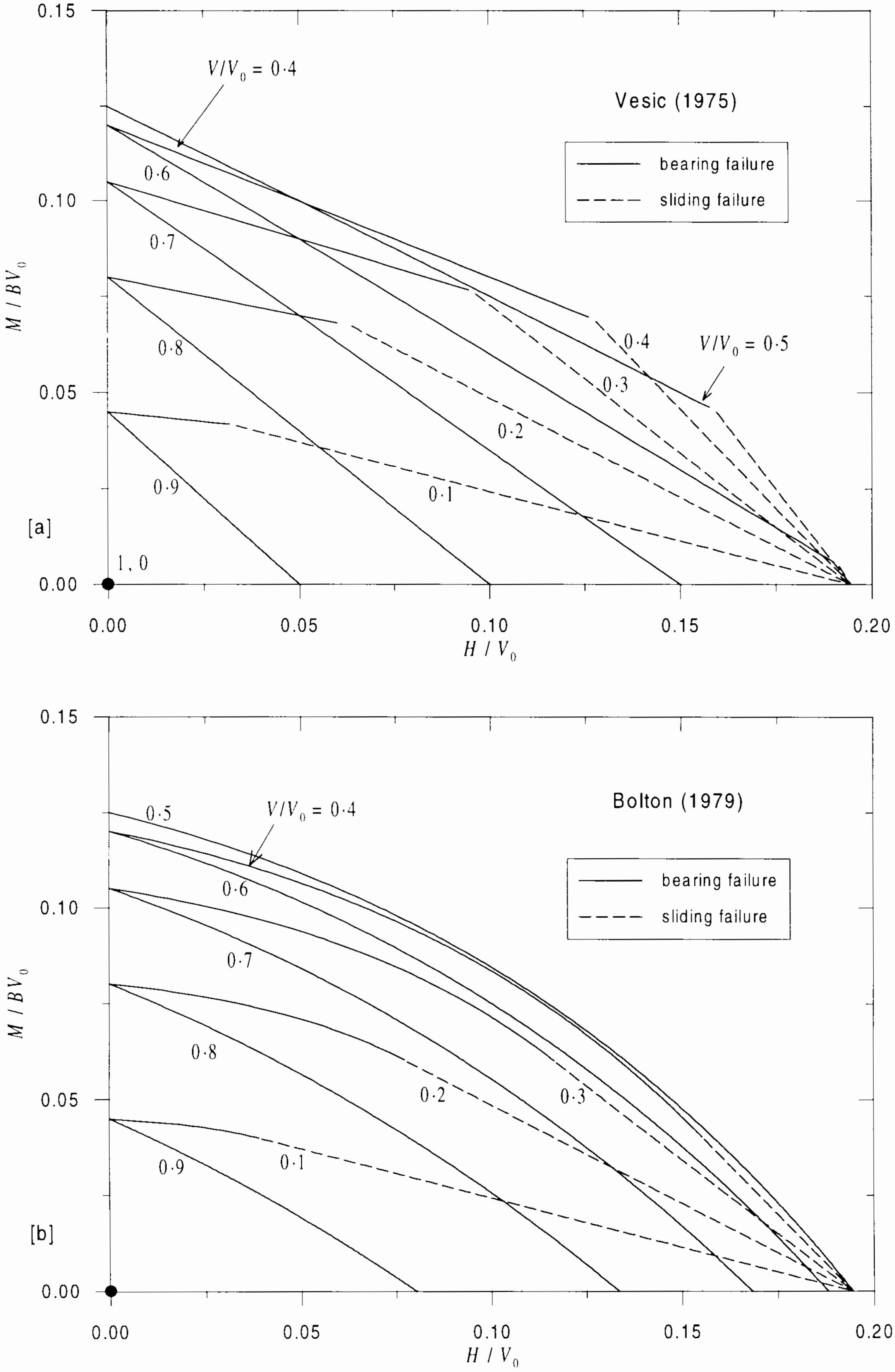

Figure 5.6: Failure envelope contours in $(H/V_0, M/BV_0)$ space: (a) Vesic's method; (b) Bolton's method.

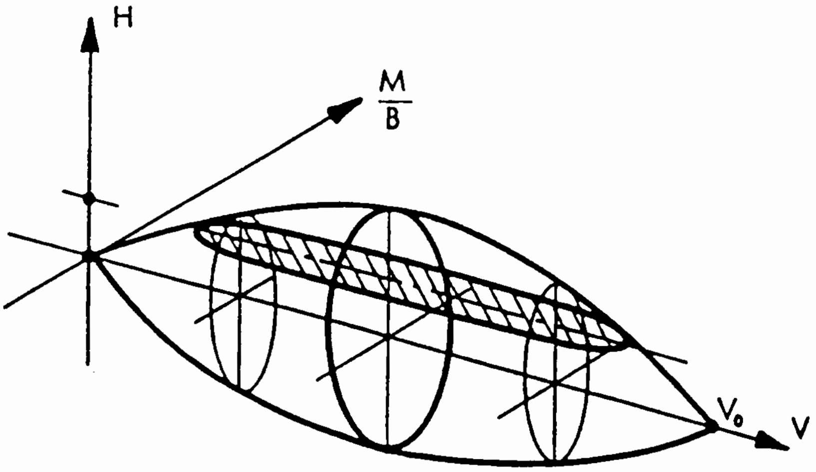

Figure 5.7: Cigar-shaped (V, H, M) failure envelope (after Butterfield & Ticof, 1979).

Figure 5.8: Two cases of eccentricity.

This complication can be avoided by using a different approach using 'interaction diagrams', by which the interaction between (V, H, M) is defined by purely empirical analytical expressions. Butterfield & Ticof (1979), on the basis of several hundred load-controlled tests, suggested the use of an elliptical (H, M) locus at constant V. Furthermore, by combining this shape with parabolic (V, M) and (V, H) loci, they proposed a simple three dimensional failure surface as shown in Fig. 5.7. For a surface strip footing on sand, Butterfield & Ticof (1979) recommended that the size of their (V, H, M) failure surface should be fixed using dimensionless peak loads $M_0/BV_0 = 0{\cdot}1$ and $H_0/V_0 = 0{\cdot}12$. Both peak moment and peak horizontal load occur at $V/V_0 = 0{\cdot}5$.

This approach has been used by various researchers to investigate the bearing capacity of footings under combined loading. Dean et al. (1992) derive a failure envelope for spudcans on sand with a similar shape. Houlsby & Martin (1992) suggest a similar enevelope for spudcans on clay.

The contours in Fig. 5.5 and Fig. 5.6 are plotted in the first quadrant in the (H, M) space, which corresponds to positive eccentricity as shown in Fig. 5.8a. Even though the four methods reviewed above do not distinguish negative eccentricity from positive one, it is of interest to find out how the footing behaves when the eccentricity is negative as illustrated in Fig. 5.8b. Meyerhof (1953) drew attention to the fundamental difference between the two cases but did not demonstrate how negative eccentricity should be treated. The first detailed investigation was undertaken by Zaharescu (1961). Using a flat footing on sand, he found that with H and V fixed, the footing can bear a negative moment larger in magnitude than that of a positive one. For strip footings, Gottardi & Butterfield (1993) conducted a series of tests on sand and their results, shown in Fig. 5.9, confirm Zaharescu's (1961) finding. As can be seen from the figure, the locus is not symmetrical with respect to the H and M axes; Gottardi & Butterfield (1993) suggest an ellipse rotated about the origin by an angle $\rho = 12{\cdot}7^\circ$ to describe the data. The maximum values of both moment and horizontal load lie in the quadrants corresponding to negative (backward) eccentricity. Note that the sign convention of M used by Gottardi & Butterfield (1993) in Fig. 5.9 is opposite to that adopted in this thesis (see Fig. 5.13).

Despite this finding, there are no further tests at other V/V_0 levels to modify the cigar-shaped failure enevelope suggested by Butterfield & Ticof (1979) (see Fig. 5.7). However, if the inclination angle ρ is assumed to be constant for all V/V_0 levels, the failure envelope can be then defined by the following expression (Butterfield, 1993):

$$\left(\frac{m}{t_M}\right)^2 + \left(\frac{h}{t_H}\right)^2 - 2C\frac{m}{t_M}\frac{h}{t_H} - (v(1-v))^2 = 0 \qquad (5.13)$$

where $v = V/V_0$, $h = H/V_0$, $m = M/BV_0$ and t_M, t_H, C are constants determining the shape of the envelope.

The same effect of the sense of eccentricity is also observed by Martin (1994) for circular footings on clay. A detailed review of Martin's (1994) failure envelope is made in Section 7.3.6.

5.2.1.6 Uniqueness and convexity of the bearing capacity envelope

Even though from the physical point of view, it may be expected that there must be one and only one failure envelope for any footing, it is of interest whether such uniqueness can be proven theoretically for the problem which involves a von Mises soil subjected to complicated load paths. The inclusion of interface elements in the system also causes some concern about the uniqueness.

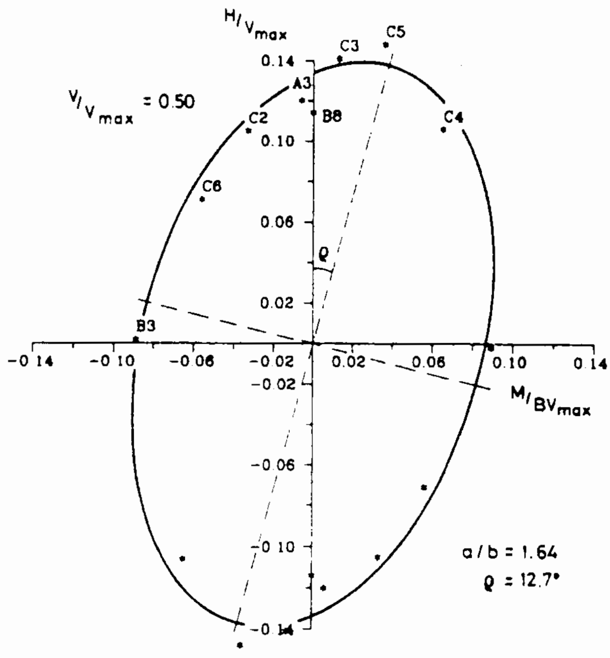

Figure 5.9: $(H/V_0,\ M/BV_0)$ failure locus at $V/V_0 = 0{\cdot}5$ for surface strip footing on dense sand (after Gottardi & Butterfield, 1993).

Similarly, though it appears from experimental research that only convex envelopes are suggested, it is necessary to prove that the envelope which is to be found theoretically using the finite element method is also convex.

The problem of solution uniqueness and convexity is dealt with by Palmer et al. (1967), in which the load–deflection relations for structural elements are related to the stress–strain relations for materials of which the structure is made. It is proven that if a (perfectly plastic) material 'in the small' possesses the following characteristics:

- The yield surfaces are convex;
- The material obeys the associated flows; and
- There is no work-softening.

It will result in a structural system 'in the large' (which is comprised of the material) having the following features:

- There is a unique failure surface;
- The failure surface is also convex;

- Associated flow also happens; and
- Lower and upper bound theorems for the structure are valid.

Turning to this research, the materials used, unfortunately, include both those which obey and those which do not obey the criteria ‘in the small’. The soil used in this thesis is a von Mises material and thus obeys the criteria, whereas the interface does not always obey the criteria. The interface has two states of behaviour: sliding and contact-breaking. In terms of sliding, the interface, as formulated in Chapter 3 and Chapter 4, can slide in frictional mode or cohesive mode, of which only the cohesive mode meets the material criteria. The contact-breaking behaviour violates the criteria.

Therefore, in the absence of contact-breaking and frictional sliding at the interface between the footing and the soil, the failure envelope must be unique and convex. For footings under combined loading, this happens when the vertical load is high, which in effect prevents contact-breaking from taking place. High vertical load also forces the interface to slide – if sliding happens – in the cohesive mode.

However, for the other part of the envelope where the vertical load is low, the convexity of the envelope as well as the uniqueness of the solution can not be proven. Nonetheless, a concave failure envelope is difficult to justify, and appears unrealistic from the experimental point of view. Extensive experiments on the subject of failure envelope for various types of footings (strip and circular footings) on various types of soil (sand and clay) shows that the failure surface is convex at both low and high vertical load (Butterfield & Ticof, 1979; Dean et al., 1992; Houlsby & Martin, 1992; Gottardi & Butterfield, 1993; Martin, 1994). It is therefore assumed that at low vertical load the failure envelope (which is to be found) by finite element solution is also convex.

Two aspects of this research relate directly to the problem of convexity and uniqueness. Firstly, making use of the convexity characteristic of the envelope, all the resulting loads are filtered by finding the smallest convex hull in the load space (V, H, M) covering all the load points. Only load points lying on the convex hull are retained and all the load paths crossing inside the envelope are eliminated. The retained load points are then used to plot the contour of the envelope. The algorithm is described in Sedgewick (1988) and implemented in a computer programme by Anderton (1992).

Secondly, in an attempt to confirm the uniqueness of the failure envelope, the results

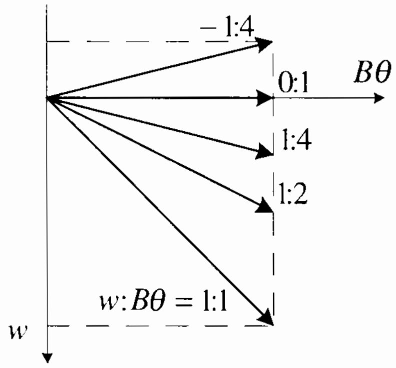

Figure 5.10: Exploration of (V, M) interaction using probing tests.

by the finite element method are compared to the results obtained by a different numerical method – the finite difference method – which was performed by Frydman (1995). The method is implemented into a computer package called FLAC. A brief review of FLAC and the comparison is given in Section 5.5.3.

5.2.2 Experiment strategy

5.2.2.1 Displacement-controlled probing tests

The first method used to explore the failure envelope can be considered as a direct analogy with the displacement-controlled procedure used to determine the purely vertical bearing capacity, in which vertical displacement is applied and by examing the load-displacement curve, the ultimate load can be determined. Thus in order to find, for example, a (V, H) failure load, the footing is applied with vertical and horizontal displacements w and u simultaneously. This will give a load path in (V, H) space with the ultimate load point being one point in the (V, H) failure locus. By varying the ratio of w and u, various points in the (V, H) failure locus can be obtained to establish the whole picture of the locus.

Fig. 5.10 shows an example of this displacement control with no horizontal displacement ($u = 0$). Each vector represents a combination of the vertical and rotational displacements w, θ. This kind of displacement control is used in two series of analyses in this chapter and will be described later. The ultimate bearing capacity found by these tests is exact.

5.2.2.2 Tracking tests

The problem with the probing test procedure is that for each analysis only one yield point can be obtained, and hence the exploration of the whole bearing capacity envelope using the finite element method would be computationally expensive. To overcome this problem Tan (1990) uses an analogy between footing testing and undrained triaxial testing in order to derive a new test procedure which allows the failure envelope to be explored more quickly. By using an analogy between the vertical load V (of the footing bearing capacity problem) and the effective mean stress p', between the horizontal load H and the deviator stress q, between vertical displacement w and the specific volume v, etc., Tan (1990) showed that a probing test performed at a constant vertical footing embedment is analogous to an undrained triaxial test. The yield locus of the Cam clay model is therefore analogous with the footing bearing capacity envelope. Furthermore, whilst the size of the yield locus of the work-hardening Cam-clay model is specified by p'_0 (the value of p' on the yield locus during isotropic compression), the size of the bearing capacity envelope is specified by V_0 – the vertical bearing capacity obtained from vertical penetration. A detailed discussion can be found in Tan (1990) or Martin (1994).

From this analogy Tan (1990) shows that the load paths obtained in just two sideswipe tests, one commencing from $V/V_0 = 1$ and the other from low V/V_0, could be combined to define the entire $(V/V_0, H/V_0)$ yield locus of a footing for a given embedment.

Dean et al. (1992) also uses the same technique to explore the vertical load–moment load interaction (instead of vertical load – horizontal load as originally proposed by Tan, 1990). This is done by applying footing rotation θ at constant penetration z_D.

There is also the further possibility of applying combined displacements u and θ simultaneously at constant z_D. This should give a load path in (V, H, M) space lying in a track which is close to the initial yield surface. For this reason, following Martin's (1994) terminology, any footing tests conducted at constant embedment depth z_D involving horizontal displacement, rotation, or a combination of the two, will be referred to in this thesis as tracking tests. The complete yield surface could be determined by using a series of tracking tests conducted with different $u\!:\!B\theta$ ratios (or $u\!:\!R\theta$ for circular footings) as shown in Fig. 5.11. This procedure is used by Martin (1994) to establish the bearing capacity envelope in a complete (V, H, M) space for a conical footing on clay. Martin (1994) extends the procedure

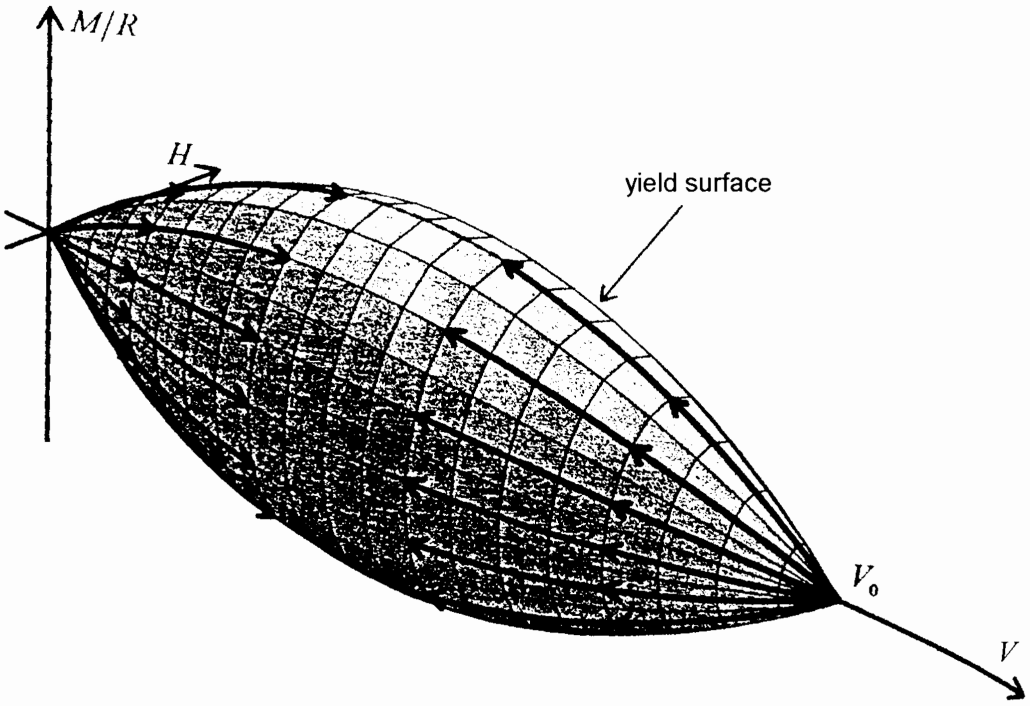

Figure 5.11: Schematic representation of tracking tests commencing from $V/V_0 = 1$ and from very small V/V_0 (after Martin, 1994).

to investigate the envelope of footing at different embedment depths. Bell (1991) also used the tracking test procedure for his three-dimensional finite element analyses for the similar problem of circular footings on clay.

The tracking test procedure applied to finite element analyses differs from the procedure originally designed for physical modelling in a number of aspects. In physical modelling, after a tracking test has been performed at a certain footing embedment, the footing can be then further penetrated to a larger embedment, resulting in the bearing capacity envelope enlarging with footing depth. Thus the same soil sample can be used for several tests with different footing embedments. The small strain analyses used in this research, however, do not allow footing to penetrate progressively into the soil. Therefore, when footings with different embedment need to be investigated (Chapter 7), a different mesh for each embedment depth is generated.

Also, in physical model testing, before the tracking tests commencing from low V/V_0 are started, it is necessary that the footing is driven into the soil to a specified embedment corresponding to a vertical load V_0, then unloaded to a low V/V_0. Even though the finite element analyses follow the same procedure, note that by using von Mises material, the preloading and unloading phase is not necessary because behaviour of the footing (or, more accurately, the soil) is not dependent on load path or loading history.

Overall, the procedure is as follows. First, the vertical displacement is applied until the footing reaches its vertical bearing capacity. At this stage, a stop/restart file which stores the status of the analysis (such as node and element list, nodal load and displacement, stress, strain and yield status of all integration points, etc.) is written to disk so that the calculation does not need to be repeated for each analysis. Then the analysis for each combination of the horizontal displacement and rotation is started after the stop/restart file is read into the memory. For analyses commencing from low V/V_0, the stop/restart file after reaching vertical bearing capacity is also read before the footing is unloaded. When the vertical load reduces to $V/As_u = 1$, another stop/restart file is written. Analyses for each combination of displacements are then started using the $V/As_u = 1$ stop/restart file in the same way as the previous analyses commencing from $V/V_0 = 1$.

The resulting load points are then filtered using the convex hull filtration as discussed in Section 5.2.1.6. Note that due to the use of the interface with two-part yield surface, when the vertical load reduces to zero, the horizontal load capacity also decreases to zero. As has been mentioned in Section 3.4, this yield criterion models the undrained beheviour of the footing under low vertical load. Fig. 5.11, obtained by Martin (1994) from his undrained loading tests, demonstrates that the drained behaviour under low vertical load does, in fact, occur. Therefore, a zero load point $(V, H, M) = (0, 0, 0)$ added into the obtained load points before the convex hull filtration is made.

5.3 Mesh preparation

5.3.1 Mesh dimensions and topology

The mesh dimensions required for accurate bearing capacity calculation is found by some researchers to be much smaller than the mesh dimension necessary for accurate elastic calculations. Sloan (1981) discovered that for strip footing the mesh width needs only be of the order of five times the width of the footing. Using the method of characteristics, Houlsby & Martin (1992) show that a mesh of $0{\cdot}85R \times 0{\cdot}85R$ is sufficient. Bell (1991), having performed a series of runs for strip footings using OXFEM, concludes that a mesh which has a

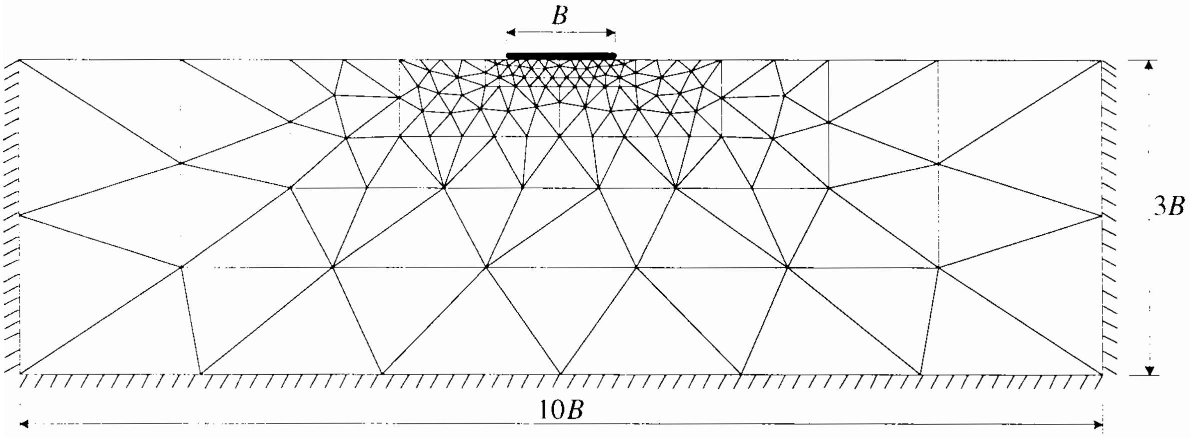

Figure 5.12: Mesh dimensions and grading: 3650 nodes, 218 six-noded continuum elements, 10 interface elements.

radial dimension of $2{\cdot}33R$ and a depth of $1{\cdot}33R$, where R is the footing radius, is adequate and adopts it for his three dimensional calculations.

As the results of this study are to be compared with those of the FLAC program, the mesh size and grading used in this study are made comparable with the one used in calculation with FLAC. The mesh required for calculation with FLAC was found to be larger than the dimensions discussed above. Both OXFEM and FLAC studies use a mesh of the same size of $10B \times 3B$, where B is the width of the footing, as shown in Fig. 5.12, which is the size found to give accurate results with vertical load with FLAC. The mesh is also refined such that the total number of degrees of freedom are similar for both OXFEM and FLAC (approximately 3000 degrees of freedom). The mesh used for OXFEM as shown in Fig. 5.12 has 3650 DOF, 218 elements (excluding interface nodes and elements) and 10 interface elements. It was proven by Sloan & Randolph (1982) that the plane strain six-noded triangular finite element used is suitable for predicting collapse load as well as for undrained loading footing analyses. With the mesh shown in Fig. 5.12 the vertical ultimate load is $V_0/Bs_u = 6{\cdot}05$, which is only 1·9% higher than the exact solution ($V_0/Bs_u = 5{\cdot}94$). The load–displacement curve of the vertical load test is not shown here but the vertical load test resulted in a steady load where further vertical displacement did not induce change in the load. This steady load was determined as the vertical ultimate load for this problem.

The sign conventions of displacements and applied loads are illustrated in Fig. 5.13.

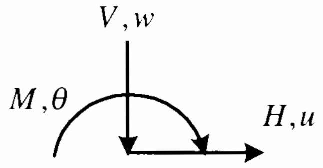

Figure 5.13: Sign Convention.

5.3.2 Material properties

Even though inhomogeneity is one of the main features of offshore foundations, particularly gravity foundations (Smith, 1982), the foundation investigated in this chapter has a uniform profile. The effect of soil inhomogeneity of circular footings is studied in Chapter 7.

The soil used is a von Mises material with the following properties:

$$s_u = 1{\cdot}0$$
$$G = 100$$
$$\nu = 0{\cdot}49$$

Note that as this research is a parametric study and the load results are to be normalised, the soil properties (s_u and G) given above only have a representative meaning. The bearing capacity envelope, to be obtained in terms of dimensionless loads V/As_u, H/As_u and M/ARs_u is not dependent upon the soil properties, or the size of the footing (and the mesh) used in the analyses.

A Poisson's ratio of $\nu = 0{\cdot}49$ enforces the condition of undrained loading.

The interface element model as described in Chapter 3 is used to model the interaction between footing and soil in all analyses of this chapter. The interface has properties as follows:

$$K_s = K_n = 10000$$
$$c_1 = 0;\ \phi_1 = 30^\circ;\ \psi_1 = 0^\circ$$
$$c_2 = \frac{2}{\sqrt{3}};\ \phi_2 = 0^\circ;\ \psi_2 = 0^\circ$$

By using interface elements, it is clear that if the normal stress in the interface is compressive, because the coordinates of the two sides of the interface are identical, one side of the interface can penetrate the other side (by a length of $\varepsilon_n = \sigma_n/K_n$). Therefore, there may be a concern about the condition of the footing being *rigid*. However, with $K_n = 10000$, and the normal stress in the footing expected to be of the order of 10 (or $(\pi + 2)\frac{2}{\sqrt{3}}$ to be exact), the penetration should be in the order of $1/1000$, which is about 1/100th the thickness of the continuum elements around the footing (the side of the continuum elements adjacent to the footing is about 0·1 in length). This is thought to be sufficient for the condition of rigidity to be enforced along the footing.

Analogously, with the existence of K_s, the mesh will behave as if there were an extra continuum layer to deform under shear stress. This extra layer, however, is very thin; To compare with the continuum elements closest to the interface, the extra layer has a thickness of $G/K_s = 1/100$, which is considered negligible.

5.4 Programme of analyses

The tests are divided into three sets which explore the interaction between different components of loads as follows:

- The interaction between the vertical loads and moments;
- The interaction between the vertical and horizontal loads;
- The interaction between between all the three components vertical, moment and horizontal loads.

For the first two sets, both the probing test and tracking test procedures are used to allow comparison between the two. Even though the tracking test procedure can provide a quick method to construct the failure envelope, there is a concern that the envelope obtained by tracking tests may deviate from the true envelope as described in Section 5.2.2.2. The probing test on the other hand can give an exact envelope. If the difference between the two is found to be small, the tracking test procedure can then be used to construct the whole envelope.

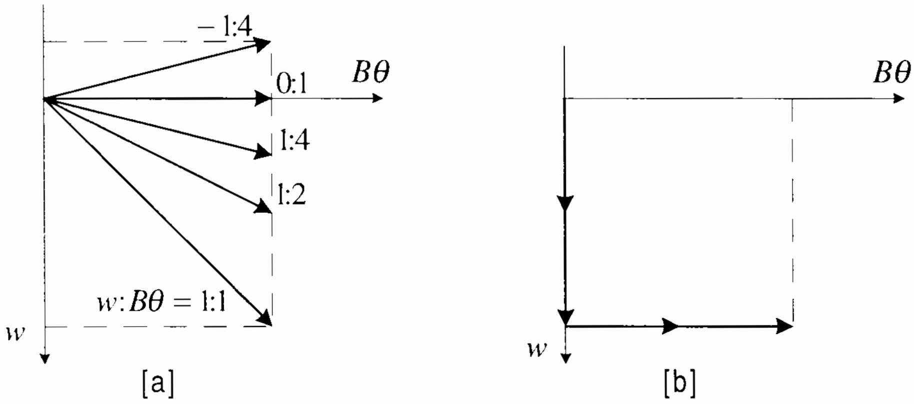

Figure 5.14: (V, M) interaction: displacement paths (a) Probing tests; (b) Tracking test.

5.4.1 Interaction between vertical load and moment

Both probing tests and tracking tests are used to investigate the interaction between vertical load and moment.

5.4.1.1 Probing tests

The test involves a series of analyses, each of which uses a different combination of w, θ as depicted in Fig. 5.14a. No horizontal displacement is applied in these tests. The (V, M) interaction curves are plotted in Fig. 5.15. Horizontal load in the tests is found to be very small, so the curve in Fig. 5.15 can be assumed to be on the $H = 0$ plane. The end points of the load paths obtained from the analyses appear to form a parabolic trend.

5.4.1.2 Tracking test

In this test, the first load stage involves only vertical displacement (until the footing reaches its vertical bearing capacity), followed by horizontal displacement in the second load stage as illustrated in Fig. 5.14b.

As seen in Fig. 5.15, the load path from this analysis does not coincide exactly with the locus of end points of the probing test load paths, but follows a track slightly inside the envelope of the probing tests. The difference is greater at high vertical load, when the rotation begins in this test. This difference gets smaller when more rotation is applied: at $V/Bs_u \approx 4$, the failure envelopes obtained from both the tests are almost the same.

The peak of moment does appear to take place at $V/V_0 = 0{\cdot}5$ as the Meyerhof (1956)

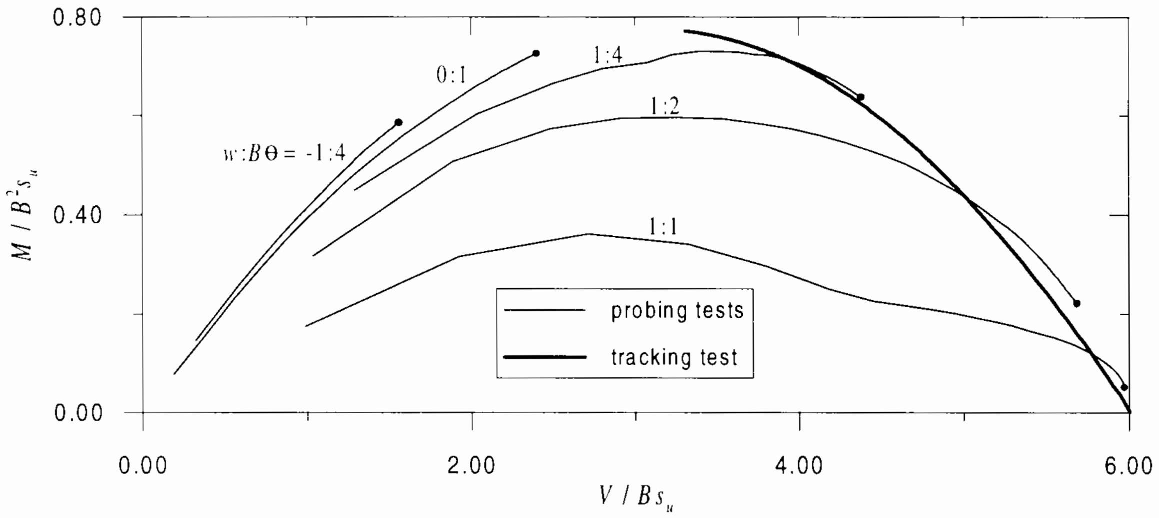

Figure 5.15: (V, M) interaction curves.

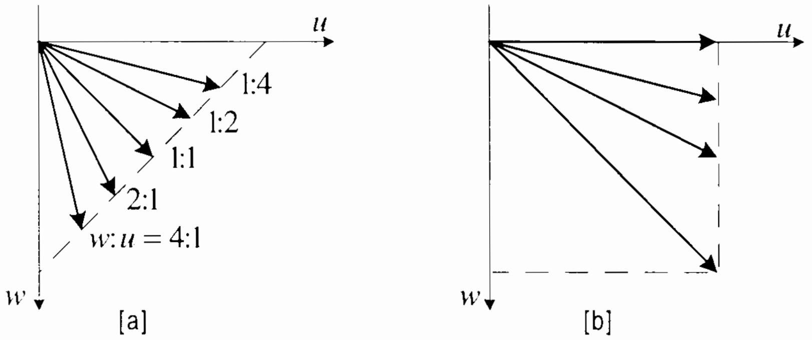

Figure 5.16: Displacement Paths of (V, H) probing tests (a) Displacement paths used in the study; (b) Alternative paths.

method predicts. The failure curve, however, does not go further towards the region of low vertical load after it reaches maximum moment.

5.4.2 Interaction between vertical and horizontal loads

5.4.2.1 Probing tests

These analyses combine vertical displacement with horizontal displacement applied simultaneously. In each probing test a different combination of horizontal and vertical displacement is applied as shown in Fig. 5.16a. It is slightly different from the (V, M) probing tests. The displacement path for (V, H) tests, if made directly comparable to the (V, M) probing tests, might be expected to look like the one depicted in Fig. 5.16b. However, the resulting load paths of the displacements would not track down to the point $(V,H) = (V_0,0)$, where V_0 is

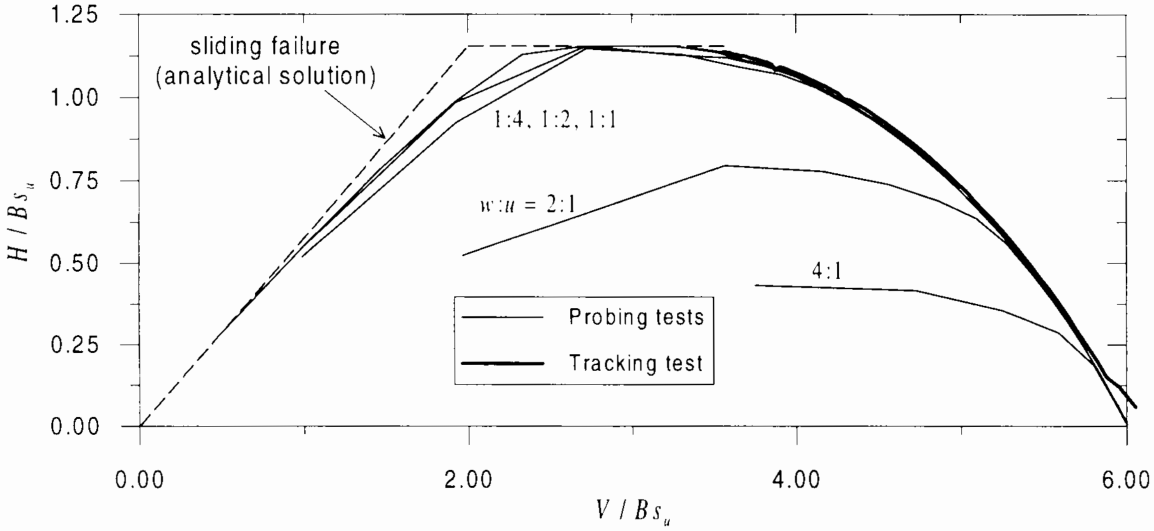

Figure 5.17: (V, H) interaction curves.

the vertical bearing capacity, to complete the envelope as desired.

It is pleasing to see the resulting load paths follow a predicted trend. For those tests with higher horizontal displacement (i.e. $w : u = 1 : 1,\ 1 : 2,\ 1 : 4$), the horizontal load increases quickly and almost linearly with the vertical load, but then when the load paths hit the horizontal load limit of $H_0/Bs_u = 2/\sqrt{3}$, they immediately level off, indicating the footing undergoing a sliding failure. For two tests with $w{:}u = 1{:}2,\ 1{:}4$, the load paths pass from this sliding failure mode into the bearing failure mode when the vertical load gets higher (as more vertical displacement is applied). It appears that the transition point lies somewhere close to $V/V_0 = 0{\cdot}5$, or a little higher as the exact solution predicts (Bolton, 1979). The transition is smooth, rather than pointed as some of the empirical methods predicted. The two remaining analyses with higher vertical displacement (i.e. $w{:}u = 2{:}1,\ 4{:}1$) fill the (V, H) locus in the region of high V.

5.4.2.2 Tracking test

This test has two load stages: vertical displacement in the first stage; horizontal displacement in the second stage. The resulting load path is plotted in a bold line in the same chart with the (V, H) probing tests to compare in Fig. 5.17. The load path of this tracking test follows a parabolic track which is almost exactly the same as the (V, H) interaction loci obtained from the previous probing test. It should be noted that the load path of this tracking test does not go further after it reaches the point of maximum horizontal load $H_0/Bs_u = 2/\sqrt{3} = 1{\cdot}155$ at

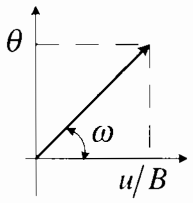

Figure 5.18: Combination of horizontal and rotational displacements.

approximately $V = 0{\cdot}583V_0$. The continuing line beyond that critical point towards the origin is the result of the closed form solution for the type of interface elements used as described in Section 5.3.2.

In this test, at the beginning of the second loading stage ($V \approx V_0$) when the horizontal displacement is first applied, there is a noticable deviation from the main trend (or an overestimation in the horizontal load direction). This deviation is soon overcome when more horizontal displacement is applied. This can be explained by the fact that when the footing displacement changes the direction in the second loading stage, some interface elements change their yielding status from elastic to plastic, or even debonding. However, these elements have their stiffness matrix calculated as elastic because at the end of the previous vertical loading (the first loading stage), the yielding status of most of the interface is elastic. This results in an overestimation in horizontal load as seen in Fig. 5.17. Another consequence is significant unbalanced nodal forces. In the non-linear solution scheme used in this study, these unbalanced forces are then compensated in the next calculation increments and the solution is then stabilised, as seen in the figure when horizontal force H increases. This also shows that displacement application rate should be small when the footing displacement direction is changed, particularly to horizontal direction, which can cause instability to the overall solution.

Except for the tip at $V \approx V_0$, the two (V, H) envelopes are almost exactly the same. For the (V, M) interaction shown in Section 5.4.1, though tracking tests give smaller loci than probing tests, the difference is fairly small. In addition, the values given by the tracking tests tend to be conservative. The tracking test procedure is therefore used to explore the whole bearing capacity envelope in the following section.

Table 5.1: Combination of horizontal and rotational displacements.

Test Number	$u : B\theta$	ω
1	1:3	71·6°
2	1:1	45·0°
3	3:1	18·4°
4	3:−1	−18·4°
5	1:−1	−45·0°
6	1:−3	−71·6°

5.4.3 Interaction between vertical, horizontal loads and moment

In this series of tracking tests, different ratios of rotation and horizontal displacements are applied. The main combination of horizontal and rotational displacement are given in Table 5.1, which are also depicted in Fig. 5.18. The combination thus contains both cases of positive and negative eccentricity; the first three tests investigate the positive eccentricity case, and the last three the negative eccentricity case.

In order that the failure envelope is explored at both high and low levels of vertical load, tracking tests commencing from both high ($V/V_0 = 1$) and low vertical load are performed for each $u:B\theta$ combination.

5.4.3.1 High V/V_0 level

The results of tracking tests starting from $V/V_0 = 1$ are shown in Fig. 5.19. Note that because of their small magnitude the horizontal load (H/Bs_u) and moment (M/B^2s_u) are plotted in a scale four times as large as the vertical load. In a similar way to the (V, H) and (V, M) tracking tests, when the combination of u and θ is applied, the vertical load drops, associated with an increase in horizontal and moment loads. However, for the case of positive eccentricity, particularly for higher u such as $u:B\theta = 3:1$, the horizontal load can drop after it reaches its peak value. At the same time, moment picks up sharply (therefore the load path is probably still close the true bearing capacity envelope). This also means that the load path of a displacement combination does not always follow a track lying on a $M/BH =$ const plane.

The load paths (see (H, M) plot in Fig. 5.19) of negative eccentricity sense are not symmetric to that of the corresponding positive eccentricity one. This can also be seen in (V, M) space. Note that in spite of this, it is still difficult to conclude from this plot how the

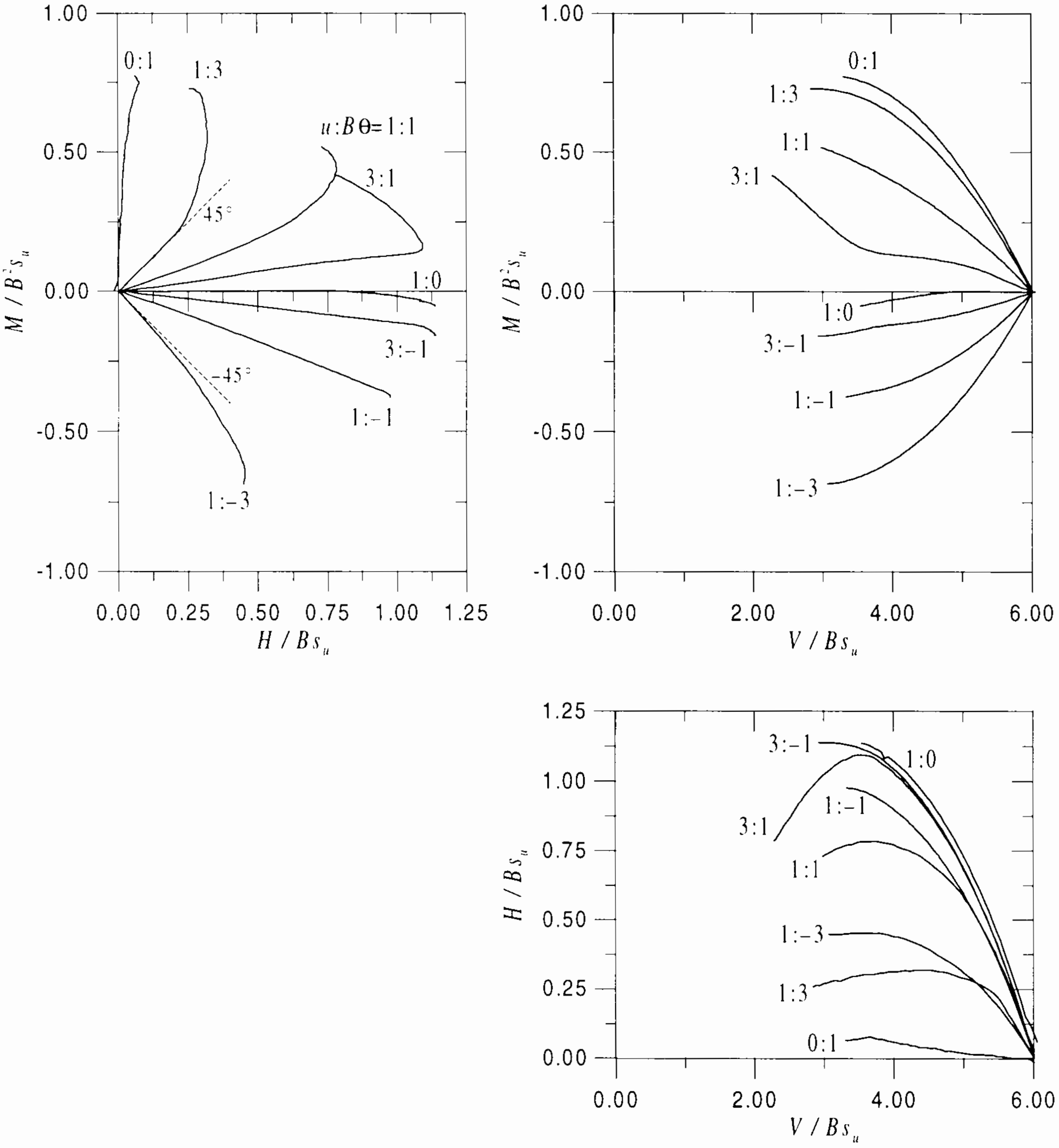

Figure 5.19: (V, H, M) curves at high V/V_0 level.

load eccentrity affects the shape of the failure envelope. In order to do that, the results need to be plotted in three dimensions using contours.

The $(H/Bs_u, M/B^2s_u)$ plot in Fig. 5.19 shows that the series of tests gives a good coverage of the bearing capacity envelope in $(H/Bs_u, M/B^2s_u)$ view. Nevertheless, tests with higher rotation (e.g. $u\!:\!B\theta = 1:1$ to $0:1$ and $1:-1$ to $1:-3$) leave a wider gap between them than those with higher horizontal displacement. In order to construct the envelope in more detail, another series of tests was conducted. The combined displacements used in these tests are: $u\!:\!B\theta = 1:5; 1:2; 1:-2; 1:-5$. Their results are not plotted in Fig. 5.19 for clarity. The results are however used in plotting the contours of the envelope, which is presented in Section 5.4.4.

5.4.3.2 Low V/V_0 level

In order to explore the envelope at low V/V_0 levels, the footing is loaded until it reaches vertical bearing capacity. It is then unloaded to $V/Bs_u = 1$ $(V/V_0 = 0{\cdot}167)$ before a combination of horizontal and rotational displacements are applied. Fig. 5.20 shows the resulting load paths. For all tests except the one with $u\!:\!B\theta = 0:1$ initially there is a sharp increase in horizontal load associated with small change in vertical and moment load (e.g. $V \approx 1$ and $M \approx 0$) and this phase is interpreted as elastic loading. For the case of $u\!:\!B\theta = 1:1$, $3:1$, $3:-1$, and $1:-1$, the vertical load remains almost constant at $V = 1$. The horizontal load then stops at just below $0{\cdot}625$, indicating that the footing is undergoing a sliding failure because the ultimate horizontal load is $H \approx V \tan 30^\circ = 0{\cdot}577$. The horizontal load then remains at this level, but moment increases with a increase in vertical load.

Another set of combined displacements is also applied in order to construct the envelope in detail. The combinations are: $u\!:\!B\theta = 1:5;\ 1:8;\ 1:10;\ 1:-5;\ 1:-8;\ 1:-10$. The results are omitted in Fig. 5.20 for clarity but used in plotting the contour of the failure envelope in the following section.

5.4.4 Bearing capacity envelope

Combining the results from the two previous tracking tests from high and low V/V_0, we can plot the contours of the bearing capacity envelope with respect to V as shown in Fig. 5.21 and Fig. 5.22.

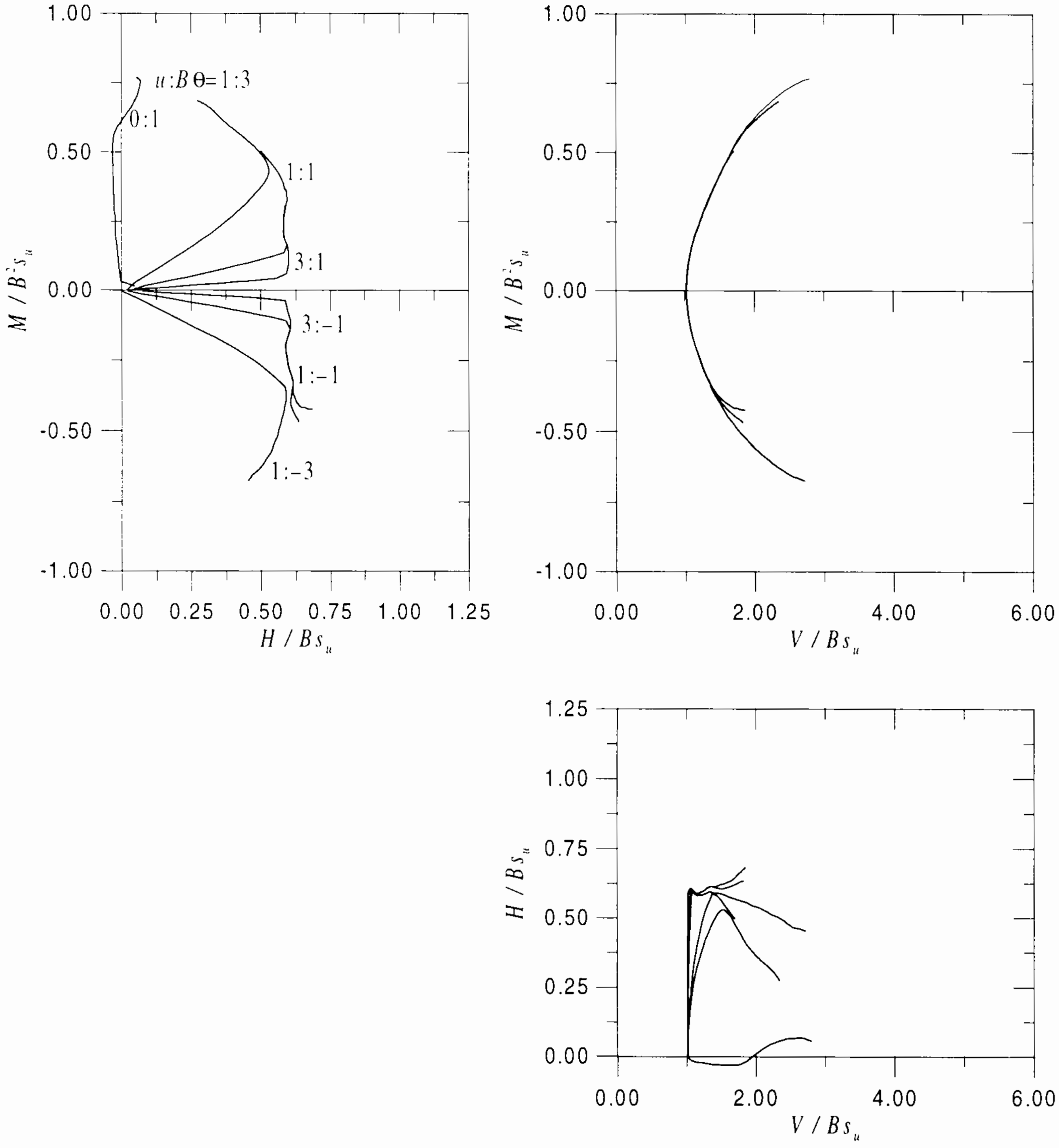

Figure 5.20: (V, H, M) curves at low V/V_0 level.

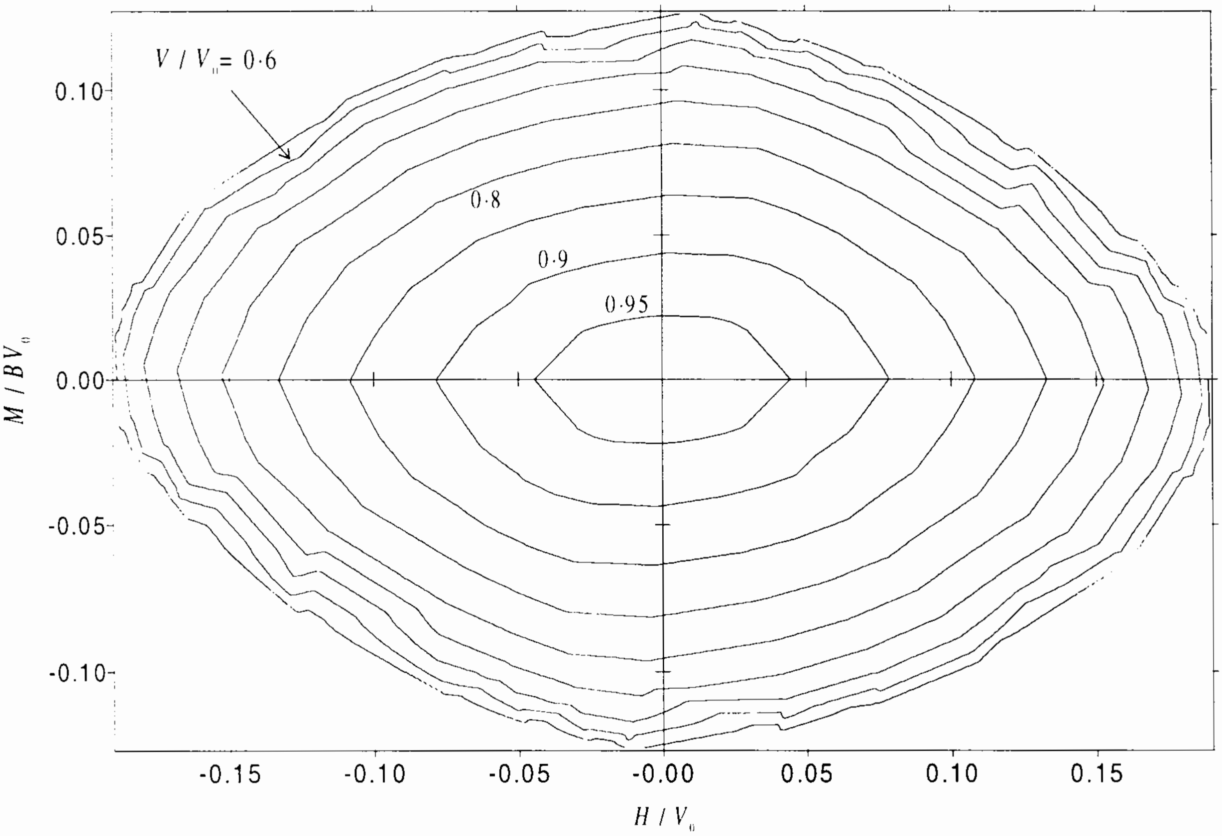

Figure 5.21: Contour with respect to V/V_0 of the bearing capacity envelope, for $V/V_0 \geq 0{\cdot}5$.

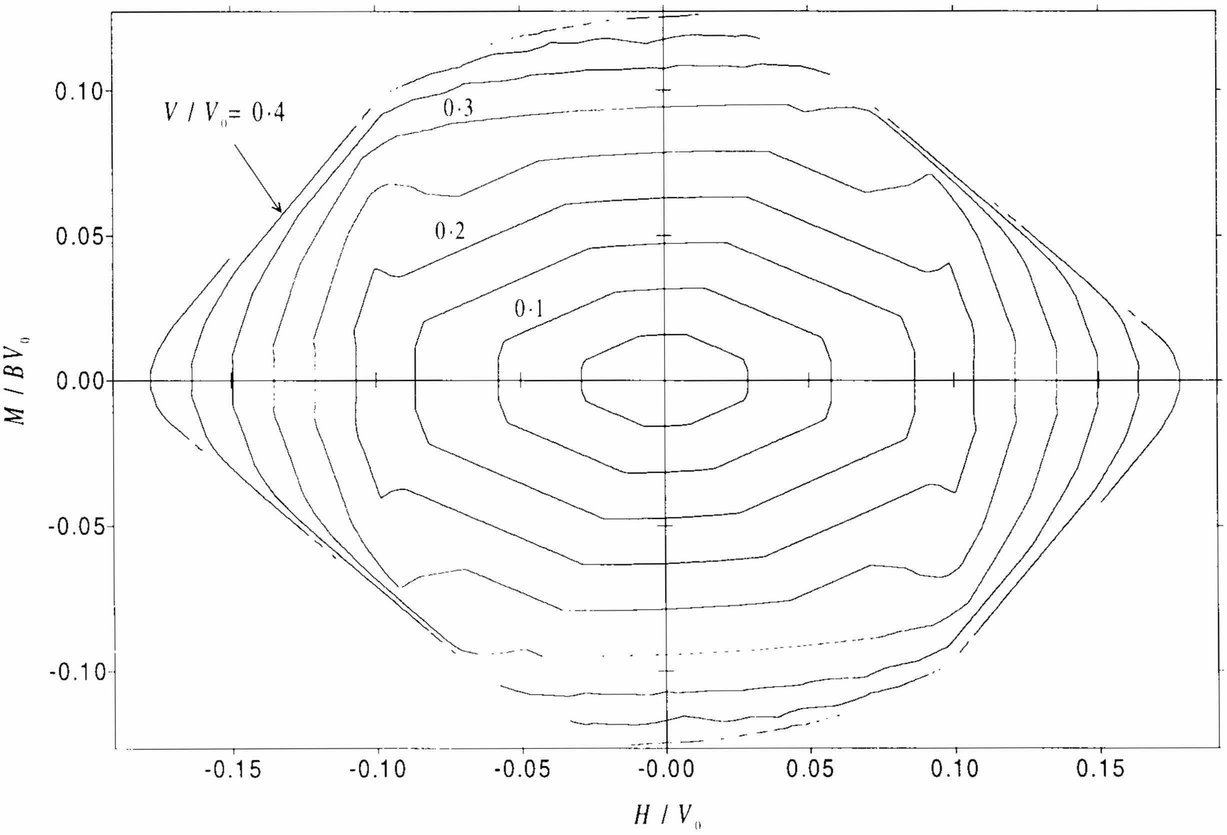

Figure 5.22: Contour with respect to V/V_0 of the bearing capacity envelope, for $V/V_0 \leq 0{\cdot}5$.

The most surprising feature of the contours at both high and low V/V_0 levels is that they are almost symmetrical about the M/BV_0 and H/V_0 axes. This is in contrast to the expectation as mentioned in Section 5.2.1.5, also to the experimental result by Gottardi & Butterfield (1993) for strip footings on sand.

Another interesting point about the contour of high V/V_0 level (see Fig. 5.21) is that it has a pointed shape; in these contours the transition from positive moment to negative moment is not smooth, particularly for higher V/V_0. This means that for a constant vertical load, an introduction of moment load causes a sharp reduction in horizontal bearing capacity.

At low V/V_0 levels (see Fig. 5.22), the contours are similar to those at high V/V_0 levels in the sense that they are almost symmetrical about the M/BV_0 and H/V_0 axes. Nonetheless the contours at low V/V_0 levels have some distinctive features. First of all, because of the use of interface elements which behave as frictional interfaces for V/V_0 values less than $2/(\pi + 2)\frac{2}{\sqrt{3}} = 0{\cdot}337$ (which is the calculated value below which frictional sliding will occur), at high H, the footing fails by frictional sliding. Therefore a small application of moment does not cause the horizontal load capacity to drop. This fact is represented by near vertical segments in the left and right hand sides of the contours. At $V/V_0 \geq 0{\cdot}33$, this vertical segment of course disappears when frictional sliding cannot happen. The contour quickly turns to a more pointed shape (at $M/BV_0 = 0$) and that pointed shape is clearly seen in the previous contour plot for high V/V_0 levels.

The second characteristic of the contours at low V/V_0 levels is the existence of horizontal segments at the top and bottom part of the contours. This indicates that to a certain extent, the horizontal load does not affect the moment bearing capacity of the footing. This range of horizontal load gets larger at higher V/V_0 (see contours at $V/V_0 = 0{\cdot}3$ and $0{\cdot}4$). However this feature is not seen for $V/V_0 > 0{\cdot}5$, where in the region around peak moment, moment change gradually and smoothly with horizontal load.

As Fig. 5.21 and Fig. 5.22 show, it is difficult to calculate the contour of the envelope in the range of $V/V_0 \approx 0{\cdot}5$. To avoid this problem, the bearing capacity envelope can also be plotted in contours with respect to moment as shown in Fig. 5.23. In this case, the whole bearing capacity envelope can be seen (In fact only the $M \geq 0$ half of the bearing capacity envelope can be seen, but the other half can be deduced from symmetry). The semi-envelope has a shape of a boat hull. The vertical segments on the left (low V/V_0) confirm the observation made for the previous plot Fig. 5.22 about the horizontal segments of the contour.

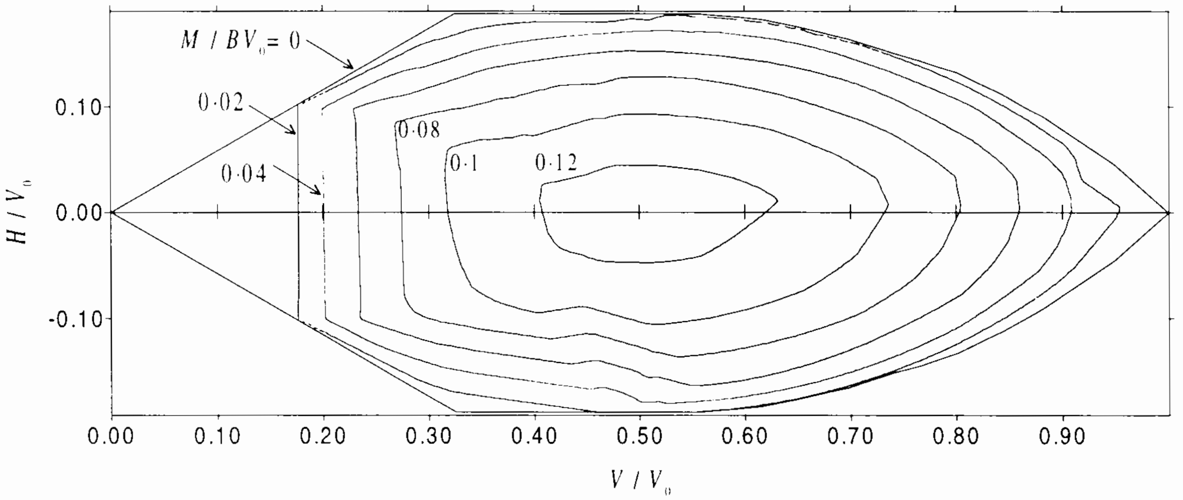

Figure 5.23: Contour with respect to M/BV_0 ($M \geq 0$).

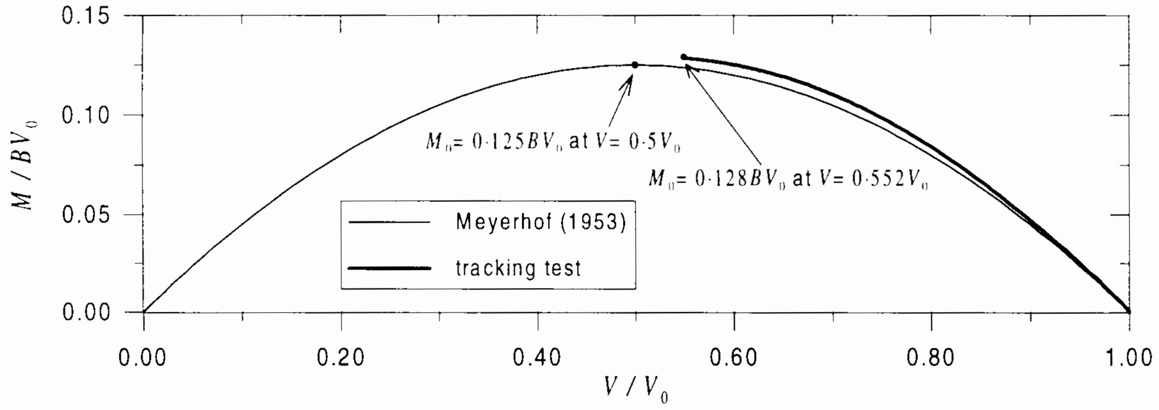

Figure 5.24: Comparison of the results of (V, M) interaction.

5.5 Comparison with other solutions

5.5.1 Comparison with analytical solutions: (V, M) and (V, H) planes

In order to compare the solution by Meyerhof for the (V, M) interaction (Section 5.2.1.2) with the current research, the curve in Fig. 5.3 and the curve of (V, M) tracking test (e.g. Fig. 5.15) are plotted in Fig. 5.24.

It can be seen that the two curves have similar shape. It is interesting that even though the solution by Meyerhof uses the simple assumption of the effective area, its predicted maximum value of M_0, when normalised againtst BV_0, is only 2·4% lower than the OXFEM value: $M_0 = 0{\cdot}125BV_0$ compared to the ultimate value obtained by OXFEM $M = 0{\cdot}128BV_0$. Interestingly, Meyerhof (1963) states that "[for strip footings] detailed model tests have shown

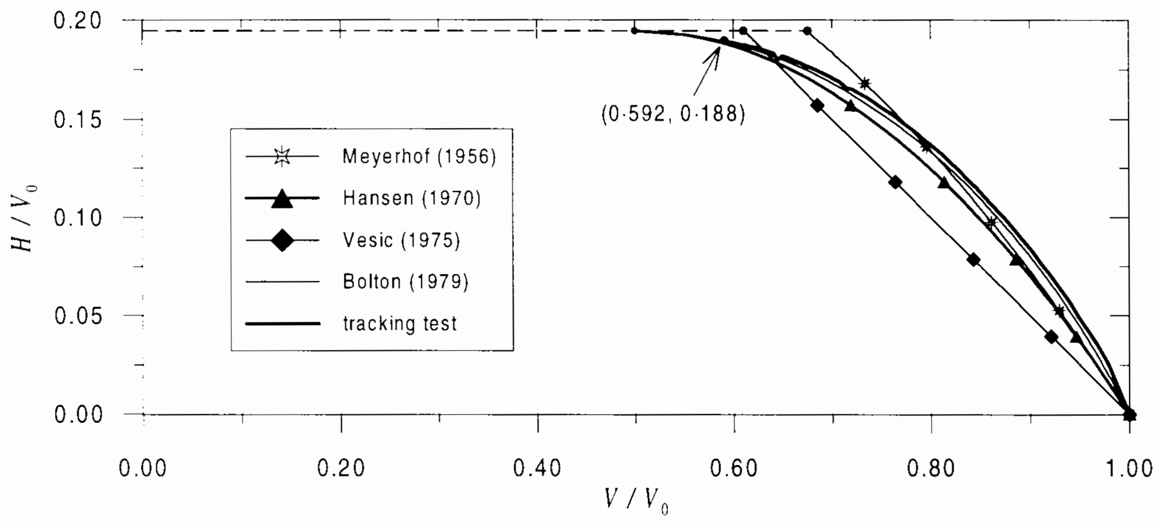

Figure 5.25: Comparison of the results of (V, H) interaction.

that the [effective area] procedure is on the safe side", which is also the case found in this study.

Regarding the interaction between vertical and horizontal loads on the $M = 0$ plane, it appears that the numerical results bear a close resemblance to the Bolton (1979) method (see Fig. 5.25). The two curves are almost exactly the same throughout the range in which the footing fails in the bearing failure mode.

The numerical results in Fig. 5.24 and Fig. 5.25 have one feature in common: during the second loading regime in which either horizontal or rotational displacement are applied, the resulting load path reaches a critical state, at which further displacement does not induce further change in the resulting loads, before V reaches $0{\cdot}5V_0$. In the case of (V, H) interaction, it is clear that at the critical point, the horizontal load does not reach its peak value $H_0 = 0{\cdot}194V_0$. This may also be true for the case of (V, M) interaction though this is not clear in Fig. 5.24 because the exact value of the peak moment is not known.

5.5.2 Comparison with analytical solutions: the bearing capacity envelope

Fig. 5.26 shows the contour plot of the bearing capacity envelopes (only $V/V_0 > 0{\cdot}5$) determined by OXFEM superimposed on the envelope using Hansen (1970). At all levels of V/V_0, the Hansen (1970) method is conservative compared to OXFEM result.

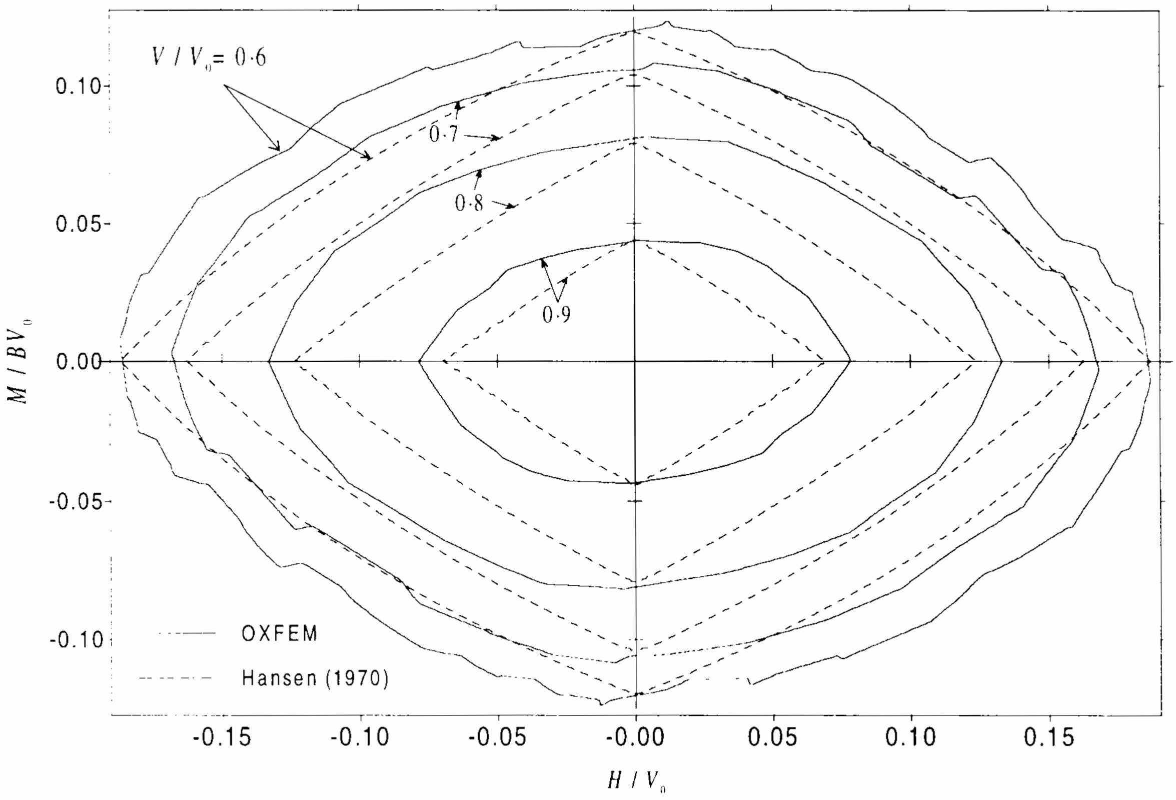

Figure 5.26: Bearing capacity envelope: comparison between the OXFEM results and Hansen (1970) (for $V/V_0 > 0{\cdot}5$).

Note that the two methods are not compared for the envelope at low V/V_0 levels because the two methods have different ways of treating the footing at low V/V_0: this study uses a frictional interface, which leads to an envelope pointed at the origin (see Fig. 5.23), whereas the Hansen (1970) method gives, for zero moment, the full horizontal load for all cases of sliding failure (see Section 5.2.1.4).

5.5.3 Comparison with FLAC

5.5.3.1 Overview of FLAC

FLAC (Fast Lagrangian Analysis of Continua) is a two dimensional finite difference code. It uses an explicit, time-marching method to solve the governing field equations in which every derivative is replaced by an algebraic expression written in terms of the field variables (e.g. stress or displacement) at discrete points in space; these variables are undefined elsewhere. The general calculation scheme invokes the equations of motion to derive new velocities and displacements from stresses and forces. Then strain rates are derived from velocities, and new stresses from strain rates. This cycle takes place within one time step which is small enough so that information cannot physically pass from one element to another in that interval. The calculational 'wave speed' always keeps ahead of the physical wave speed, so that the equations always operate on known values that are fixed for the duration of the calculation. As a result, no iteration process is necessary when computing stress from strain in an element during one solution step, even if the constitutive law is extremely non-linear.

Further information can be found in the FLAC manual.

5.5.3.2 Result of FLAC analyses

The FLAC analyses were performed by Frydman (1995). The mesh used for analyses with FLAC has approximately same number of degrees of freedom as the mesh used with the finite element method, which is mentioned earlier in Section 5.3. The soil model used in FLAC is Mohr-Coulomb soil with shear strength of $s_u = 1 \cdot 0$. The mesh also uses the interface elements as provided by FLAC. The interface has the same properties as those used in the analyses by the finite element method. A series of tracking tests was performed using the same set of displacement ratios as listed in Table 5.1.

The stress results from these analyses are then multiplied by $2/\sqrt{3}$ to take into account the difference of shear strength between the Mohr-Coulomb soil used in the analyses by FLAC and the von Mises soil used in the analyses by the finite element method. The result of FLAC analyses is plotted in Fig. 5.27 in bold lines. It shows that oscillation in the load path occurs in these analyses. It is believed that this oscillation is due to the inclusion of purely cohesive interface elements in the problem analysed with FLAC. It is noted that the oscillation happens solely in the H direction in the load space. As discussed in Chapter 3, if purely cohesive interface elements are used, the finite element analyses also suffer from the same problem.

In order to eliminate the irregularity in the load paths, the load data are filtered by finding the smallest convex hull in the load space (V, H, M) covering all the load points. Only load points lying on the convex hull are retained. The filtered data are plotted in Fig. 5.27 in thin lines.

In Fig. 5.27 the results of combined loading at high V/V_0 by OXFEM and FLAC are plotted in the same charts for comparison with Fig. 5.19. There are a slight difference in the

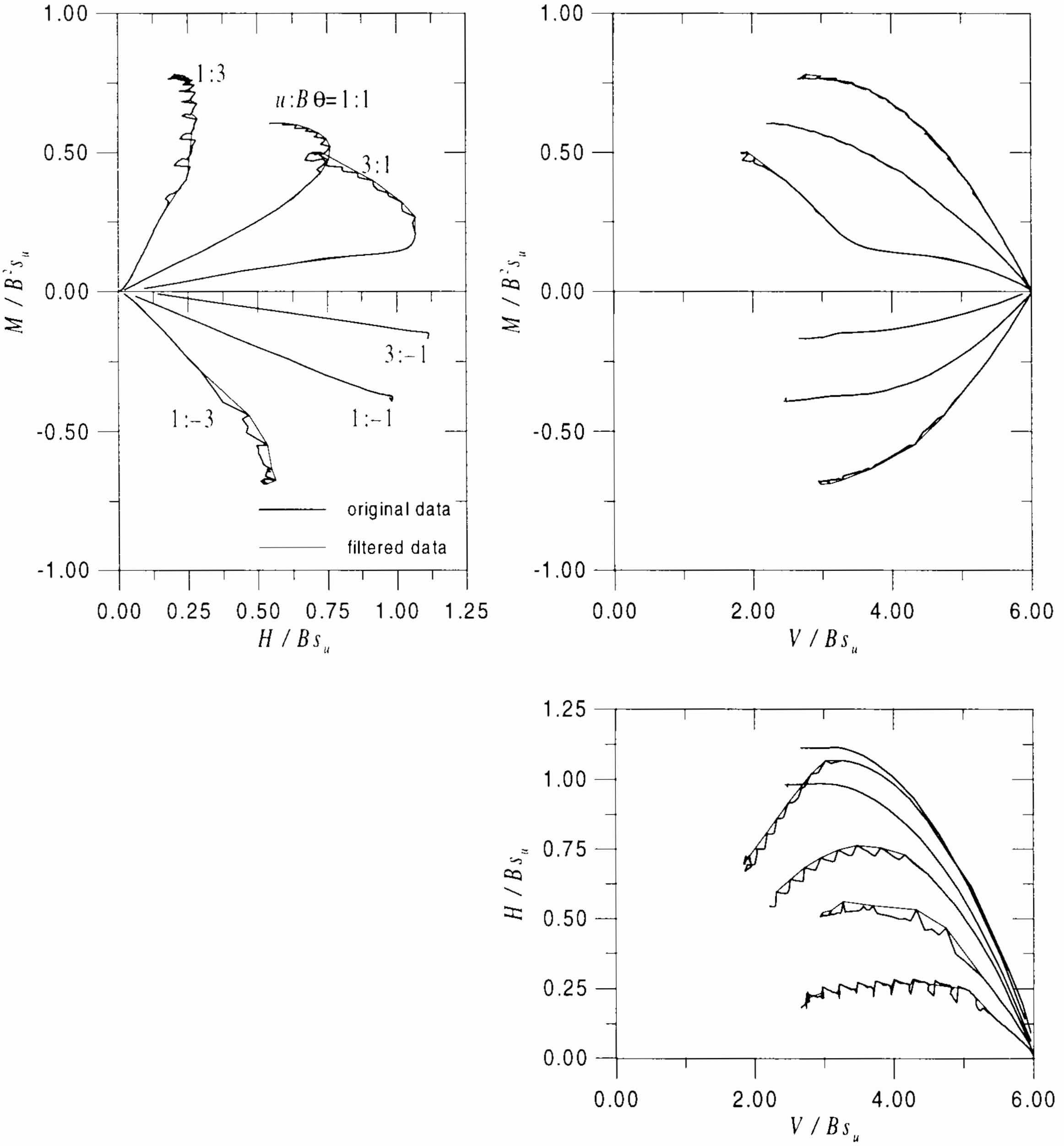

Figure 5.27: (V, H, M) interaction at high V/V_0: results from FLAC (data from Frydman, 1995).

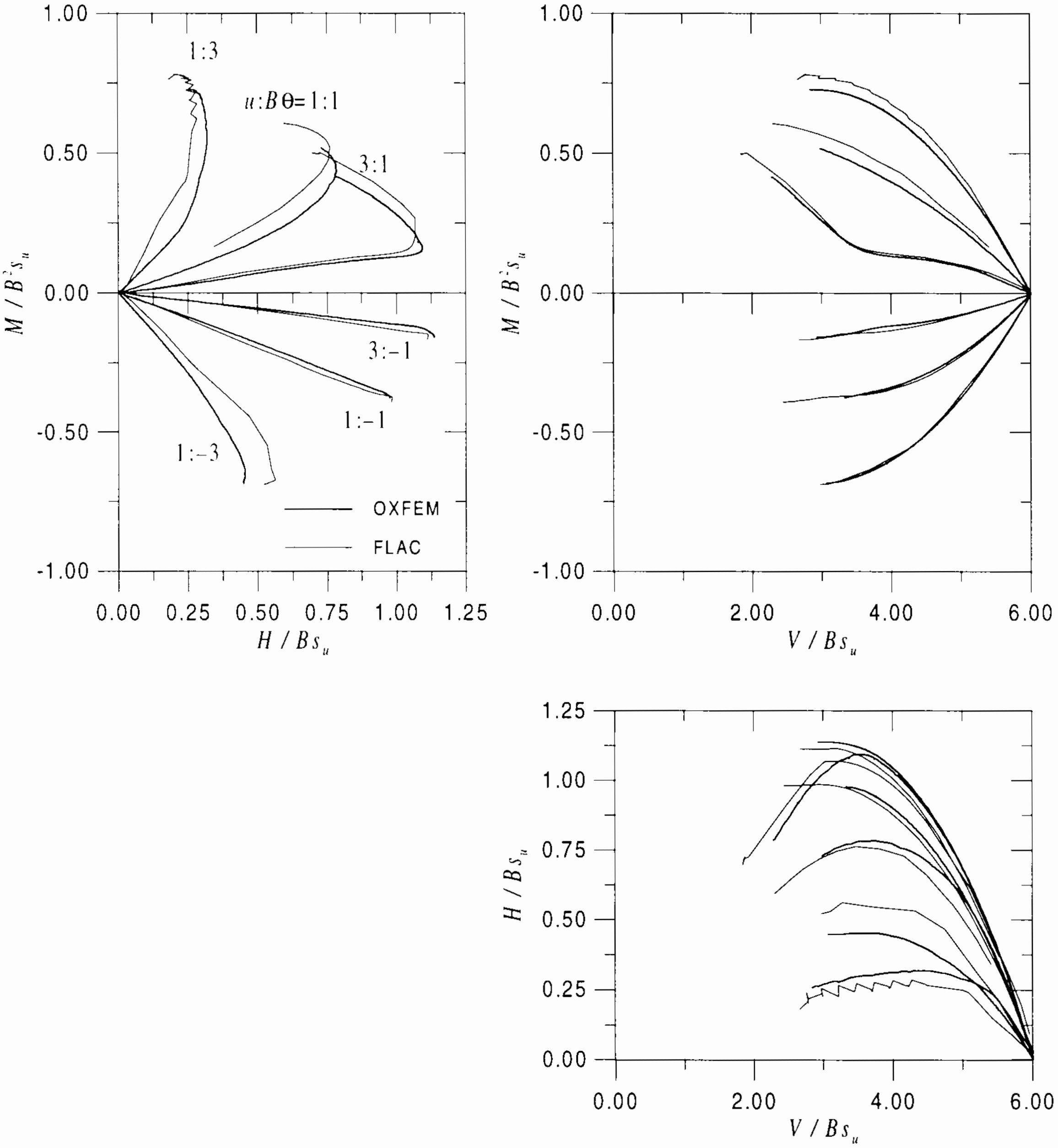

Figure 5.28: (V, H, M) interaction at high V/V_0: comparison between FLAC (filtered data) and OXFEM.

H direction: FLAC gives a higher horizontal force in magnitude if the rotation is positive and slide is negative, or vice versa; and a lower value if both the rotation and slide are positive or negative. However, as shown in Fig. 5.28 to a large extent the two methods give almost identical load paths.

It is important that the two different methods using two different numerical techniques yield results in very close agreement. Most significantly, for the case of $u\!:\!B\theta = 3:1$ the two methods give similar load paths, which have significant change in direction in both $(V,\ M)$ and $(H,\ M)$ spaces. The difference between the results are mainly in the horizontal load. OXFEM tends to give smaller values than FLAC for negative eccentricity, and vice versa for positive eccentricity. The FLAC results also give contours similar to the OXFEM results as shown in Section 5.4.4, notably the FLAC contours are also almost symmetrical about the H/V_0 and M/BV_0 axes. They also have a pointed transition from negative to positive moment at high V/V_0 level. As discussed in Section 5.2.1.6, this similarity between the two methods give evidence for the uniqueness of the failure surface.

In closing, it is worth noting that the interface element model worked well in all tests. It modelled the loss of contact and sliding between the soil and the footing as desired, without causing instability or loss of accuracy. Encouraged by this, the research is extended to cover circular footings as presented in the next chapter.

Chapter 6

Bearing Capacity Envelope of Circular Footings

6.1 Introduction

In this chapter, the bearing capacity envelope for a flat surface circular footing will be investigated. This is done by using a similar numerical experimental technique as for the previous chapter for strip footings. However, due to the circular shape of the footing and the non-symmetric load combination, a three dimensional analysis is needed. Thus the analyses in this chapter make use of three dimensional continuum finite elements (see, for example, Bell, 1991), as well as the two dimensional interface elements as developed in Chapter 4.

The chapter is organised as follows. In Section 6.2, various methods commonly used to predict the bearing capacity of circular footings under combined loadings are reviewed. Also reviewed are several (more recent) approaches to the problem of combined loading on circular footings using physical and numerical modelling. The preparation for the main series of analyses (such as mesh preparation, the choice of finite elements, etc.) is discussed in Section 6.3 before the main results are presented with preliminary discussion in Section 6.4. This leads to a more detailed analysis of the results, including the derivation of an empirical formula to define the bearing capacity envelope in Section 6.5. A comparison between the obtained results and other previously reviewed methods follows in Section 6.6.

6.2 Literature review

6.2.1 Vertical bearing capacity

There are no known exact solutions for the vertical bearing capacity. However, for both smooth and rough footing on Tresca soil ($\sigma_{\max} - \sigma_{\min} = 2s_u$), *lower bound* solutions exist:

For a smooth footing (Shield, 1955):

$$V/As_u = 5{\cdot}69 \tag{6.1}$$

For a rough footing (Eason & Shield, 1960):

$$V/As_u = 6{\cdot}05 \tag{6.2}$$

in which s_u is the maximum shearing stress of the Tresca material.

Houlsby & Wroth (1984) use the method of characteristics to compute lower bound vertical collapse loads. The effect of footing embedment in combination with cone angle, roughness and strength increasing with depth were also investigated. Their results for rough and smooth flat surface footings on a uniform soil are in agreement with the solution by Shield (1955) and Eason & Shield (1960).

There is no known exact solution for a von Mises soil either. In addition, because in the problem of bearing capacity for axi-symmetric footing, the shear stress along the failure surface ranges from s_u to $2/\sqrt{3}s_u$, the Eason & Shield (1960) solution for rough footings multiplied by $2/\sqrt{3}$:

$$V/As_u = \frac{2}{\sqrt{3}}6{\cdot}05 = 6{\cdot}99 \tag{6.3}$$

is not an exact lower bound solution for footings on a von Mises soil. However, this value may be regarded as a reasonable approximation to the actual capacity.

To calculate vertical bearing capacity of circular footings, empirical and semi-empirical bearing capacity formulae, notably those of Hansen (1970) and Vesic (1975), use the exact solution for strip footings (Equ. 5.1) modified by a shape factor. For circular footings, this shape factor is 1·2 for Hansen's (1970) method and $1 + 1/(\pi + 2) = 1{\cdot}194$ for Vesic's (1975) method, resulting in $V/As_u = 6{\cdot}17$ and $6{\cdot}14$ respectively, both slightly higher than the Eason & Shield (1960) solution.

Due to the lack of exact solutions, Bell (1991) performed a two dimensional axi-symmetric calculation using the high-order cubic strain 15-noded triangular elements, with a fine mesh and found the collapse load to be $V/As_u = 6{\cdot}65$. Using this as the benchmark value for his three dimensional analyses, Bell (1991) found that 10-noded and 20-noded tetrahedral meshes overestimate by about 13% and 3%, respectively.

6.2.2 Interaction between vertical load and moment

For circular footings, Hansen (1970) proposes that eccentrically loaded circular footing be treated using the assumption of effective area shown in Fig. 5.2b. Hansen (1970), however, does not elaborate how the length to width ratio L'/B' of the equivalent rectangle should be determined. American Petroleum Institute (1993) suggests that the equivalent rectangle be determined by the following equation:

$$\begin{aligned} A' = B'L' &= \pi R^2 - 2e\sqrt{R^2-e^2} - 2R^2\sin^{-1}(e/R) \\ L'/B' &= \sqrt{\frac{R+e}{R-e}} \end{aligned} \tag{6.4}$$

This leads to the following relation between vertical and moment bearing capacity for circular footings on clay:

$$\frac{V}{V_0} = \left(\frac{1+0{\cdot}2(B'/L')}{1{\cdot}2}\right)\frac{A'}{A} \tag{6.5}$$

where $B = R\sqrt{\pi}$ and A is the gross footing area πR^2.

Using the same concept of the effective area, the Vesic (1975) formula for vertical bearing capacity leads to the following vertical bearing bearing capacity interaction formula:

$$\frac{V}{V_0} = \left(\frac{\pi+2+(B'/L')}{\pi+3}\right)\frac{A'}{A} \tag{6.6}$$

The two methods of Vesic and Hansen are plotted in Fig. 6.1. The peak moment does not occurs at $V/V_0 = 0{\cdot}5$, as in the case of strip footings, but at $V/V_0 = 0{\cdot}47$ for both methods. The peak moment values of both are also very close: the difference is only half a percent, resulting in the two predictions of $(V,\ M)$ being almost identical.

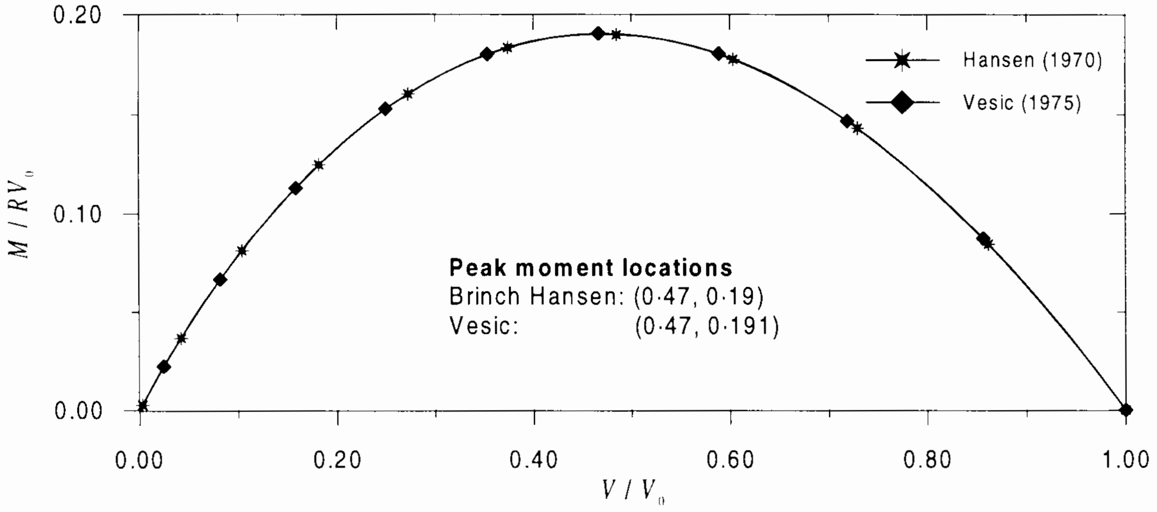

Figure 6.1: (V, M) interaction chart of a circular footing.

6.2.3 Interaction between vertical and horizontal loads

Even though this case of loading for circular footings does not have a known exact solution, it is dealt with by all the three semi-empirical methods reviewed in Chapter 5. While the Meyerhof (1953) formula is unchanged for circular footings (see Equ. 5.5), the other two methods change as follows:

Hansen (1970) (cf. Equ. 5.7):

$$\frac{V}{V_0} = \frac{1{\cdot}2 - 0{\cdot}7(1-\sqrt{1-H/H_0})}{1{\cdot}2}, \quad H \le H_0 = As_u \tag{6.7}$$

Vesic (1975) (cf. Equ. 5.8):

$$\frac{V}{V_0} = 1 - \frac{1{\cdot}5H}{(\pi+2)H_0}, \quad H \le H_0 = As_u \tag{6.8}$$

The three formula are plotted in Fig. 6.2. For circular footings the Meyerhof method is still the least conservative method, as it is for strip footings (see Fig. 5.4). It will be recalled that the Vesic method is the most conservative one for strip footings (see Section 5.2.1.3). It is, however, taken over by the Hansen method as the most conservative method for circular footings. The Hansen method also predicts a smooth transition from sliding to bearing failure, as it does for strip footings, whereas the other two methods predict an abrupt change. Furthermore, the transition for the Vesic or Meyerhof method is predicted to occur at V/V_0 levels significantly higher than that of Hansen's (1970) method.

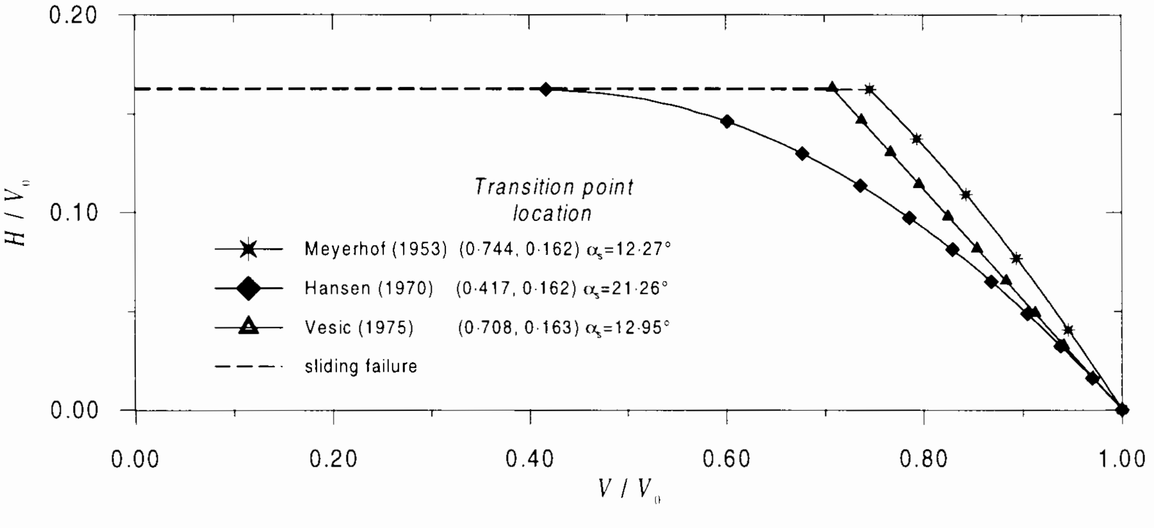

Figure 6.2: (V, H) interaction chart of a circular footing.

6.2.4 Interaction between vertical, horizontal load and moment

The same approach for strip footings (see Section 5.2.1.4) can be used to obtain the (V, H, M) failure envelope for circular footings:

Hansen (1970) (cf. Equ. 5.10):

$$\frac{V}{V_0} = \frac{1 + 0{\cdot}2B'/L' - 0{\cdot}5\left(1 - \sqrt{1 - H/A's_u}\right)\left(1 + 0{\cdot}4B'/L'\right)}{1.2}\frac{A'}{A}, \quad H \leq A's_u \tag{6.9}$$

where $V_0 = 1{\cdot}2(\pi + 2)As_u$, $A = \pi R^2$ and A', B' and L' depends on eccentricity via Equ. 6.4.

Vesic (1975) (cf. Equ. 5.11):

$$\frac{V}{V_0} = \left(1 - \frac{\frac{2+B'/L'}{1+B'/L'}H}{(\pi + 2)A's_u}\right)\left(\frac{\pi + 2 + B'/L'}{\pi + 3}\right)\frac{A'}{A}, \quad H \leq A's_u \tag{6.10}$$

where $V_0 = (1 + \frac{1}{\pi+2})(\pi + 2)As_u$.

By nominating V/V_0 values, Equ. 6.9 and Equ. 6.10 can be used to plot the contours of the envelope as shown in Fig. 6.3. The contours bear close resemblance to their counterparts for strip footings (see Fig. 5.5b and Fig. 5.6a). The Vesic contours are pointed at the transition from sliding and bearing failure, whereas the Hansen ones are smooth.

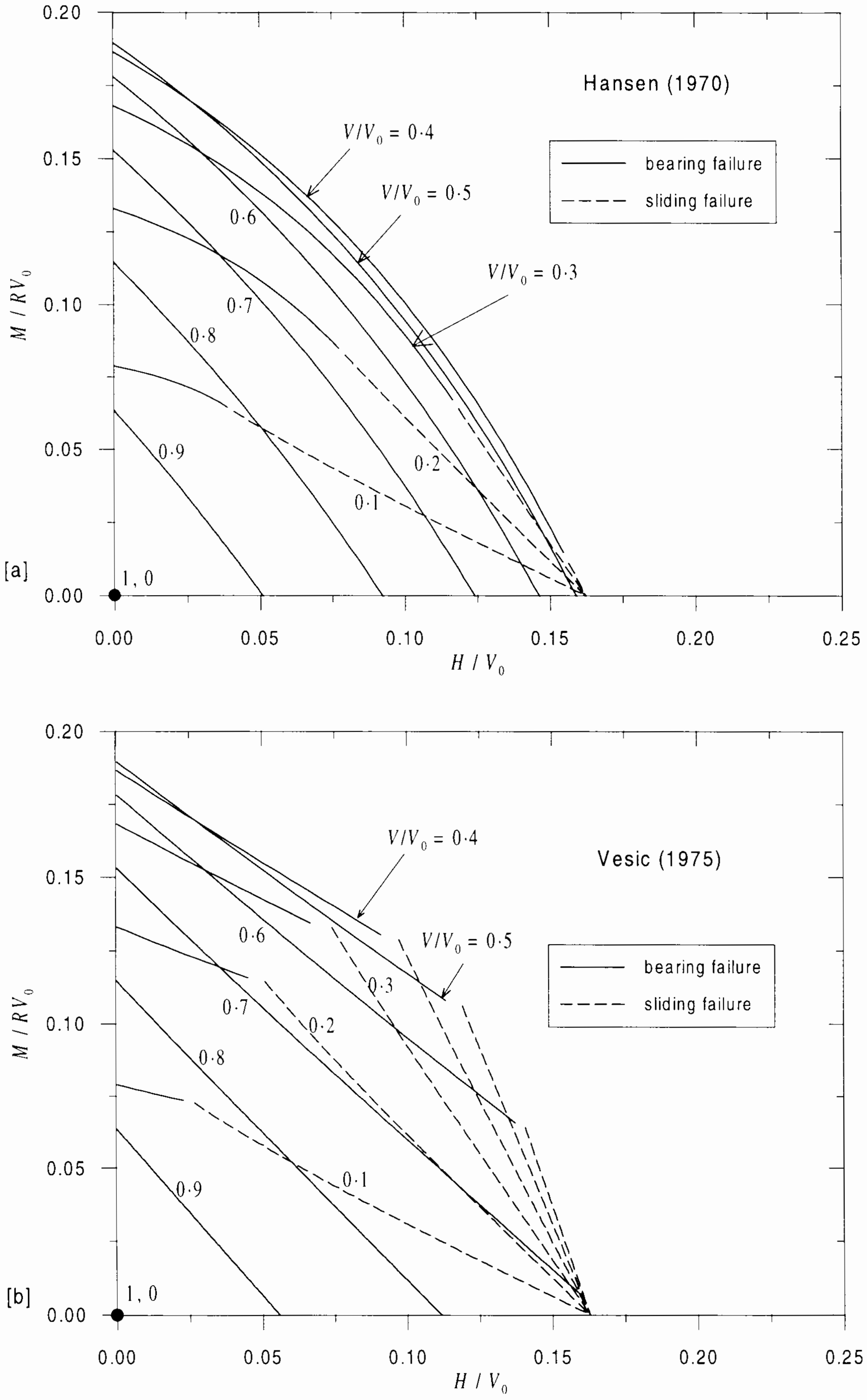

Figure 6.3: Failure envelope contours in $(H/V_0, M/BV_0)$ space: (a) Hansen's method; (b) Vesic's method.

6.2.5 Finite element research

A series of finite element analyses were conducted by Fugro Ltd as part of a Joint Industry Project coordinated by Noble Denton & Associates (1987). Using the harmonic loading method (rather the three dimensional finite element method), they investigated the interaction between the vertical, horizontal loads and moment. The (H, M) failure loci at $V/\pi R^2 s_u = 3{\cdot}6$ is shown in Fig. 6.4. It shows that sharper cone angle causes a larger increase in horizontal bearing capacity than in moment bearing capacity. There is a poor agreement between Hansen's (1970) prediction and the results of Noble Denton & Associates (1987). The latter results show no gradual change between horizontal and moment bearing capacity. Instead, they show that a small reduction of horizontal load from its peak value causes a sharp increase in moment bearing capacity, and vice versa. There may be some doubts about the accuracy of the Noble Denton & Associates (1987) results with respect to the adequacy of mesh refinement around the footing, and the fact that no attempt was made to model the partial loss of contact between the footing and the soil which occurs under large moment loads. Loss of contact can also occur for conical footings under large *horizontal* load. However, the two reasons can hardly explain for the rectangle-like shape of the (H, M) failure loci.

Further research into the problem of combined loading of circular footings on clay was performed by Bell (1991). Unlike Noble Denton & Associates (1987), Bell (1991) used the truly three dimensional finite element method. Bell (1991), however, investigated flat footings only. First of all, Bell (1991) used purely cohesive interface elements (without contact breaking) to model the interface under horizontal load. By comparing with analyses in which no interface elements were used, Bell (1991) showed that using continuum elements to model the soil-footing interface resulted in horizontal loads 35% in excess of the true amount.

However, even with these interface elements, the analyses already suffered from numerical instability. This led to a modification of the interface element material stiffness matrix $\mathbf{D}^{\mathrm{ep}}$ in order to reduce the effect of abrupt change in stiffness from elastic to plastic as follows:

$$\mathbf{D}^{\mathrm{ep}} = \mathbf{D}^{\mathrm{e}} + C\mathbf{D}^{\mathrm{p}} \tag{6.11}$$

where the parameter C can vary from 0 (for a purely elastic matrix) to 1 (for the standard elastic perfectly-plastic matrix). However, in Bell's (1991) analyses, a value of $C = 0{\cdot}99$

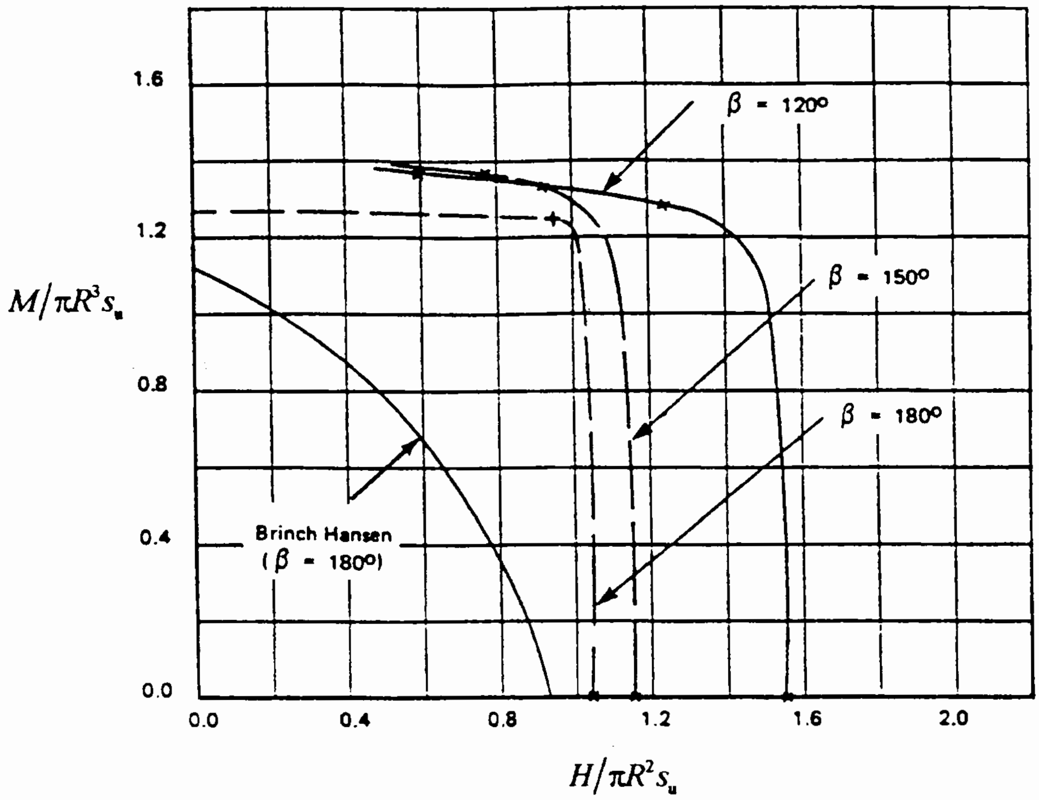

Figure 6.4: (H, M) failure loci at $V/\pi R^2 s_u = 3{\cdot}6$ $(V/V_0 = 0{\cdot}6)$ for various conical footings by Noble Denton & Associates (1987).

was used for the standard elastic perfectly-plastic matrix. This allowed a nominal 1% elastic stiffness of the interface to be retained under full plasticity conditions. This was believed by Bell to prevent the global stiffness matrix from becoming ill-conditioned, and proved to produce a stable solution for the case of purely horizontal displacement. These observations were then applied into debondable interface elements to model the footing under rotation. But difficulties were still encountered including numerical instability and a spurious stress distribution on the base of the footing.

Bell therefore resorted to using a footing rigidly connected to the soil without interface elements. To take into account the loss of footing contact, the footing loads are calculated only from the footing nodes where the vertical load is compressive.

Despite use of these assumptions, Bell's (1991) results show some interesting features of the bearing capacity envelope for circular footings on clay (see Fig. 6.5). The difference between positive and negative eccentric loads as described by Zaharescu (1961) is confirmed. Furthermore, the cross section of the envelope at each V/V_0 level bears the shape of an ellipse rotated about the origin. Also, the direction of the ellipse at different vertical loads changes

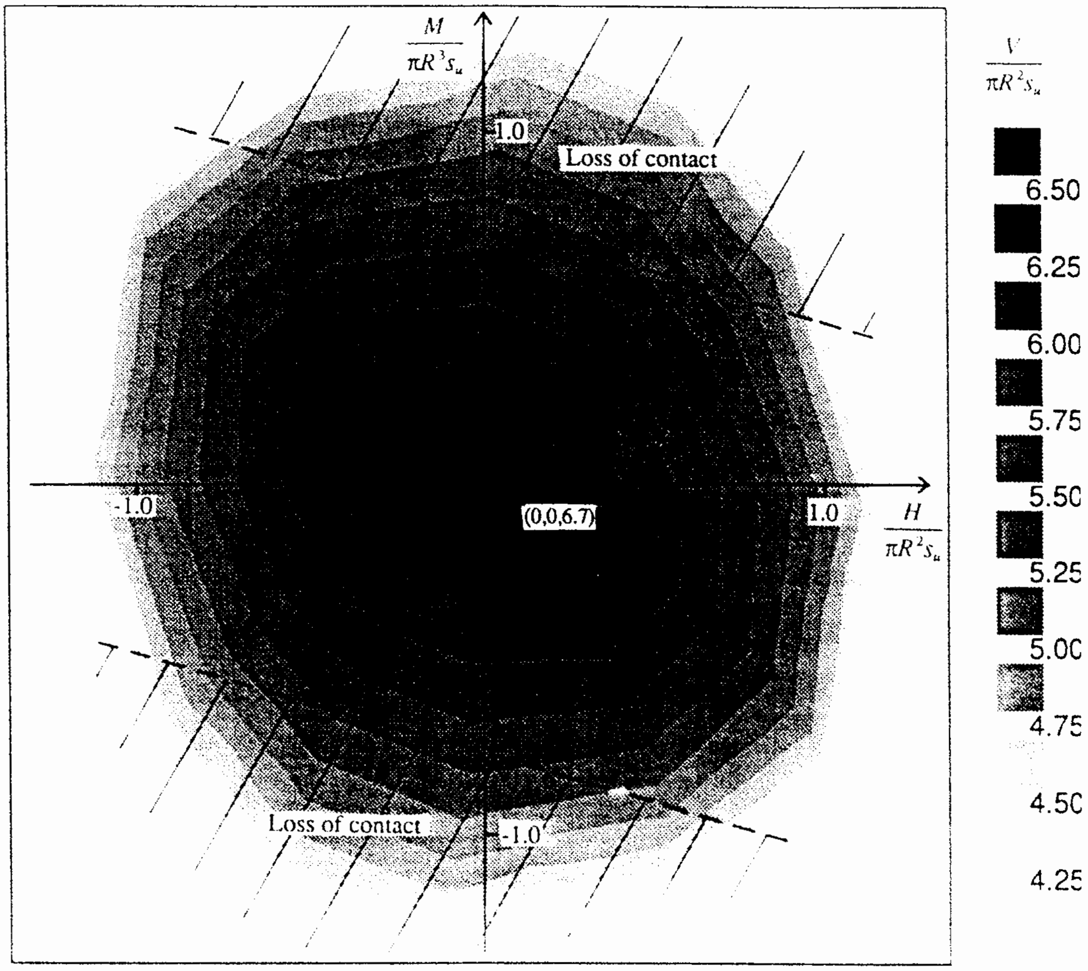

Figure 6.5: Bell's (1991) bearing capacity envelope for circular footings on clay, determined by the finite element method.

with vertical load level at lower V/V_0 levels, where the contours takes on a more circular shape. As the vertical load gets lower ($V/As_u < 5$), the contours even seem to rotate such that the major axis lies in the first and third quadrants.

Compared to both of the methods mentioned above, the Hansen (1970) is more conservative. However, Bell's (1991) results are in better agreement with Hansen's than those of Noble Denton & Associates (1987).

Note that with the development of the interface element as presented in Chapter 4, the difficulties encountered in Bell's (1991) analyses are eliminated. This study is shown in the following sections.

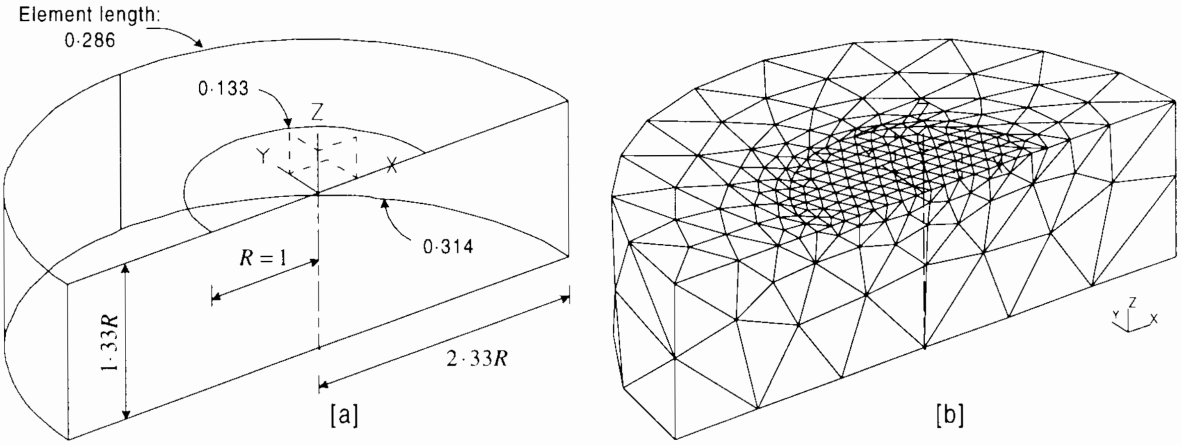

Figure 6.6: Ten-noded mesh: 2744 nodes and 1645 elements.

6.3 Mesh Characteristics

6.3.1 Material properties

The soil used in this study has the same properties as the soil used in previous study for strip footings (see Section 5.3.2).

6.3.2 Mesh topology

The meshes are generated using a commercial package called `I-DEAS` which can generate solid meshes using free meshing. The mesh grading is controlled by specifying the number of elements along the edges of the solid model (the rim of the footing, the boundary edge). In order to compare the performance of 10-noded tetrahedral elements and 20-noded tetrahedral elements, two meshes are generated: one for 10-noded tetrahedral elements and the other one for 20-noded tetrahedral elements. The mesh grading control for both meshes are given in Fig. 6.6a and Fig. 6.7a.

As discussed in the previous chapter (Section 5.3.1), Bell (1991), having performed a series of runs for strip footings using OXFEM, concludes that a mesh which has a radial dimension of $2{\cdot}33R$ and a depth of $1{\cdot}33R$, where R is the footing radius, is adequate. Bell (1991) thus adopts it for his three dimensional calculations. Therefore the meshes used in this study also have the same size.

Note that because of free meshing, both generated meshes which are shown in Fig. 6.6b

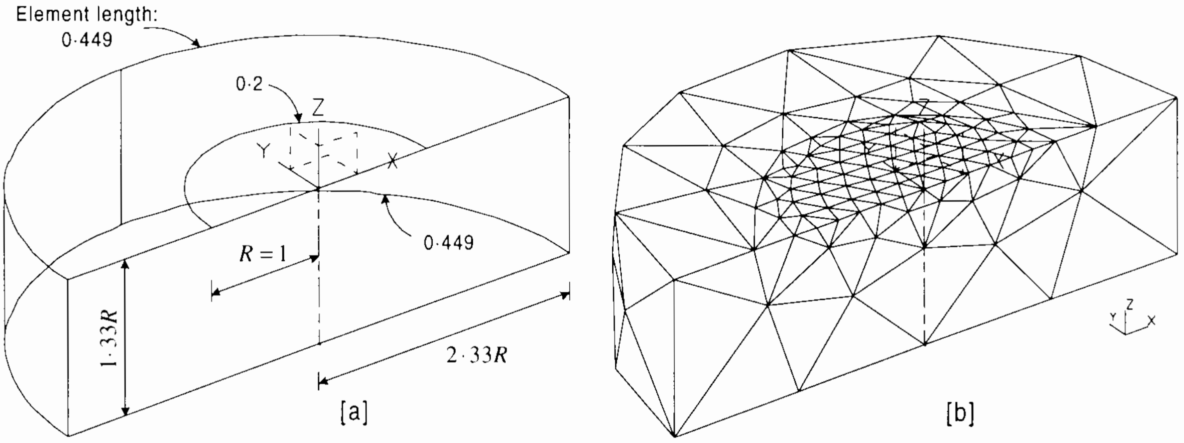

Figure 6.7: Twenty-noded mesh: 1105 nodes and 612 elements.

and Fig. 6.7b are not exactly axi-symmetrical. This results in a small force in the x direction when only vertical displacement is applied. Axi-symmetry of the mesh can be achieved by using axi-symmetrical meshing as used by Bell (1991). Bell generates three dimensional meshes by first generating a two dimensional mesh and then rotating the plane about the axis. The mesh is then divided into tetrahedra to form the final mesh. There are, however, drawbacks for this method of meshing. Firstly, because faces of elements are rotated about the axis, nodes along the axis belong to many elements. This results in increase of the front width and, hence, the execution time, which is an important consideration for three dimensional analyses. The other drawback is that this method of meshing produces long thin elements, particularly around the axis at the bottom of the mesh, where the elements have long sides in the radial and vertical directions but short sides in the circumferential direction (because it is close the centre of rotation). Due to these drawbacks the free meshing method is chosen over the axi-symmetrical meshing method.

For both of the meshes, all the nodes in the $y = 0$ plane are constrained in the y direction. Those nodes which are on the radial and bottom boundaries are constrained in all three x, y and z directions.

The two meshes give results (Fig. 6.8) in close agreement with Bell's (1991) results: Bell (1991) obtained $V/As_u = 6{\cdot}85$ (compared to $V/As_u = 6{\cdot}86$ of this study) using a 20-noded mesh and 7·51 (compared to 7·53 of this study) using a 10-noded mesh. Both meshes give results higher than that obtained by Bell (1991) using 15-noded triangular finite elements in an axi-symmetric analysis. The 10-noded tetrahedral mesh gives a result which is +13% whereas the 20-noded tetrahedral one overestimate by only +3%.

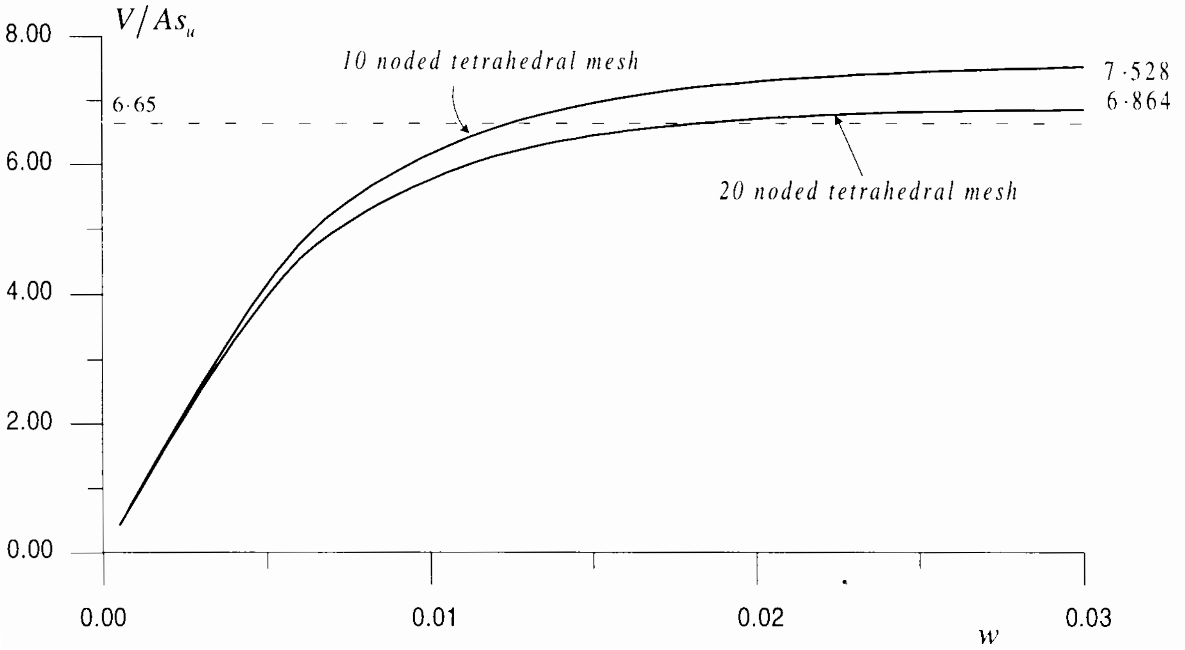

Figure 6.8: Performance of 10-noded and 20-noded tetrahedral meshes (without interface elements).

Unfortunately, the twenty-noded tetrahedral mesh takes significantly longer (more than twice as long) to run than the ten-noded tetrahedral mesh. For analyses in three dimensions this means for an average load regime, the twenty-noded mesh takes two to four days longer on the machines available to the author. The 10-noded mesh is thus chosen for all analyses which are presented in this chapter. In an attempt to improve the performance of the 10-noded mesh, a larger mesh of $2 \times 3R$ was tried. However, the larger mesh was not found to give a better result than the original mesh of $1{\cdot}33 \times 2{\cdot}33R$, confirming that the mesh size chosen is adequate.

Interface elements are then introduced into the mesh. The same vertical loading analysis now gives a vertical bearing capacity of $V_0/As_u = 7{\cdot}044$, which makes the 10-noded mesh more acceptable for the analyses.

The normal stress distribution on the footing-soil surface is investigated by comparing different integration schemes in the interface such as 6, 12 and 16 point Gauss integration and 7-point Newton-Cotes. Under vertical loading, the difference between the integration schemes are very small. Nonetheless, the stress distribution of 7 points Newton-Cotes, shown in Fig. 6.9, is better. In general, normal stress is evenly distributed in a large part (about 70% of the area) of the footing. In the region close to the edge of the footing the normal stress

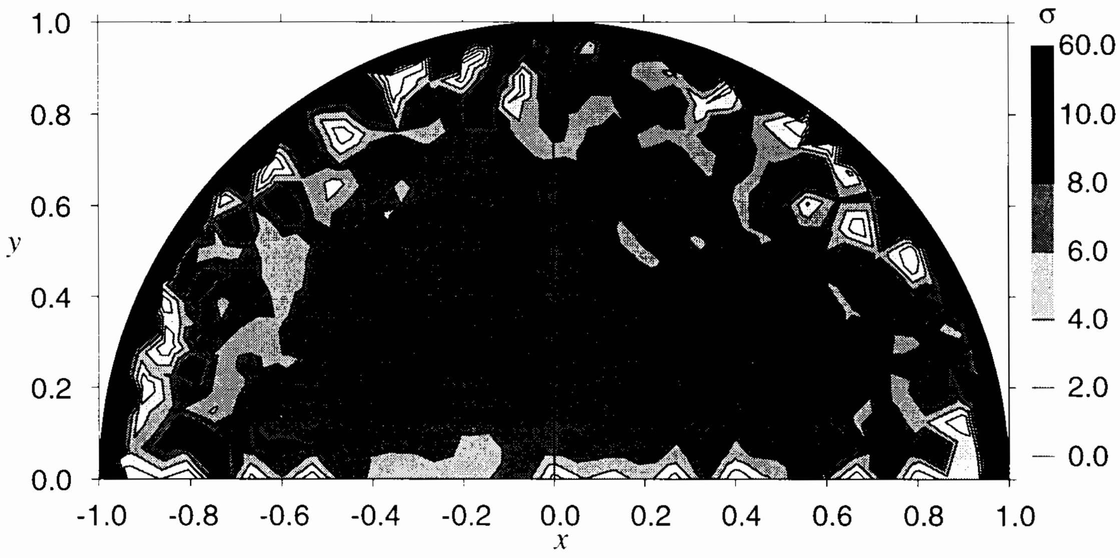

Figure 6.9: Distribution of normal stress using 7-point Newton-Cotes integration for the interface.

increases, and can reach $\sigma = 42$ in value. At the same time, in the vicinity of these high stress areas, stress falls belows the average stress. One explanation of the fall in stress is that it happens in order to maintain the average normal stress level. A much finer mesh may be able to reduce the stress concentration. However, such a solution is computationally expensive, and the stress fluctuation does not seem to affect the overall performance.

The yield status of the integration points of the interface elements in the footing is also examined. The result is shown in Fig. 6.10. The plot shows that almost all the integration points are behaving elastically or yielding with the cohesive part of the yield surface (cohesion in the interface is fully mobilised). It is therefore concluded that the numerical result obtained by the finite element method here should be comparable to that of the exact solution for an absolutely rough footing.

6.3.3 Control of footing displacement rates

In the implementation of OXFEM an incremental approach (Sloan, 1981) is used to solve the problem of non-linear materials. In such a process the rate of displacement application (displacement increment per iteration) can affect the accuracy of the solution. Also, due to the use of interface elements, applying a fast displacement on the footing could lead to severe numerical instability. Furthermore, in a finite element analysis like this, the nodal results are

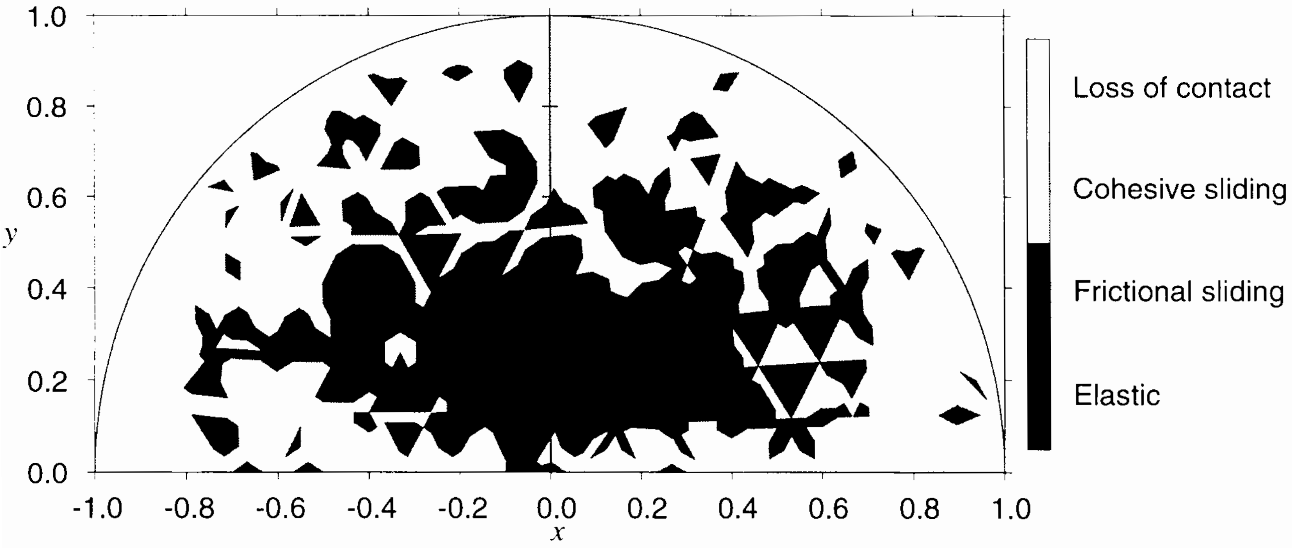

Figure 6.10: Yield status of the integration points of interface elements in the footing.

output after every increment. A fast displacement would not give a load–displacement plot in sufficient detail to define the shape of the bearing capacity envelope. On the other hand, applying load or displacement in too many small increments entails long execution time. Therefore it is desirable to determine, possibly empirically, reasonable displacement rates for the footing.

From the elastic stiffness coefficients determined in Chapter 2, an elastic load, for example moment load, can be calculated as follows:

$$M = K_3 \theta R^3 G \tag{6.12}$$

Therefore the displacement corresponding to the size of the envelope in the M direction is:

$$\theta_0 = \frac{M_0}{G R^3 K_3} \tag{6.13}$$

if the behaviour of the footing is elastic. With $K_3 = 5{\cdot}5627$ (Chapter 2), and $M_0 = 0{\cdot}19 R V_0 = 1{\cdot}33$, we have:

$$\theta_0 = 2{\cdot}386 \times 10^{-3} \approx 0{\cdot}002 \tag{6.14}$$

Analogously, with $K_2 = 5{\cdot}5541$ and $H_0 = A s_u = 3{\cdot}6276$, the horizontal displacement corresponding to the size of the envelope in H direction is:

$$u_0/R = 6{\cdot}455 \times 10^{-3} \approx 0{\cdot}007 \tag{6.15}$$

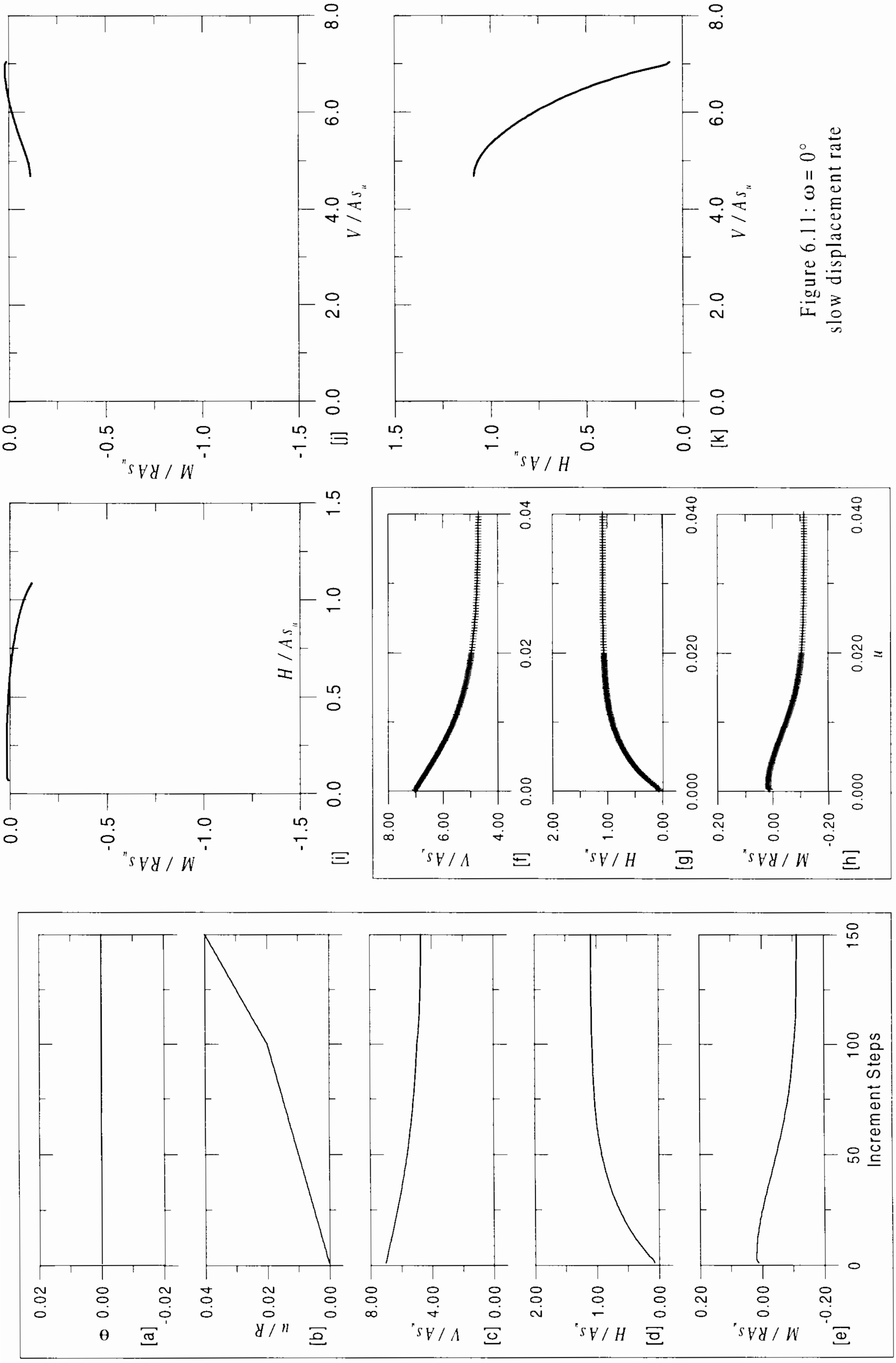

Figure 6.11: ω = 0°
slow displacement rate

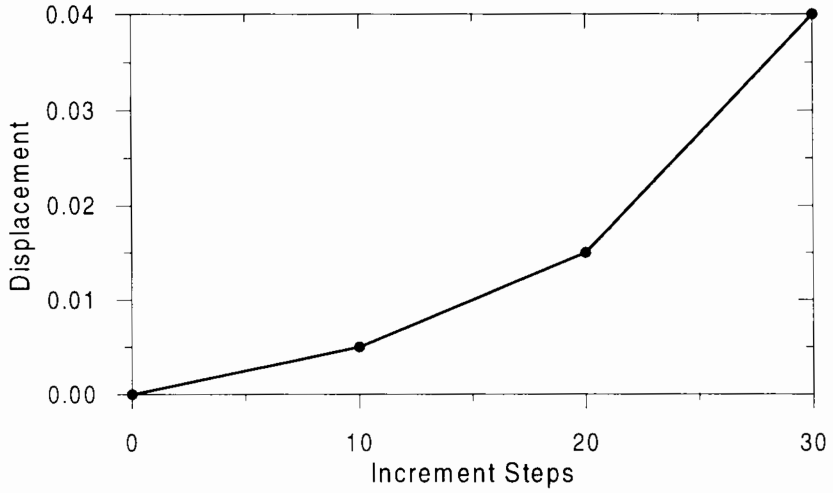

Figure 6.12: Variation of displacement rate.

Using this result, a tracking test involving only horizontal displacement was performed as a trial analysis. The footing is first loaded until it reaches the vertical bearing capacity, then displaced horizontally at the rate of $\dot{u}/R = 2 \times 10^{-4} = u_0/10R$. When the displacement reaches $u/R = 0{\cdot}02$ (e.g. after 100 increments), the displacement rate is doubled to $\dot{u}/R = 4 \times 10^{-4}$, until the total displacement reaches $u/R = 0{\cdot}04 \approx 6u_0/R$.

Fig. 6.11 shows a detailed picture of the footing behaviour during the test. The first block, Fig. 6.11a to e, shows the variation of footing displacements and footing loads with increment number. The load–displacement curves are shown in the second block (f, g and h), with data markers for each increment. The third block (i, j and k), shows the process in the load space (V, H, M).

Though the resulting load paths are all satisfactory, the execution time was too long; on Sun Sparc 10, the whole analysis with 150 increments takes more than 110 hours. Densely distributed data markers in the plots Fig. 6.11f, g and h suggest that the displacement rate can be increased.

In addition, several trial tests showed that the rate of displacement can be varied during the course of the analyses. When the displacement is first applied, the load changes very rapidly with displacement; thus the displacement needs to be applied in smaller steps. Smaller steps also help maintain good stability for the interface element when the direction of displacement is changed from vertical movement to horizontal movement or rotation. After that, when the load change with respect to displacement is smaller, the displacement can be applied at a higher rate.

Based on this observation, the displacement rates used are varied in a manner shown in Fig. 6.12. The total displacement is applied in three stages, each has the same number of increments but the displacement magnitude gets larger with the stages. The displacement rate during the first load stage is $\dot{u}/R = 5 \times 10^{-4}$, which is more than twice as fast as the previous test. This rate is increased two-fold in the second stage to $\dot{u}/R = 1 \times 10^{-3}$, which in turn is increased by a factor of 2·5 in the third stage. This results in a test procedure which is five times as fast as the previous one. As shown in Fig. 6.13, the analysis using the new displacement rates gives results comparable with the previous one (cf. Fig. 6.11).

The fast displacement rate also gives satisfactory results for tests involving footing rotation. Fig. 6.14 shows in detail the behaviour of the footing during a test involving only rotation. The resulting load path is smooth except at the first increment where there is one isolated oscillation – again, in the H direction.

Fig. 6.14 reveals that a total displacement of $\theta = 0{\cdot}04$ is not sufficient for the load to reach its steady state (e.g. when an increase in displacement does not cause change in load) even though for purely horizontal loading, a total displacement of $u/R = 0{\cdot}03$ is sufficient (see Fig. 6.13). The displacement applied in the third loading stage is therefore increased so that the total displacement is 0·055. This value is used for all the analyses which are presented in the following section.

6.4 Programme of analyses

Fig. 6.15 shows six different combinations of horizontal and rotation displacement used to investigate the failure envelope. In all tests, the horizontal displacement is positive (i.e. sliding to the right) and both positive and negative eccentricity are investigated.

6.4.1 Analyses commencing from high V/V_0 level

The results of analyses commencing from high V/V_0 are presented in Fig. 6.16. The results show that a pure horizontal displacement results in small moment, and a pure rotation without horizontal displacement causes small horizontal load. The analogy for combined horizontal and moment loading also holds: if an analysis involves a combined displacement specified by an angle ω in $(u/R,\ \theta)$ space, its resulting load path also lies in the $(H,\ M)$

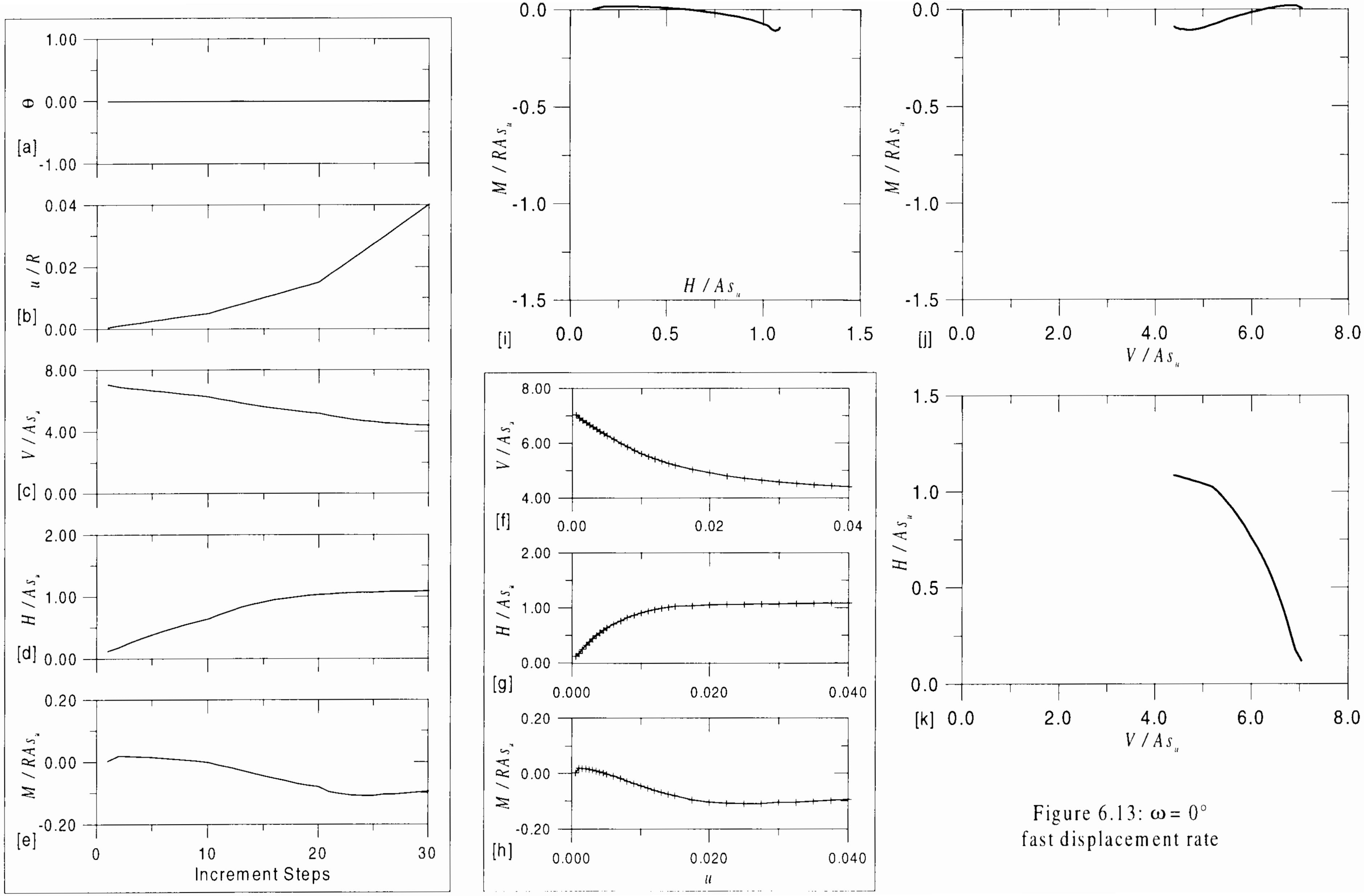

Figure 6.13: ω = 0°
fast displacement rate

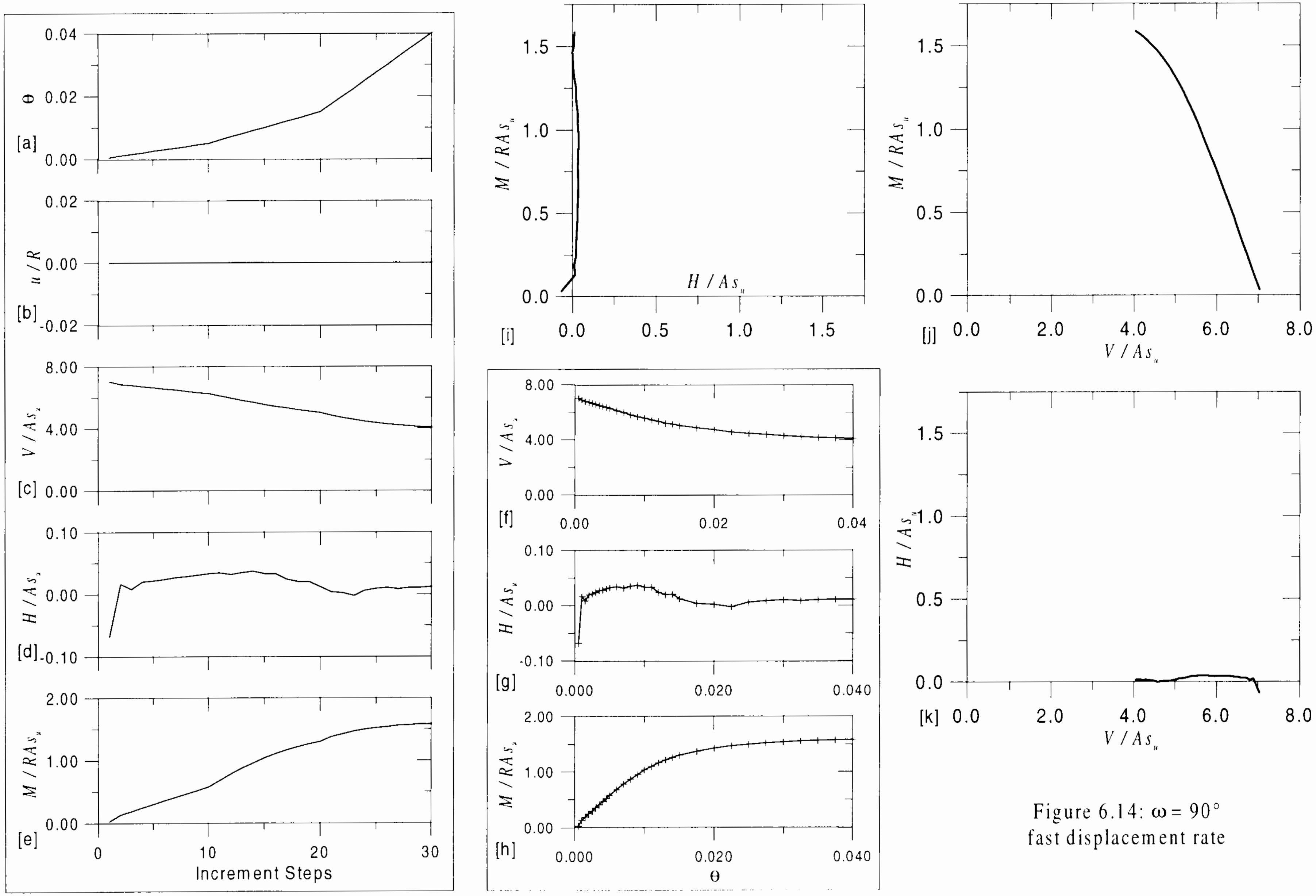

Figure 6.14: ω = 90°
fast displacement rate

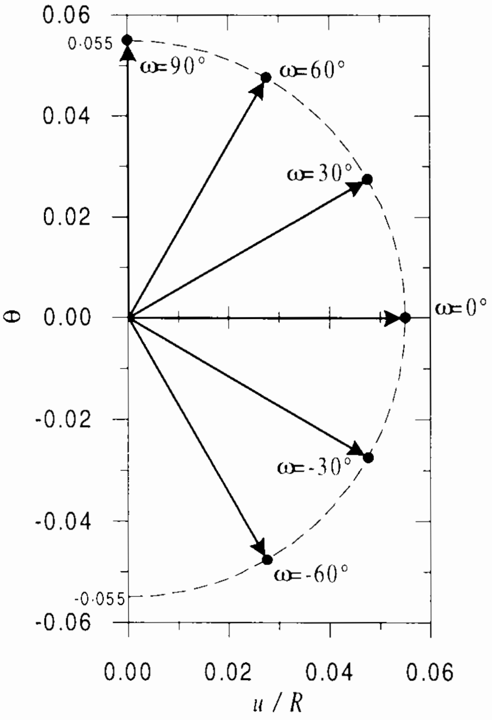

Figure 6.15: Programme of tests: combined displacements.

space at an angle Ω which is close to ω. Therefore with different displacements directed at equally spaced angles ω as shown in Fig. 6.15, a good coverage of the bearing capacity envelope in the $(H/As_u,\ M/ARs_u)$ space is achieved. Nevertheless, the resulting load paths in $(H/As_u,\ M/ARs_u)$ space are not straight lines: the load paths gradually diverge from their original direction Ω. This happens when horizontal load stops increasing with the reduction of vertical load, whereas moment increases almost linearly throughout the reduction of vertical load (except for $\omega = 0°$). The change in the direction of load paths in $(H/As_u,\ M/ARs_u)$ space is also seen with strip footings (see Fig. 5.19).

In all the analyses displacements are applied until the load reaches a steady state, but the vertical load does not decrease beyond $V/As_u \approx V_0/2 \approx 3{\cdot}5$. In fact only two of the analyses $\omega = 30°$ and $\omega = 60°$ reach this vertical load.

6.4.2 Analyses commencing from low V/V_0 level

The load paths of the analyses commencing from low V/V_0, shown in Fig. 6.17, in general are not so smooth as those of the analyses commencing from high V/V_0, though the overall stability (determined by small unbalanced forces after each increment) is maintained.

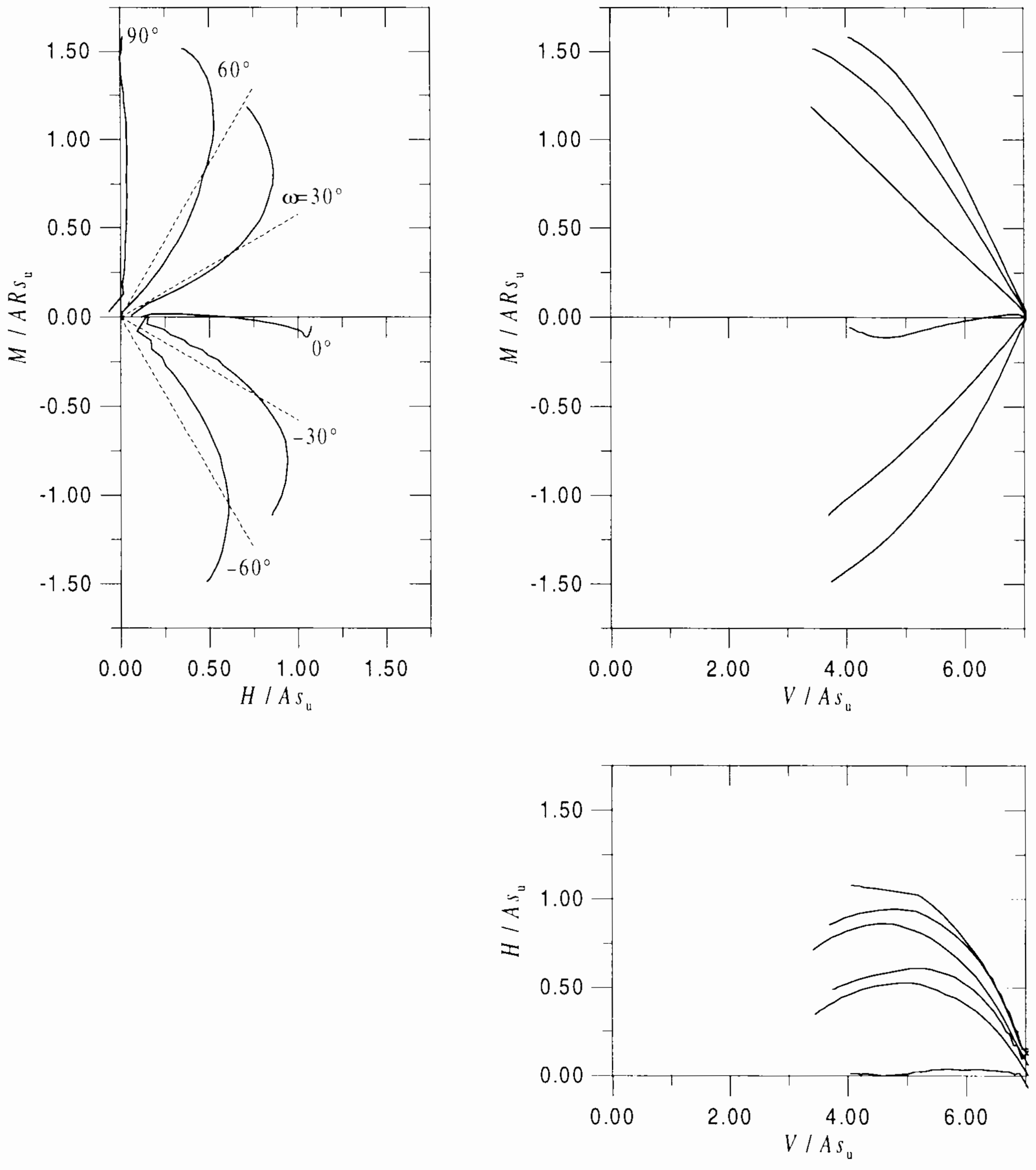

Figure 6.16: (V, H, M) curves from high V/V_0.

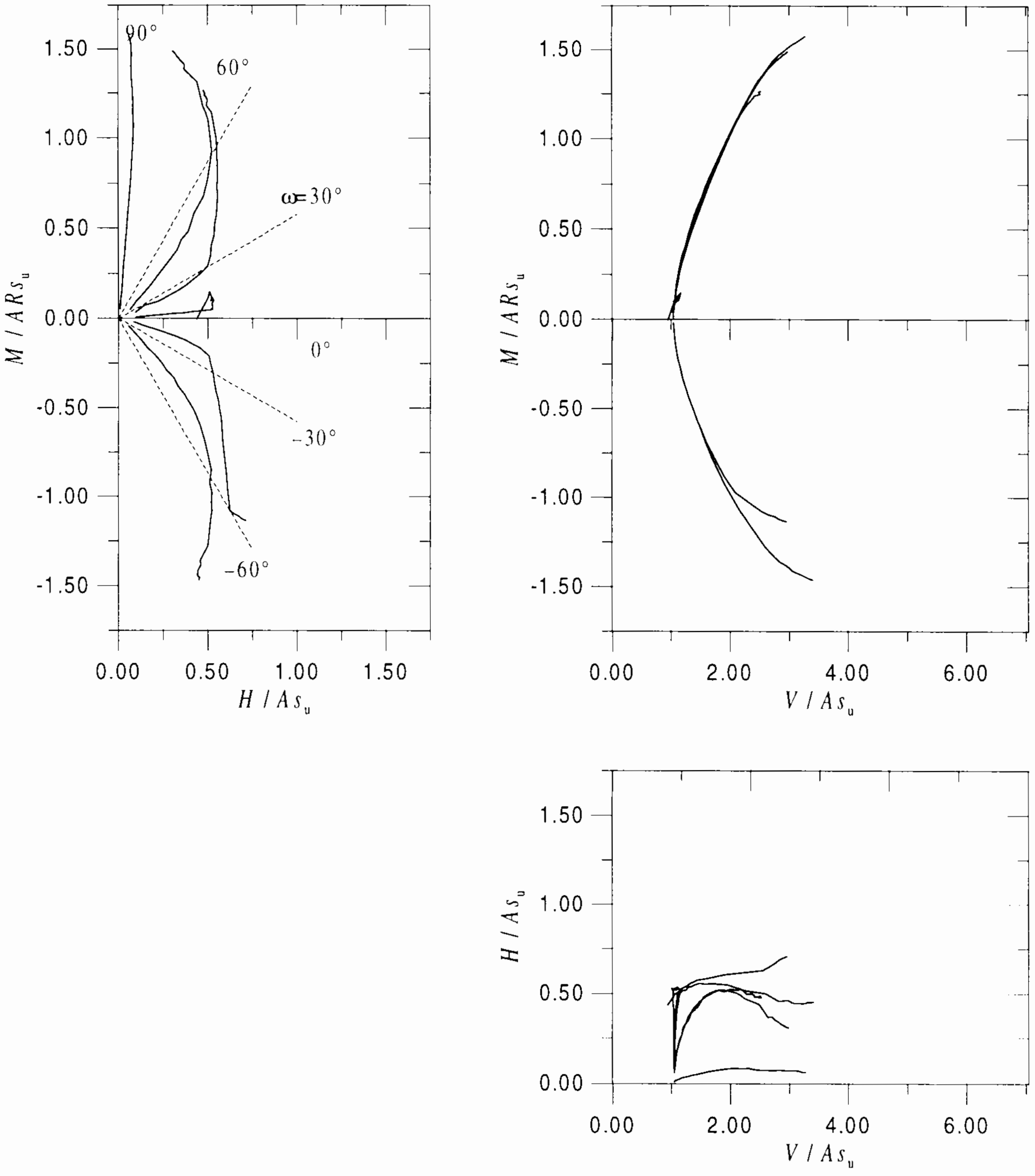

Figure 6.17: (V, H, M) curves from low V/V_0.

The load paths also bear a close resemblance to those of strip footings (see Fig. 5.20). The relation between vertical load and moment is almost the same for all analyses as shown in the $(V/As_u,\ M/ARs_u)$ in Fig. 6.17, regardless of their different behaviour in terms of horizontal load. Except for the pure rotation test ($\omega = 90°$), initially the horizontal load increases sharply with smaller change in vertical and moment load. The horizontal load, however, stops at about 0·6, indicating that frictional sliding failure is occurring because the ultimate horizontal load at $V/As_u \approx 1$ is $H/As_u = (V/As_u)\tan 30° \approx 0{\cdot}577$.

Another feature of the results is the load paths for negative and positive eccentricity ($\omega = 30°$ and $\omega = -30°$, $\omega = 60°$ and $\omega = -60°$) are almost symmetrical in the $(H/As_u,\ M/ARs_u)$ plot.

The two figures also show that not all analyses give a load path reaching $V/V_0 = 0{\cdot}5$. For the analyses commencing from high V/V_0, only two analyses with $\omega = 30°$ and $\omega = 60°$ reach just over $V/V_0 = 0{\cdot}45$. Similarly, for those commencing from low V/V_0, only two ($\omega = 90°$ and $\omega = -60°$) reach $V/V_0 = 0{\cdot}5$. This means that there are fewer points to define the shape of the envelope near $V/V_0 = 0{\cdot}5$. However, the cross-sectional shape and size of the envelope at $V/V_0 = 0{\cdot}5$ does not vary much from the adjacent V/V_0 levels. At that V/V_0 level, the footing is in cohesive sliding mode, and therefore the size of the envelope in the H direction remains constant at $H = \frac{2}{\sqrt{3}}As_u$. Similarly, in the M direction, as observed for a strip footing (see Fig. 5.15), moment also almost reaches its peak when the footing hits its 'critical state' even though the load path does not reach $V/V_0 = 0{\cdot}5$.

Nonetheless, for $\omega = 0°$ (pure horizontal displacement), the load path does not advance toward higher vertical load at all. Because the interface is non-dilatant, when the displacement is applied, the horizontal load increases sharply, while the moment and vertical load remains almost unchanged. The horizontal load stops increasing at about $H/As_u = 0{\cdot}6$, which is also the limit of horizontal load due to frictional sliding at $V/As_u = 1{\cdot}0$: $H/As_u = (V/As_u)\tan\phi$, where $\phi = 30°$ is the angle of friction of the interface between the footing and the soil. Thus there are no data points to define the envelope in the $M/RAs_u = 0$ plane at low V/V_0. However, this can be overcome by including the load that can be calculated directly from the frictional behaviour of the footing $H = V\tan\phi$. Two load points are therefore added: one at $V/As_u = 0$ and the other at $V/As_u = 2$, which is the transition point between frictional and cohesive sliding.

6.4.3 Stress distribution on the footing

Even though the (V, H, M) load paths in Fig. 6.16 and Fig. 6.17 are fairly smooth and all the analyses are stable, there is some concern about how the interface element behaves for different cases of loading, particularly because both horizontal and rotational displacement involved are large. One way of checking the behaviour of the interface is to examine the normal stress distribution on the footing, from which the area of loss contact between the footing and the soil can also be investigated. The distribution of normal stress is shown in Fig. 6.18 and Fig. 6.19 for the analyses starting from high V/V_0 level and from low V/V_0 level, respectively. For each of them, three cases of loading are shown: one for pure (positive) rotation ($\omega = 90°$), one for pure sliding ($\omega = 0°$) and one for combined loadings involving negative rotation $\omega = -60°$.

For both analyses started from high and low V/V_0, it is clear from Fig. 6.18 and Fig. 6.19 that for loading involving rotation, the footing exhibits a clear division between the areas at which the footing is and is not in contact with the soil.

For the analyses commencing from high V/V_0 involving pure horizontal displacement as shown in Fig. 6.18b, the stress distribution is also good. The stress distribution does not fluctuate, except at the rim of the footing, nor does loss of contact happen. Fig. 6.19b, however, shows that the stress distribution under low V/V_0 does not behave so well. Low vertical load ($V/V_0 = 1/7{\cdot}0436$), and hence low normal stress, makes it easier for the interface to debond. Fig. 6.20 shows the stress distribution after the footing has been vertically unloaded (after it was loaded to vertical bearing capacity). It is surprising that during vertical unloading the rim of the footing changes from high stress concentration area to a low stress area. This helps to explain why it is the rim which separates with the soil in Fig. 6.19b when horizontal load is applied.

It is interesting to note that although the stress contours show on occasions quite severe local stress fluctuation, the overall response (e.g. the vertical bearing capacity, the maximum horizontal bearing capacity) seems to compare well with other solutions when they are available.

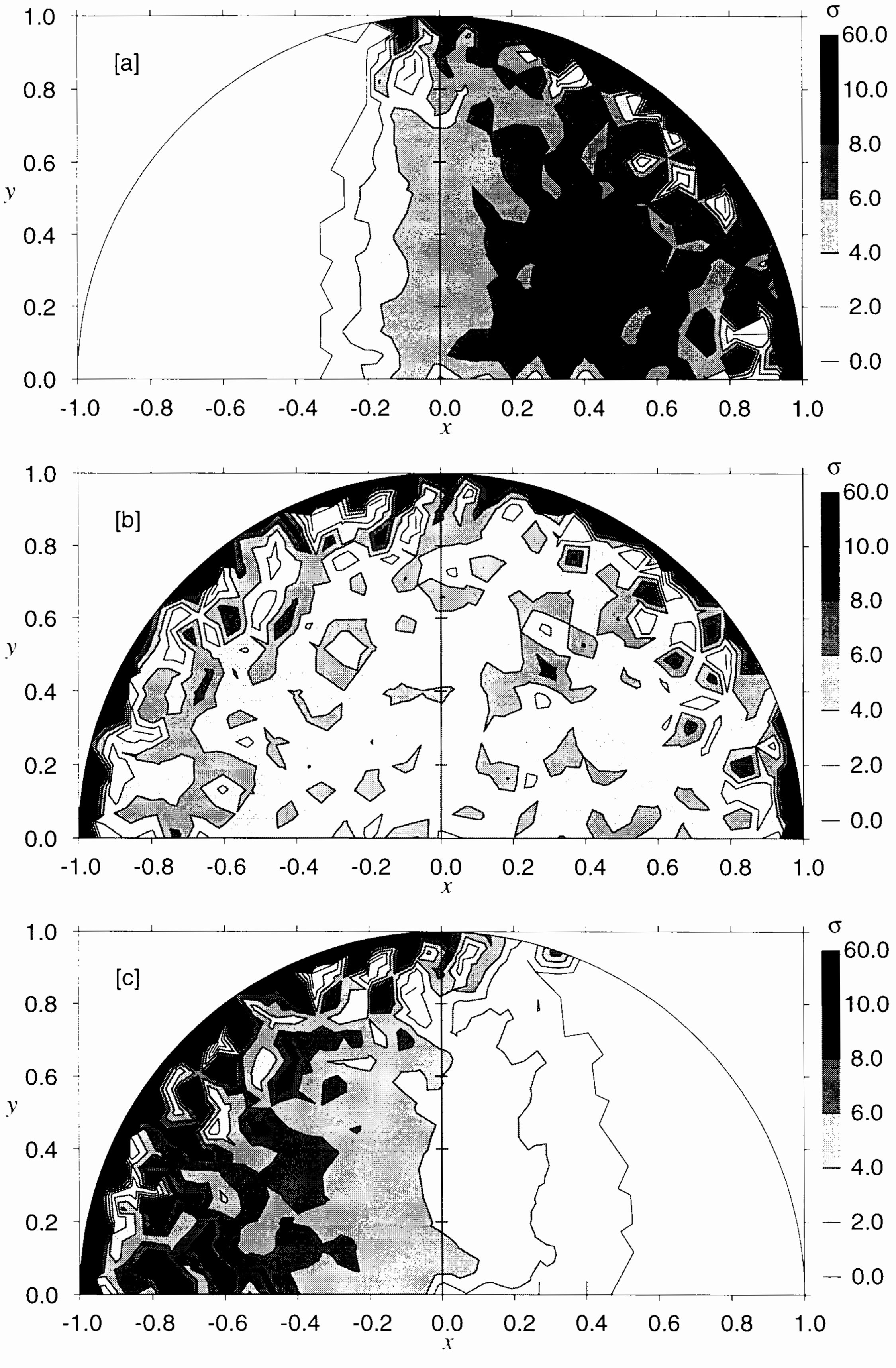

Figure 6.18: Distribution of normal stress (analyses from high (a) Pure rotation ω = 90°; (b) Pure horizontal sliding ω = 0°; (c) Combined rotation and horizontal displacement ω = −60° (negative rotation).

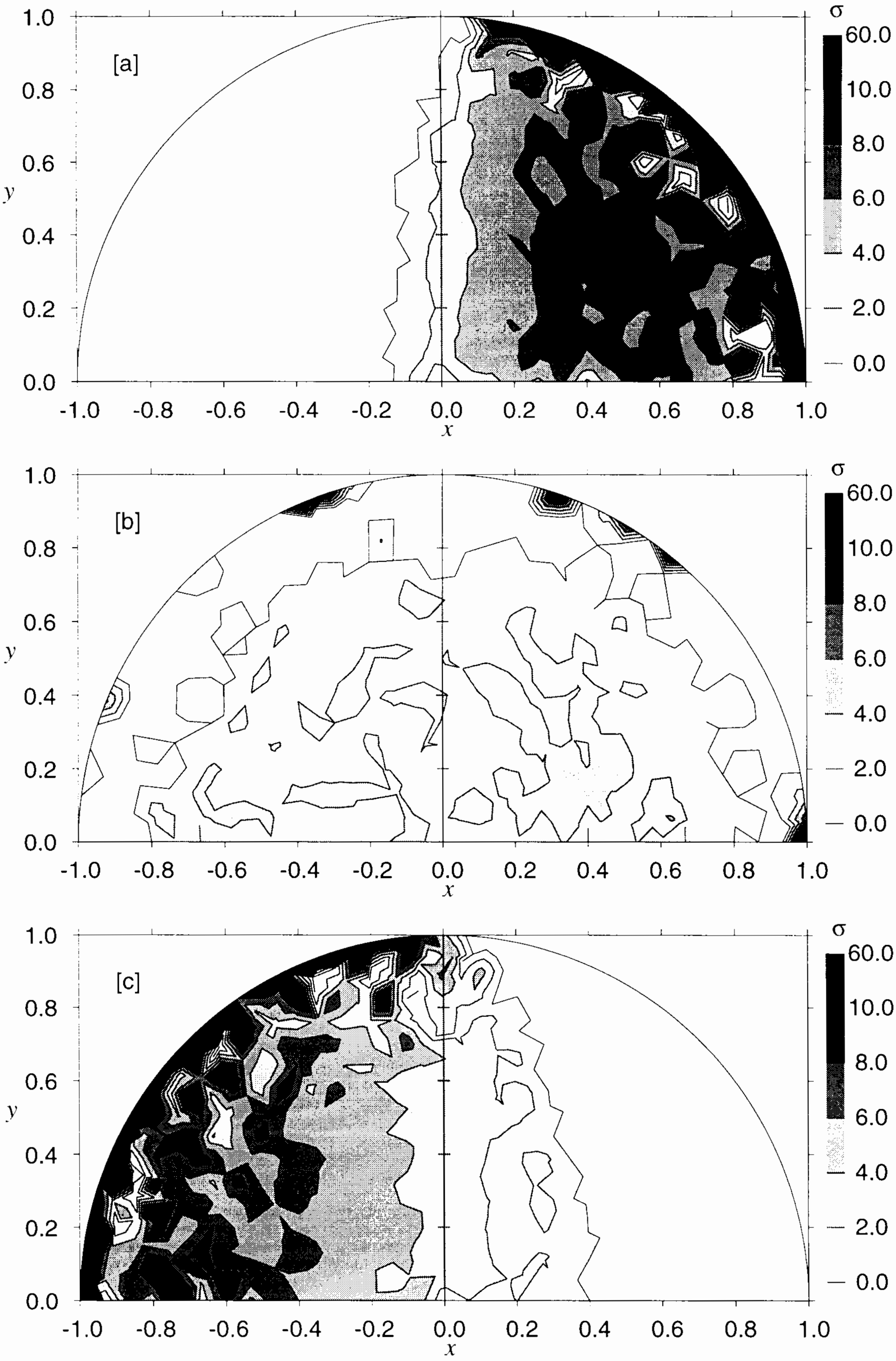

Figure 6.19: Distribution of normal stress (analyses from low (a) Pure rotation ω = 90°; (b) Pure horizontal sliding ω = 0°; (c) Combined rotation and horizontal displacement ω = −60° (negative rotation).

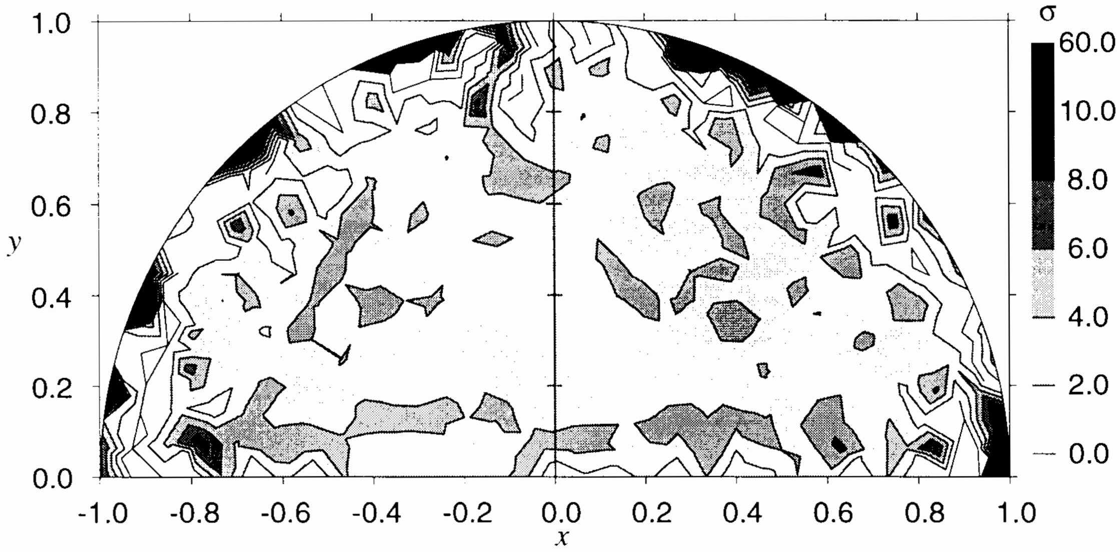

Figure 6.20: Distribution of normal stress after the footing is unloaded to $V/V_0 = 0{\cdot}14$.

6.5 Bearing capacity envelope

The bearing capacity envelope is presented in two different forms. In the first form, the data is filtered using the convex hull filter as described in Section 5.2.1.6, before contours with respect to V/V_0 are made. In the second form, the data (without being filtered) are used to determine some algebraic formula that can best describe the data.

6.5.1 Contours of data

In general, at each level of V/V_0, $2N = 12$ load points (including reflected points due to symmetry) are obtained because there are 6 analyses commencing from either low or high V/V_0. However, at $V/V_0 = 0{\cdot}5$ there are only $2N = 4$ points, because, as mentioned earlier, only two analyses yield load paths that advance beyond $V/V_0 = 0{\cdot}5$. Also, for analyses commencing from low V/V_0 the number of points is $2N = 10$ due to the results of the analysis of $\omega = 0°$. This number drops to $2N = 8$ at $V/V_0 = 0{\cdot}4$ because one analysis ($\omega = 60°$) reaches critical state before $V/V_0 = 0{\cdot}4$.

In order to contour the envelope, all the load data, including those from the analytical solution for frictional sliding, are first filtered using the convexity characteristics of the envelope. Fig. 6.21 shows the load points that are retained after the filtration. It is pleasing to see that most of the data obtained from the analyses, particularly the analyses commencing from high V/V_0, lie on a convex surface and are thus retained after filtration. Whereas the envelope is well defined by data at $V/V_0 = 0{\cdot}9, 0{\cdot}8, 0{\cdot}7$, and, to a lesser extent, at $V/V_0 = 0{\cdot}6$ and $0{\cdot}2$, there is insufficient data to define the envelope well at $V/V_0 = 0{\cdot}5$. As discussed earlier, the section at $V/V_0 = 0{\cdot}5$ can be adequately interpolated from the adjacent V/V_0 levels $0{\cdot}40$ with $2N = 8$ and $0{\cdot}55$ with $2N = 8$.

The filtered data is then used to calculate the V/V_0 contours of the envelope in the $(H/V_0,\ M/RV_0)$ space. The contours are shown in Fig. 6.22. Unlike the bearing capacity envelope of strip footings, the envelope of circular footings in Fig. 6.22b shows a significant effect of the sense of eccentricity on bearing capacity at high V/V_0. The elliptic contours at various V/V_0 levels have their major axes lying in the second and fourth quadrants. Therefore at each level, the maximum horizontal load and moment take place when the eccentricity is negative.

However, the rotation of the ellipses, or the effect of the sense of eccentricity, changes at smaller vertical load. At high V/V_0 (say $V/V_0 = 0{\cdot}9$ in Fig. 6.22b), the ellipse is clearly a rotated one with its major axes lying in the second and fourth quadrants. With lower V/V_0 the ellipse turns into a more upright one indicating a smaller effect of the sense of eccentricity on the bearing capacity of the footing. For $V/V_0 \leq 0{\cdot}5$, the effect of load eccentricity seems to diminish with a group of contours of $V/V_0 \leq 0{\cdot}4$ being symmetrical with respect to the coordinate axes as shown in Fig. 6.22a.

Another significant feature of the envelope at low V/V_0 is that at each V/V_0 level, the footing can sustain the same maximum moment together with a wide range of horizontal load. At $V/V_0 = 0{\cdot}2$ for example, the footing can sustain a horizontal load up to $H/V_0 = 0{\cdot}076$, which is about 66% of the maximum horizontal capacity at this vertical load level, without reducing its moment bearing capacity. This feature is also seen for strip footings (cf. Fig. 5.22) but for strip footings, the moment bearing capacity starts to decrease sooner with the increase of horizontal load. Note that at $V/V_0 = 0{\cdot}2$, the plot of data points retained after the convex hull filtration (Fig. 6.21) shows that only four points are retained. Though this is a direct reason for the contour of this vertical load to be flat at the maximum moment (at the top and bottom of the contour), there is evidence that the contour is not distorted due to lack of data at this vertical load. Fig. 6.23 shows that the raw data which are not excluded from convex hull filtration at this level also form a similar shape, notably the two edges parallel to the H/V_0 axis.

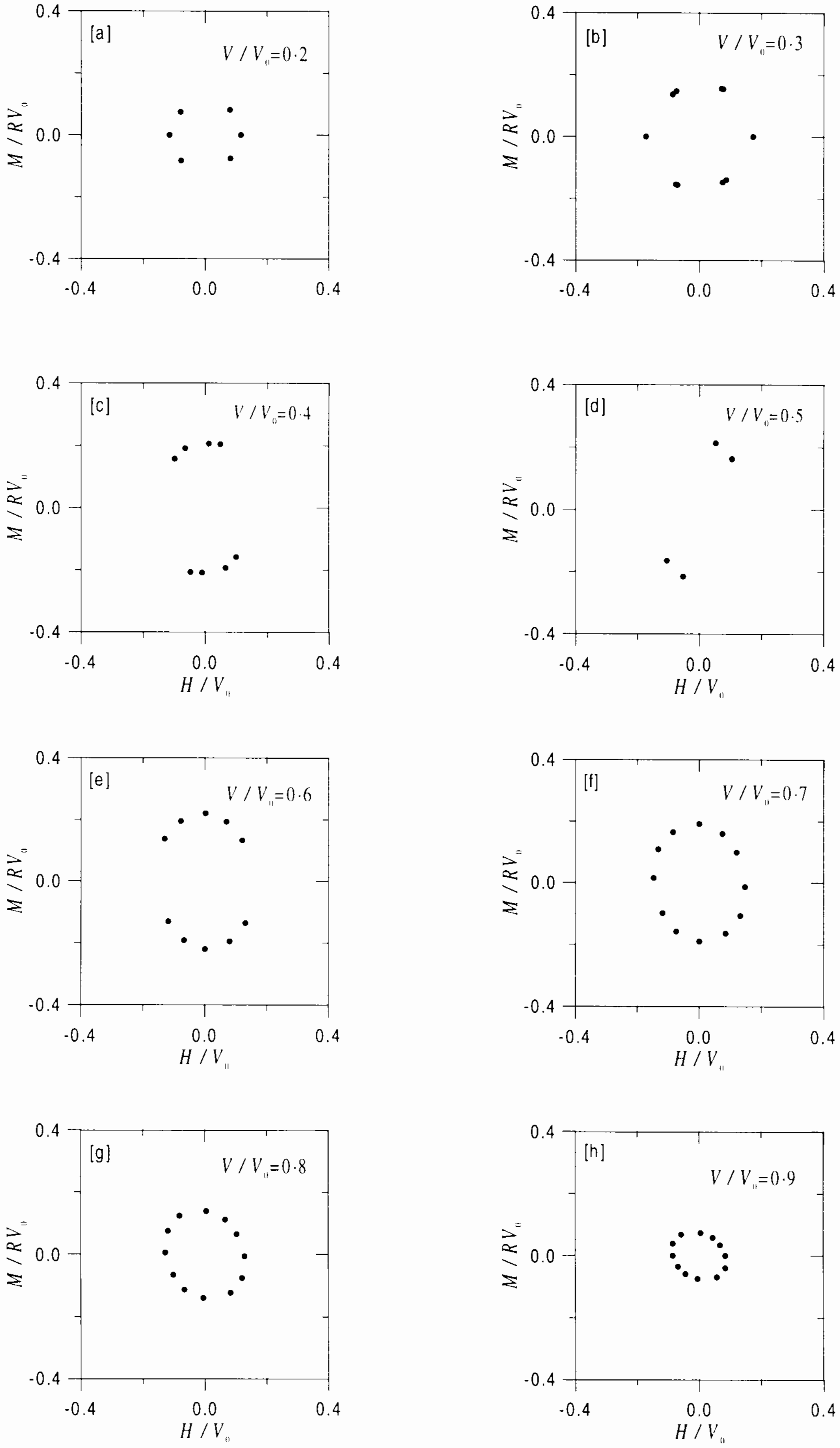

Figure 6.21: Load points retained after convex hull filtration at various V/V_0 levels.

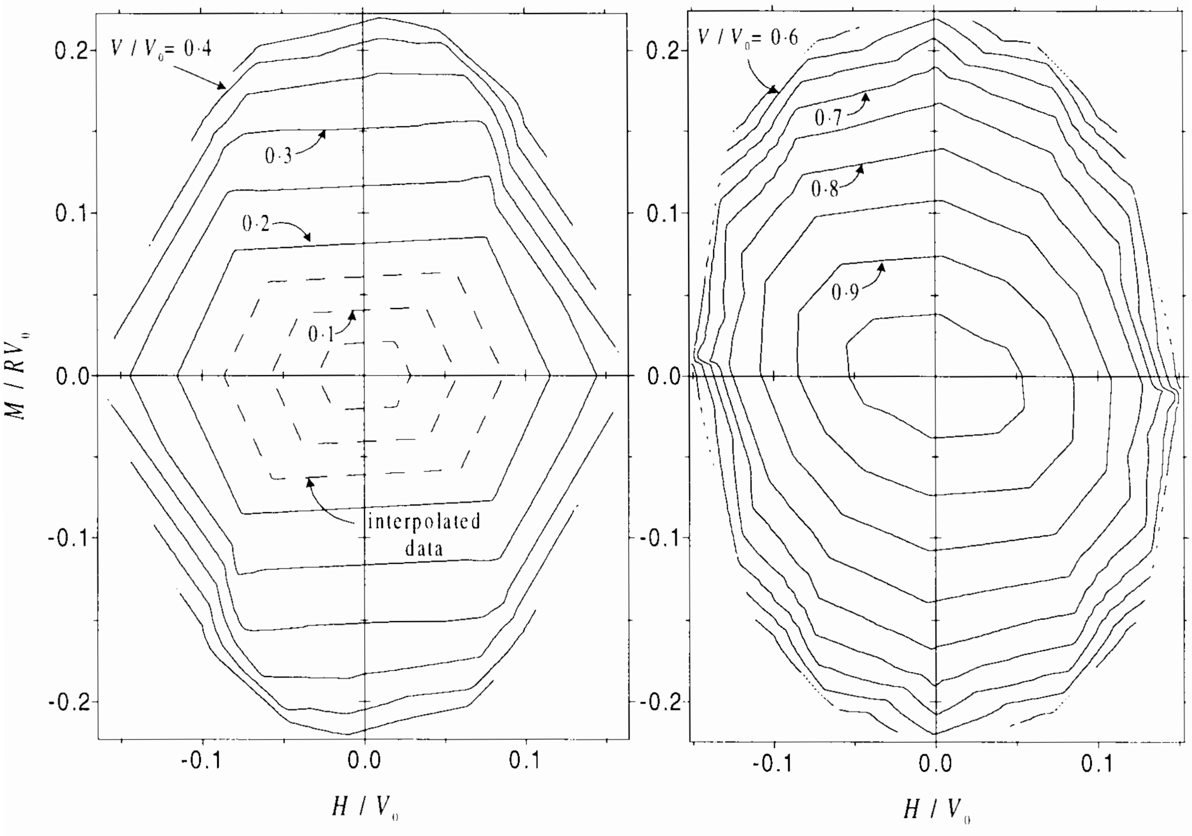

[a] $V / V_0 \leq 0{\cdot}5$

[b] $V / V_0 \geq 0{\cdot}5$

Figure 6.22: Contours of the bearing capacity envelope with respect to V/V_0.

On the other hand, the vertical lines on the left and right hand sides due to frictional behaviour (which exists for strip footings as shown in Fig. 5.22) have disappeared. However it is believed that this disappearance is caused by the lack of analyses which can give more details at the region of maximum horizontal load. The exact contour thus has some sort of round-off at the corners but the shape, in general, is similar to the one show in Fig. 6.22a.

6.5.2 Empirical formula of the bearing capacity envelope

The empirical formula of the bearing capacity envelope is determined in two steps (Martin, 1994). Firstly, ellipses at the cross section of the envelope ($V =$ const plane) are calculated. The relationship between parameters of the ellipses and the vertical load is then determined in the second step.

6.5.2.1 Fitting ellipses at cross sections of the envelope

From the contour of the envelope for $V/V_0 \geq 0{\cdot}5$, it is obvious that at each level of V/V_0, the cross-section of the envelope has an approximately elliptic shape. The size, shape and the rotation angle of the ellipses change with V/V_0. For $V/V_0 \leq 0{\cdot}5$, though it appears that the contours do not bear the elliptic shape, the shape can also be adequately approximated by ellipses. The equation of the ellipse can be written as:

$$A\left(\frac{H}{V_0}\right)^2 + B\left(\frac{M}{RV_0}\right)^2 + C\,\frac{H}{V_0}\,\frac{M}{RV_0} = 1 \tag{6.16}$$

where A, B, C are coefficients to be determined by regression analysis. It is more useful to write the equation of the ellipse in terms of the intersection of the ellipse with the H and M axes (which corresponds to the cases of eccentric and inclined load respectively) as follow:

$$\left(\frac{H/V_0}{H_{\text{int}}/V_0}\right)^2 + \left(\frac{M/RV_0}{M_{\text{int}}/RV_0}\right)^2 - 2e\,\frac{H/V_0}{H_{\text{int}}/V_0}\,\frac{M/RV_0}{M_{\text{int}}/RV_0} = 1 \tag{6.17}$$

where H_{int}/V_0 and M_{int}/RV_0 are the points at which the ellipse intersects the coordinate axes, and e is an eccentricity parameter. While the parameters A, B and C in Equ. 6.16 can be determined easily by the linear least square regression technique, the parameters in Equ. 6.17 H_{int}/V_0, M_{int}/RV_0 and e cannot be determined directly in this way. Nonetheless, the two sets of parameters in Equ. 6.16 and Equ. 6.17 are related by:

$$H_{\text{int}}/V_0 = \frac{1}{\sqrt{A}};\quad M_{\text{int}}/RV_0 = \frac{1}{\sqrt{B}};\quad e = \frac{-C}{2\sqrt{AB}} \tag{6.18}$$

Note that if an ellipse in its upright position defined as $\left(\frac{x}{a}\right)^2 + \left(\frac{y}{b}\right)^2 = 1$ is rotated about the origin at an angle ρ clockwise, the parameter C in Equ. 6.16 and the rotation angle ρ of the ellipse about the origin are related by:

$$C = -\sin 2\rho \left(\frac{1}{a^2} - \frac{1}{b^2}\right) \tag{6.19}$$

Therefore if C is negative (hence the eccentricity parameter e is positive) the major axis of the ellipse lies in the first and third quadrants in the $(H,\ M)$ space. As discussed in the previous section, for high V/V_0, the cross-sectional ellipse of the envelope has the major axis in the second and fourth quadrants. Therefore for these cases, the ellipse eccentricity parameter e is negative. Note that Equ. 6.19 also shows that the parameter C (and hence e) does not depend solely on the rotation angle of the ellipse but also the ratio between the length of the two principle axes of the ellipse. A smaller C in magnitude means either the ellipse takes on a more circular shape or the ellipse is not rotated; both of which indicate a smaller effect of the sense of eccentricity on the bearing capacity of the footing.

A series of regression analyses are performed to obtained the best fit ellipses at various vertical load $V/V_0 = 0{\cdot}2,\ 0{\cdot}25,\ \ldots,\ 0{\cdot}95$. Ellipses are not calculated for $V/V_0 < 0{\cdot}2$ as the analyses from low V/V_0 were commenced from $V = 1$ or $V/V_0 = 0{\cdot}143$, so there is no data below this level available. Even though data at $V/V_0 = 0{\cdot}15$ can be obtained, it is doubted that the load paths of the low V/V_0 analyses have reached the yield surface at this level. Therefore the load data at $V/V_0 = 0{\cdot}15$ is excluded from the regression analysis. Fig. 6.23 shows eight of these regressions (for $V/V_0 = 0{\cdot}20,\ 0{\cdot}30, \ldots,\ 0{\cdot}90$) including with the raw data points, the best fit ellipses and their numerical details: the ellipse parameters H_{int}/V_0, M_{int}/RV_0 and e, the standard error of estimates s_e, and the number of raw data points for each regression $2N$. It is pleasing to see the good coverage in the $(H/V_0,\ M/RV_0)$ plane that the high V/V_0 analyses yield (i.e. $V/V_0 = 0{\cdot}6, \ldots,\ 0{\cdot}9$). Both visual inspection and small standard error of estimates s_e shows that the raw data is very well described by rotated ellipses.

As discussed earlier, at each of $V/V_0 = 0{\cdot}2,\ 0{\cdot}25$ and $0{\cdot}3$, two data points obtained from the analytical solution for frictional sliding behaviour are added to the raw data. This raises the number of independent data points at $V/V_0 = 0{\cdot}2$ to $N = 6$, at $V/V_0 = 0{\cdot}3$ to $N = 5$. At $V/V_0 = 0{\cdot}5$ at which there are only $N = 2$ independent data points, clearly there is not enough raw data to perform a least square regression for an ellipse given in Equ. 6.16. The data for $V/V_0 = 0{\cdot}5$ is therefore excluded from further analyses.

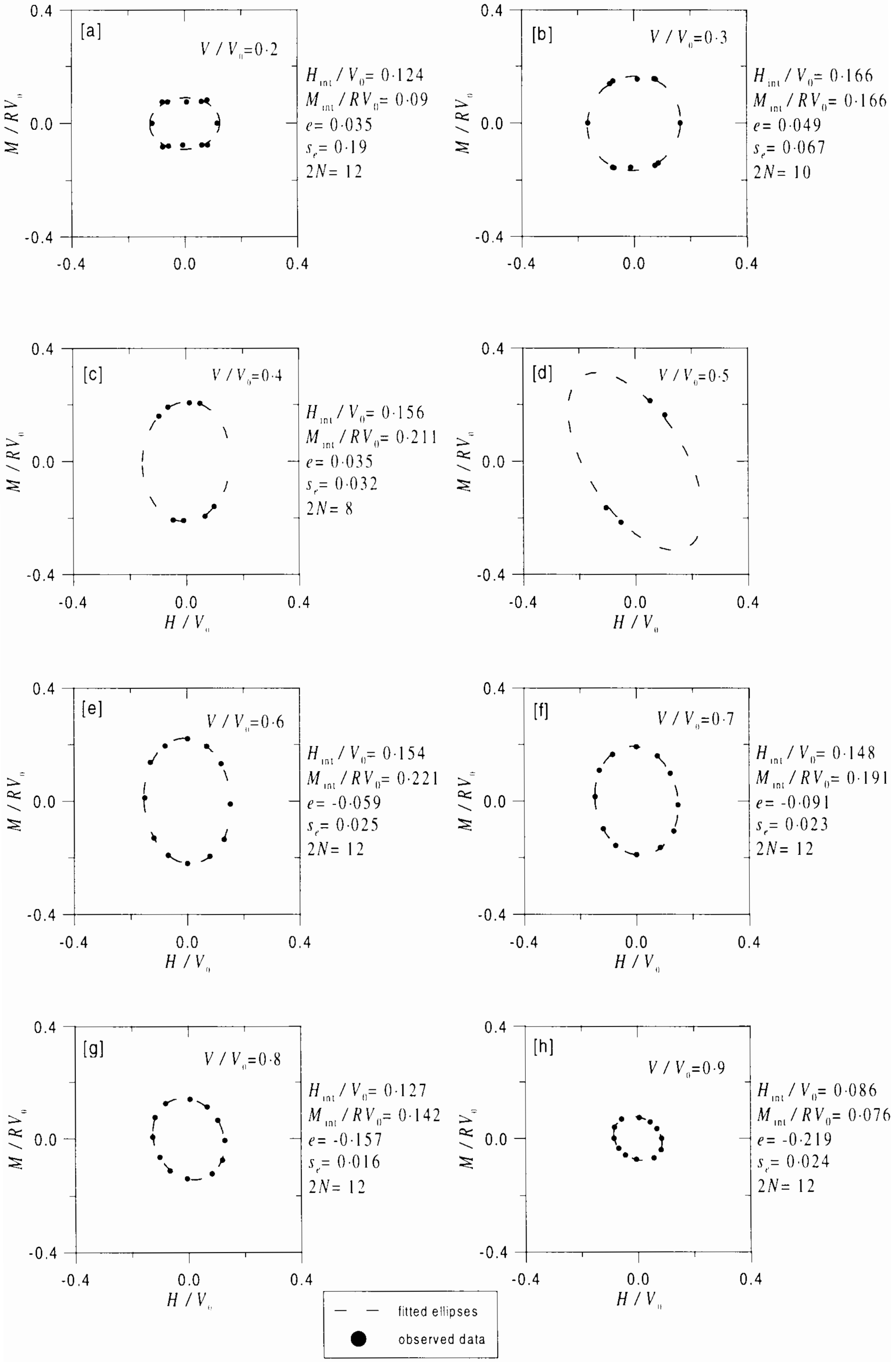

Figure 6.23: Ellipses best fitted to finite element data.

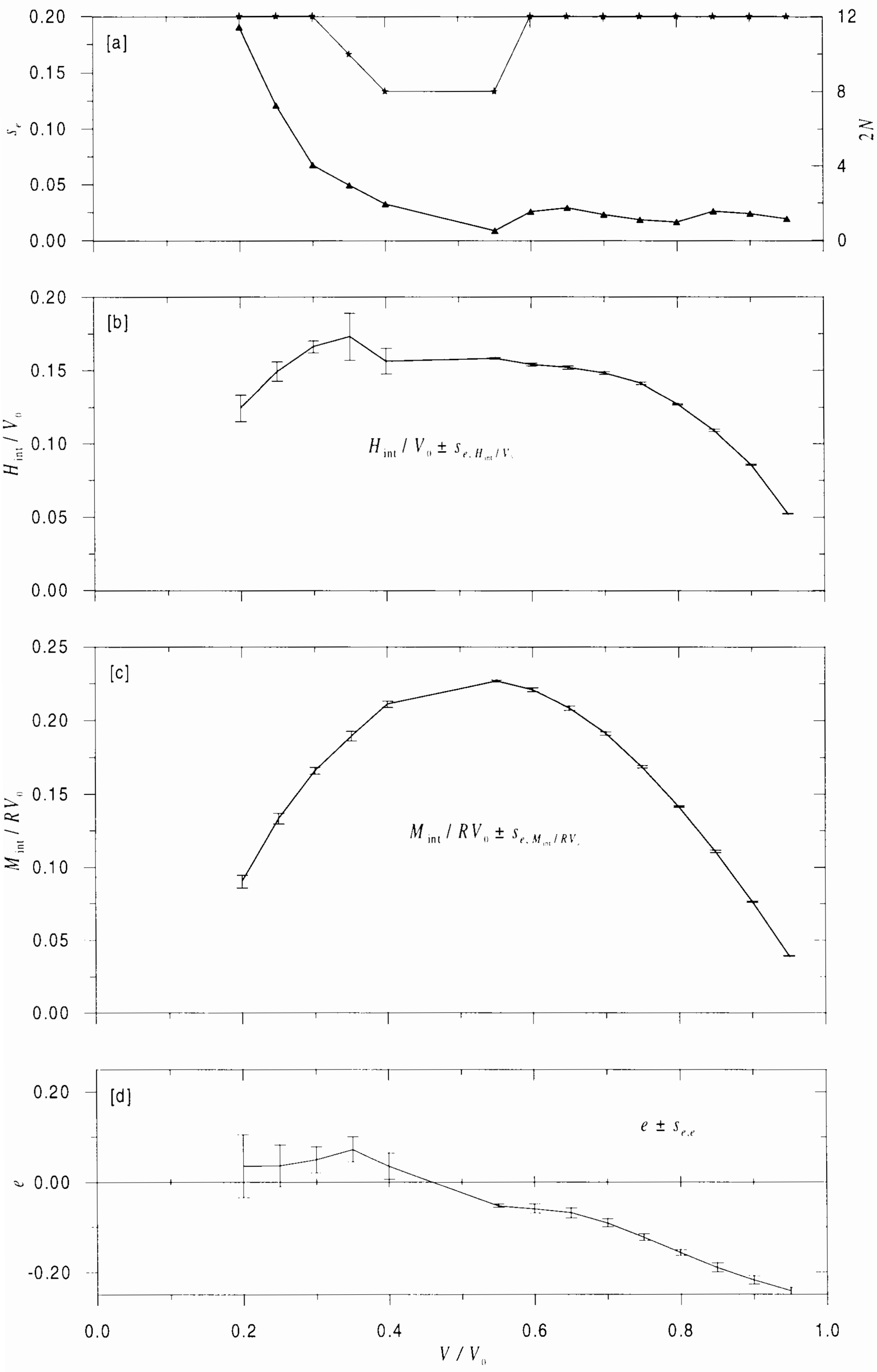

Figure 6.24: Best fit parameters of rotated ellipses.

Fig. 6.24 shows the variation of N, s_e and the three ellipse parameters H_{int}/V_0, M_{int}/RV_0 and e with vertical load level. In general, the plots show that the elliptic shape can fit the cross sections of the envelope better at high V/V_0 than at low V/V_0. Fig. 6.24a shows that the standard error of the fit s_e is very small for $V/V_0 \geq 0{\cdot}55$, but it increases consistently with vertical load levels below $V/V_0 = 0{\cdot}55$. The degree of uncertainty of each ellipse parameters H_{int}/V_0, M_{int}/RV_0 and e are represented by the length of the error bars in Fig. 6.24b, c and d. The length of these error bars is twice the standard error of estimates of each parameter.

The variation of e in the range of $V/V_0 = 0{\cdot}2$ to $0{\cdot}95$ also shows a well-defined trend. It suggests that the relation between e and V/V_0 can be described approximately by a linear relation.

The plot of H_{int}/V_0, M_{int}/RV_0 in Fig. 6.24b and c shows the similar shape to those shown in Section 6.2.3 and Section 6.2.2. The $(V/V_0, H_{\text{int}}/V_0)$ curve shows a familiar shape with three different modes of failure as discussed in Section 6.2.3: bearing failure mode (at high V/V_0), cohesive sliding failure mode and frictional sliding failure mode (at low V/V_0). The $(V/V_0, M_{\text{int}}/RV_0)$ curve shows a familiar parabolic trend.

High confidence for the parameters H_{int}/V_0, M_{int}/RV_0 at higher V/V_0 is shown by very small error bars in Fig. 6.24b and c. It also shows that the data at low V/V_0 are are not so well defined by rotated ellipses than those at higher V/V_0. For the data at low V/V_0, an equation of the form:

$$A\left(\frac{H}{V_0}\right)^D + B\left(\frac{M}{RV_0}\right)^D = 1 \qquad (6.20)$$

where D is an additional regression parameter, may be a better fit equation than the elliptic one. However, the further complication involved makes this development unattractive.

It is interesting that though the error bars of H_{int}/V_0, M_{int}/RV_0 are consistently short in the range of $V/V_0 = 0{\cdot}55, \ldots, 0{\cdot}95$, those of the eccentricity parameter e are not. At $V/V_0 = 0{\cdot}55$, there is a significant improvement in the degree of certainty for e whereas at higher V/V_0 the degree of certainty degrades. This can be explained by the fact that at $V/V_0 = 0{\cdot}55$, the ellipse have one axis significantly longer than the other. Therefore the eccentricity parameter e can be determined with a higher certainty than those at other high V/V_0 levels, at which the ellipses have a more circular shape. Analogously, at $V/V_0 = 0{\cdot}35$ and $0{\cdot}4$, the degree of certainty is lower for H_{int}/V_0 than for M_{int}/RV_0 because more raw data are clustered around the M/RV_0 axis than the H/V_0 axis.

It is worth noting that the standard errors of H_{int}/V_0, M_{int}/RV_0 and e in Fig. 6.24 are not determined directly from the least square fit of each ellipse. From the usual law of propagation of errors (see, for example, Rektorys, 1969), the standard errors of H_{int}/V_0, M_{int}/RV_0 and e can be determined from those of A, B and C as follows:

$$\begin{aligned} s_{e,H_{\text{int}}/V_0} &= \frac{A^{-3/2}\, s_{e,A}}{2} \\ s_{e,M_{\text{int}}/RV_0} &= \frac{B^{-3/2}\, s_{e,B}}{2} \\ s_{e,e} &= \frac{1}{4\sqrt{AB}}\left[C^2\left(\frac{s_{e,A}^2}{A^2}+\frac{s_{e,B}^2}{B^2}\right)+4s_{e,C}^2\right]^{05} \qquad (6.21) \end{aligned}$$

6.5.2.2 Variation of H_{int}/V_0, M_{int}/RV_0 and e with vertical load

With the three paramters of cross-sectional ellipses of the envelope determined (Fig. 6.24), the aim of this section is to derive a set of equations that can best describe the H_{int}/V_0, M_{int}/RV_0 and e curves in Fig. 6.24. For moment load which has a parabolic trend as shown in Fig. 6.24b, it will be recalled that the Meyerhof method for bearing capacity of strip footings under eccentric load as described in Chapter 5 yields a parabola of the form (cf. Equ. 5.2):

$$\frac{M}{2BV_0} = \frac{1}{4}\frac{V}{V_0}\left(1-\frac{V}{V_0}\right) \qquad (6.22)$$

for which the peak moment takes place at $V/V_0 = 0{\cdot}5$. However, as suggested by Nova & Montrasio (1991) extra flexibility can be added to the equation as follows to control the level of vertical load at which the peak moment load occurs:

$$\frac{M_{\text{int}}}{BV_0} = \mu\frac{V}{V_0}\left(1-\frac{V}{V_0}\right)^{\beta} \qquad (6.23)$$

A value of β smaller than unity will shift the location of peak moment from $V/V_0 = 0{\cdot}5$ towards $V/V_0 = 0$. A β smaller than unity also make the tangent at $V/V_0 = 1$ vertical. Martin (1994) proposed the following equation:

$$\frac{M_{\text{int}}}{BV_0} = \mu\left(\frac{V}{V_0}\right)^{\beta_1}\left(1-\frac{V}{V_0}\right)^{\beta_2} \qquad (6.24)$$

so that the parabola has vertical tangents at both $V/V_0 = 0$ and $V/V_0 = 1$, and at the same time the location of peak moment can occur at vertical load V/V_0 either smaller or greater than $0{\cdot}5$. This equation is further refined so that it can be written in terms of peak moment

M_0/RV_0 as follows:

$$\frac{M_{\text{int}}}{RV_0} = \frac{M_0}{RV_0}\left[\frac{(\beta_1+\beta_2)^{\beta_1+\beta_2}}{\beta_1^{\beta_1}\beta_2^{\beta_2}}\right]\left(\frac{V}{V_0}\right)^{\beta_1}\left(1-\frac{V}{V_0}\right)^{\beta_2} \tag{6.25}$$

Martin (1994) also uses an exactly analogous expression for the vertical–horizontal load interaction locus:

$$\frac{H_{\text{int}}}{V_0} = \frac{H_0}{V_0}\left[\frac{(\beta_1+\beta_2)^{\beta_1+\beta_2}}{\beta_1^{\beta_1}\beta_2^{\beta_2}}\right]\left(\frac{V}{V_0}\right)^{\beta_1}\left(1-\frac{V}{V_0}\right)^{\beta_2} \tag{6.26}$$

Incidentally, Equ. 6.26 also provides a good fit for the three phases of the vertical – horizontal interaction locus as shown in Fig. 6.24. A set of $\beta_1 < 1$, and $\beta_2 < 1$ gives a curve which is flatter around its peak than a parabola. The curve therefore follows more closely the cohesive sliding part of the locus at which the locus is horizontal.

The problem arises when Equ. 6.25 and Equ. 6.26 are substituted into the elliptic equation Equ. 6.17. The final equation is too complicated if two different sets of β_1 and β_2 are used. The equation will be substantially simpler if the two equations Equ. 6.25 and Equ. 6.26 use the same pair of parameters β_1 and β_2. Therefore the parameters in Equ. 6.25 and Equ. 6.25 will be determined from regression analyses on H and M simultaneously, as well as separately.

Using non-linear least square regression, the three parameters H_0/V_0, β_1, β_2 are determined. The resulting predicted curve, shown as 'not weighted' in Fig. 6.25a, however, deviates from the data which has high confidence, and results in an unrealistic $(V/V_0, H/V_0)$ interaction locus. A weighted regression is therefore used to take into account the degree of certainty associated with each data. Each data point is associated with a weight depending on the standard error:

$$w_i = \frac{1}{s_{e,i}^2} \tag{6.27}$$

The optimum set of coefficients is determined by minimizing the merit function:

$$\chi^2 = \sum_i w_i \varepsilon_i^2 \tag{6.28}$$

The results of weighted regression for H_0/V_0, β_1, β_2 are shown in Fig. 6.25a. The predicted locus shows a significant improvement over the non-weighted one; it follows closely the data at high V/V_0 for which the level of confidence is high. The predicted peak horizontal load of $H_0/V_0 = 0{\cdot}16$ is slightly lower than the exact solution $H_0/V_0 = 0{\cdot}165$. It is pleasing

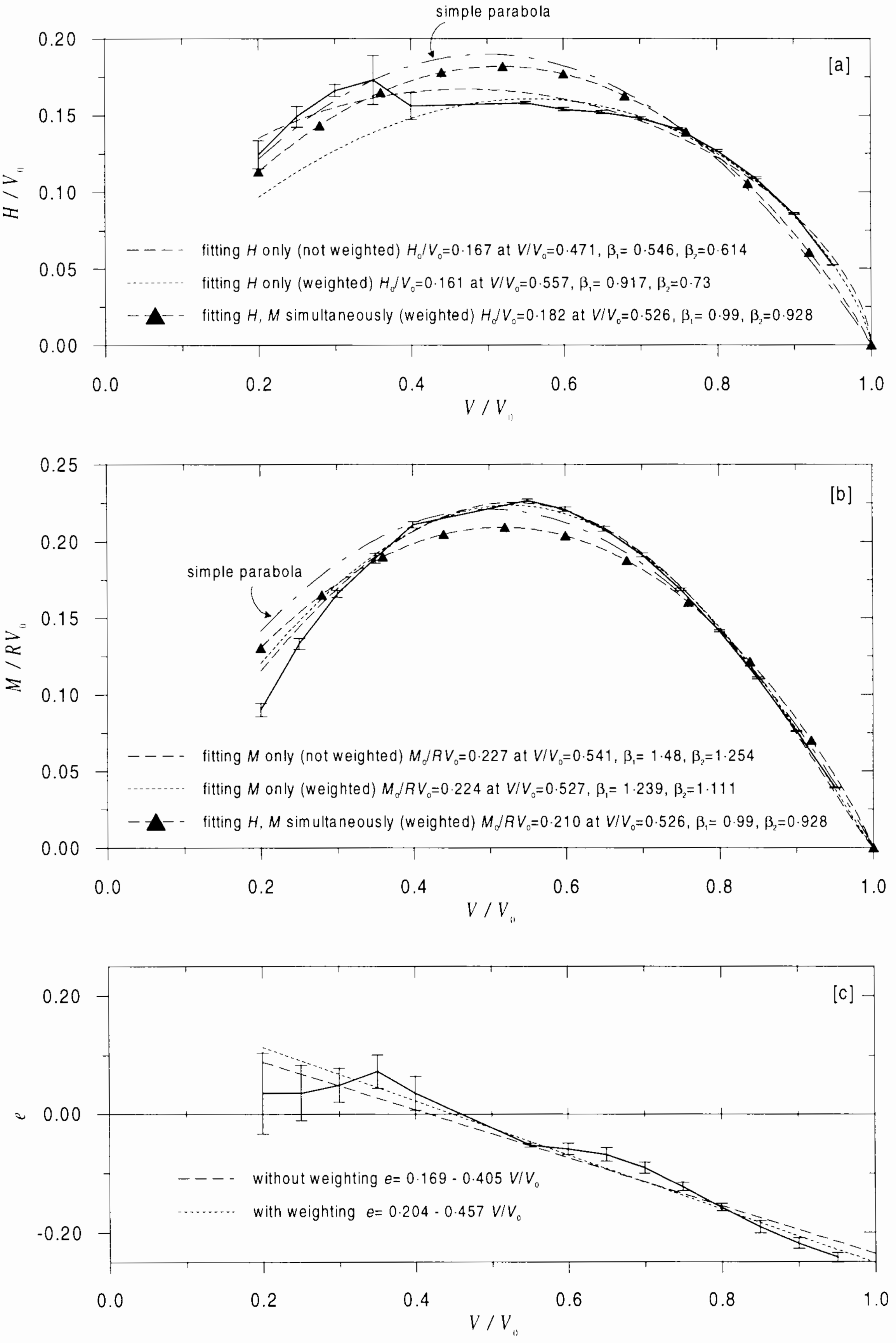

Figure 6.25: Curve fitting for H_{int}/V_0, M_{int}/RV_0 and e.

to see that the peak load obtained from regression is also close to the horizontal load where the locus exhibits cohesive sliding failure.

As for moment load the level of uncertainty does not fluctuate so considerably as for horizontal load, the weighted regression does not differ from the non-weighted one as compared to that of the horizontal load (Fig. 6.25b). Nonetheless, the predicted $(M/RV_0, V_0)$ locus again follows closely the observed data at high V/V_0, but the two deviate at low V/V_0.

Both the loci for horizontal and moment loads have their peak values occurring at a vertical load slightly higher than $V/V_0 = 0{\cdot}5$.

As discussed earlier, the final equation of the yield surface would be very complicated if both sets of β_1, β_2 for horizontal load and moment are accomodated. Combining Equ. 6.25 and Equ. 6.26, one set of β_1, β_2 shared by both the equation can be determined, with the weight for each data point being accounted for, by minimising the following loss function:

$$\chi^2 = \left[\sum_i w_i \varepsilon_i^2\right]_{\text{Equ. 6.25}} + \left[\sum_i w_i \varepsilon_i^2\right]_{\text{Equ. 6.26}} \tag{6.29}$$

The weighted regression based on the above loss function gives:

$$\begin{aligned} \frac{H_0}{V_0} &= 0{\cdot}182; \\ \frac{M_0}{RV_0} &= 0{\cdot}21; \\ \beta_1 &= 0{\cdot}99; \\ \beta_2 &= 0{\cdot}928 \end{aligned} \tag{6.30}$$

The results of this combined regression on two data sets H/V_0 and M/RV_0 are shown in Fig. 6.25a and b together with other results from the previous regression analyses. Though combining the two sets does not shift significantly the location of peak horizontal load and moment, it does change the peak horizontal load and moment. The peak horizontal load H_0/V_0 is increased from 0·16 to 0·181, whereas the peak moment is decreased from 0·225 to 0·209.

The variation of eccentricity parameter e with vertical load can be described as linear in the range of V/V_0 from 0·35 to 0·95. For $V/V_0 < 0{\cdot}35$, the parameter e appears to decrease towards zero as the vertical load goes to zero. Unfortunately, this trend is accompanied with high uncertainty. It is therefore decided that a linear equation of the form:

$$e = e_0 + e_1 \frac{V}{V_0} \tag{6.31}$$

is used to describe the data. Again, a weighted regression analysis is used to give:

$$\begin{aligned} e_0 &= 0{\cdot}207 \\ e_1 &= 0{\cdot}461 \end{aligned} \tag{6.32}$$

The resulting curve is shown in Fig. 6.25c. Very good modelling of the data, particularly for $V/V_0 \geq 0{\cdot}4$, is achieved.

Before ending this section, it is worth noting that the simple parabolic equation having the same form as Equ. 6.22 (or Equ. 6.26 with β_1, β_2 forced to take the value of unity) does not model the data very well. The attempted regression analyses are shown in Fig. 6.25a and b in dash-dotted lines.

6.5.2.3 The three dimensional yield surface equation

Upon substituting Equ. 6.25 and Equ. 6.26 into Equ. 6.17 (noting that the same pair of β_1 and β_2 is used), an expression for the full normalised $(V/V_0,\ H/V_0,\ M/RV_0)$ yield surface is obtained:

$$\begin{aligned} &\left(\frac{H}{H_0}\right)^2 + \left(\frac{M/R}{M_0/R}\right)^2 - 2\left(e_0 + e_1\frac{V}{V_0}\right)\frac{H}{H_0}\frac{M/R}{M_0/R} \\ &\quad - \left[\frac{(\beta_1+\beta_2)^{\beta_1+\beta_2}}{\beta_1^{\beta_1}\,\beta_2^{\beta_2}}\right]^2 \left(\frac{V}{V_0}\right)^{2\beta_1}\left(1-\frac{V}{V_0}\right)^{2\beta_2} = 0 \end{aligned} \tag{6.33}$$

in which the best fit parameters, as determined in the previous section, are:

$$\begin{aligned} H_0/V_0 = 0{\cdot}182;&\quad M_0/RV_0 = 0{\cdot}21; \\ \beta_1 = 0{\cdot}99;&\quad \beta_2 = 0{\cdot}928; \\ e_0 = 0{\cdot}207;&\quad e_1 = -0{\cdot}451 \end{aligned} \tag{6.34}$$

6.6 Comparison and discussion

6.6.1 Comparison with analytical solutions: $(V,\ H)$ and $(V,\ M)$ planes

The two finite element tests commencing from low and high V/V_0 which involve only footing rotation are shown in Fig. 6.26, with the two other previously-reviewed methods Hansen

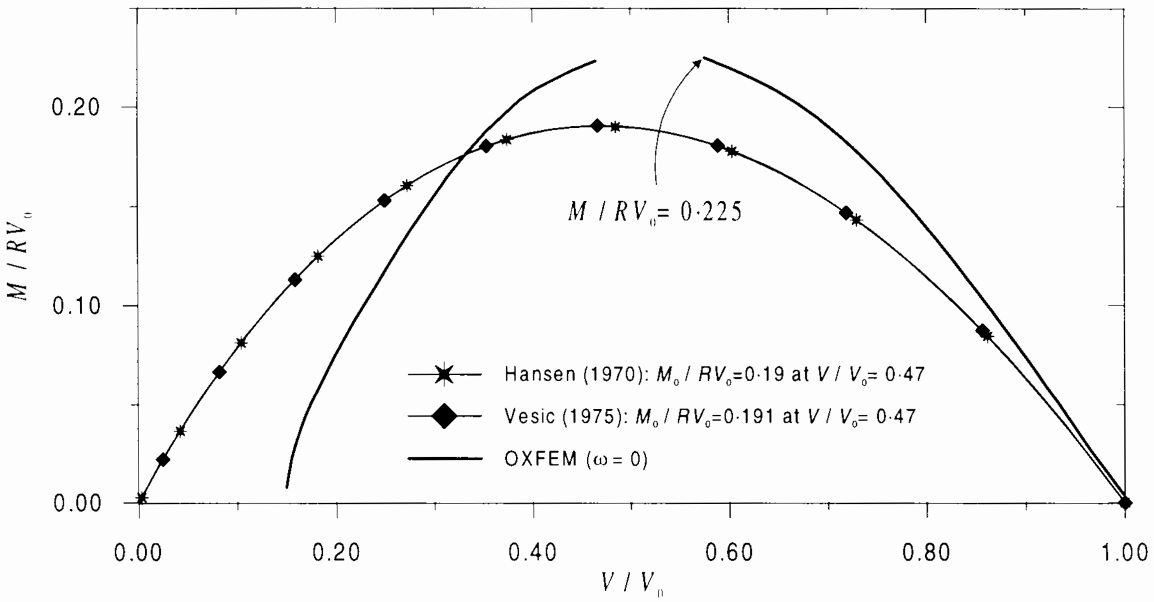

Figure 6.26: Comparison on $(V,\ M)$ plane.

(1970) and Vesic (1975). Even though the two load paths do not meet[1] (resulting in a gap in the interaction locus unexplored), the trend of the paths from both high and low V/V_0 sides shows that the maximum moment should be very close to the moment loads at which the two analyses stops. Both the analyses give similar maximum moment: the one from low V/V_0 gives $M/RV_0 = 0{\cdot}223$ and the one from high V/V_0 $M/RV_0 = 0{\cdot}225$. This value is significantly higher than the maximum moment determined by the approximate solutions of Hansen and Vesic; the finite element solution is 17·8% higher than the approximate analytical solution, which is $M/RV_0 = 0{\cdot}191$.

Fig. 6.27 shows the $(V,\ H)$ interaction locus of the finite element analysis and the other analytical methods. In general the finite element analysis is less conservative than all three analytical solutions in the bearing failure mode, except for a small range of $0{\cdot}6 \leq V/V_0 \leq 0{\cdot}8$ it is more conservative than the Meyerhof and Vesic methods.

However, the finite element solution of $\omega = 0°$ underestimates the maximum horizontal load; its maximum horizontal load is only $H/V_0 = 0{\cdot}154$, which is 5·5% smaller than the exact value of 0·163. Even though the finite element analysis does generate a small moment load (and thus the horizontal load bearing capacity is reduced), it is believed that the normal

---

[1] Note also that in these two tests a small horizontal load is generated. Therefore the load paths do not lie exactly on the $H = 0$ plane as desired for the purpose of this comparison. Also, not all the load path of the finite element analysis commencing from low V/V_0 lie on the $(V,\ M)$ failure locus. Because the analysis commences from an unloaded position, the first part of the load path is elastic reloading.

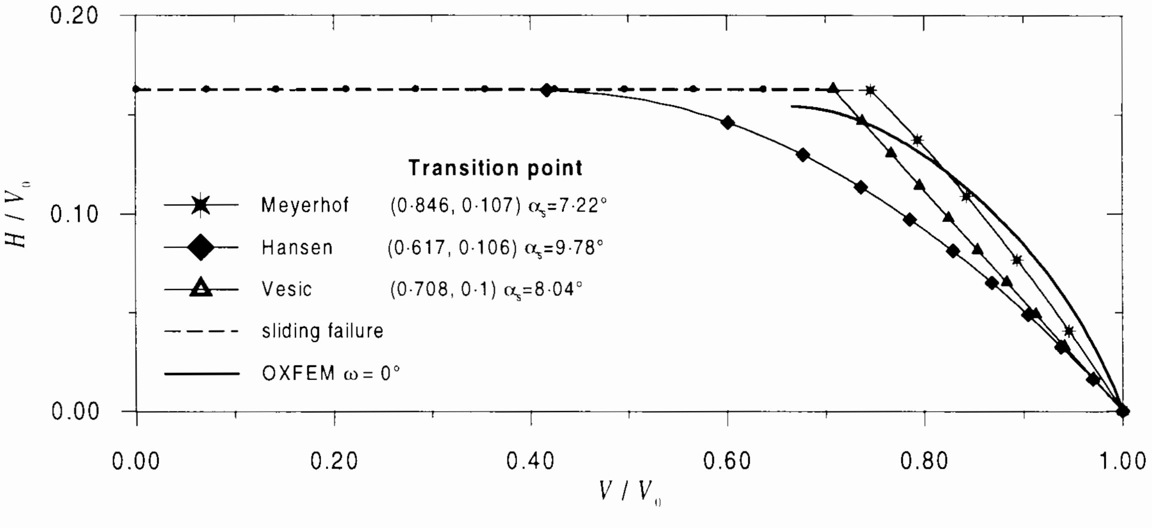

Figure 6.27: Comparison on (V, H) plane.

stress concentration in the soil-footing interface is the main cause of this underestimation. As shown in Fig. 6.18b, the existence of high normal stress concentration in the rim of the footing causes stress reduction in some adjacent areas. In these areas, the normal stress can fall under $\sigma = 2$ as shown in Fig. 6.18b, compared to $2 \leq \sigma \leq 4$ in most part of the footing. This means that subjected to large horizontal displacement, these areas slides under frictional failure mode, which results in a horizontal stress $\tau = \sigma \tan 30°$ smaller than $c = 2/\sqrt{3}s_u$ for $\sigma < 2$. Note that for $\sigma > 2$, the maximum shear stress in the interface is limited by cohesive sliding, in which case the maximum shear stress is $\tau = c$. Therefore the total horizontal load is smaller than the expected value $H_0 = Ac$, or $H_0/V_0 = 0{\cdot}163$.

6.6.2 Comparison with analytical solutions: complete (V, H, M) interaction

Not only is the Hansen method more conservative than the finite element method in (V, H) and (V, M) planes, but it is also more conservative in full interaction between vertical, horizontal and moment loads. A comparison between Hansen (1970) and the finite element results is shown in Fig. 6.28. The Hansen method also fails to capture the effect of the sense of load eccentricity, particularly at high vertical load levels. This results in the Hansen method being even more conservative in case of negative eccentricity, e.g. in the second and fourth quadrants in the (H, M) space.

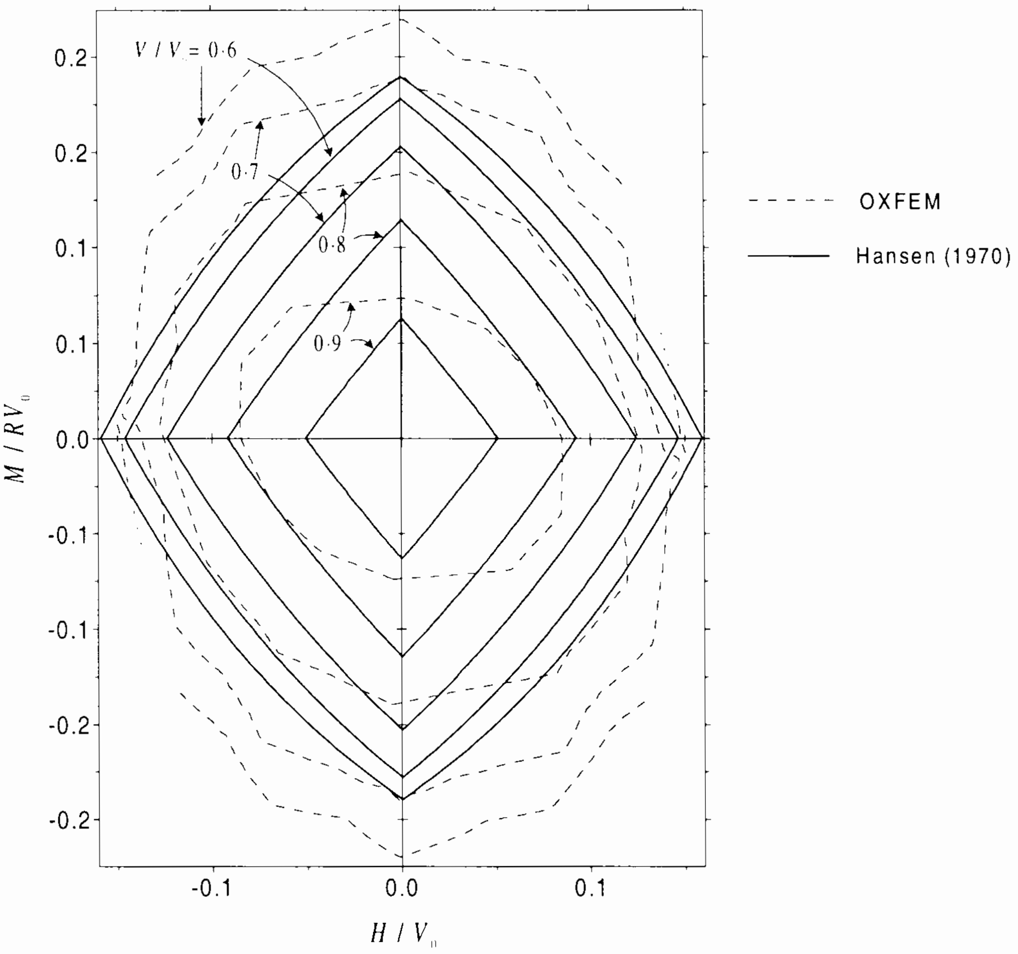

Figure 6.28: Comparison with Hansen (1970).

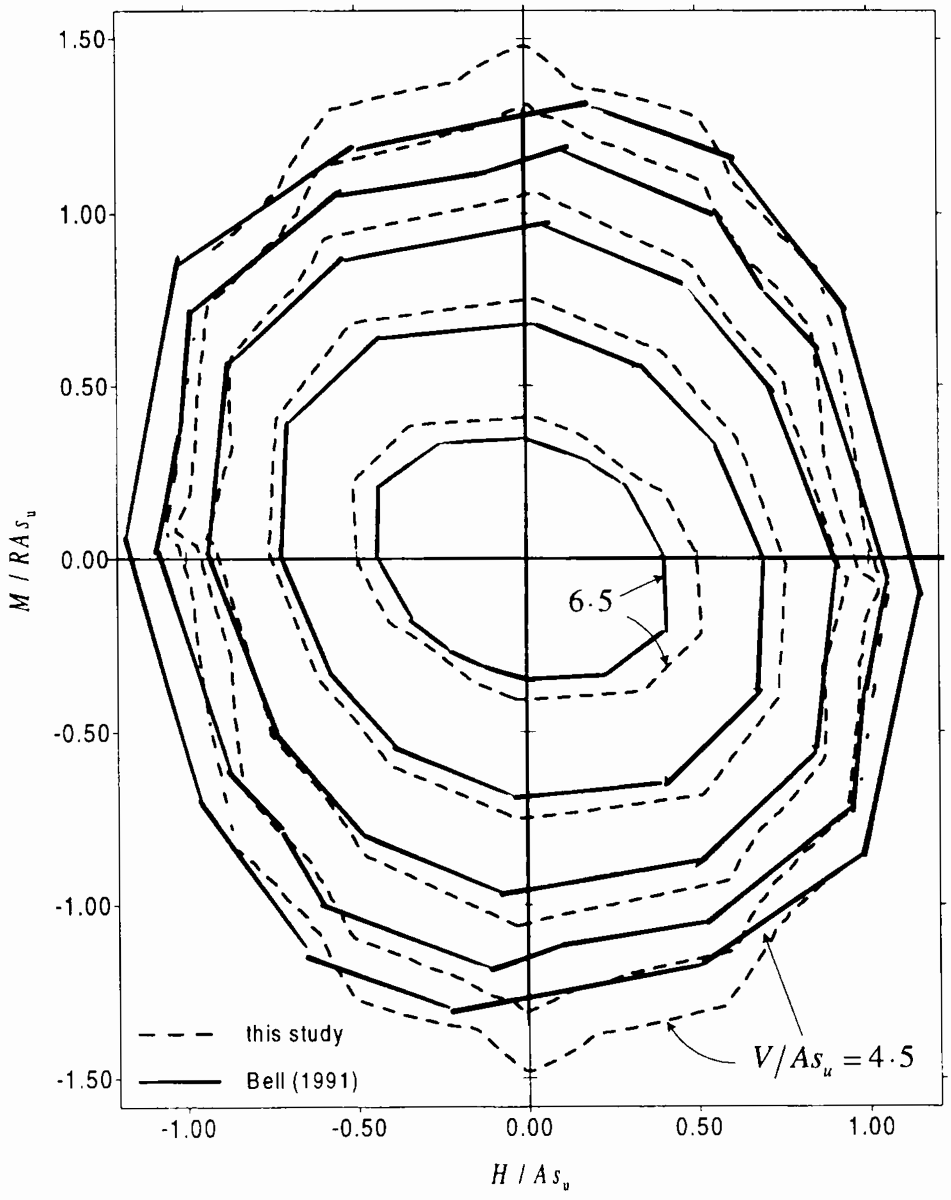

Figure 6.29: Comparison with Bell (1991).

6.6.3 Comparison with other finite element analyses

A comparison with Bell's (1991) is shown in Fig. 6.29. Compared to this study, Bell's (1991) contours are more conservative in the range $V/As_u > 5{\cdot}5$. Note that the shape and the rotation of the contours of the two sets are also very similar in this range ($V/As_u > 5{\cdot}5$). At lower vertical load, Bell's (1991) contours give higher peak horizontal loads and lower peak moment loads than the contours of this study. Note that Bell's (1991) analyses do not allow loss of contact between the footing and the soil, which happens under low vertical load and high moment and horizontal loads. Loss of contact in Bell's (1991) analyses is taken into account approximately as discussed in Section 6.2.5.

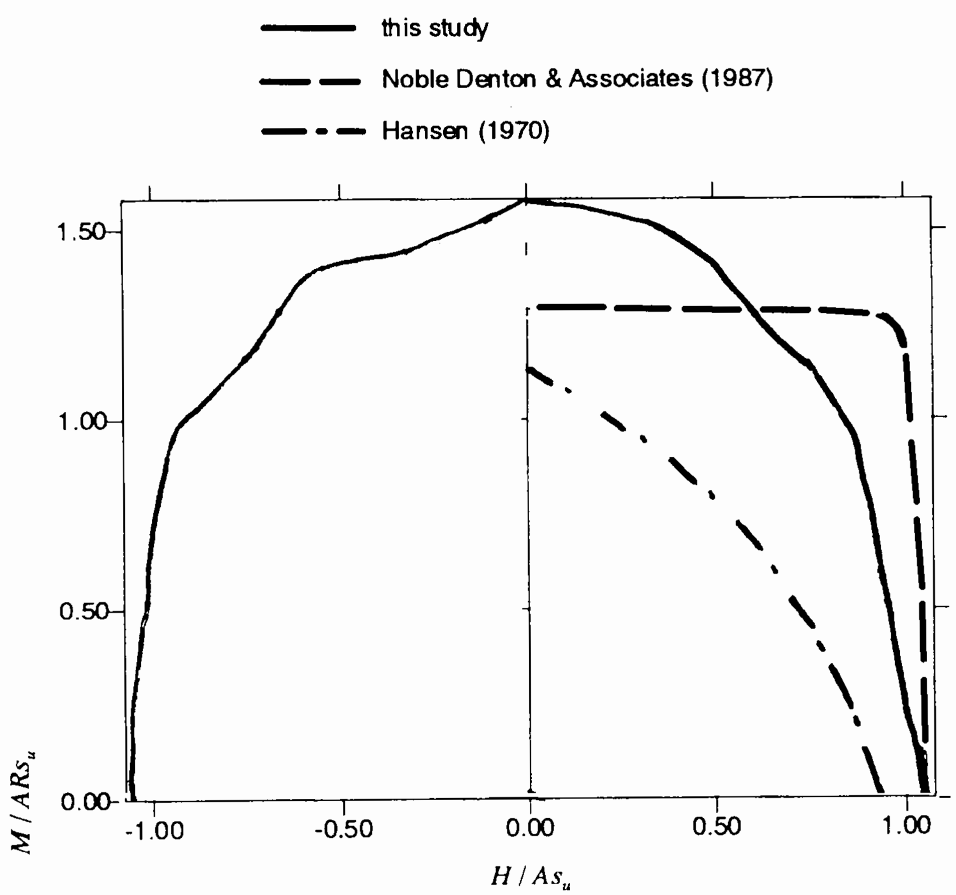

Figure 6.30: Comparison with Noble Denton & Associates (1987): $V/As_u = 3{\cdot}6$.

Fig. 6.30 shows the contour at $V/As_u = 3{\cdot}6$ of both this study and Noble Denton & Associates's (1987) research. It can be seen that though the two methods give similar peak horizontal loads, they are in poor agreement as to the peak moment; Noble Denton & Associates's (1987) give much smaller peak moment. The two methods also differ in the shape of the contours. As mentioned earlier, Noble Denton & Associates (1987) used the harmonic loading method. However, there are doubts with respect to the adequacy of the mesh fineness. Also, the loss of contact between the footing and the soil was not taken into account in Noble Denton & Associates's (1987) calculations.

Chapter 7

Effect of Soil Strength Increasing with Depth, Cone Angle and Embedment

7.1 Introduction

This chapter addresses some features of offshore foundations which represent common departures from the simplest case of a flat footing on the surface of a homogenenous clay. Firstly, offshore foundations, particularly gravity foundations, are usually placed on an inhomogeneous soil base. One particular type of soil inhomogeneity, which is strength increasing linearly with depth will be investigated in this chapter.

The second feature, which is relevant to jack-up foundations, is that the footings usually have a conical shape (McClelland et al., 1982; Young et al., 1984). As the study in Chapter 2 shows, the cone angle affects the footing elastic behaviour significantly under both horizontal and moment load. This chapter investigates the effect of cone angle on the footing collapse behaviour.

Another feature of offshore foundations is the large footing embedment. In order to increase the safety, jack-up foundations are usually preloaded to force the foundations to penetrate to the soil. Also, for gravity structure foundations are usually provided with skirts which effectively cause the footing to be embedded to a significant depth. This is also true for caisson foundations, which have the perimeter skirt.

As the title suggests, this chapter is divided into three main sections. In Section 7.2, the

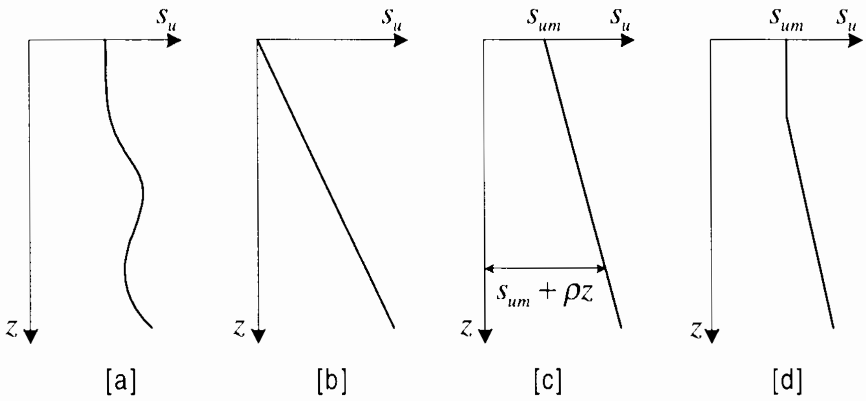

Figure 7.1: Variation of cohesion with depth (after Davis & Booker, 1973).

effect of soil strength increasing with depth is investigated. The effects of the cone angle and embedment depth are taken up in Sections 7.3 and 7.4, respectively. All of the three sections have the same structure, starting with a literature review, then continuing with a description of the finite element calculations and an analysis of the results. Each section ends with a comparison with the results obtained from the previous chapter for flat surface footings on a homogeneous soil, in addition to a comparison with other available methods.

7.2 Effect of soil strength varying with depth

7.2.1 Literature review

The problem of variation of soil strength with depth is depicted in Fig. 7.1. The general case of strength inhomogeneity is shown in Fig. 7.1a; other cases Figs. 7.1b, c and d, have been studied by Davis & Booker (1973) for the case of smooth and rough footings in plane strain, in which case the strength increase is expressed by the factor ρ.

Houlsby & Wroth (1984) use the method of characteristics to compute the lower bound vertical collapse loads taking into account footing roughness, embedment, cone angle and also soil with varying strength. Detailed results of soil strength increasing linearly with depth (Fig. 7.1c) are tabulated in Martin (1994). Fig. 7.2 shows the results for rough surface and flat footings. The strength increase is expressed by a dimensionless factor $\rho 2R/s_{um}$, where s_{um} is the undrained strength at the mud-line level (and is also the footing level for surface footings). The soil yield criteria used is the Tresca yield criteria ($\sigma_{\max} - \sigma_{\min} = 2s_u$). At

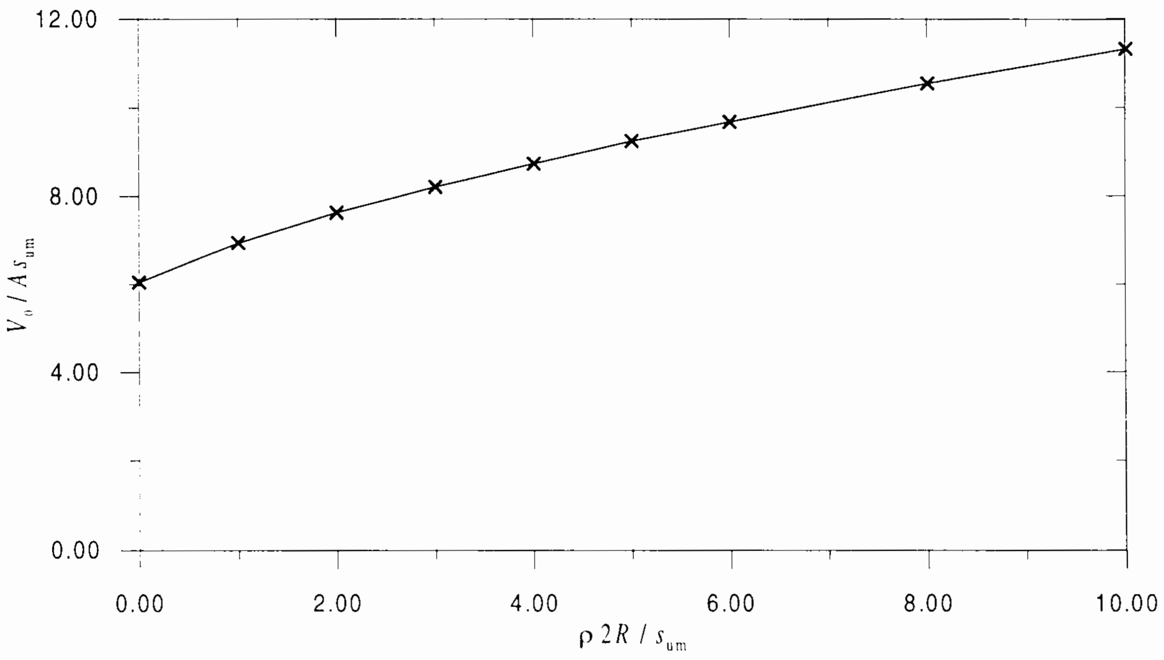

Figure 7.2: Variation of the vertical bearing capacity V_0/As_{u0} with strength increase rate $\rho 2R/s_{um}$ (for a rough surface flat circular footing on a Tresca soil).

$\rho 2R/s_{um} = 0$ (homogeneous soil), the vertical bearing capacity is $V_0/As_u = 6{\cdot}05$, which is identical to Eason & Shield's (1960) solution (Section 6.2.1).

It should be noted that by multiplying the solution for Tresca material by $2/\sqrt{3}$, the solution does not become an exact lower bound solution for a von Mises material because the undrained strength in axi-symmetry is not constantly $2s_u/\sqrt{3}$ if s_u is the triaxial undrained shear strength.

All the solutions mentioned above are for vertical loads, and there are no known solutions for foundations subjected to combined loadings. This problem of combined loading is investigated in the following sections using the finite element method.

7.2.2 Vertical bearing capacity

The mesh used in the analyses of the previous chapter is re-used, with the only difference being the material properties. In OXFEM, the strength increase factor ρ can be specified in defining a von Mises material. The program will then calculate the strength of each integration point in the element before the usual finite element routine is started.

This study investigates the effect of soil strength varying linearly with depth as shown in

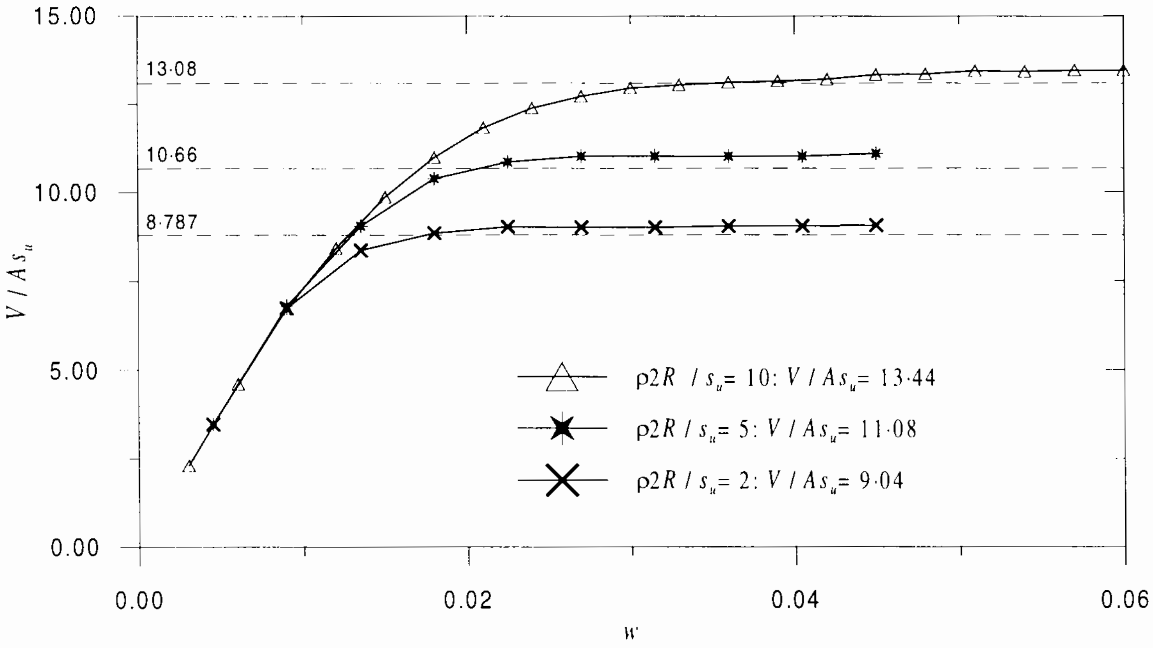

Figure 7.3: Calculation of vertical collapse loads for different cases of soil with strength increasing with depth.

Fig. 7.1c. Three cases of strength increase are examined: $\rho 2R/s_{um} = 2$, 5 and 10. The vertical bearing capacity results are shown in Fig. 7.3. Also shown in the figure is the lower bound solution by Houlsby & Wroth (1984) for a Tresca material multiplied by $2/\sqrt{3}$ ($V/As_u = 8{\cdot}787$, $10{\cdot}66$ and $13{\cdot}08$ for $\rho 2R/s_{um} = 2$, 5 and 10, respectively). As has been mentioned, these values are by no means exact or strictly lower bounds. Nonetheless they can be used as reference values. The reference results are from 2·8% to 3·9% lower than the finite element results. Thus the finite element results are considered acceptable.

7.2.3 Programmes of analyses

The analyses in this study are similar to those of Chapter 6. For each case of $\rho 2R/s_{um}$, once the vertical bearing capacity has been reached, six combinations of horizontal and rotational displacements corresponding to $\omega = 0°, 30°, 60°, 90°, -30°$ and $-60°$ (see Fig. 6.15) are applied.

Unlike the analyses in the previous chapter, only analyses commencing from high V/V_0 are performed in this chapter. Because at low V/V_0, the plastic zone under the footing at failure is shallower, the shape and size of the envelope at low V/V_0 is not affected by soil strength increasing with depth to such an extent as that at high V/V_0. In addition, at low

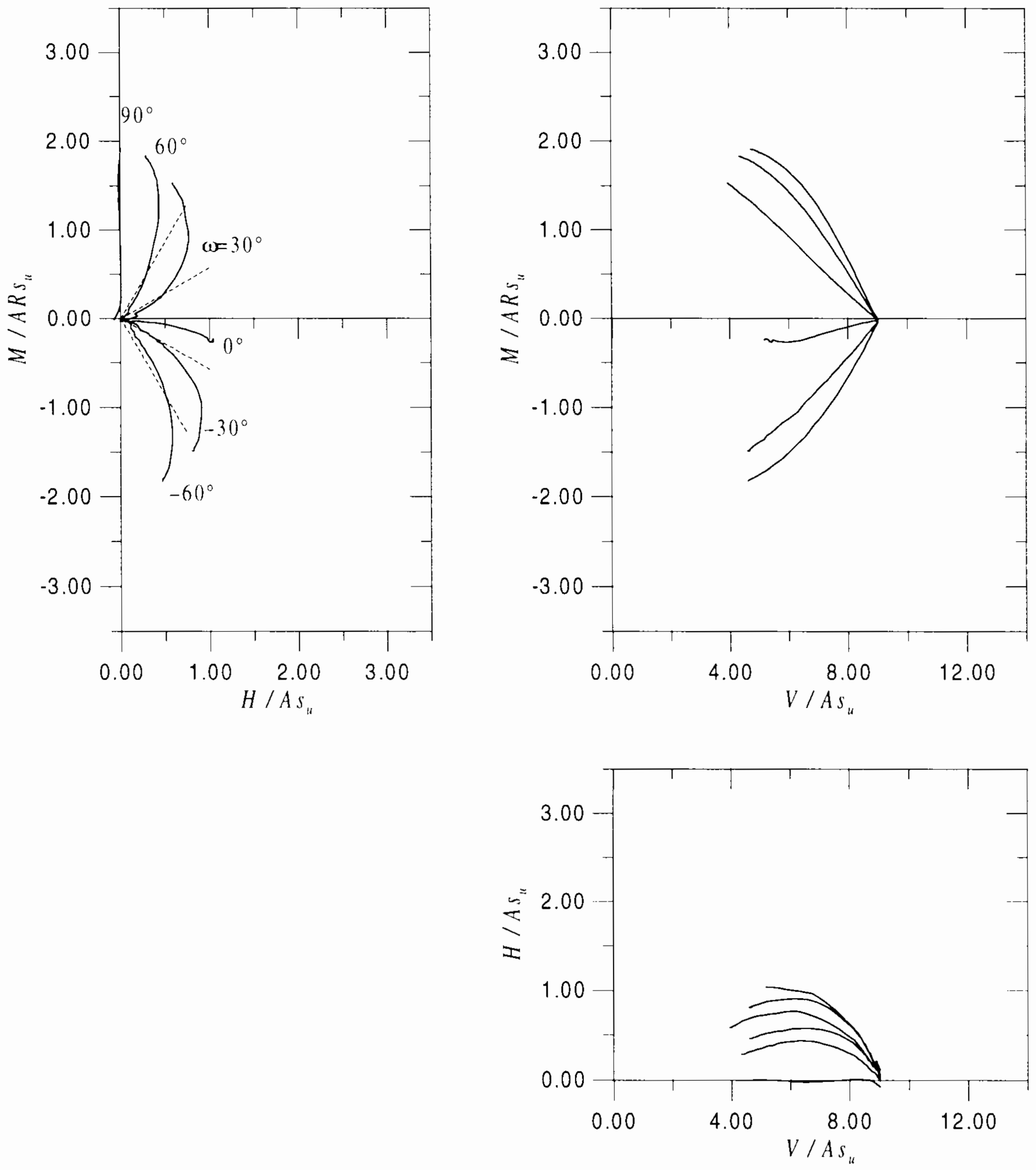

Figure 7.4: (V, H, M) curves from high V/V_0: $\rho 2R/s_{um} = 2$.

V/V_0, the behaviour of the footing under horizontal load is governed by the frictional sliding of the interface, which is independent of soil strength increasing with depth.

Fig. 7.4 shows the resulting load paths of the smallest strength increasing rate $\rho 2R/s_{um} = 2$. The load paths look similar to those of the uniform soil (see Fig. 6.16) in many ways. As can be seen from the (H/As_{um}, M/ARs_{um}) plot in Fig. 7.4, the chosen values of ω give load paths that cover well the envelope in (H/As_{um}, M/ARs_{um}) space. Pure rotation ($\omega = 90^\circ$) generates almost no horizontal load while pure horizontal displacement causes small, but significant moment.

Whilst the largest horizontal load (under pure horizontal sliding) is almost unchanged ($H_0/As_{um} = 1{\cdot}04$ for $\rho 2R/s_{um} = 2$ compared to $H_0/As_{um} = 1{\cdot}07$ for a uniform soil), peak moment has gone up from $M_0/RAs_{um} = 1{\cdot}58$ for a uniform soil to $M_0/RAs_{um} = 1{\cdot}91$ for $\rho 2R/s_{um} = 2$. This increase in peak moment is $+21\%$, which is comparable to the increase in vertical bearing capacity of $+28\%$.

Similar feaures are also seen for the load paths of $\rho 2R/s_{um} = 5$ and $\rho 2R/s_{um} = 10$, though the results of the two cases in $(V/As_{um}, H/As_{um}, M/ARs_{um})$ are not shown here.

From the previous discussion, it is thought that it is more useful to plot the load paths *normalised* by the vertical bearing capacity V_0, instead of by As_{um}. By doing this, all the analyses commence from $V/V_0 = 1$ precisely and therefore the shape of the load paths of different cases of strength increase rates, including the case of a uniform soil, can be easily compared to each other. Figs. 7.5, 7.6 and 7.7 show the load paths of $\rho 2R/s_{um} = 2$, 5 and 10; each plotted with the load paths of the analyses on a uniform soil for comparison.

As seen from the $(V/V_0, M/RV_0)$ plot in Fig. 7.5, after normalising the load paths for the case of a uniform soil are very similar to those for $\rho 2R/s_{um} = 2$. As has been mentioned, when the soil changes from a uniform soil $\rho 2R/s_{um} = 0$ to $\rho 2R/s_{um} = 2$, the peak moment load does not increase as much as the vertical bearing capacity. In the $(V/V_0, M/RV_0)$ plot in Fig. 7.5, a small drop in moment can be seen. However, this change is small and the shape of the load paths for both cases of strength increase rates are broadly similar.

This similarity is also seen between the load paths of a uniform soil and a higher rate of strength increase $\rho 2R/s_{um} = 10$ in Fig. 7.6. The load paths of $\rho 2R/s_{um} = 5$ (Fig. 7.7) are, to a less extent, similar to those of a uniform soil.

Whilst the size and shape of the normalised load paths in the moment directions (M/RV_0) remain almost unchanged over a large increase in strength increase rate, the size and shape of the load paths in the horizontal direction (H/V_0) reduces significantly. As mentioned earlier, the horizontal load peak value H_0/As_{um} is unchanged. Consequently, the size and shape of the load paths would remain almost unchanged if the horizontal load component is normalised by $V_{0,\rho=0}$, where $V_{0,\rho=0}$ is the vertical bearing capacity of a uniform soil, whereas the moment and vertical load components are normalised by V_0, where V_0 is the vertical bearing capacity corresponding to the strength increase rate $\rho 2R/s_{um}$. The new normalised load paths of $\rho 2R/s_{um} = 2$, 5 and 10 are plotted in Figs. 7.8, 7.9 and 7.10, respectively. As

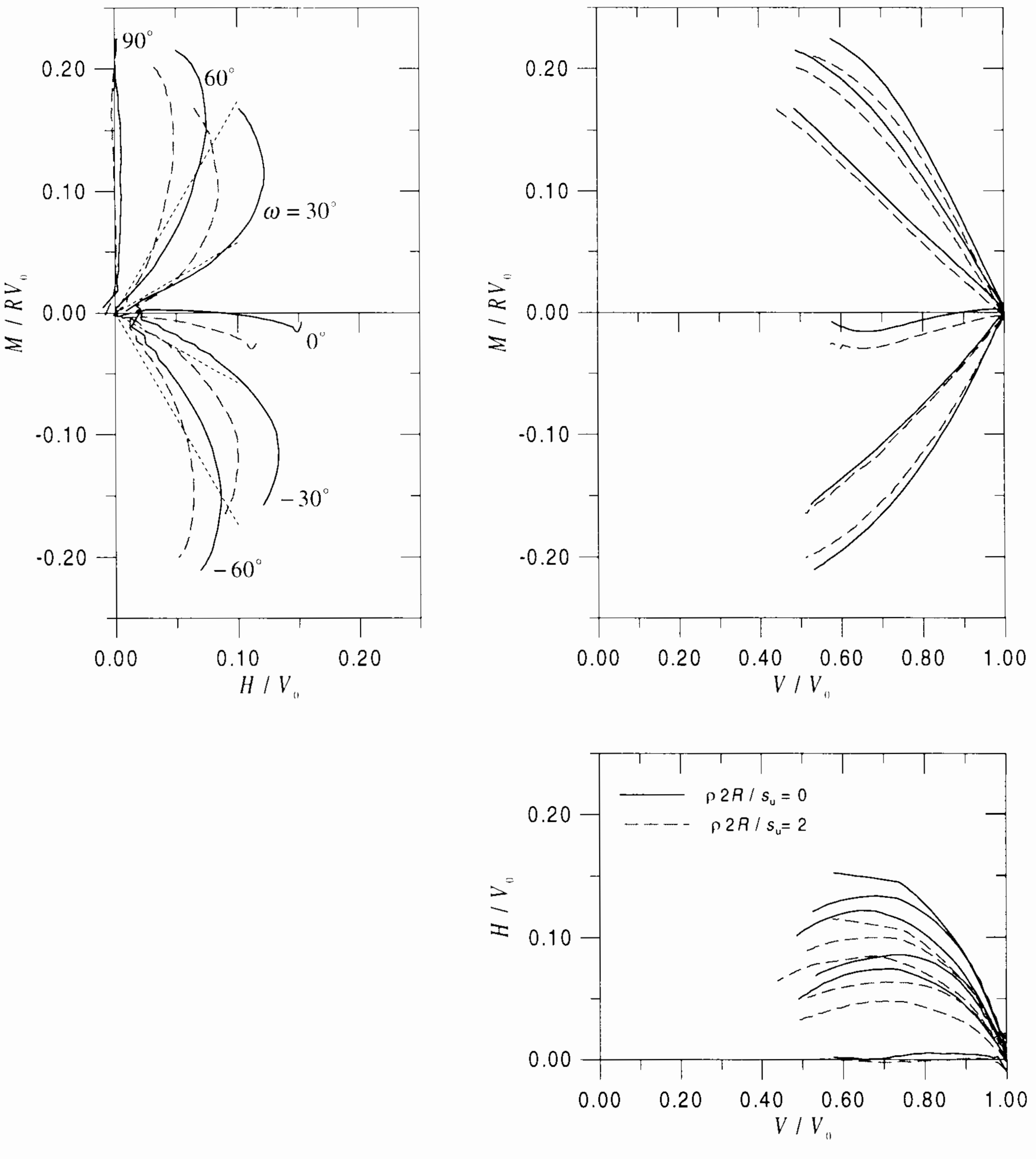

Figure 7.5: Comparison between load paths of $\rho 2R/s_{um} = 0$ and 2 (with H normalised to V_0).

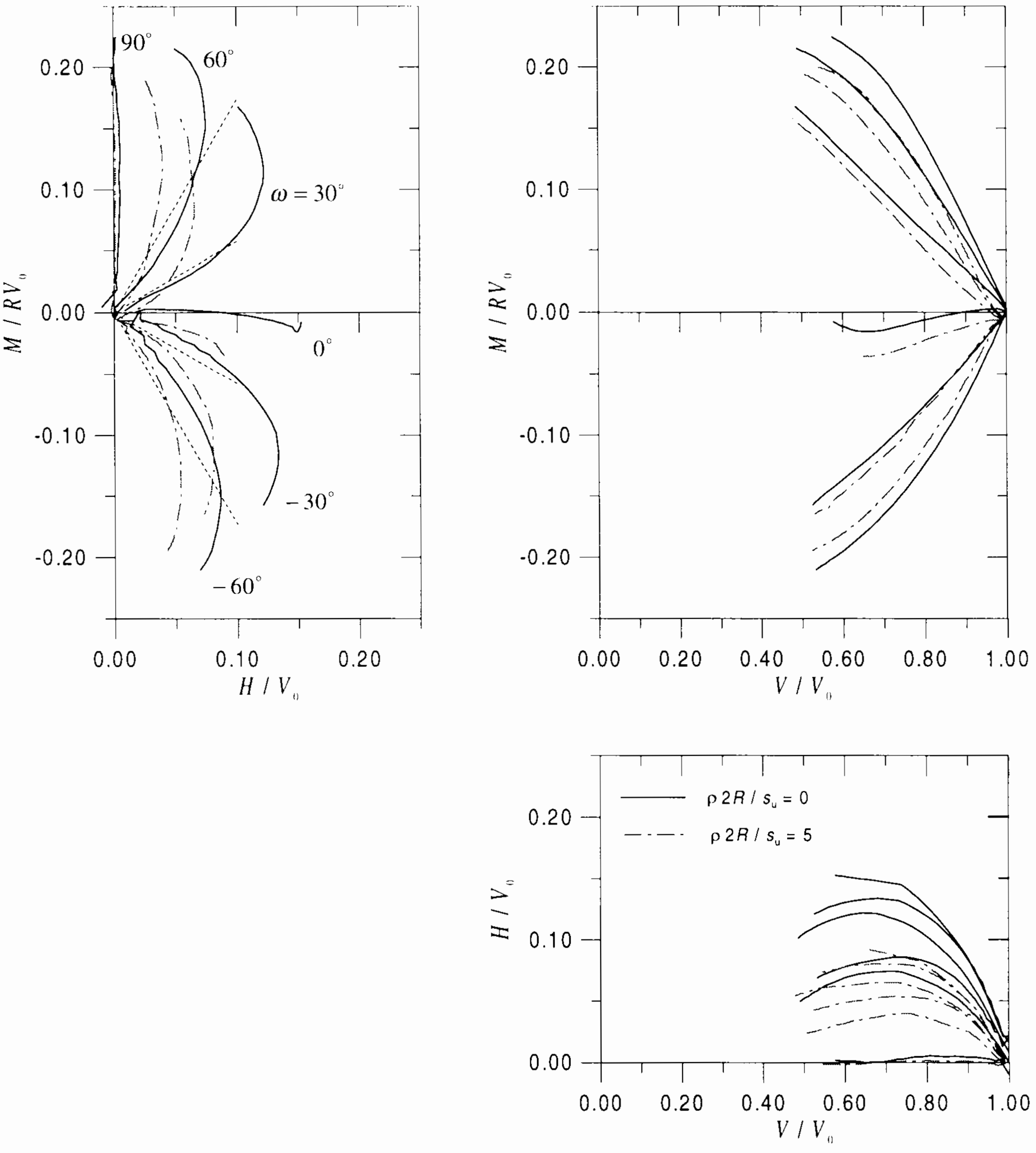

Figure 7.6: Comparison between load paths of $\rho 2R/s_{um} = 0$ and 5 (with H normalised to V_0).

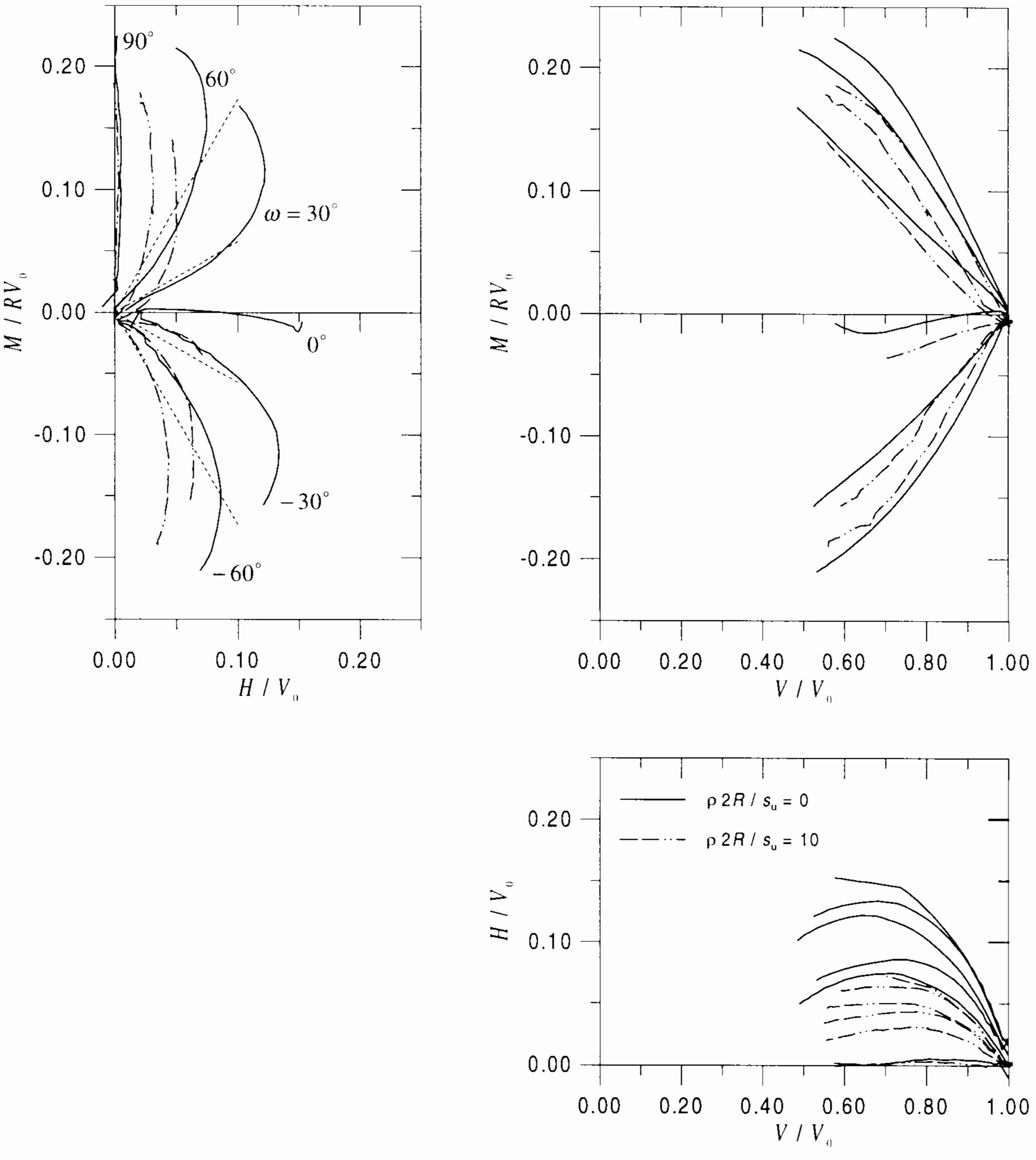

Figure 7.7: Comparison between load paths of $\rho 2R/s_{um} = 0$ and 10 (with H normalised to V_0).

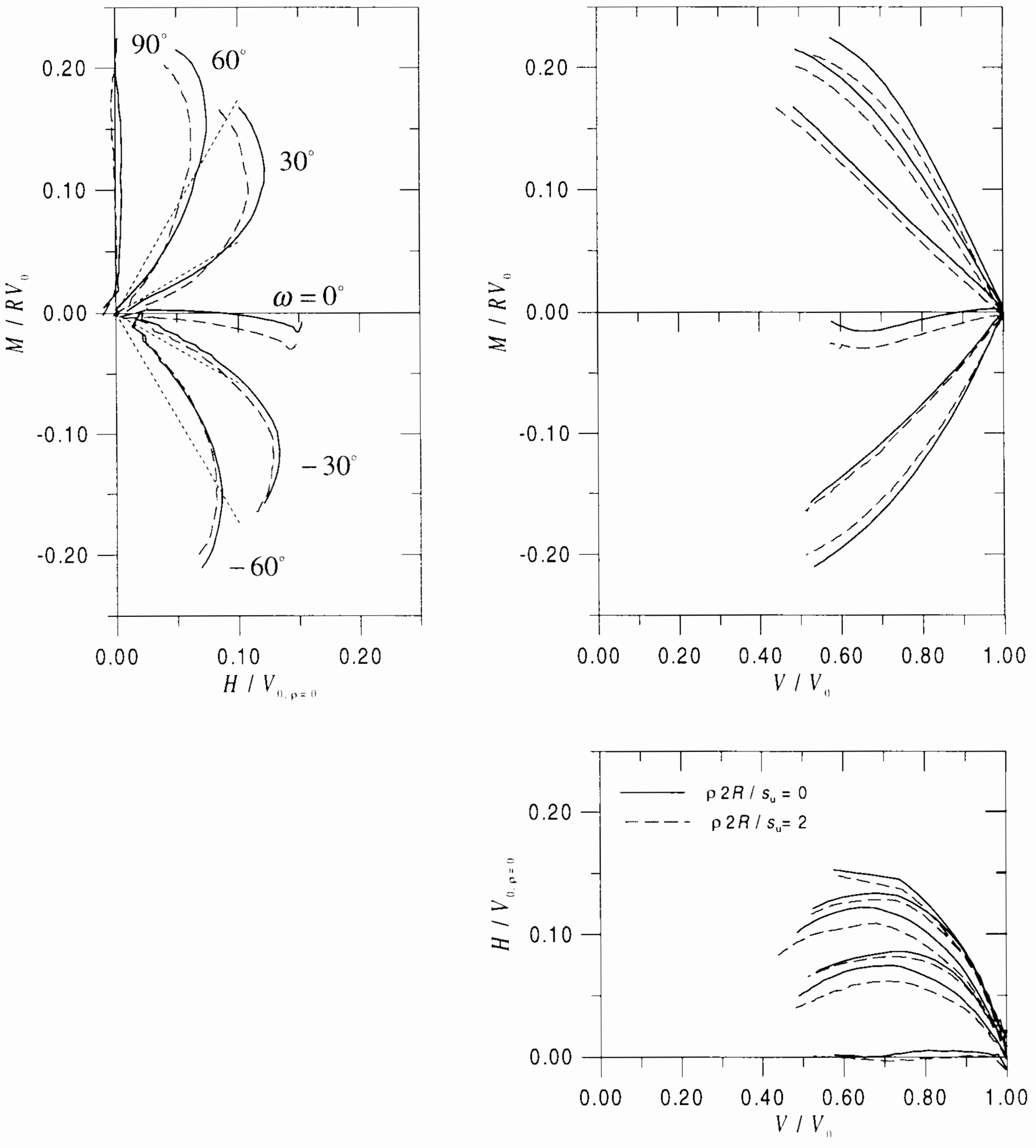

Figure 7.8: Comparison between load paths of $\rho 2R/s_{um} = 0$ and 2 (with H normalised to $V_{0,\rho=0}$).

can be seen in the $(V/V_0, H/V_0)$ and $(H/V_0, M/RV_0)$ plots of Fig. 7.8, the load paths of a uniform soil and $\rho 2R/s_{um}$ follow each other closely. The same can also be seen in Fig. 7.9, which compares the load paths of the analyses on a uniform soil and soil with $\rho 2R/s_{um} = 5$. Again, the load paths of $\rho 2R/s_{um} = 10$ does not compare so well with those of uniform soils as $\rho 2R/s_{um} = 2$ or 5.

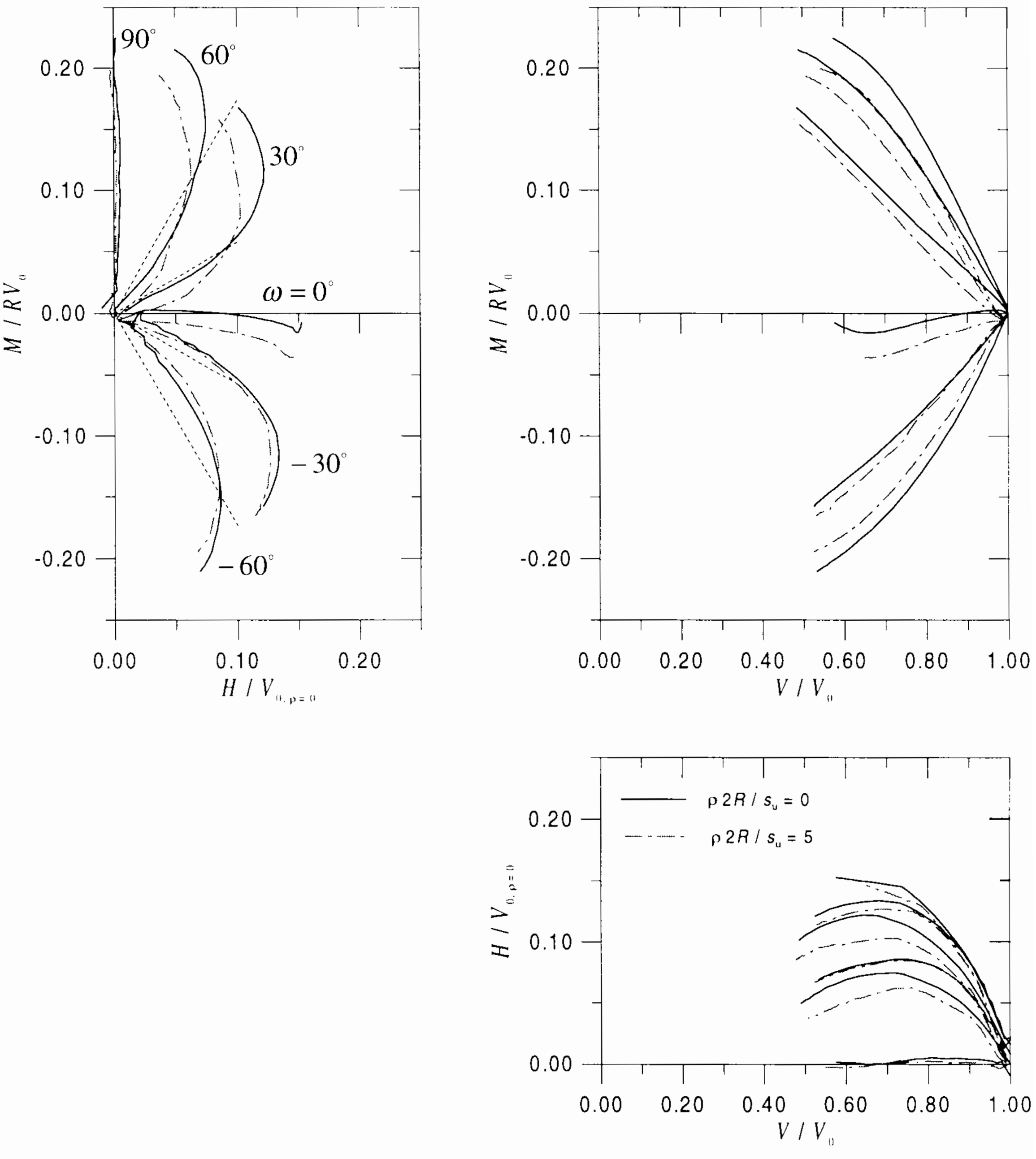

Figure 7.9: Comparison between load paths of $\rho 2R/s_{um} = 0$ and 5 (with H normalised to $V_{0,\rho=0}$).

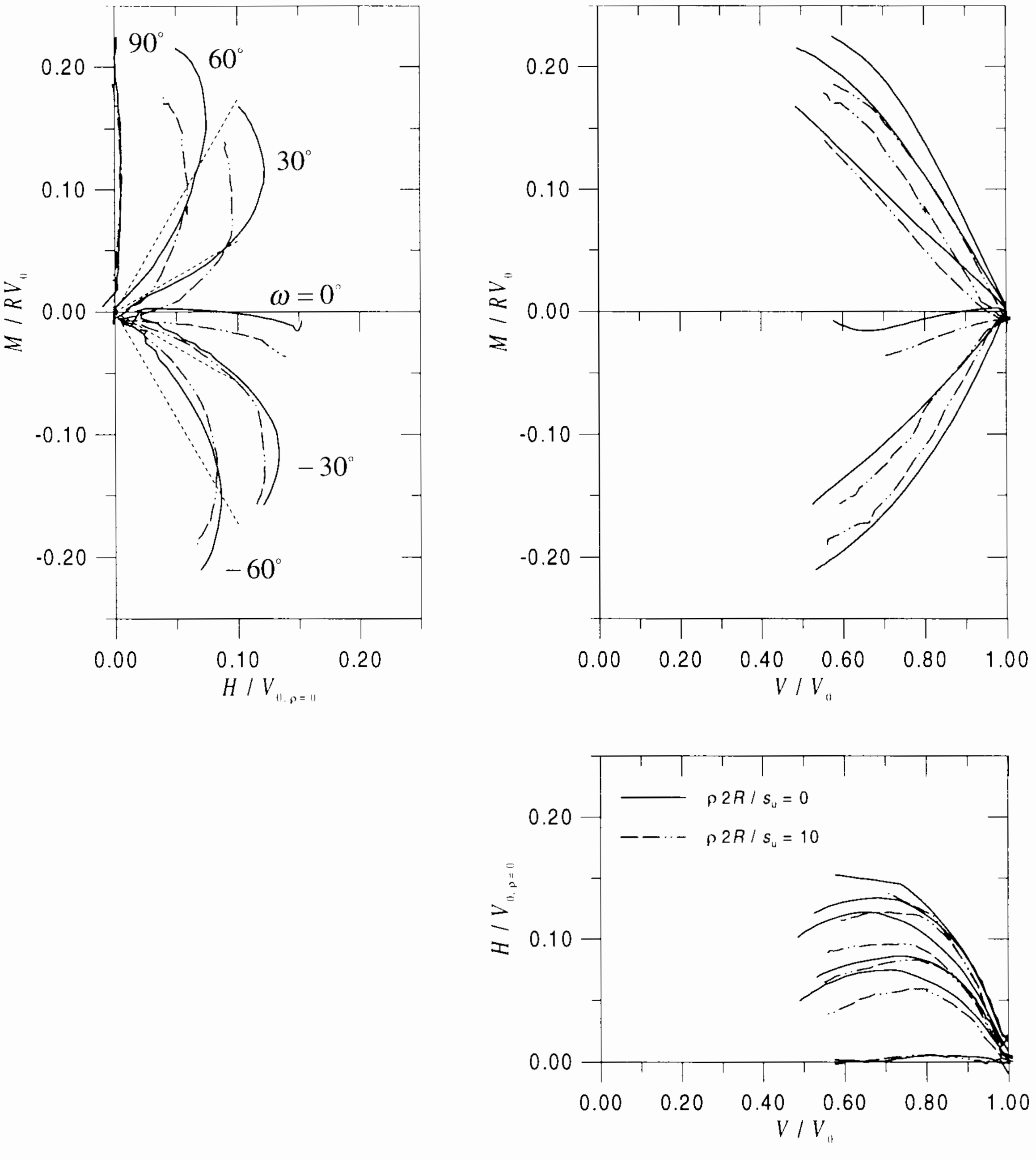

Figure 7.10: Comparison between load paths of $\rho 2R/s_{um} = 0$ and 10 (with H normalised to $V_{0,\rho=0}$).

7.2.3.1 Contours of the bearing capacity envelope

Using the load data, contours with respect to V/V_0 are plotted in Fig. 7.11. With horizontal loads normalised to $V_{0,\rho=0}$, the contours of different $\rho 2R/s_{um}$ rates also exhibit a degree of similarity with those for uniform soils (see Fig. 6.22b). The contours for three rates of increase of strength with depth also have an approximately elliptic shape. Exception are at $V/V_0 = 0{\cdot}8$ and $0{\cdot}85$ for $\rho 2R/s_{um} = 10$, however, it is believed that this irregular shape is caused by the lack of load data at these load levels). All the three envelopes show the effect of the sense of eccentricity with both maximum moment and horizontal loads occurring in negative eccentricity. As for the case of uniform soils (Fig. 6.22b) the rotation of the ellipses in Fig. 7.11 also changes with vertical load. At lower vertical load, the ellipses take on a more upright position. The overall size of the envelopes for $\rho 2R/s_{um} = 2$, 5 and, to a less extent, $\rho 2R/s_{um} = 10$, are comparable with that for a uniform soil.

It should be noted that the strength increase rate of $\rho 2R/s_{um} = 10$ is a very large value and less likely to be encountered in practice than the other two rates examined in this study ($\rho 2R/s_{um} = 2$ and $\rho 2R/s_{um} = 5$). For footings with radius $R <$ 10m, as stated by Gemenhardt & Focht (1970), the strength increase rate is usually less than $\rho 2R/s_{um} \leq 5$.

Therefore, it is concluded that for most applications, the shape and size of the bearing capacity envelope with horizontal load normalised to $V_{0,\rho=0}$, and vertical and moment loads to V_0 remain almost unchanged with strength increase rate.

7.3 Effect of cone angle

7.3.1 Literature review

As has been mentioned in Section 7.2.1, Houlsby & Wroth (1984) also considered the effect of cone angle on the vertical bearing capacity. The result of their lower bound solution for rough cones on a Tresca soil is shown in Fig. 7.12. It can be seen that from a flat footing ($\beta = 180°$) to a conical footing of $\beta = 90°$ (which is also the range of cone angles most commonly used for spud-can footings), the vertical bearing capacity does not change significantly.

It should be noted that the results shown in Fig. 7.12 are not the exact solution but the

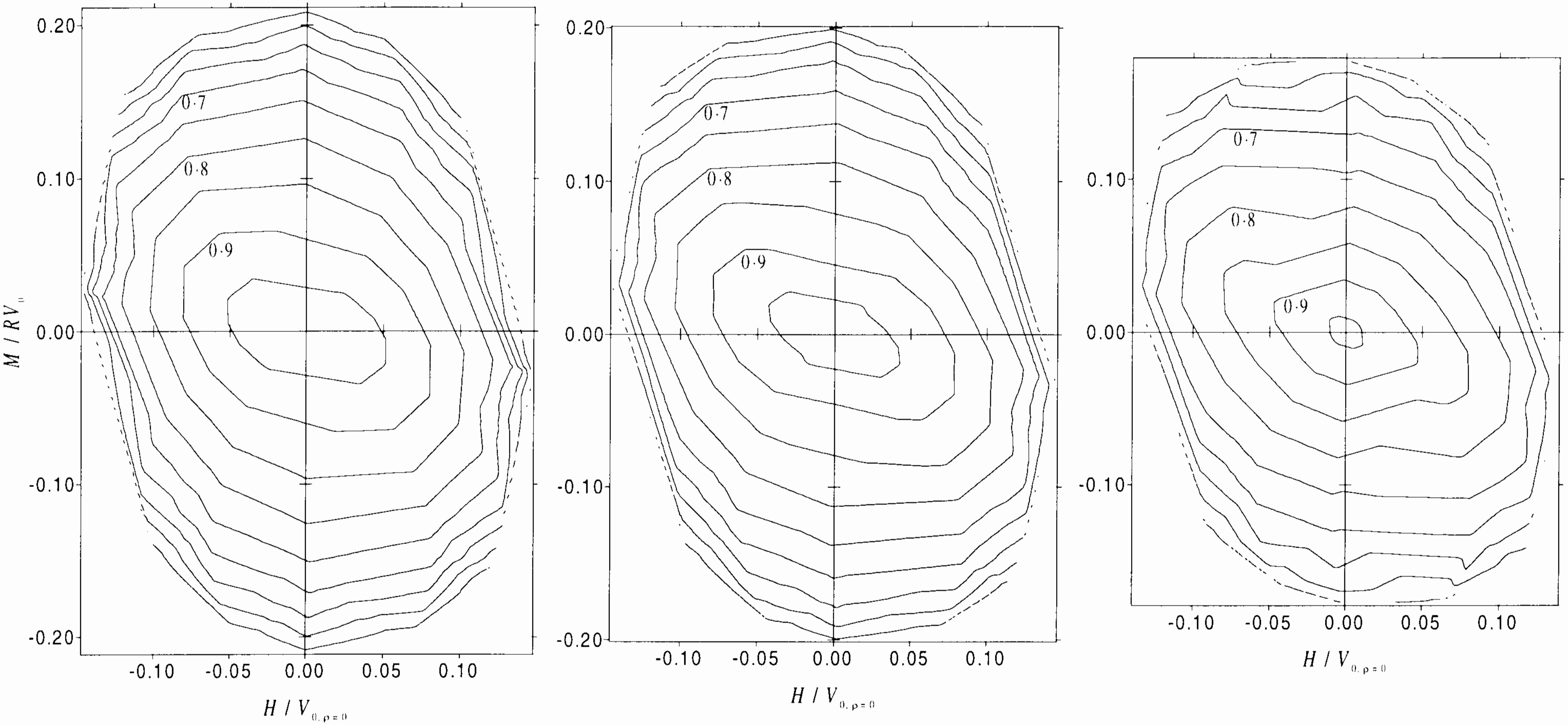

[a] $\rho 2R / s_{um} = 2$ [b] $\rho 2R / s_{um} = 5$ [c] $\rho 2R / s_{um} = 10$

Figure 7.11: Bearing capacity envelopes: contours with respect to V / V_0

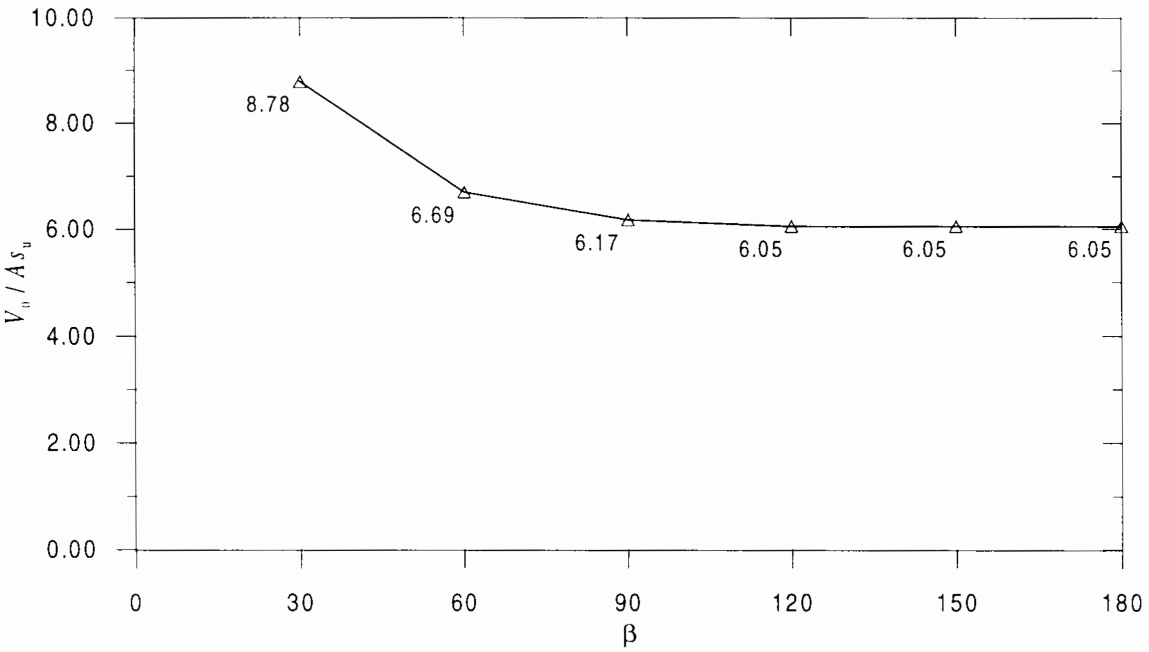

Figure 7.12: Variation of the vertical bearing capacity V_0/As_u with footing cone angle β (after Houlsby & Wroth, 1984).

lower bound results for Tresca soils. In addition, as discussed in Section 7.2.1, by multiplying these results by $2/\sqrt{3}$, the results are not the exact lower bound solution for von Mises soils.

Though cone angles in the range from $\beta = 180°$ (flat footings) to $\beta = 120°$ do not affect the vertical capacity significantly, it is expected that the horizontal bearing capacity will rise. Unfortunately, as with the case of soil strength increasing with depth, there are no known solutions for conical footings subjected to combined loading, except from finite element analyses. As mentioned in Section 6.2.5, a series of finite element analyses were conducted by Fugro Ltd as part of a Joint Industry Project coordinated by Noble Denton & Associates (1987). Footings with different cone angles were investigated (see Fig. 6.4). However, no attempt was made to model the loss of contact between the footing and the soil. It should be noted that for conical footings, significant loss of contact not only occurs under moment loading but also under horizontal loading. This causes some concern about the accuracy of the results by Noble Denton & Associates (1987).

7.3.2 Mesh preparation

Two cone angles $\beta = 150°$ and $\beta = 120°$, which cover the range of commonly used cone angle for spud-can footings, are investigated in this study. The mesh size and grading for

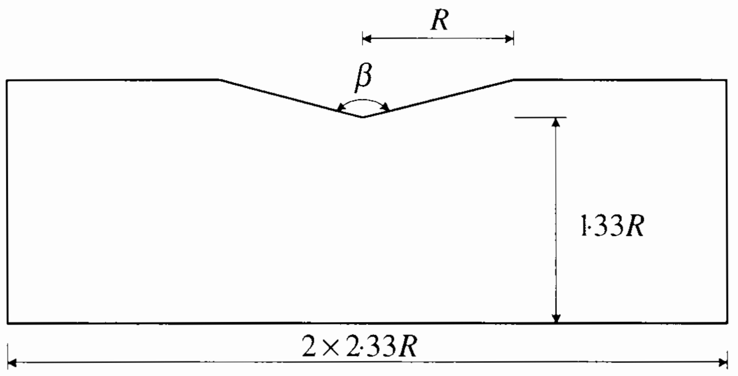

Figure 7.13: Mesh dimension used in the analyses for conical footings: 2427 nodes and 1407 elements for β = 120°; 2707 nodes and 1358 10-noded tetrahedral elements for β = 150°.

conical footings are similar to that of flat surface footing used in Section 6.3, except that the dimension of the mesh is changed so that the depth from the tip of the cone to the bottom of the mesh remains 1·33*R* as shown in Fig. 7.13. The radial dimension of the mesh remains unchanged at 2·33*R*. I-DEAS is capable of creating the solid model for the problem of this analysis, but it has difficulties when generating the mesh at the tip of the cone. To work around this, the mesh was generated for a flat footing and the *z* coordinate of the generated nodes was then transformed to form the conical shape.

7.3.3 Vertical bearing capacity results

Fig. 7.14 shows the results of the vertical bearing capacity analyses for the two conical footings. The lower bound solution for rough footings on Tresca suggests that the vertical bearing capacity remains constant at $V_0/As_u = 6{\cdot}05$ as the footing gets sharper from β = 180° to β = 150°. As mentioned earlier, $V_0/As_u = 6{\cdot}05 \times 2/\sqrt{3} = 6{\cdot}99$ is not the exact lower bound solution for a von Mises material but can serve as a resonable approximate solution. It will be recalled that the finite element result for a flat footing obtained in the previous chapter is $V_0/As_u = 7{\cdot}04$. As shown in Fig. 7.14 the vertical bearing capacity obtained from finite element analyses are 6·85 and 6·73 for β = 150° and β = 120°, respectively. This means that the vertical bearing capacity drops slightly as the footing gets sharper. This is believed to be caused by the introduction of the interface elements, which allows sliding in some parts of the interface between the footing and the soil. The yield state of the integration points in the interface is shown in Fig. 7.15. About 80% of the integration points for β = 150°, and 97% for β = 120°, are in cohesive yielding mode, so that the footing has some additional freedom

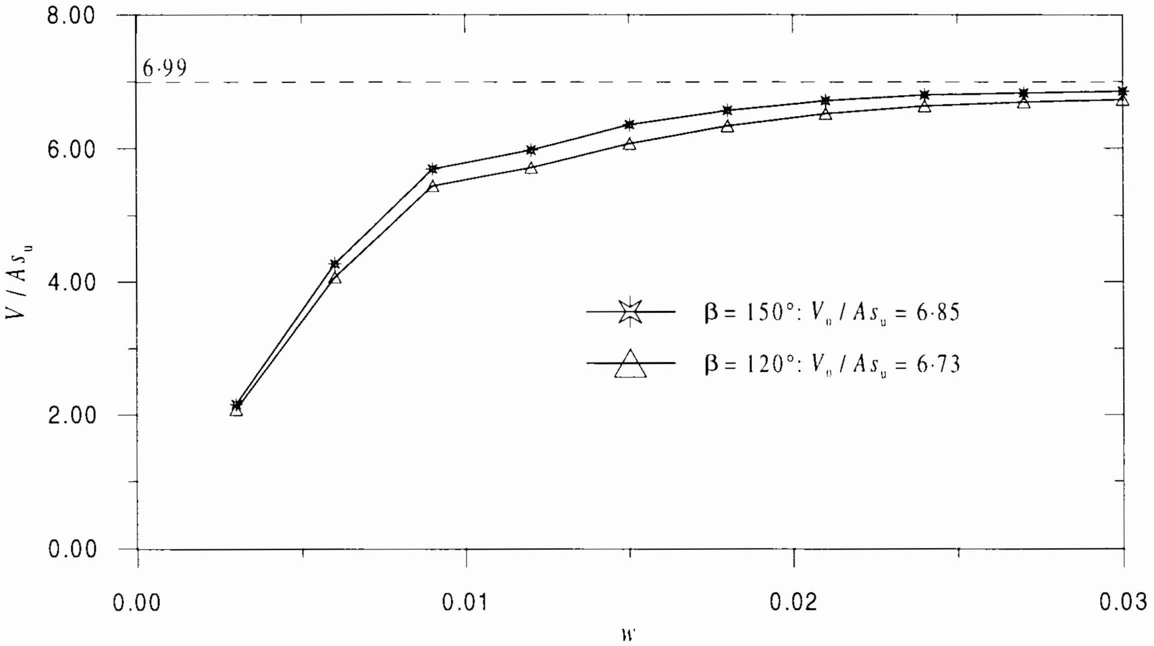

Figure 7.14: Vertical capacity results.

which lowers the vertical bearing capacity. The normal stress distribution in Fig. 7.16 shows that, for both cases of the cone angles, the interface elements behaves as well as for the flat footing.

7.3.4 Analysis of the test results

The point of reference to apply rotations and calculate moment loads is the intersection between the footing centre line and the plane containing the footing rim, which is the same as the reference point used in the elastic calculations in Chapter 2 (see Fig. 2.1).

The analyses in this study are similar to those of Chapter 6: for the case of each cone angle β, once the vertical bearing capacity has been reached, six combinations of horizontal and rotational displacement corresponding to $\omega = 0°, 30°, 60°, 90°, -30°$ and $-60°$ (see Fig. 6.15) are applied.

Fig. 7.17 shows the resulting load paths of a footing of $\beta = 150°$ plotted with the load paths of a flat footing obtained from the study in the previous chapter. As the (H, M) plot in Fig. 7.17 shows, pure sliding ($\omega = 0°$) generates a significant moment for a footing of $\beta = 150°$ compared to an almost zero moment for a flat footing. On the other hand, the pure rotation ($\omega = 90°$) test induces small horizontal load – very much the same as for flat

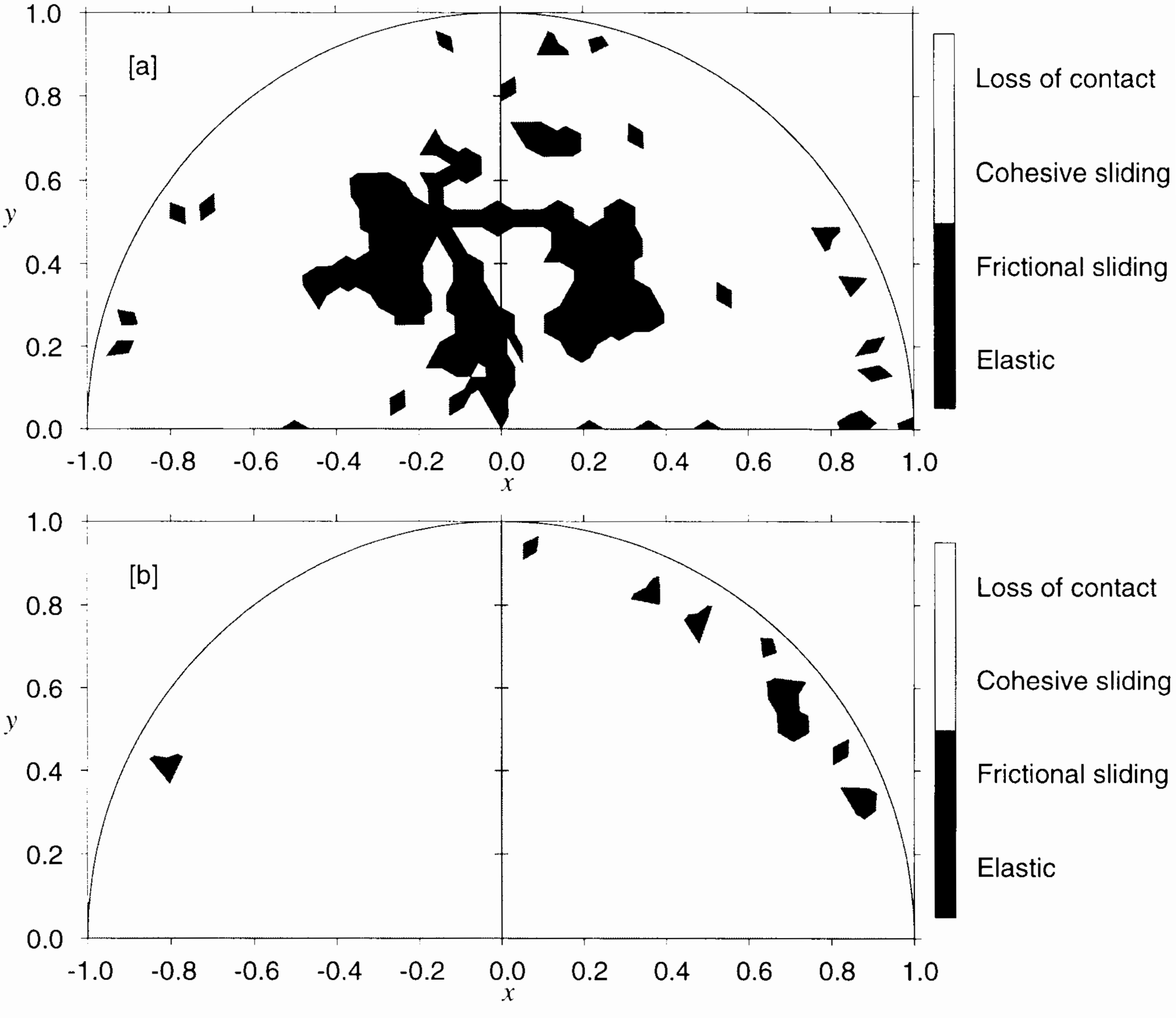

Figure 7.15: Yield state of the integration points in the interface at vertical bearing capacity (a) $\beta = 150°$; (b) $\beta = 120°$.

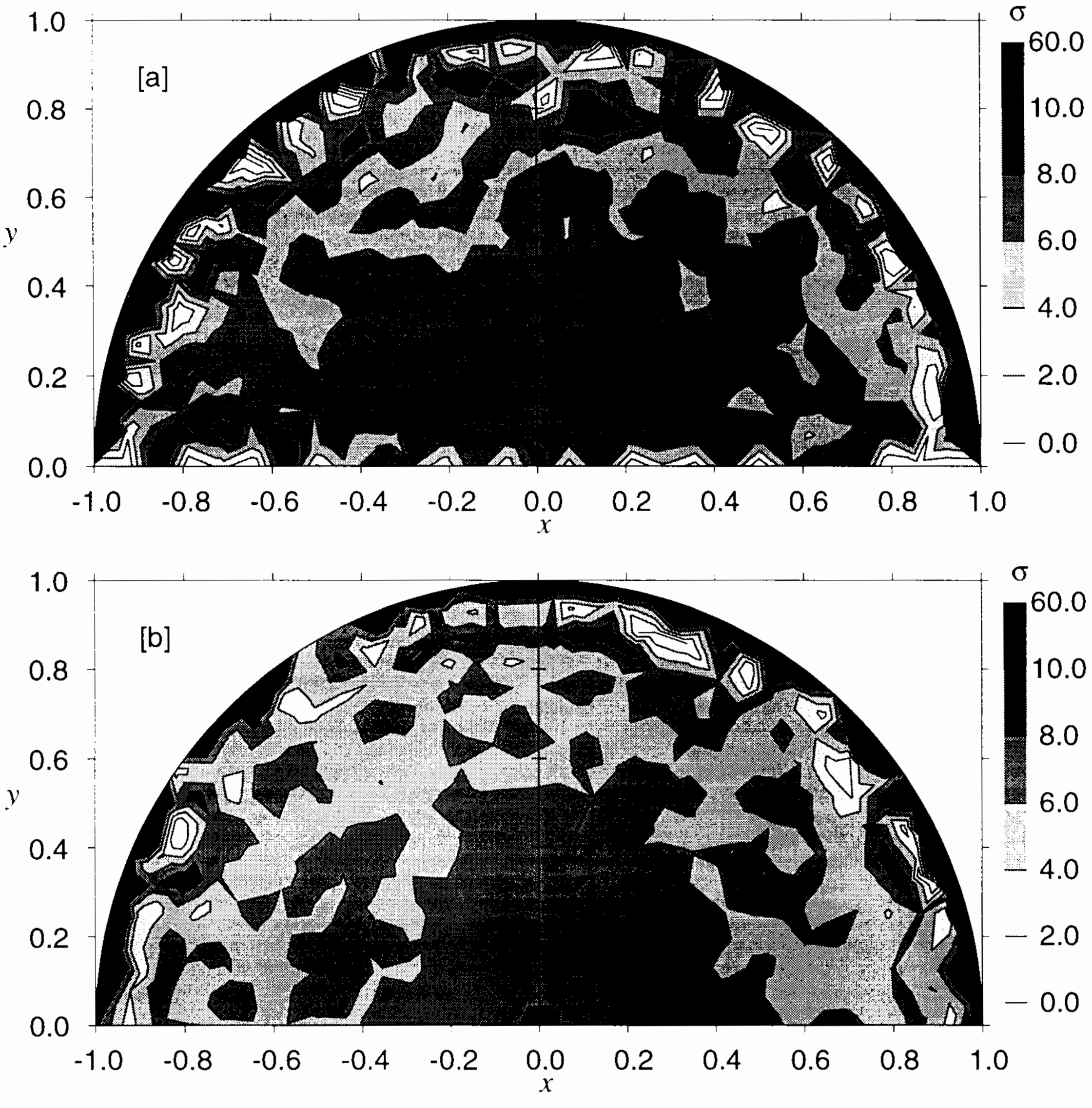

Figure 7.16: The distribution of normal stress in the footing–soil interface (a) $\beta = 150°$; (b) $\beta = 120°$.

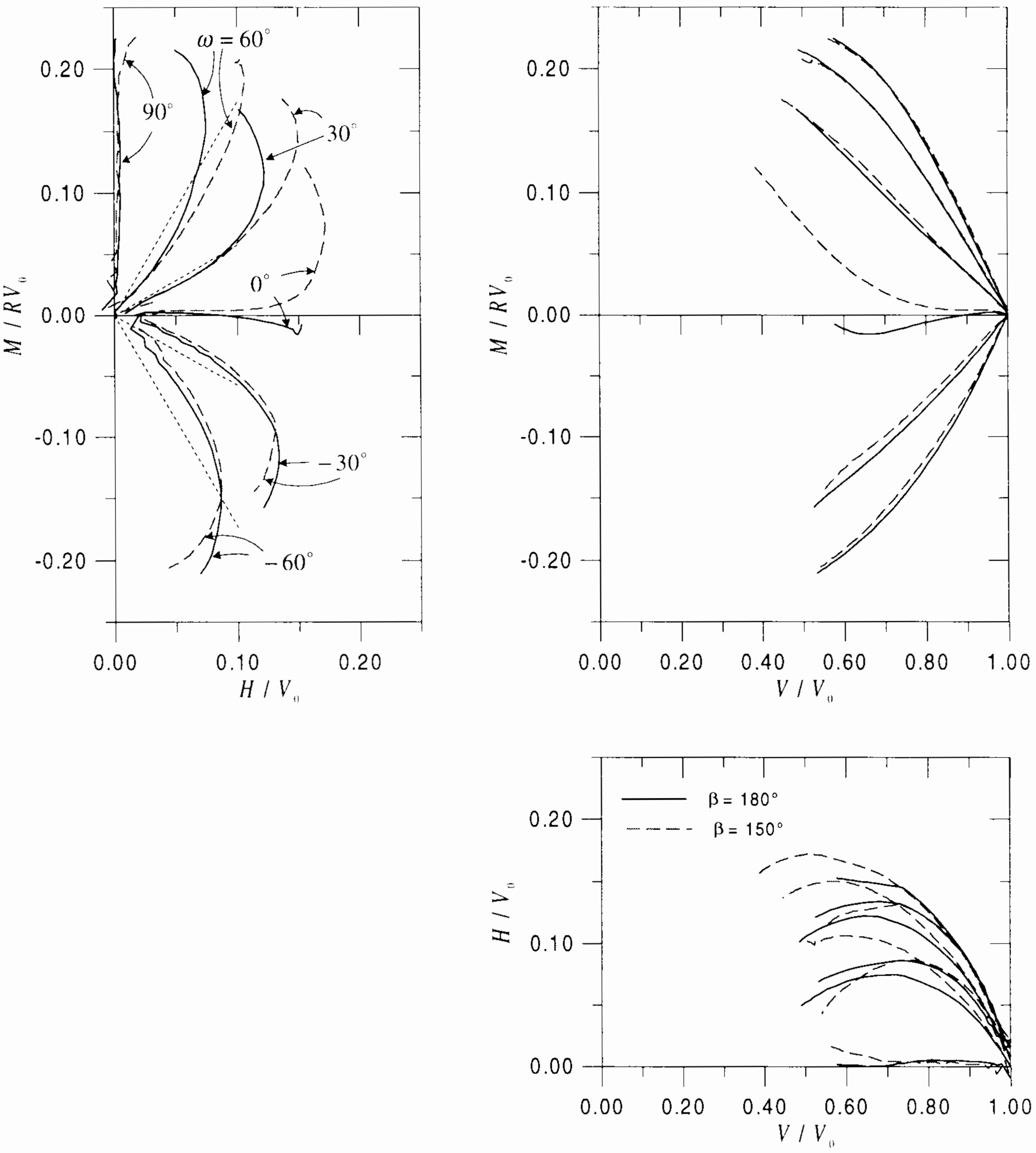

Figure 7.17: (V, H, M) curves from high V/V_0: β = 150°.

footings. The load paths in the (V, M) plot of β = 180° and β = 150° are almost identical, except for the pure sliding analysis (ω = 0°), in which a significant moment is generated.

These features of β = 150° can also be seen in the results of β = 120° in Fig. 7.18. The pure sliding analysis now generates even higher moment. The load paths in (V, M) are also quite similar between β = 180° and β = 120°.

For the footing of β = 150°, towards the end of the pure rotation analysis, a small horizontal load is generated (see the (H,M) plot in Fig. 7.17). For the footing of β = 120°, the horizontal load generated in the pure rotation analysis is more pronounced (see the (H,M)

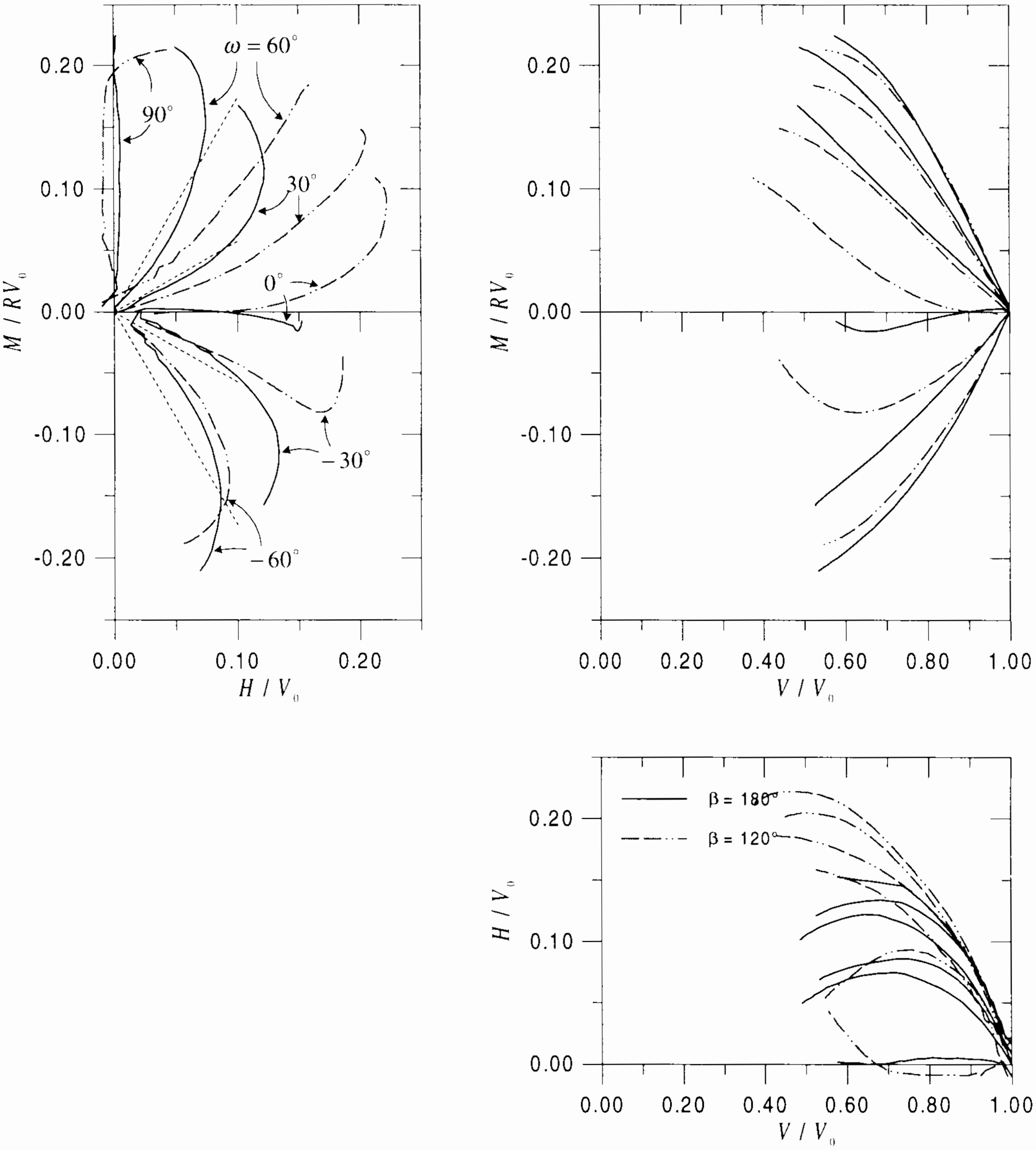

Figure 7.18: (V, H, M) curves from high V/V_0: $\beta = 120°$.

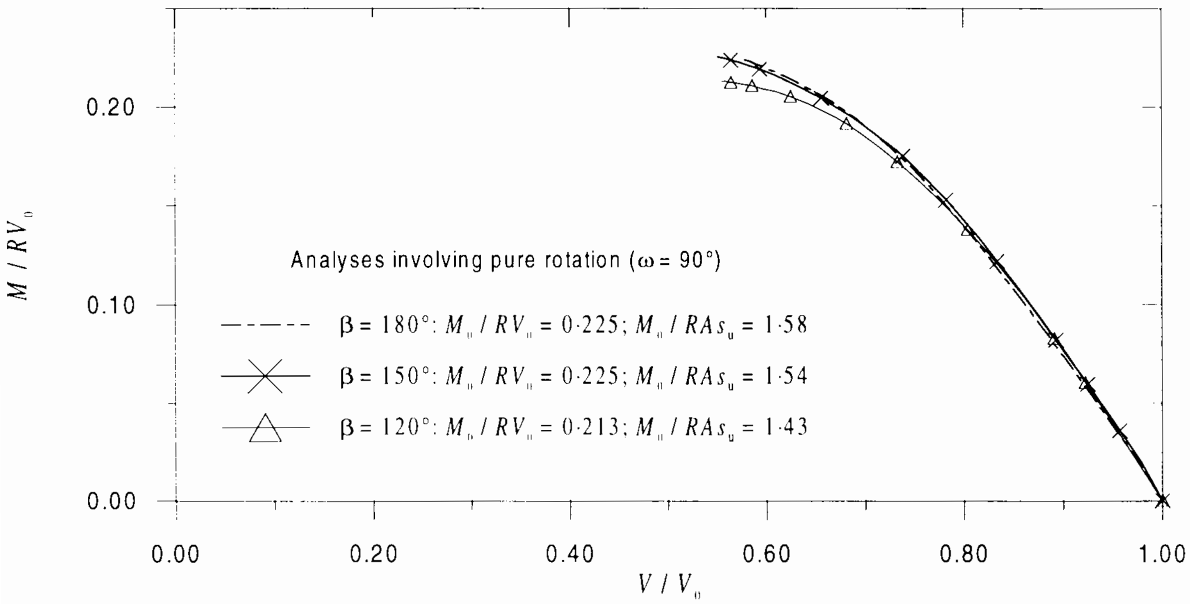

Figure 7.19: (V, M) interaction loci for footings with different cone angles.

plot in Fig. 7.18).

This horizontal load generated in the pure rotation analysis seems to reduce the peak moment load. As shown in Fig. 7.19, the peak moment in absolute terms (i.e. normalised against RAs_u) falls slightly when the the cone gets sharper. As the footing changes from flat to $\beta = 120°$, the peak moment M_0/RAs_u drops from 1·58 to 1·43 – a difference of 10%.

The effect of the cone geometry on the peak horizontal load is significantly larger. Fig. 7.20 shows the load paths of analyses involving pure horizontal displacements of a flat footing and two conical footings with $\beta = 150°$ and $\beta = 120°$. The figure shows that the peak horizontal load normalised against V_0 increases with sharper cones. The peak horizontal load normalised against RAs_u also increases as the cone gets sharper; as the cone changes from flat to $\beta = 120°$, the peak horizontal load H_0/As_u increases from 1·07 to 1·49 – a difference of 39%.

It is worth noting that one way to estimate the peak horizontal load for conical footings is to assume passive soil pressure on one side of the cone (Houlsby, 1996). Therefore, the following simple expression is obtained:

$$H_0 = As_u + 2A_v s_u \tag{7.1}$$

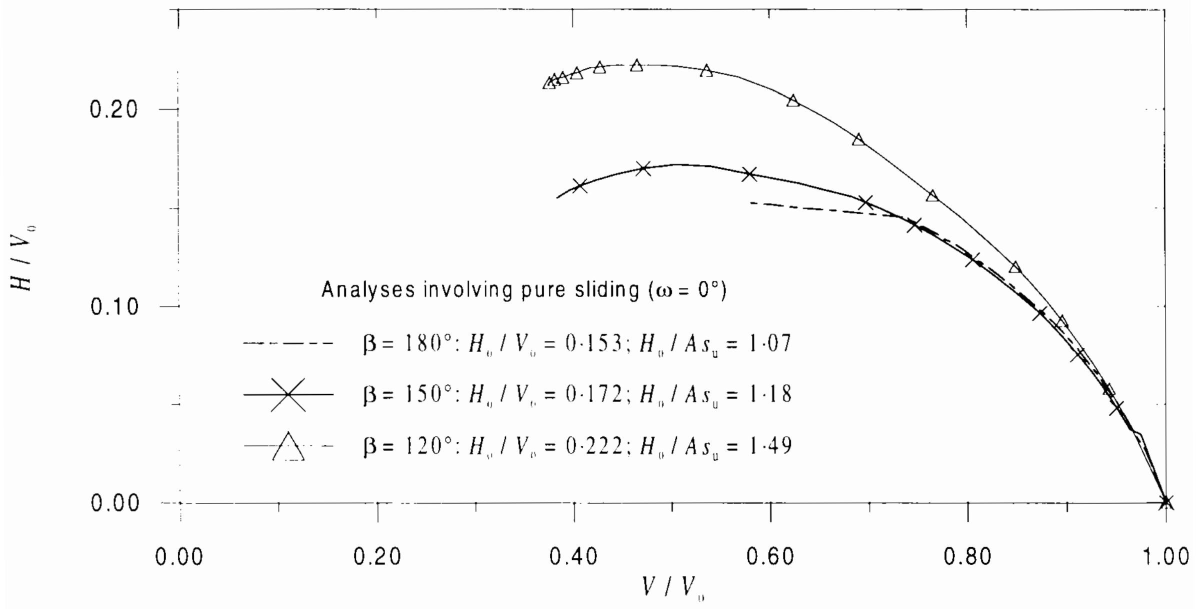

Figure 7.20: (V, H) interaction loci for footings with different cone angles.

where $A_v = R^2 \tan\left(\frac{\pi-\beta}{2}\right)$ is the vertical projected area of the footing. For $\beta = 120°$,

$$H_0 = s_u R^2 \left(\pi + 2 \times \frac{1}{\sqrt{3}}\right) = 4{\cdot}3 R^2 s_u \tag{7.2}$$

This value is a +37% increase compared to the peak horizontal load of a flat footing. This result is therefore in very good agreement with the finite element results.

The bearing capacity envelopes of the two conical footings is shown in the form of contours in Fig. 7.21. It can be seen that the bearing capacity envelope changes with cone angles in a more complicated way than it does with soil strength varying with depth as presented in Section 7.2. As has been mentioned, when the cone gets sharper, the maximum moment M_0/RV_0 decreases a little whereas the peak horizontal load H_0/V_0 increases significantly; this can also be seen in the contour plot.

Also, at the vertical load level at which the maximum horizontal load and moment occur (i.e. $V/V_0 = 0{\cdot}55$ for both cones), the ellipse-like contours rotate such that both the peak horizontal load and moment clearly occur in the quadrants of *positive* eccentricity.

As the vertical load progresses towards higher levels, the contours rotate to an upright position. At high vertical load levels ($V/V_0 > 0{\cdot}8$), both peak horizontal load and moment occur in negative eccentricity; the contours rotate such that their major axis lying in the second and the fourth quadrant, which is similar to the bearing capacity of flat footings. This suggests that when the vertical is high and is the most dominant of the three load components,

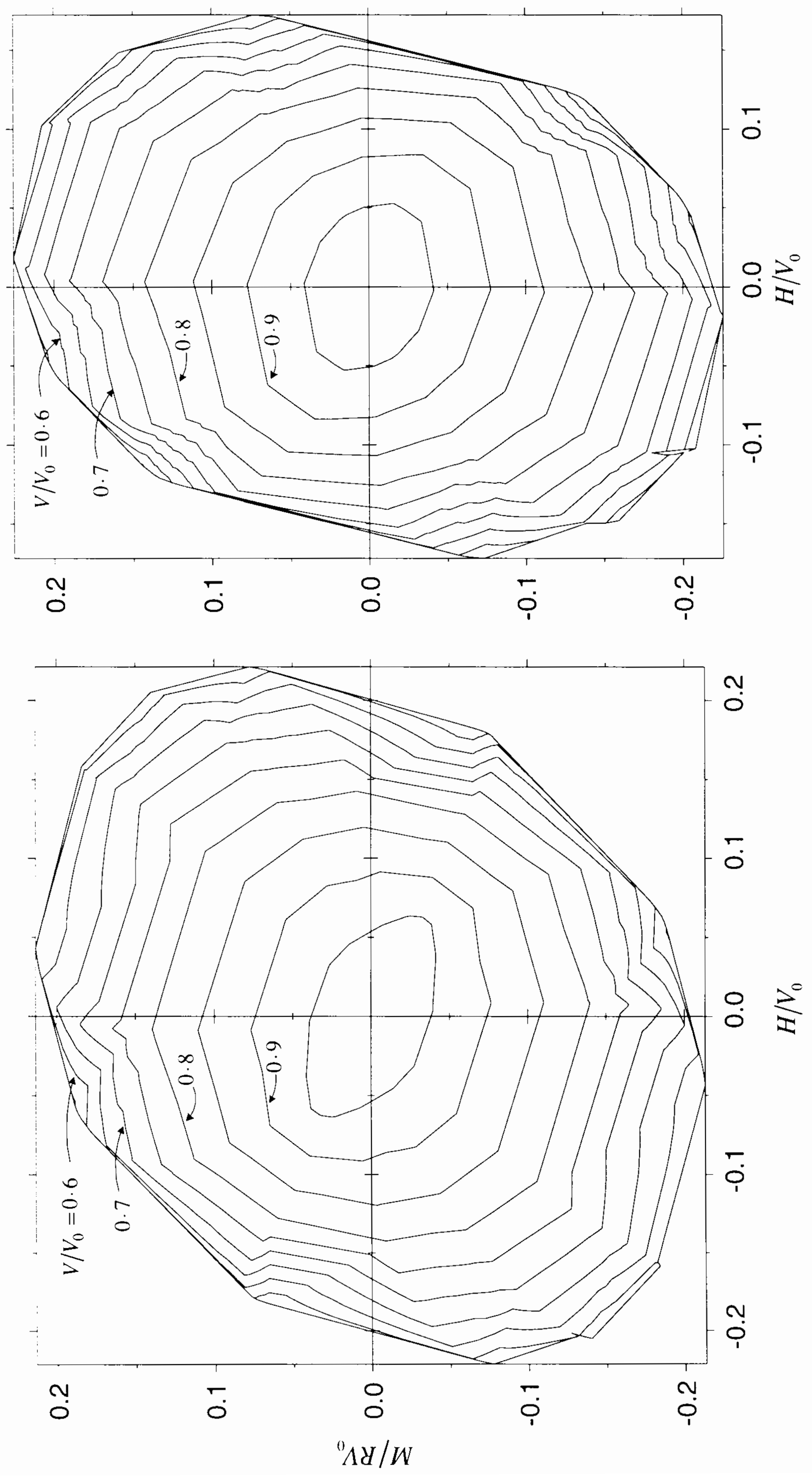

$\beta = 120°$ $\beta = 150°$

Figure 7.21: Contours of the bearing capacity envelopes for conical footings

changing the geometry of the footings does not significantly affect the failure behaviour under combined loading.

7.3.5 Stress distribution in the interface between the footing and the soil

The distribution of normal stress in the interface between the footing and the soil is plotted in Fig. 7.22 so that the behaviour of the interface elements can be examined. As in the previous chapter (see Section 6.4.3), three cases of loading are examined: pure rotation, pure horizontal displacement and a combined loading case with negative rotation. The results for the sharpest of the two cones examined in this study which is $\beta = 120°$ are plotted in Fig. 7.22. It can be seen that in all cases of loading, the stress distribution plot shows both the area in contact and in loss of contact with the soil as expected. It is also pleasing to see a clear division between the two areas for each case of loading.

Under horizontal loading, unlike the flat footing (see Fig. 6.18b), a large area of the conical footing loses contact with the soil. In fact, for the conical footing, a larger area of the footing loses contact with the soil under horizontal loading than under moment loading.

The significant change in geometry at the cone tip causes a stress concentration at this point. This behaviour at the cone tip is, however, reasonable. Under pure rotation (Fig. 7.22a), for example, the normal stress is high to the left of the tip and low to the right of the tip, which corresponds to the tip movement to the left during the loading. An opposite picture is seen in the stress plot of pure horizontal displacement (sliding to the right) in Fig. 7.22b. An extreme case for the cone tip is seen in the case of positive horizontal displacement combined with negative rotation in Fig. 7.22c. Both movements of the footing (i.e. positive horizontal displacement and negative rotation) push the cone tip to the right. At the same time, the negative rotational displacement keeps the footing area on the left in contact with the soil. This results in a small area at the left of the cone tip losing contact with the soil.

7.3.6 Comparison with recent experimental research

As mentioned earlier, Martin (1994) performed a series of combined loading tests using a conical footing involving different footing embedment on a soil with strength varying with

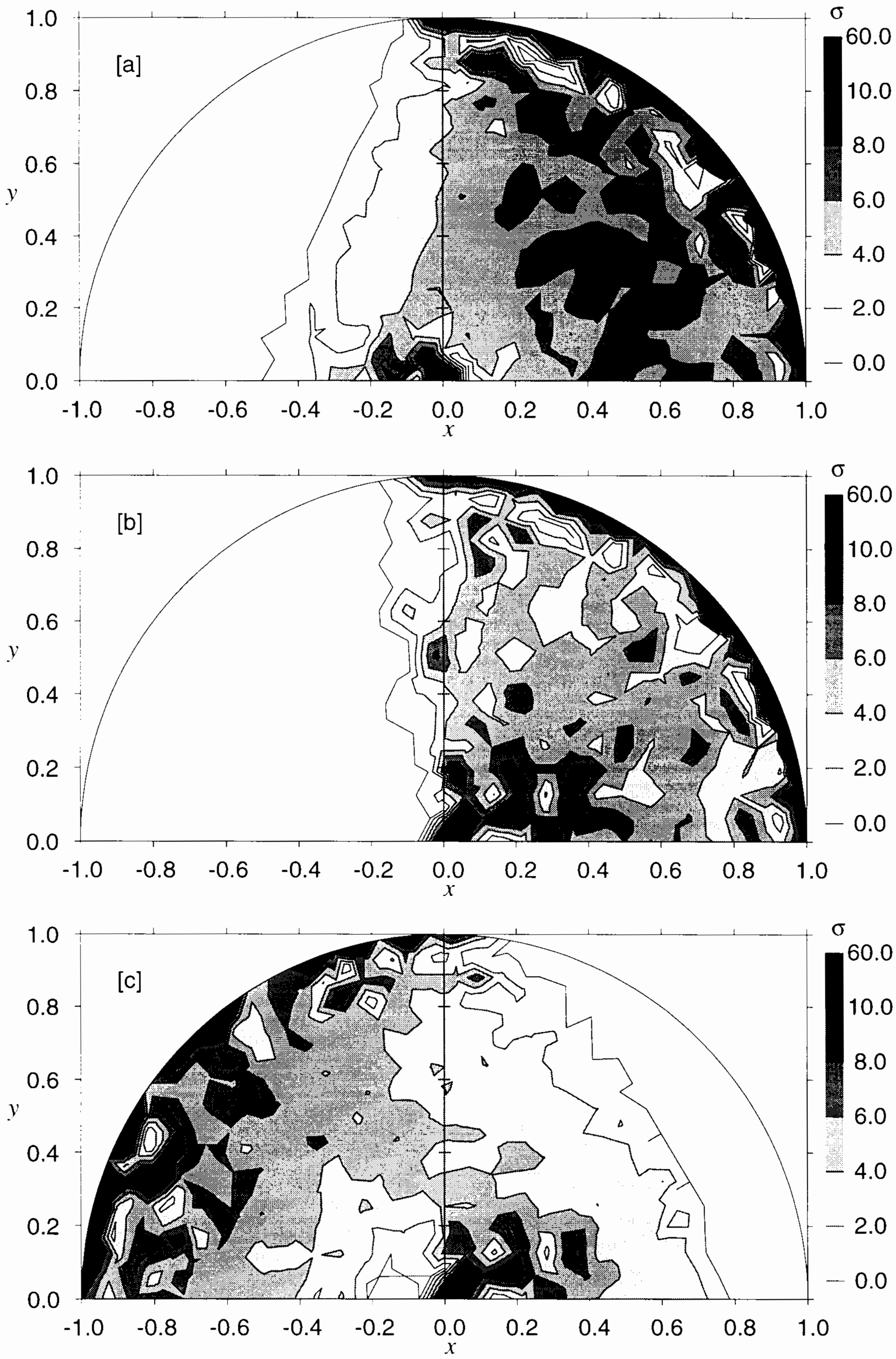

Figure 7.22: Distribution of normal stress in the footing–soil interface for the footing of $\beta = 120°$ (a) Pure rotation $\omega = 90°$; (b) Pure horizontal sliding $\omega = 0°$; (c) Combined rotation and horizontal displacement $\omega = -60°$ (negative rotation).

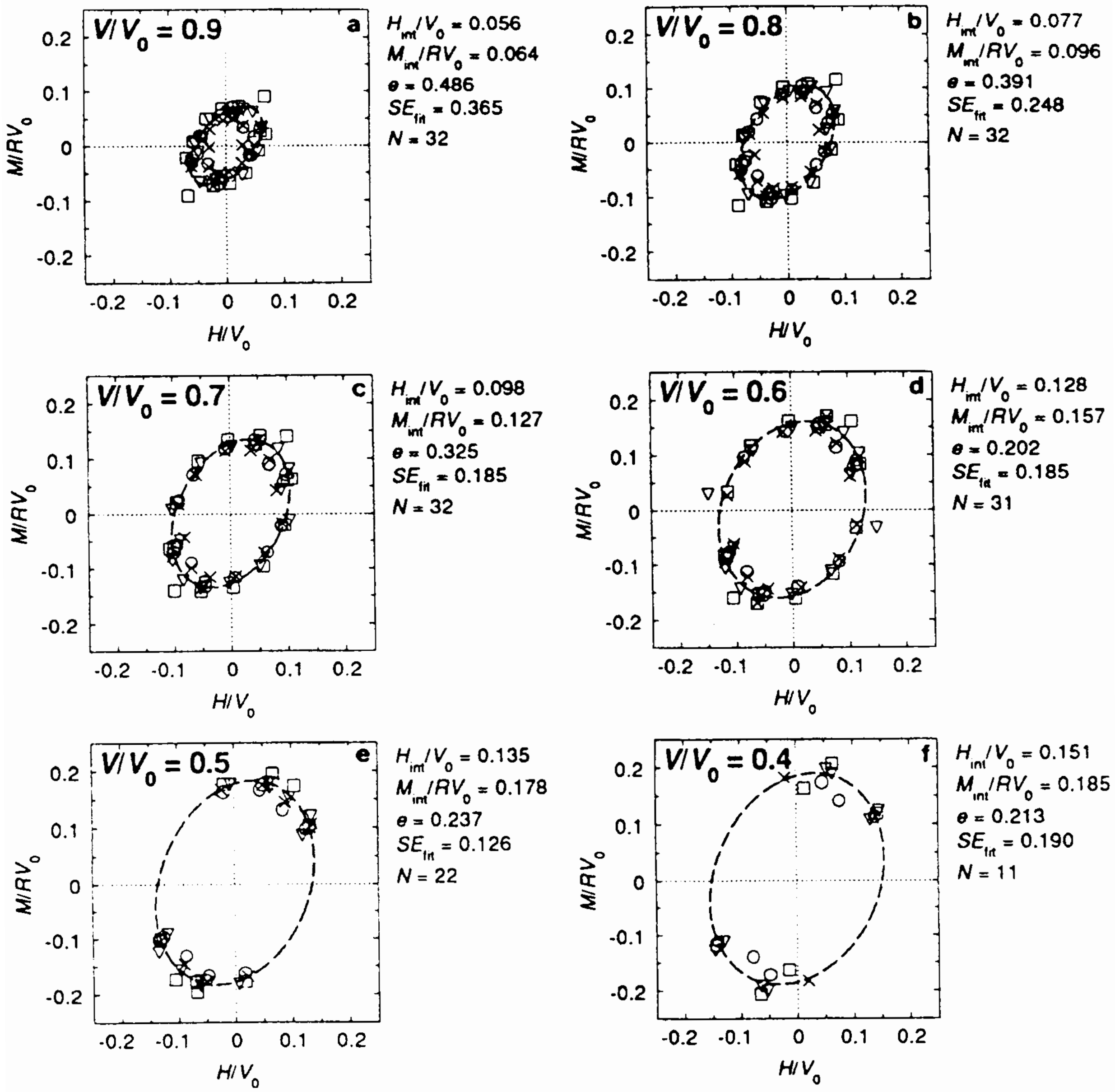

Figure 7.23: Martin's (1994) experimental results and fitted ellipses.

depth. Therefore, the results by Martin (1994) and by this study cannot be directly compared. However, the two sets of results are expected to be comparable to a certain extent.

In fact, one pronounced feature of the failure envelope for conical footings obtained in this study is that the ellipse-like contours (at lower vertical load levels) rotate such that both the peak horizontal load and moment clearly occur in the quadrants of positive eccentricity. This pronounced feature is also seen in Martin's (1994) results (Fig. 7.23).

However, Martin's (1994) results show that the ellipse rotation is relatively unchanged for vertical load from $V/V_0 = 0{\cdot}4$ to $V/V_0 = 0{\cdot}9$. The results of this study, however, show that when the vertical load is large and is the dominant collapse load, the failure envelope

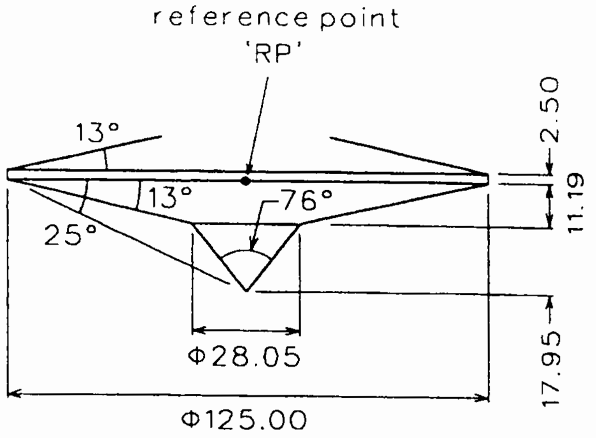

Figure 7.24: Dimension of the footing used in Martin's (1994) experiments.

takes on a more familiar shape as for flat footings with the peak moment and horizontal load occur in the quadrants of negative eccentricity.

The overall size of the envelope obtained from both studies are comparable. Martin (1994) used a conical footing with shape and dimensions shown in Fig. 7.24. In practice, such a footing is usually approximated to a cone with the same soil displacement volume (Houlsby & Martin, 1992). The footing used by Martin (1994) is therefore equivalent to a cone of $\beta \approx 140^\circ$. Compared to the finite element results of the cone of $\beta = 150^\circ$, the maximum horizontal load H_0/V_0 by Martin (1994) is about $H_0/V_0 = 0{\cdot}155$ – about 14% lower than that obtained from this study. The maximum moment load M_0/RV_0 by Martin (1994) is about 0·19, which is 18% lower than that obtained from this study.

It should be noted that in arriving at these figures, Martin (1994) performed least-squares analyses on the results of different embedment depths, but the results of the surface footing were excluded. This exclusion is based on the ground that the normalised load paths, i.e. $(V/V_0,\ H/V_0,\ M/RV_0)$, at $z_D = 0$ are remarkably different from those of embedded footings. Fig. 7.25a shows that the rotation test at the soil surface give higher normalised moment in tests commencing from $V/V_0 = 1$. Similarly, in the horizontal displacement test at the soil surface (see Fig. 7.25b), the normalised horizontal load is higher than that of other embedment depths. Therefore, for surface footings, the maximum horizontal and moment load obtained by the two studies are, in fact, in very close agreement.

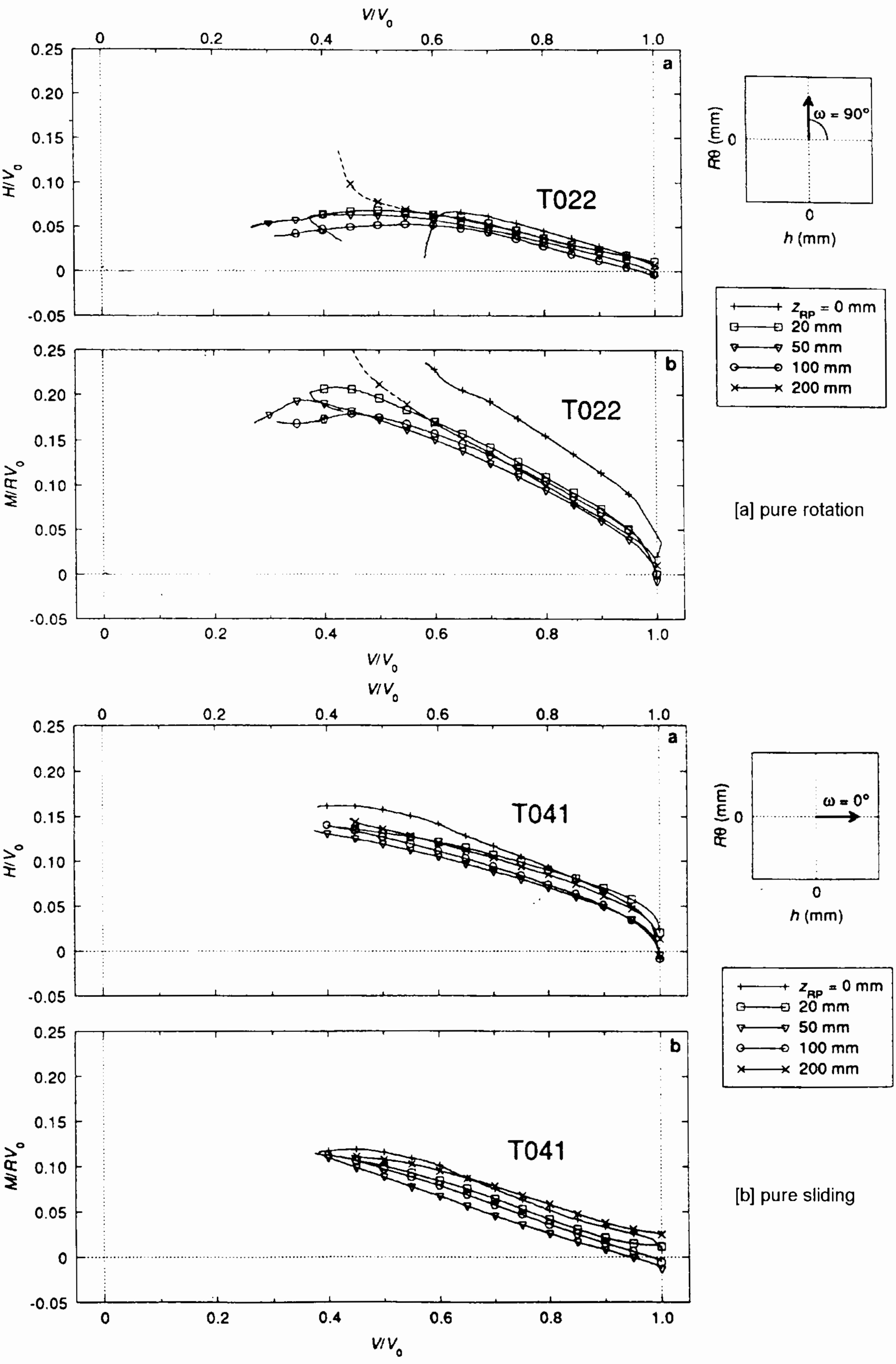

Figure 7.25: Normalised load paths (after Martin, 1994) (a) pure rotational displacement test; (b) pure horizontal displacement test.

7.4 Effect of footing embedment

7.4.1 Literature review

7.4.1.1 Vertical bearing capacity

As jack-up footings on clay can penetrate several meters, it is desirable to predict the footing penetration as accurate as possible. The empirical equation proposed by Skempton (1951) is recommended by both Gemenhardt & Focht (1970) and Young et al. (1984):

$$V_0/A = 6s_u(1+0{\cdot}2z_D/2R)+\gamma' z_D \;\leq\; 9s_u+\gamma' z_D \tag{7.3}$$

where γ' is the soil effective unit weight. The surcharge component of bearing capacity $\gamma' z_D$ in Equ. 7.3 is only applicable to cases where the hole above the footing remains open, but in practice (particularly on soft clays) there is usually at least partial backfilling during intallation of the jack-up. Endley et al. (1981) state that Equ. 7.3 gives better predictions of penetrations if complete backfilling is assumed and the $\gamma' z_D$ term is omitted.

The well-known formulae by Hansen (1970) and Vesic (1975) are also applicable to embedded footings. For the case of a square footing under purely vertical loading on undrained clays, the Hansen method gives:

$$\begin{aligned} V_0/A &= (\pi+2)s_u(1{\cdot}2+0{\cdot}4z_D/B)+\gamma' z_D, \quad z_D/B \leq 1 && (7.4)\\ V_0/A &= (\pi+2)s_u(1{\cdot}2+0{\cdot}4\arctan(z_D/B))+\gamma' z_D, \quad z_D/B > 1 && (7.5)\end{aligned}$$

For square footings on clay, the Vesic method gives:

$$\begin{aligned} V_0/A &= (\pi+2)s_u\left(1+\frac{1}{\pi+2}\right)(1+0{\cdot}4z_D/B)+\gamma' z_D, \quad z_D/B \leq 1 && (7.6)\\ V_0/A &= (\pi+2)s_u\left(1+\frac{1}{\pi+2}\right)(1+0{\cdot}4\arctan(z_D/B))+\gamma' z_D, \quad z_D/B > 1 && (7.7)\end{aligned}$$

Circular footings are treated as square footings with the same area, i.e. $B = R\sqrt{\pi}$.

The transition beteen Equ. 7.4 and Equ. 7.5 (as well as between Equ. 7.6 and Equ. 7.7) at $z_D/B = 1$ is not smooth because $\arctan(1) \neq 1$. Martin (1994) therefore suggests the use of $\arctan(\tan(1)z_D/B)$ instead of $\arctan(z_D/B)$ in Equ. 7.5 and Equ. 7.7. Fig. 7.26a shows vertical bearing capacity against footing penetration for various methods. The figure shows

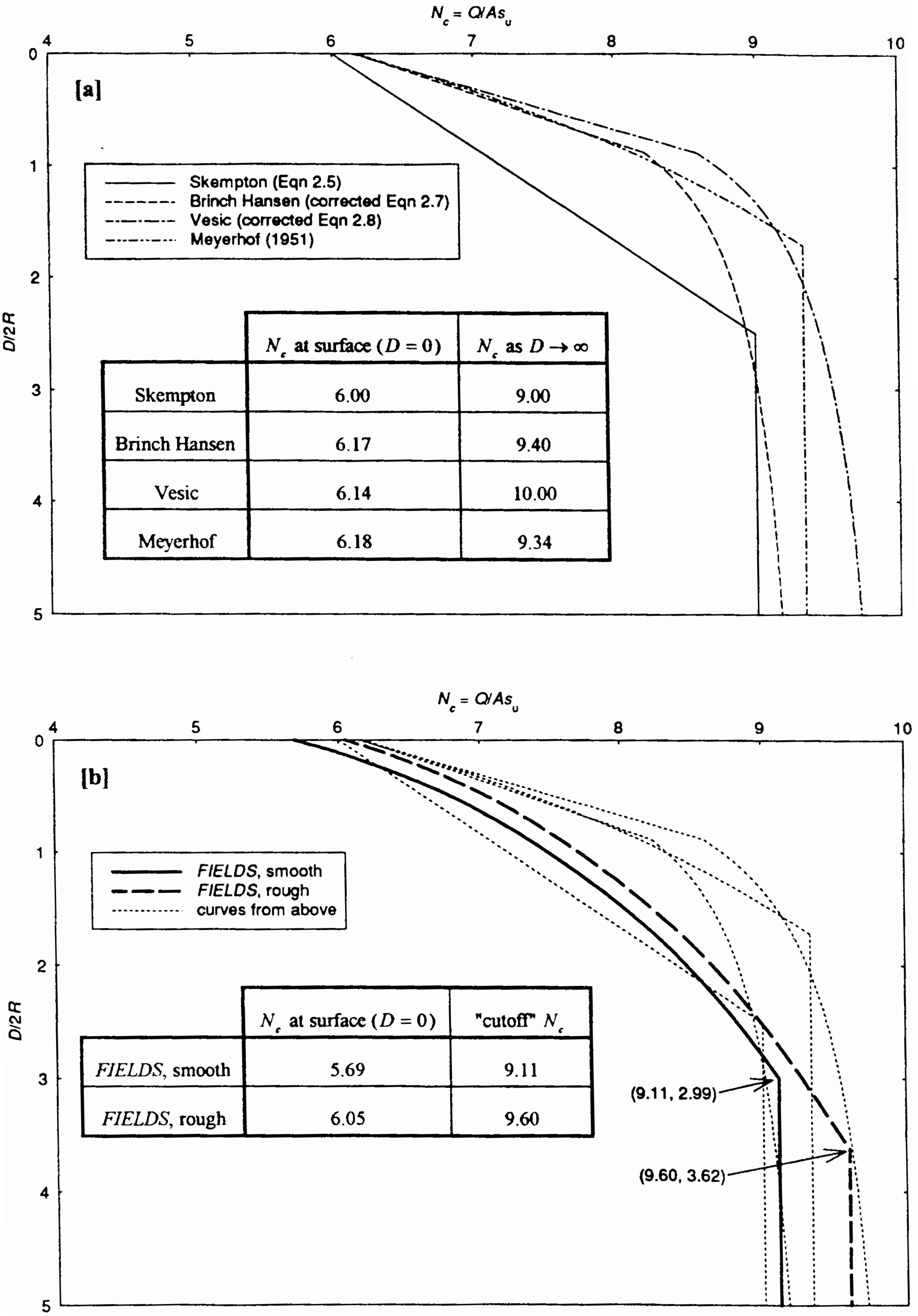

	N_c at surface ($D = 0$)	N_c as $D \rightarrow \infty$
Skempton	6.00	9.00
Brinch Hansen	6.17	9.40
Vesic	6.14	10.00
Meyerhof	6.18	9.34

	N_c at surface ($D = 0$)	"cutoff" N_c
FIELDS, smooth	5.69	9.11
FIELDS, rough	6.05	9.60

Figure 7.26: Variation of vertical bearing capacity factor with embedment depth for flat circular footings (after Martin, 1994) NB: D is the embedment depth.

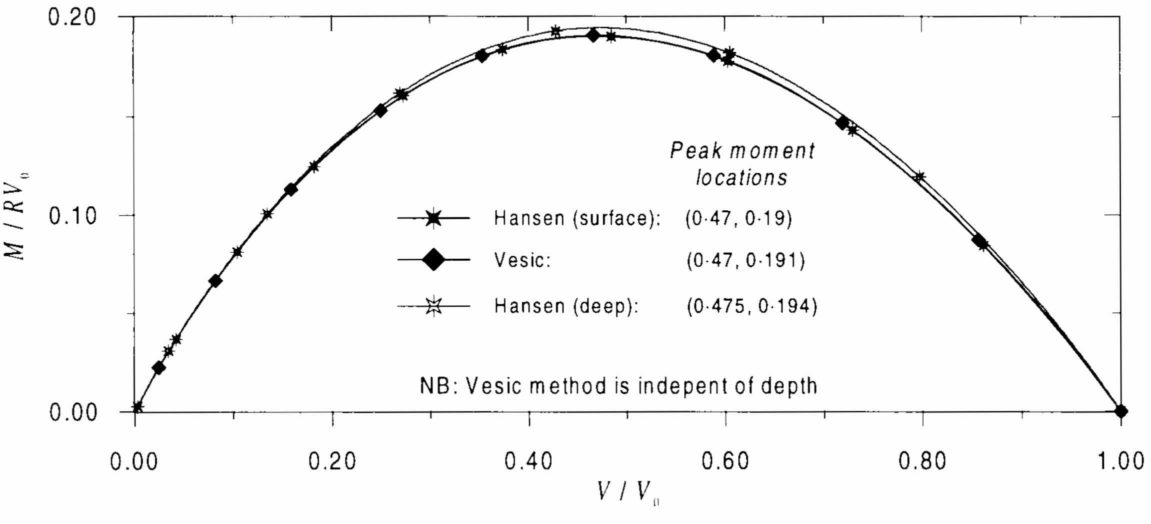

Figure 7.27: (V, M) interaction chart of a deep circular footing.

that up to embedments of about two diameters, Skempton's empirical formula is significantly conservative with respect to other three methods.

Using the method of characteristics (Houlsby & Wroth, 1984), Martin (1994) computed the lower bound collapse load of embedded circular footings using the computer programme FIELDS written by Professor G. T. Houlsby. Fig. 7.26b shows the results of the method of characteristics for smooth and rough footings. Also shown in the figure are the methods by Skempton (1951), Hansen (1970) and Vesic (1975) for comparison. The lower bound curve by the method of characteristics is slightly less conservative than the Skempton method.

7.4.1.2 Interaction between vertical load and moment

Using the concept of effective area, the Hansen method gives the following relation between vertical and moment bearing capacity for embedded circular footings on clays (cf. Equ. 6.5):

$$\frac{V}{V_0} = \left(\frac{1 + 0{\cdot}2(B'/L') + 0{\cdot}4 z_D/B'}{1{\cdot}2 + 0{\cdot}4 z_D/B} \right) \frac{A'}{A} \tag{7.8}$$

where $B = R\sqrt{\pi}$ and A is the gross footing area πR^2. Vesic's (1975) formula for surface circular footings (Equ. 6.6) remains unchanged for embedded footings. The two methods of Vesic and Hansen are plotted in Fig. 7.27, which shows that the $(V/V_0, M/RV_0)$ interaction loci for both surface and deep footings are very similar.

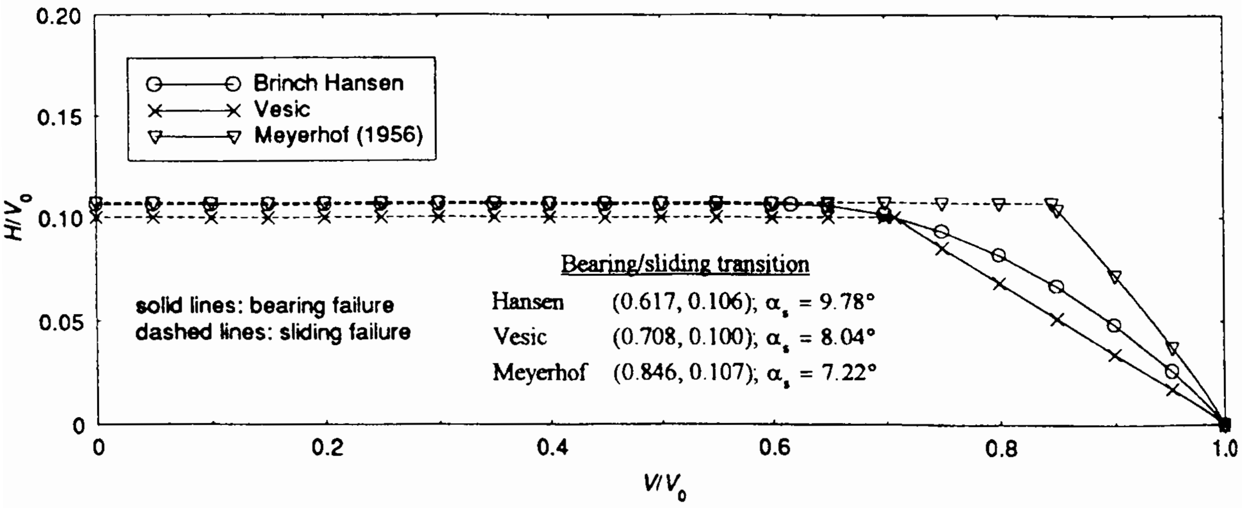

Figure 7.28: (V, H) interaction chart of a deep circular footing $(z_D \to \infty)$ (after Martin, 1994).

7.4.1.3 Interaction between vertical and horizontal loads

For embedded footings, the Hansen formula becomes (cf. Equ. 6.7):

$$\frac{V}{V_0} = \frac{1{\cdot}2 - 0{\cdot}7\left(1 - \sqrt{1 - H/H_0}\right) + 0{\cdot}4 z_D/B}{1{\cdot}2 + 0{\cdot}4 z_D/B}, \quad H \leq H_0 = A s_u \tag{7.9}$$

Vesic's (1975) formula for surface circular footings (Equ. 6.8) remains unchanged for embedded footing. Fig. 7.28 compares the normalised $(V/V_0,\ M/RV_0)$ failure envelopes obtained from the Meyerhof, Hansen and Vesic methods. At very deep penetrations in uniform clay all three methods give V_0 which increases up to a limiting value, whereas the maximum hotizontal load H_0 remains unchanged at $H_0 = As_u$. Therefore, the maximum normalised horizontal load H_0/V_0 drops significantly compared to that of surface footings (see Fig. 6.2). Fig. 7.28 also shows that the Vesic method is the most conservative for deep footings, whereas the Meyerhof method is the least conservative.

7.4.1.4 Interaction between vertical, horizontal loads and moment

Using the same approach described in Section 5.2.1.4 for a strip footing (i.e. an inclined load of magnitude $\sqrt{V^2 + H^2}$ is assumed to act centrally on a effective (reduced) foundation area), the bearing capacity envelopes for various methods described so far can be determined. The bearing capacity envelopes are not shown here but can be found in Martin (1994).

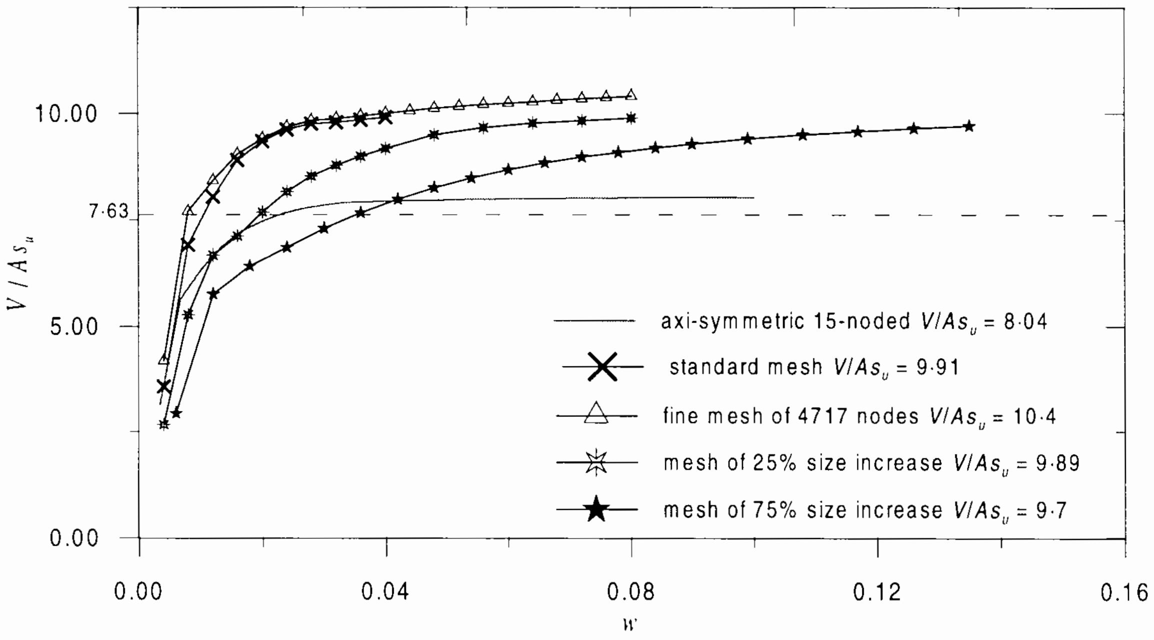

Figure 7.29: Vertical bearing capacity for $z_D/2R = 0{\cdot}25$.

7.4.2 Vertical bearing capacity

In practice, the most relevant range of jackup footings penetration is $z_D/2R \leq 2{\cdot}5$. As has been mentioned, Martin (1994) investigated the behaviour of a cone footing at different embedment depths ranging from $z_D/2R = 0$ to $z_D/2R = 1{\cdot}6$. From these tests, Martin (1994) found that though the $(V, H, M/R)$ bearing capacity envelope expands with increasing footing embedment depth, the shape of the bearing capacity remains unchanged. In this study one embedment depth $z_D/2R = 0{\cdot}25$ is investigated to examine the constant shape hypothesis.

For this embedment depth ($z_D/2R = 0{\cdot}25$), the lower bound solution for a Tresca soil using the method of characteristics is $V_0/As_u = 6{\cdot}61$. This suggests an approximate solution of $V_0/As_u = 7{\cdot}63$ for von Mises materials. A fine axi-symmetric mesh using high-order 15-noded triangular elements is used to calculate the vertical bearing capacity. As shown in Fig. 7.29, this 15-noded triangular mesh gives $V_0/As_u = 8{\cdot}04$, which is slightly higher than the approximate solution by the method of characteristics (+5·4%). This close agreement between the two methods confirms that both can serve as good approximate solutions to the problem of embedded footings.

A three dimensional mesh with the same grading and same size as the one used in Chapter 6 (i.e. the distances from the centre of the footing to the side and bottom boundary are

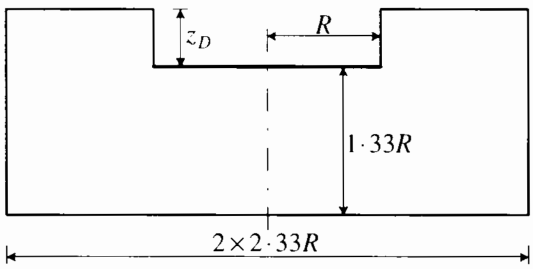

Figure 7.30: Standard mesh size for $z_D/2R = 0{\cdot}25$.

$2{\cdot}33R$ and $1{\cdot}33R$ as shown in Fig. 7.30) was generated. The result of the vertical bearing capacity analysis on this mesh, referred to as 'standard mesh' in Fig. 7.29, is $V/As_u = 9{\cdot}91$, which is +23% higher than the axi-symmetric result.

In order to improve the solution, different meshes were tried. Firstly, with the mesh dimensions unchanged, a new mesh with 4717 nodes, which is significantly finer than the standard mesh (with 2755 nodes) was generated. The other two meshes have the same mesh grading as the standard mesh, but their mesh depth and radial dimensions increase by 25% and 75%.

However, these larger and finer meshes do not deliver a better result as shown in Fig. 7.29; the fine mesh and the mesh with 25% dimension increase give the vertical ultimate load results which are within 1% of that of the standard mesh. The mesh with 75% dimension increase give a result only 3% lower than the standard result at $w/R = 0{\cdot}135$. At this stage the analysis is halted, but the vertical load had not reached its steady value by then. The trend of the load–displacement curve as shown in Fig. 7.29 seems to suggest that the ultimate load would be very close to that from the standard mesh.

The results from different meshes seems to suggest that unless an extremely fine mesh or better finite elements (such as 20-noded or 35-noded tetrahedral elements) are used, the solution cannot be improved. Unfortunately, both solutions demand excessive computation time. Therefore, the standard mesh is used in the following study of footing behaviour under combined loading.

It is worth noting that the meshing method used by Bell (1991) was also tried. As has been mentioned in Chapter 6, using this method, a two dimensional mesh is first generated on a plane. The two dimensional mesh is then rotated about the axis and the mesh is divided into tetrahera to form the final mesh. A mesh generated using this method give an ultimate vertical load which is very close to that from the axi-symmetric mesh. However, there is some concern that this mesh, which is perfectly axi-symmetric, behaves well under axi-symmetric loading but not as well under combined loading. Therefore, the mesh is not used in the following study of combined loading.

7.4.3 Programme of analyses

The analyses in this study are similar to those of Chapter 6: once the vertical bearing capacity has been reached, six combinations of horizontal and rotational displacement corresponding to $\omega = 0°, 30°, 60°, 90°, -30°$ and $-60°$ (see Fig. 6.15) are applied.

The resulting normalised load paths are shown in Fig. 7.31. It can be seen that the analyses are stable. The six analyses also give a good coverage for the bearing capacity envelope as shown in the $(H/As_u, M/RAs_u)$ plot in Fig. 7.31.

Compared with surface footings, the peak moment increases from $M_0/RAs_u = 1{\cdot}58$ (for surface footing) to $M_0/RAs_u = 2{\cdot}38$ – an increase of $+51\%$. It will be recalled from Section 7.4.2 that the peak vertical load for this embedded footing is $V_0/As_u = 9{\cdot}91$ which is $+41\%$ higher than that of the surface footing.

At the same time, the peak horizontal load remains almost unchanged at $H_0/As_u = 1{\cdot}05$ compared to $H_0/As_u = 1{\cdot}07$ of the surface footing. This value is, however, lower than the exact value $H_0/As_u = 2/\sqrt{3} = 1{\cdot}155$. This is believed to be caused by the stress concentration on the footing as discussed in Section 6.6.1.

As the peak vertical load and moment increase with embedment and the peak horizontal load remains unchanged, the load paths with H normalised to $V_{0,\mathrm{surf}}$, where $V_{0,\mathrm{surf}}$ is the vertical load capacity of the surface footing, is used to compare with those of the surface footing. The other two components, V and M, are normalised to V_0 and RV_0, respectively, where V_0 is the appropriate vertical load capacity at each embedment depth. Fig. 7.32 shows the normalised load paths $(V/RV_0, H/V_{0,\mathrm{surf}}, M/RV_0)$ of both surface footing and the embedded footing. The figure shows that for all analyses with combined displacements ($\omega = 60°, 30°, -30°$ and $-60°$) of the embedded footing, horizontal load $H/V_{0,\mathrm{surf}}$ is significantly higher than the corresponding analyses of the surface footing.

Figs. 7.33 and 7.34 show in detail the analyses involving pure rotation and pure horizontal displacements of both the surface and the embedded footings. It can be seen that

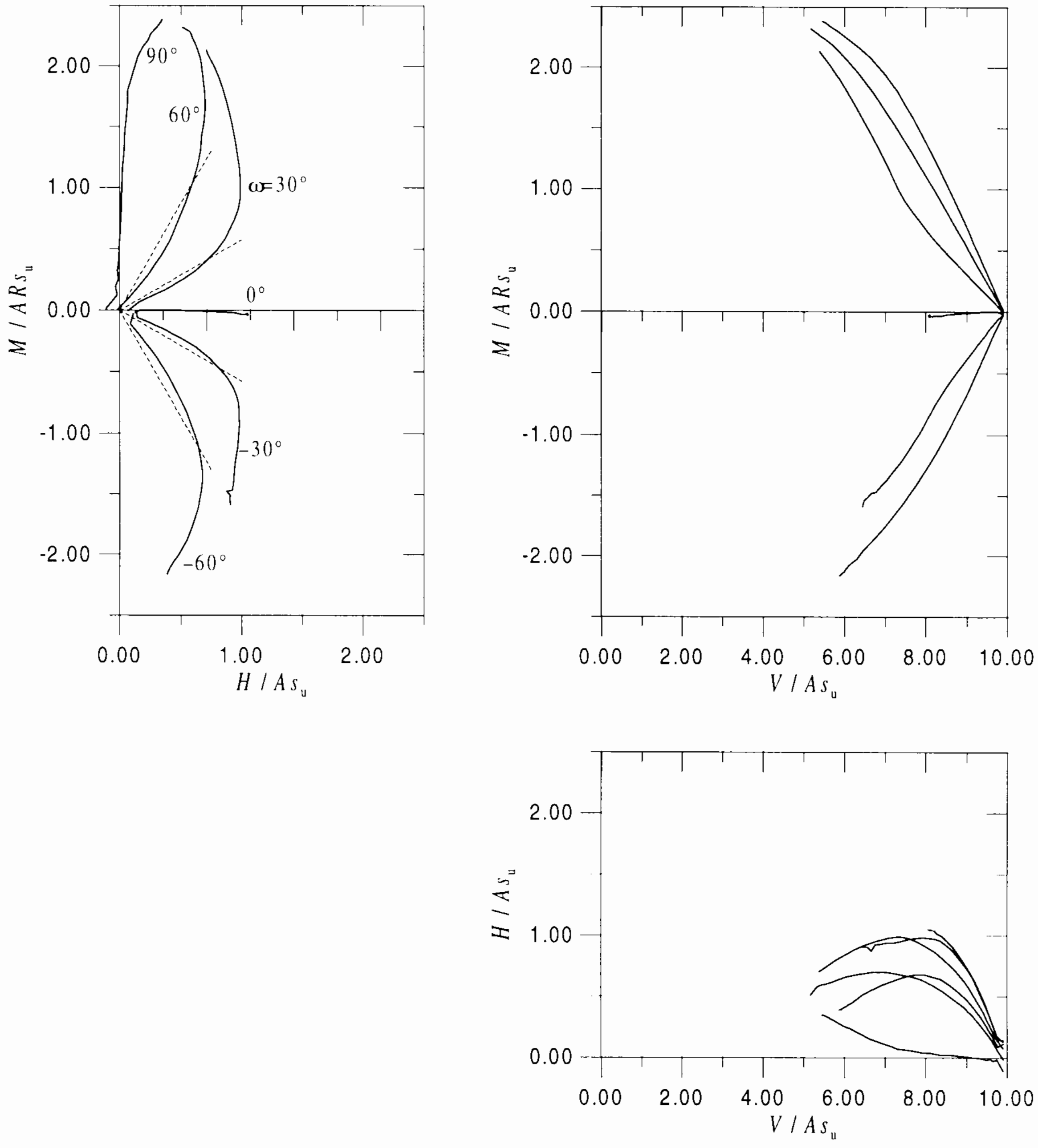

Figure 7.31: (V, H, M) curves from high V/V_0 of $z_D/2R = 0{\cdot}25$.

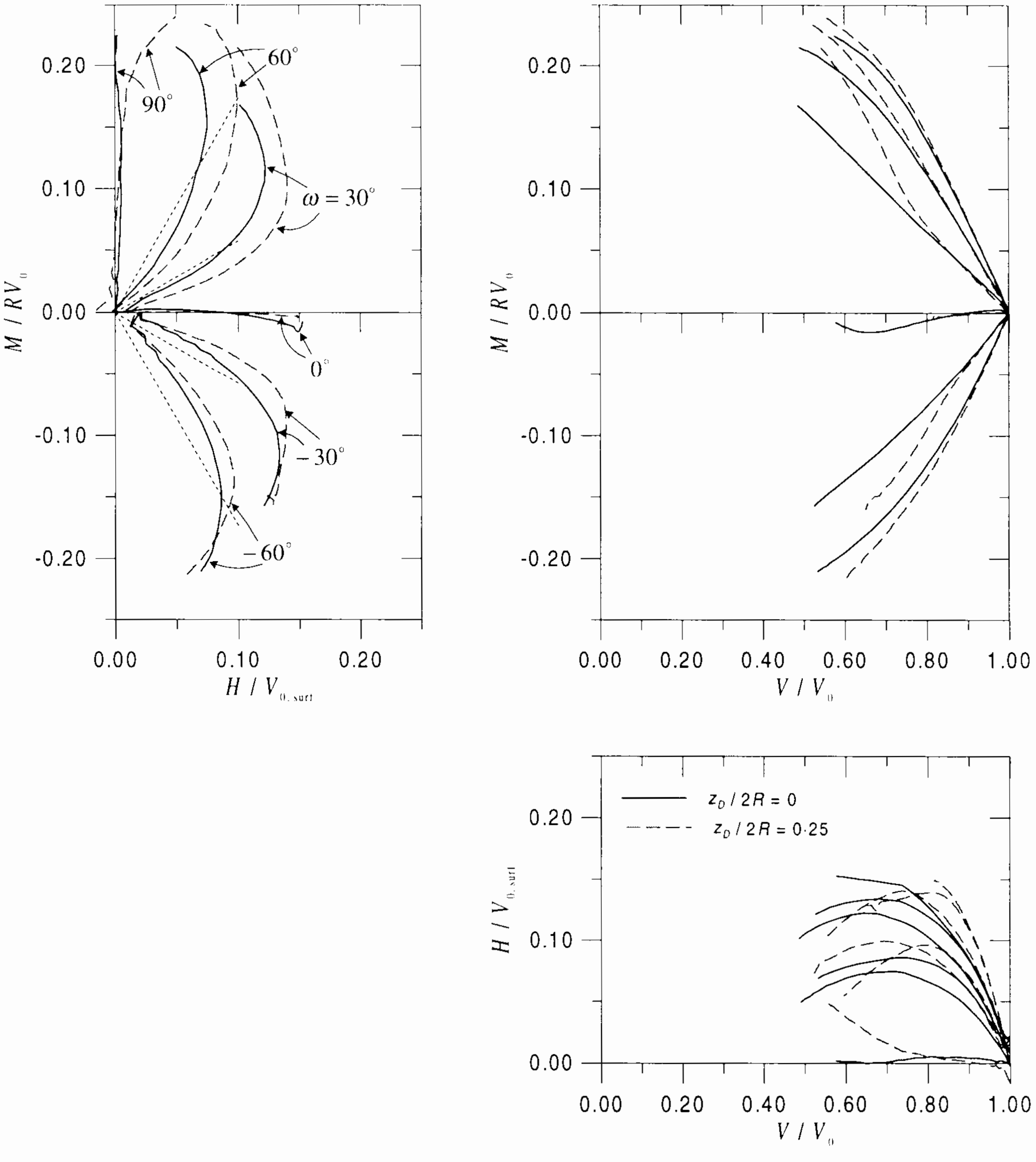

Figure 7.32: (V, H, M) curves from high V/V_0 of $z_D/2R = 0{\cdot}25$ and $z_D/2R = 0$ (H normalised to $V_{0,\mathrm{surf}}$).

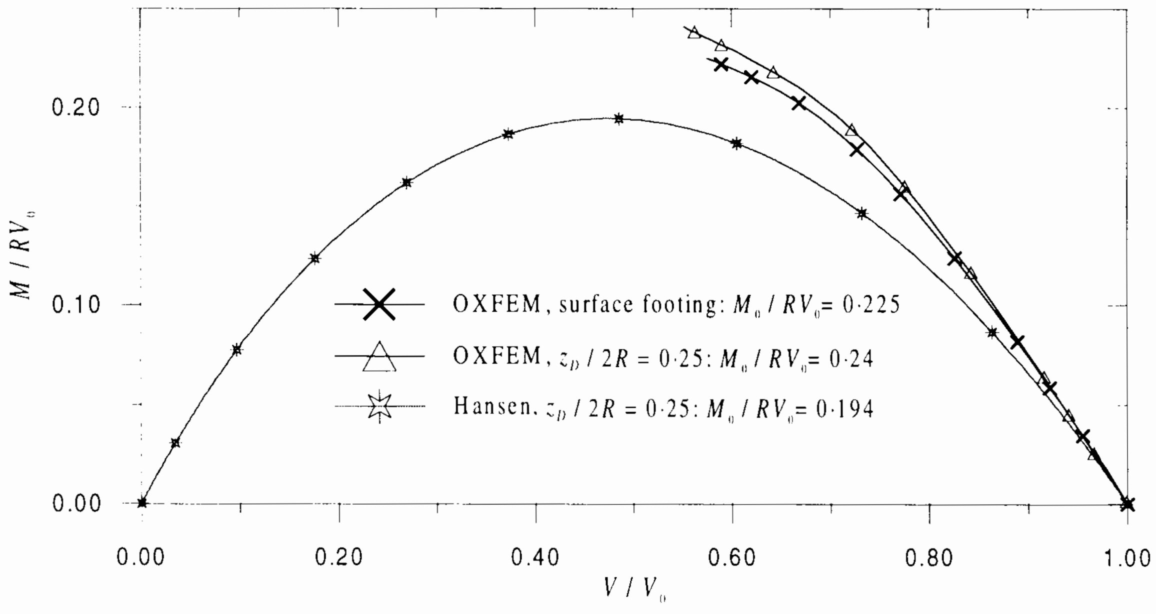

Figure 7.33: Interaction between vertical and moment loads (comparison between surface and embedded footings).

while the (V, M) interaction loci of the two are quite similar, the (V, H) interaction loci are significantly different. With the reduction of vertical load from $V/V_0 = 1$, the embedded footing can sustain a higher horizontal load $H/V_{0,\mathrm{surf}}$ than the surface footing. The transition between sliding failure and bearing failure for the embedded footing, therefore, occurs at a higher vertical load level than that of the surface footing.

As a result, the contours of the two bearing capacity envelopes are quite different. As can be seen in Fig. 7.35, though the two envelopes share similar features such as ellipse-like contours and the contour major axis lying in the quadrants of negative eccentricity, the size and the rotation of the ellipses are quite different.

7.4.4 Comparison with semi-empirical bearing capacity formulae

Also shown in Figs. 7.33 and 7.34 are the solutions by Vesic and Hansen for eccentric and inclined loads for a footing with embedment depth of $z_D/2R = 0{\cdot}25$. As for the case of surface footings, the two empirical methods for embedded footings are also conservative for eccentric loads (see Fig. 7.33) and even more so for inclined loads (see Fig. 7.34).

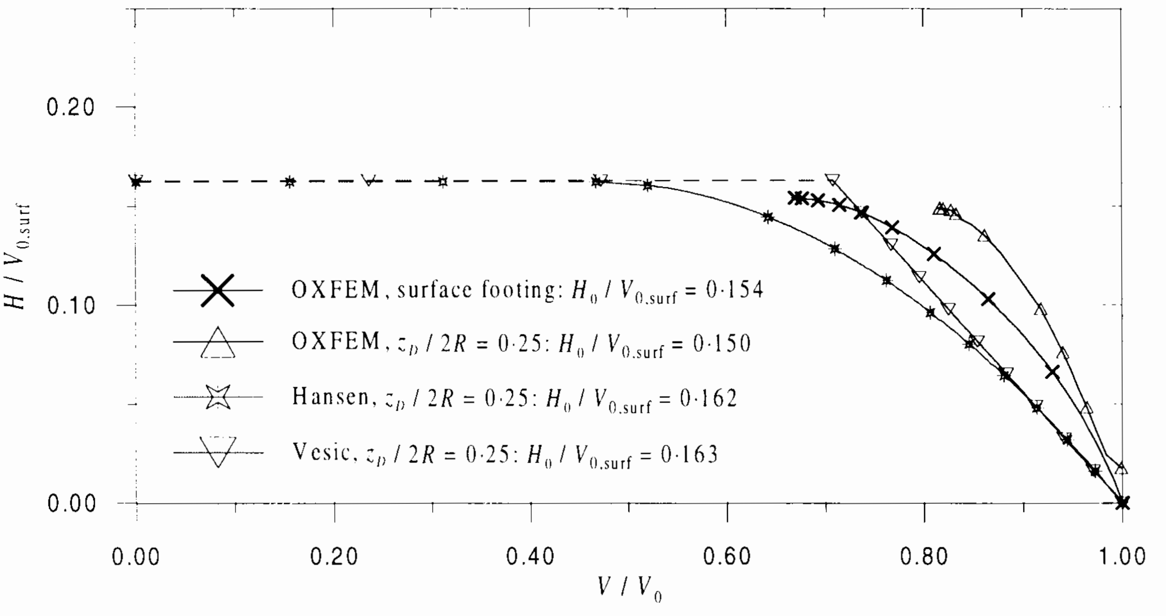

Figure 7.34: Interaction between vertical and horizontal loads (comparison between surface and embedded footings).

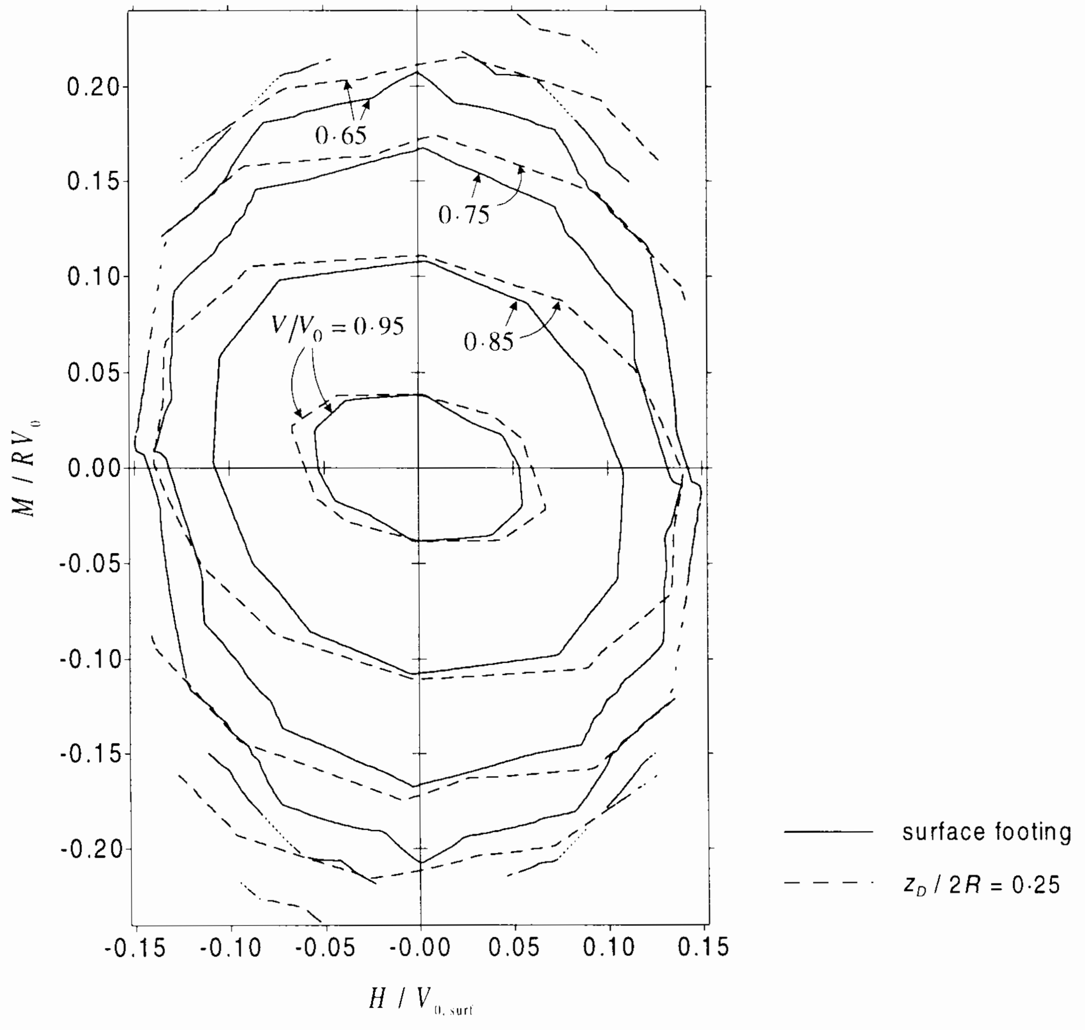

Figure 7.35: Comparison between the contours of surface footings and $z_D/2R = 0{\cdot}25$.

Chapter 8

Concluding remarks

8.1 Main findings

- As part of the study, a finite element program called OXFEM written by previous members of Oxford University Civil Engineering Group was updated and enhanced by the author. Some particular features which are relevant to this research are (a) capability to perform both two and three dimensional analyses; (b) stop and restart facility; (c) interface elements; (d) the soil strength can be varied with depth;
- The elastic behaviour of circular footings under vertical, horizontal and moment load was thoroughly investigated. The study also examined the effect of footing cone angle, embedment depths and Poisson's ratio of the soil on the behaviour. The elastic behaviour is quantified by the stiffness coefficients K_1, K_2, K_3 and K_4 (Equ. 2.1);
- In general, the results of this study shows that embedment depth has significant effect on the vertical stiffness, and also a more pronounced effect on the horizontal and moment stiffness. The cone angle was shown to have a more pronounced effect on the horizontal stiffness than on the vertical or moment stiffness;
- It was shown that the effect of embedment depth and cone angle can be decoupled and a multiplicative approach can be used to establish empirical expressions for K_1, K_2 and K_3^m (see, for example, Equ. 2.26). The effect of embedment depth and cone angle is expressed by the factors μ_{trench} and μ_{cone}. In addition, it was shown that an additive expression is suitable to express the location of the metacentre;

- Empirical expressions were then derived for all the stiffness coefficients, including the location of the metacentre, which can be used in practice for designing offshore foundations;

- For each stiffness coefficient, the effect of Poisson's ratio on μ_{trench} and μ_{cone} was investigated. It was found that the Poisson's ratio has a significant effect on μ_{trench} and μ_{cone} of K_1, and on μ_{cone} of K_3^m. The Poisson's ratio has virtually no effect on the horizontal stiffness K_2 or μ_{trench} of K_3^m;

- A new interface element, which behaves either as a frictional interface or as a cohesive interface depending on the normal stress, has been formulated. The special yield surface allowed the interface to model the soil–structure interaction problem under severe horizontal and moment loading without causing instability. The new interface element is formulated for both two dimensional and three dimensional analyses.

- A closed-formed exact solution for the integration of the stress–strain relationship of the two dimensional interface element (embedded in the three dimensional continuum) was found. This allows three dimensional analyses involving interface elements to be computed at a greater speed than using an incremental numerical integration technique;

- Before the bearing capacity envelope for strip footings was established, the two test procedures (i.e. the probing test procedure and tracking test procedure) were used to explore the (V, H) and (V, M) failure loci. The results of the faster procedure, the tracking method, were shown to be comparable to those of the probing test procedure, which is the more exact, but significantly slower, method. The tracking test procedure was then used to establish the bearing capacity envelope for both strip and circular footings;

- The bearing capacity envelope for strip footings was established. The contours of the bearing capacity envelope at high V/V_0 do not look like ellipses; they have a pointed transition from positive to negative moment. The sense of eccentricity (either positive or negative eccentricity) has practically no effect on the contours;

- The finite element results of this study were also compared with the results obtained from a different numerical method – the finite difference method as implemented in a computer package called FLAC. The similarity between the two sets of results gave a strong evidence for the uniqeness of the bearing capacity envelope;

- The bearing capacity envelope for flat surface circular footings was established. Unlike that of strip footings, the bearing capacity envelope of circular footings shows a significant effect of the sense of eccentricity on the contours (with respect to the vertical load) at high V/V_0 levels with both peak horizontal and moment loads at a certain vertical load level occur in negative eccentricity. This effect, however, diminishes as the vertical load decreases. Also, at high V/V_0, the contours have the elliptic shape. At low vertical load, the contours shows that a significant horizontal load can be applied without causing a significant drop in moment capacity;

- Based on the numerical results, an empirical expression was derived for the bearing capacity envelope of circular footings (Equ. 6.33). The envelope is essentially parabolic in the $H/V_0 = 0$ and $M/RV_0 = 0$ planes, and elliptical in the cross-sectional planes of constant V/V_0. The equation supports the equation of the same form obtained by Martin (1994) for conical footings. The simple expression allows easy hand calculations in design practice. It can also provide a model for soil to be incorporated in the analysis of the whole offshore structures;

- A comparison of the finite element results with other bearing capacity formulae (such as Meyerhof, 1956; Hansen, 1970; Vesic, 1975) showed that the bearing capacity formulae were largely more conservative (about -18%) in predicting the vertical and moment interaction locus. The bearing capacity formulae were also more conservative, though to a lesser extent (about -6%), in predicting the vertical and horizontal locus than the finite element results. For combined loading (i.e. horizontal load combined with moment load) the Hansen method was also shown to be more conservative than the finite element results, particularly in the quadrants of the negative eccentricity at high vertical load;

- The investigation of soil strength varying with depth showed that the bearing capacity envelope (V, H, M/R) is expanded by comparison with the envelope for a homogeneous soil. Its shape is also changed. However, by normalising the horizontal load to the vertical bearing capacity of uniform soil $V_{0,\rho=0}$, and normalising the other two component to V_0, the size and shape of the envelope (V/V_0, $H/V_{0,\rho=0}$, M/RV_0) remains relatively unchanged up to a large rate of of increase of soil strength. Therefore the bearing capacity envelope for flat surface footings on a uniform soil already established can be used for footings on a soil with strength varying linearly with depth with only minor changes;

- It was found that whilst the change in footing geometry from flat to conical increased significantly the maximum horizontal bearing capacity (and therefore the size of the bearing capacity envelope in the H direction), it did not change significantly the maximum moment bearing capacity nor the vertical bearing capacity (cf. the results for elastic stiffness);

- The results from the study of conical footings were shown to be comparable to Martin's (1994) results in terms of the maximum horizontal and moment bearing capacity. Both the two sets of results also showed that at lower vertical level (near $V/V_0 \approx 0{\cdot}5$), both peak horizontal and moment loads occur in *positive* eccentricity. At high vertical load levels, the results of this study, however, showed that both peak horizontal load and moment occurred in *negative* eccentricity, whereas Martin's (1994) results showed that both peak horizontal and moment loads occur in *positive* eccentricity;

- It was found that though the ten-noded tetrahedral element can give reasonably accurate results for surface footings, it cannot predict good vertical bearing capacity for embedded footings. Higher order elements may be needed to give better solutions;

- With increasing embedment depth, the vertical load capacity and the maximum moment load increase. At the same time, the maximum horizontal load remains unchanged. This feature is similar to that of soil with strength increasing with depth. However, an attempt to normalise horizontal load to $V_{0,\mathrm{surf}}$ (whereas vertical and moment loads to V_0) failed to produce a bearing capacity envelope comparable to that of the surface footing.

8.2 Future research

- Large overestimation of the vertical bearing capacity for embedded footings prompts the need for more research on this problem. A good mesh generator which can generate higher order elements (20-noded or 35-noded tetrahedra) may be needed to achieved high accuracy;

- The effect of consolidation is of great concern when designing an offshore foundation (Poulos, 1988). Under wave and storm loading, consolidation takes place. Due to the large dimensions of offshore foundations, under wave loading, the soil can only be partially drained. In investigating transient loading, it appears that the soil constitutive models and their computational efficiency are the primary concerns (Prevost, 1977; Zienkiewicz et al., 1978);
- It is shown from this parametric study that accurate solutions can be obtained by the finite element method for a wide range of problems with different soil profiles, footing geometry and complex loading. Because of the increasing number of variables involved, further research in the form of parametric studies may, however, not be so useful as a study of specific structures.

Bibliography

American Petroleum Institute (1993). *Recommended practice for planning, designing and constructing fixed offshore platforms - load and resistance factor design. RP 2A-LRFD, 1st ed.*, American Petroleum Institute, Washington DC.

Anderton, J. (1992). Finding the convex hull of a three-dimensional set of points, *Technical Report Third-year ECS project*, University of Oxford.

Atkinson, J. (1993). *An introduction to the mechanics of soils and foundations*, McGraw-Hill, London.

Bell, R. W. (1991). *The analysis of offshore foundations subjected to combined loading*, MSc thesis, University of Oxford, UK.

Bolton, M. D. (1979). *A guide to soil mechanics*, Macmillan, London.

Booker, J. R. (1984). Personal communication.

Borowicka, H. (1943). Uber ausmittig belaste starre platten auf elastich-isotropem untergrund, *Ingenieur-Archiv* **1**: 1–8.

Brocklehurst, C. J. (1993). *Finite element studies of reinforced and unreinforced two-layer soil systems*, DPhil thesis, University of Oxford, UK.

Burd, H. J. & Brocklehurst, C. J. (1991). Parametric studies of a soil reinforcement problem using finite element analysis, *Proc. of 7th IACMAG, Cairns, Australia*, Vol. 3, pp. 1783–88.

Butterfield, R. (1981). Another look at gravity platform foundations, *CISM course on Soil Mech. Fndn. Engng. in Offshore Technology, Udine.*

Butterfield, R. (1993). A new approach to safety factors for shallow foundations: load combination factors as a basis for risk assessment, *ICE Conf. on risk and reliability in fround engineering*, Thomas Telford, London, pp. 112–125.

Butterfield, R. & Banjerjee, P. K. (1971). A rigid disk embedded in an elastic half space, *Geotech. Engng.* **2**: 35–52.

Butterfield, R. & Ticof, J. (1979). Design parameters for granular soils (discussion contribution), *Proc. 7th Europen Conf. Soil Mech. Fndn. Engng. , Brighton, UK*, Vol. 4, pp. 259–261.

Bycroft, R. N. (1956). Forced vibrations of a rigid circular plate on a semi-infinite elastic space and on an elastic stratum, *Phil. Trans. Roy. Soc. A.* **248**: 327–368.

Davis, E. H. & Booker, J. R. (1973). The effect of increasing strength with depth on the bearing capacity of clays, *Geotechnique* **23**(4): 551–563.

Dean, E. H., James, R. G., Schofield, A. S., Tan, F. S. C. & Tsukamoto, Y. (1992). The bearing capacity of conical footings on sand in relation to the behaviour of spudcan footings of jack-ups, *Proc. Wroth Memorial Symp. "Predictive Soil Mechanics", Oxford, UK*, Thomas Telford, London, pp. 230–253.

Desai, C. S., Zaman, M. M., Lightner, J. G. & Siriwardane, H. J. (1984). Thin layer element for interfaces and joints, *International journal of numerical and analytical methods in geomechanics* **8**: 19–43.

Eason, G. & Shield, R. T. (1960). The plastic indentation of a semi-infinite solid by a perfectly rough circular punch, *Journal of Applied Mathematics and Physics (ZAMP)* **11**: 33–43.

Ellers, F. S. (1982). Advanced offshore oil platforms, *Scientific American* **246**(4): 31–41.

Endley, S. N., Rapoport, V., Thompson, P. J. & Baglioni, V. P. (1981). Prediction of jack-up rig footing penetration, *Proc. 13th Offshore Technology Conf., Houston*, Vol. OTC4133.

Frydman, S. R. (1995). Personal communication.

Gazetas, G., Tassoulas, J. L., Dobry, R. & O'Rourke, M. J. (1985). Elastic settlement of arbitrarily shaped foundations embedded in half-space, *Geotechnique* **35**(3): 339–416.

Gazetas, G. & Tassoulas, L. (1987). Horizontal stiffness of arbitrarily shaped embedded foundations, *Journal of geotechnical engineering, ASCE* **113**(5): 440–457.

Gemenhardt, J. P. & Focht, J. A. (1970). Theoretical and observed performance of mobile rig footings on clay, *Proc. 2nd offshore technology conf., Houston, OTC 1201*.

Gens, A., Carol, I. & Alonso, E. E. (1988). An interface element formulation for the analysis of soil – reinforcement interaction, *Computer and Geotechnics* **7**: 133–151.

Gens, A., Carol, I. & Alonso, E. E. (1989). Elasto-plastic model for joints and interfaces, *in* D. R. J. Owen, E. Hinton & E. Onate (eds), *Proc. 2nd Int. Conf. on Computational Plasticity, Barcelona*, Vol. 2, pp. 1251–1264.

Gens, A., Carol, I. & Alonso, E. E. (1990). A constitutive model for rock joints formulation and numerical implementation, *Computer and Geotechnics* **9**: 3–20.

Gens, A., Carol, I. & Alonso, E. E. (1995). Rock joints: Fem implementation and applications, *in* A. P. S. Selvadurai & M. J. Boulon (eds), *Mechanics of geomaterial interfaces*, Elsevier Science B. V., pp. 395–420.

Gerrard, C. M. (1980). Solution for point loads and generalised circular loads applied wihin cross anisotropic media, *Technical Report 28*, C. S. I. R. O Austr. Div. App. Geomech.

Gerrard, C. M. & Harrison, W. J. (1970). Circular loads applied to a cross-anisotropic half space, *Technical Report 8*, C. S. I. R. O Austr. Div. App. Geomech.

Ghaboussi, J., Isenberg, J. & Wilson, E. L. (1973). Finite element for rock joints and interfaces, *Journal of soil mechanics, ASCE* **99**(SM10).

Goodman, R., Taylor, R. L. & Brekke, T. L. (1968). A model for the mechanics of joints rock, *Journal of soil mechanics, ASCE* **94**(SM3).

Gottardi, G. & Butterfield, R. (1993). On the bearing capacity of surface footings on sand under general planar loads, *Soils and foundations of Japanese society of soil mechanics and foundation engineering* **33**(3): 68–79.

Griffiths, D. V. (1985). Numerical modelling of interfaces using conventional finite elements, *in* T. Kawamoto & Y. Ichikawa (eds), *Proc. 5th. Int. Conf. Num. Meth. in Geomech.*, Vol. 2, pp. 837–844.

Hambly, E. C. (1985). Fatigue vulnerability of jack-up platforms, *Proc. Instn. Civ. Engrs., Pt. 1*, Vol. 77, pp. 161–178.

Hansen, B. (1970). A revised and extended formula for bearing capacity, *Bulletin of Danish Geotechnical Institute, Copenhagen* **28**: 5–11.

Hohberg, J. M. (1992). *A joint element for the nonlinear dynamic analysis of arch dams*, Birkhauser Publishers, Basel.

Houlsby, G. T. (1996). Personal communication.

Houlsby, G. T. & Martin, C. M. (1992). Modelling of the behaviour of foundations of jack-up units on clay, *Proc. of the Wroth memorial symposium, Predictive soil mechanics*, Oxford, UK, pp. 339–358.

Houlsby, G. T. & Wroth, C. P. (1984). Calculation of stresses on shallow penetrometers and footings, *in* B. Denness (ed.), *Seabed mechanics, from Proc. Symp. Seabed Mech. , Univ. Newcastle upon Tyne, 1983*, Graham and Trotman, London, pp. 107–112.

Krieg, R. D. & Krieg, D. B. (1977). Accuracies of numerical solution methods for the elastic-perfectly plastic model, *Journal of pressure vessel technology, ASME* **99**: 510–515.

Martin, C. M. (1994). *Physical and numerical modelling of offshore foundations under combined loads*, DPhil thesis, University of Oxford, UK.

McClelland, B., Young, A. G. & Remmes, B. D. (1982). Avoiding jack-up rig foundation failures, *Geotech. Engng.* **13**(2): 151–188.

Meyerhof, G. G. (1953). The bearing capacity of foundations under eccentric and inclined loads, *Proc. 3rd Int. Conf. Soil Mech. Fndn. Engng. , Zurich*, Vol. 1, pp. 440–445.

Meyerhof, G. G. (1956). Rupture surfaces in sand under oblique loads (discussion), *Journal of soil mechanics, ASCE* **82**(SM3).

Meyerhof, G. G. (1963). Some recent research on the bearing capacity of foundations, *Canadan Geotech. J.* **1**: 77–87.

Noble Denton & Associates (1987). *Foundation fixity of jack-up units: a joint industry study*, Noble Denton & Associates, London.

Nova, R. & Montrasio, L. (1991). Settlements of shallow foundations on sand, *Geotechnique* **41**(2): 243–256.

Palmer, A. C., Maier, G. & Drucker, D. C. (1967). Normality relations and convexity of yield surfaces for unstable materials or structural elements, *Journal of applied mechanics, Trans. of the ASME, Series E* pp. 464–470.

Pande, G. N. & Sharma, K. G. (1979). On joint/interface elements and associated problems of numerical ill conditioning, *International journal of numerical and analytical methods in geomechanics* **3**: 293–300.

Poulos, H. G. (1988). *Marine Geotechnics*, Unwin Hyman, London.

Poulos, H. G. & Davies, E. H. (1974). *Elastic solution for soil and rock mechanics*, John Wiley & Son, New York.

Prevost, J. H. (1977). Mathematical modelling of monotonic and cyclic undrained clay behaviour, *International journal of numerical and analytical methods in geomechanics* **1**(2): 195–216.

Rektorys, K. (1969). *Survey of applicable mathematics*, Iliffe, London.

Roscoe, K. H. & Schofield, A. N. (1956). The stability of short pier foundations in sand, *British Welding Journal* (August): 343–354.

Schellekens, J. C. J. & de Borst, R. (1993). On the numerical integration of interface elements, *International journal of numerical methods in engineering* **36**: 43–66.

Sedgewick, R. (1988). *Algorithms, 2nd edition*, Addison-Wesley.

Selnes, P. B. (1982). Geotechnical problems in offshore earthquake engineering, *Technical Report Report No. 140*, NGI, Oslo.

Shield, R. T. (1955). On the plastic flow of metals under conditions of axial symmetry, *Proceedings of the Royal Society, Series A, Mathematical and Physical Sciences* **233**(1192).

Skempton, A. W. (1951). The bearing capacity of clay, *Proc. Building Reasearch Congress*, Vol. 1, pp. 180–189.

Sloan, S. W. (1981). *Numerical analysis of incompressible and plastic solids using finite elements*, PhD thesis, University of Cambridge, UK.

Sloan, S. W. & Randolph, M. F. (1982). Numerical prediction of collapse loads using finite element method, *International journal of numerical and analytical methods in geomechanics* **6**.

Smith, I. M. (1982). Analysis of fixed offshore platforms 1972-1982, *Proc. 4th Int. Conf. Num. Meth. Geomech. , Edmonton, Canada*, Vol. 3, pp. 1163–1180.

Spence, D. A. (1968). Self similar solutions to adhesive contact problems with incremental loading, *Proc. Roy. Soc. A.*, Vol. 305, pp. 55–80.

Tan, F. S. C. (1990). *Centrifuge and theoretical modelling of conical footings on sand*, PhD thesis, University of Cambridge, U. K.

Vesic, A. S. (1975). Bearing capacity of shallow foundations, *in* H. F. Winterkorn & H. Y. Fang (eds), *Foundation Engineering Handbook*, Van Nostrand, New York, pp. 121–147.

Wilson, E. L. (1965). Structural analysis of axi-symmetric solids, *J.A.I.A.A.* **3**: 2269–74.

Wilson, E. L. (1977). Finite elements for foundations, joints and fluids, *in* G. Gudehus (ed.), *Finite element methods in geomechanics*, John Wiley & Sons, chapter 10.

Young, A. G., Remmes, B. D. & Meyer, B. J. (1984). Foundation performance of offshore jack-up drilling rigs, *Journal of soil mechanics, ASCE* **110**(7): 841–859.

Zaharescu, E. (1961). Sur la stabilite des fondations rigides, *Proc. 5th Int. Conf. Soil Mech. Fndn. Engng. , Paris*, Vol. 1, pp. 867–871.

Zienkiewicz, O. C. (1983). *The finite element method*, McGraw-Hill.

Zienkiewicz, O. C., Best, B., Dullage, C. & Stagg, K. G. (1970). Analysis of nonlinear problems in rock mechanics with particular reference to jointed rock systems, *Proc. 2nd. ISRM Congr., Beograd*, Vol. 2, pp. 501–509.

Zienkiewicz, O. C., Chang, C. T. & Hinton, E. (1978). Non-linear seismic response and liquefaction, *International journal of numerical and analytical methods in geomechanics* **2**(4): 381–404.